Modelling Multi-Scale Problems in the Transmission Line Modelling Method

By

Xuesong Meng, BEng, MEng

Thesis submitted to the University of Nottingham for the degree of Doctor of Philosophy, April, 2014

ABSTRACT

Modern electromagnetic problems are becoming increasingly complex and their simulation must take into account geometrical features that are both large and small compared to the wavelength of interest. These multi-scale problems lead to a heavy computational burden in a discretised computational simulation approach since the small features require fine mesh to be used in the simulation, resulting in large run time and memory storage. To overcome such problems, this thesis presents an efficient and versatile method for embedding small features into an otherwise coarse mesh. The embedded model eliminates the need for discretising the small features and allows for a relative large mesh size to be used, thus saving the computational costs.

The subject of the thesis is embedding a thin film as a small feature into the numerical Transmission Line Modelling (TLM) method, although any small feature with known analytical response can be implemented in practice. In the embedded model, the thin film is treated as a section of transmission line, whose admittance matrix is used to describe the frequency response of the thin film. The admittance matrix is manipulated by expanding the constituent cotangent and cosecant functions analytically, and then transforming them from the frequency domain to the time domain using the inverse Z transform and general digital filter theory. In this way the frequency responses of the thin film are successfully embedded into the TLM algorithm. The embedded thin film model can be applied to both single and multiple thin film layers.

The embedded thin film model has been implemented in the one-dimensional (1D) and two-dimensional (2D) TLM method in the thesis. In the 1D TLM method, the embedded thin film model is used to investigate the reflection and transmission properties of lossy, anisotropic and lossless thin films, e.g. carbon fibre composite (CFC) panels, titanium panels, antireflection (AR) coatings and fibre Bragg gratings (FBG). The shielding performance of CFC panels is also discussed. In the 2D TLM method, the embedded thin film model is extended to model arbitrary excitations and curved thin films. The electromagnetic behaviour of infinitely long CFC panels with oblique

incidence and a CFC panel of finite length with a point source excitation are studied using the embedded thin film model. The resonant effects of CFC circular and elliptical resonators and the shielding performance of a CFC airfoil with the profile of NACA2415 are investigated using the embedded curved thin film model. In addition, the effects of small gaps in the airfoil structure on the shielding performance are also reported.

All the examples discussed in the thesis have validated the accuracy, stability, convergence and efficiency of the embedded thin film model developed. At the same time, the embedded thin film model has been proven to have the advantage of significantly saving computational overheads.

ACKNOWLEDGEMENTS

First and Foremost, I would like to express my deepest and sincere gratitude to my supervisors, Prof. Phillip Sewell, Dr. Ana Vukovic and Prof. Trevor Benson, for their excellent guidance and continuous support throughout my PhD studies. I am really grateful for their patience in helping me solve my problems and amend my writings. Without their immeasurable contributions, this thesis will not have been completed.

Furthermore, I would like to thank Prof. Dave Thomas and Dr. Steve Greedy for their suggestions and help on my research work. I would also like to thank our former secretary Ms Kathryn Sanderson for her daily support in a working environment unfamiliar to me.

My thanks also go to members of the George Green Institute for Electromagnetics Research (GGIEMR). The members of GGIEMR have contributed immensely to my personal and professional time at Nottingham. The group has been a source of friendships as well as good advice and collaboration. I am especially grateful for the help from Sendy Phang, Dr. Harshana Dantanarayana, Dr. Hiroki Wakatsuchi, Dr. Deyun Liu, Dr. Brian Teo, Dr. Ken Chan, Dr. Rawin Vongurai, Dr. Sam Cole, Ayodele Oladeji, Hayan Nasser, Ahmed Elkalsh, and Dan Simmons.

I thank all my friends at Nottingham for bringing fun to my life. Especially, I would like to thank my flatmate, Dr. Jie An, for her continuous and selfless help and support in the last three years.

Last but not the least, I would like to thank my family: my parents, Fenglan Liu and Qingyu Meng, for giving birth to me at the first place and supporting me materially and spiritually throughout my life, and my sister, Xueyan Meng, and my brother-in-law, Xiaobin Sun, for supporting me and guiding me during my life.

谨以此博士论文献给生我养我的父母孟庆玉，
刘凤兰，感谢他们二十多年来对我的理解和支持。

——孟雪松

LIST OF PUBLICATIONS

The following papers have arisen in whole or part out of the work described in this thesis.

1. **Xuesong Meng**, P. Sewell, A. Vukovic, Sendy Phang and T. Benson, "Modelling Curved Carbon Fibre Composite (CFC) Structures in Transmission-Line Modelling (TLM) method," submitted to IEEE transactions on EMC.
2. **Xuesong Meng**, P. Sewell, A. Vukovic, and T. Benson, "Application of Broadband Carbon Fibre Composite (CFC) Model with TLM," submitted to IEEE transactions on EMC.
3. **Xuesong Meng**, P. Sewell, A. Vukovic, and T. Benson, "Electromagnetic behaviour of carbon fibre composite airfoil," accepted by Electromagnetics Research Symposium PIERS 2014.
4. **Xuesong Meng**, P. Sewell, A. Vukovic, Hayan Nasser and T. Benson, "Embedded Carbon Fibre Composite (CFC) Model for Arbitrary Contour Surfaces," in Computation in Electromagnetics (CEM2014), the 9th International Conference on, pp. 1-2, 2014.
5. **Xuesong Meng**, P. Sewell, A. Vukovic, H. G. Dantanarayana and T. Benson, "Efficient Broadband Simulations for Thin Optical Structure," Optical and Quantum Electronics. Volume 45, No. 4, pp. 343-348, 2013.
6. T. Benson, **Xuesong Meng**, A. Vukovic, and P. Sewell, "Sub-wavelength Dielectric Features in Numerical Code," in Mathematical Methods in Electromagnetic Theory (MMET), 2012 International Conference on, pp. 233-236, 2012.
7. P. Sewell, T. Benson, A. Vukovic, and **Xuesong Meng**, "Time Domain Models of Thin Dielectric Layers," in Transparent Optical Networks (ICTON2012), the 14th International Conference on, Tu.C5.1, pp. 1-4, 2012.
8. **Xuesong Meng**, P. Sewell, A. Vukovic, and T. Benson, "A New TLM Model for Thin Optical Features", in Optical Waveguide Theory and

Numerical Modelling (OWTNM2012), the 19th International Workshop on, pp.27, 2012.

9. **Xuesong Meng**, P. Sewell, A. Vukovic, and T. Benson, "Efficient Embedding of Thin Sheet Models in TLM Simulations", in Electromagnetics Research Symposium PIERS 2012, the 31st Progress in, pp.305 ,2012.
10. H. G. Dantanarayana, **Xuesong Meng**, P. Sewell, A. Vukovic, and T. Benson, "Techniques for Embedding Non-linear Materials in TLM," in Transparent Optical Networks (ICTON2011), the 13th International Conference on, Tu.D6.5, pp. 1-4, 2011.

LIST OF SYMBOLS

$\vec{E}$	Electric field intensity vector
$\vec{B}$	Magnetic flux density vector
$\vec{H}$	Magnetic field intensity vector
$\vec{D}$	Electric flux density vector
$\vec{J}$	Current density vector
ρ	Electric charge density
ε	Permittivity of the material
μ	Permeability of the material
$E_x,\ E_y, E_z$	Electric field intensity components
H_x, H_y, H_z	Magnetic field intensity components
J_x, J_y, J_z	Current density components
σ_e	Electric conductivity of the material
R	Series resistance per unit length
G	Shunt admittance per unit length
L	Series inductance per unit length
C	Shunt capacitance per unit length
dz	Per unit length or the mesh size
v	Transient voltage in a circuit
i	Transient current in a circuit
μ_0	Permeability of free space
ε_0	Permittivity of free space
Z_0	Characteristic impedance of free space
Δt	Time step in the TLM
c	The velocity of the wave propagation in free space
n	A TLM node number
V_n	The total voltage at node n
VR_n^i	The incident voltage from the right side of node n
VR_n^r	The reflected voltage from the right side of node n
VL_{n+1}^i	The incident voltage from the left side of node n+1
VL_{n+1}^r	The reflected voltage from the left side of node n+1
Z_{TL}	Characteristic impedance of transmission lines
dl	The mesh size in the 2D and 3D TLM
n_x, n_y	Indices of a 2D TLM node
I_x, I_y, I_z	The current in the x, y and z directions
V_x, V_y, V_z	The voltages in the x, y, and z directions
$V_1^i, V_2^i, V_3^i, V_4^i$	The incident voltages at the ports 1, 2, 3 and 4 of node (n_x, n_y)
$V_1^r, V_2^r, V_3^r, V_4^r$	The reflected voltages at the ports 1, 2, 3 and 4 of node

	(n_x, n_y)
$\underline{\underline{S}}$	Scattering matrix
Z_C	The characteristic impedance of the capacitance
χ_e	The electric susceptibility of the medium
VC_n^i, VC_n^r	The incident and reflected voltages from the capacitive stub
J_{efy}, J_{mfz}	The free electronic current and magnetic voltage densities
σ_m	Magnetic resistivity of the medium
χ_m	Magnetic susceptibility of the medium
Y	Characteristic admittance of thin film
θ	Electrical length of thin film
ω	Angular frequency
d	Thickness of thin film
R	Reflection coefficients of thin film
T	Transmission coefficients of thin film
y_1, y_2	Characteristic admittance of TLM node from the left and right side of thin film
j	Imaginary unit
s	Complex argument in s domain
z	Complex argument in z domain
N	The number of terms used in cotangent and cosecant function expansions
$P_i(z), Q_i(z)$	First order or multiple order polynomials
$R_i(z), S_i(z)$	First order or multiple order polynomials
$x(z)$	Input of the digital filter system
$w_i(z)$	Output of a digital filter
$w(z)$	Output of a parallel combination of a number of digital filters
$y(z)$	Overall output of the digital filter system
A_1, B_1, C_1	Constant coefficients of cotangent and cosecant function expansions in Z domain
A_2, B_2	Constant coefficients of cotangent and cosecant function expansions in Z domain
A_k, B_k, C_k	Constant coefficients of cotangent and cosecant function expansions in Z domain
M_1, M_2, M_3	Constant gain of cotangent and cosecant function expansions in Z domain
φ	The angle between the electric field and the x axis
$\hat{x}, \hat{y}$	The unit vectors in the x and y directions
n_i	Refractive index of layer i
ρ_i	Reflection coefficients from the left of interface i
τ_i	The transmission coefficient to the left of interface i
k_i	Wavenumber in layer i

λ_0	Operating wavelength
$S_{11}, S_{12}, S_{21}, S_{22}$	The scattering coefficients or scattering parameters
Γ_e	Reflection coefficients for the even mode
Γ_o	Reflection coefficients for the odd mode
Z_{ine}	The input impedance for the even mode
Z_{ino}	The input impedance for the odd mode
μ_r	Relative permeability of the material
ε_r	Relative permittivity of the material
Z_L	The load impedance
E^i	Incident electric field
E^r	Reflected electric field
E^t	Transmitted electric field
δ	Skin depth
f_0	Operating frequency
θ_0	Specific electrical length corresponding to f_0
Z_{TE}	Transverse impedance for TE-polarised wave
Z_{TM}	Transverse impedance for TM-polarised wave
n_x, n_y	The index of a 2D node along x and y axis
$J_m(x)$	Bessel function with order m
χ'_{mn}	Zeroes of the derivative of the Bessel function $J_m(x)$
χ_{mn}	Zeroes of the Bessel function $J_m(x)$
r	Radius of a circle

ACRONYMS

FDTD	Finite Difference Time Domain method
TLM	Transmission Line Modelling
FEM	Finite Element Method
MOM	Method of Moments
EMC	Electromagnetic Compatibility
CFC	Carbon Fibre Composite
HSCN	Hybrid Symmetrical Condensed Node
SIBCs	Surface Impedance Boundary Conditions
INBCs	Impedance Network Boundary Conditions
VF	Vector Fitting
ESD	Electrostatic Discharge
1D	One-Dimensional
2D	Two-Dimensional
3D	Three-Dimensional
AR	Antireflection
FBG	Fibre Bragg Grating
SCN	Symmetrical Condensed Node
EM	Electromagnetic
FFT	Fast Fourier Transform
SE	Shielding Effectiveness
TE	Transverse Electric
TM	Transverse Magnetic
PEC	Perfect Electric Conductor
NACA	National Advisory Committee for Aeronautics

Contents

1.Introduction

1.1. Background

Simple electromagnetic problems can be solved analytically using the Maxwell equations. However, it is difficult to get analytical solutions for the electromagnetic problems involved in modern complex systems. With improved computer performance and especially parallel computer architectures, computer simulations have come to dominate the analysis of electromagnetic wave propagation through complex geometries mixed material compositions. Over the years, a number of electromagnetic simulation techniques have been developed, such as the Finite Difference Time-Domain (FDTD) method [1.1], the Finite Element Method (FEM) [1.2], the Method of Moments (MOM) [1.3] and the Transmission Line Modelling (TLM) method [1.4].

The FDTD and TLM methods are numerical full-wave techniques for the solutions of Maxwell equations in the time domain. At first sight, they offer significant advantages for dealing with complex geometries in a relatively straightforward manner. Moreover, as the trend towards wider bandwidth systems continues, the use of time domain algorithms that can obtain a response over a range of frequencies in one time domain simulation is very attractive. Furthermore, in the presence of complex materials, such as non-linear [1.5] materials, time domain simulations are necessary. However, one major disadvantage of such numerical techniques is their computational intensity as they require that the full detail of the geometry of the problem at hand is explicitly discretised.

The disadvantage of the time domain methods becomes more obvious in a multi-scale problem, which often exists in practice [1.6]. It is quite common to have very different physical scales (relative to the wavelength) in the same problem, especially in the study of Electromagnetic Compatibility (EMC). For example, carbon fibre composite (CFC) materials have been extensively used in the aircraft industries [1.7] due to their high strength-to-weight ratio and ease of fabrication [1.8], and one key area of research is in the reaction of the

CFC materials used in aircraft to lightning strikes [1.9 ~ 1.12]. The thickness of the CFC panel used in C-27J aircraft [1.9] is around 1 mm while the maximum length of the aircraft is around 22 m. The small thickness of the CFC panel thus needs to be dealt within a large problem space. If the conventional TLM or FDTD method is used to model such a system, the mesh size should be much smaller than the thickness of the panel in order to accurately consider its effects. For example, if the mesh size is chosen to be 0.1 mm for the whole problem in the 1D TLM or FDTD model, there will be at least 220,010 nodes in the simulation. If 2D or 3D TLM or FDTD model is considered, the number of nodes will increase substantially, which results in huge computational costs, including both run time and memory storage.

One possible method for handling multi-scale problems is to use a non-uniform mesh [1.6], which allows that the very small mesh is only applied to areas where the fine features are present, thus maintaining the computational efficiency. As examples of this technique, the multi-grid or sub-grid technique has been reported for the FDTD method in [1.13 ~ 1.17] and the TLM method in [1.18 ~ 1.21]. A hybrid mesh for the TLM method, the hybrid symmetrical condensed node (HSCN), was also discussed in [1.4] and [1.22 ~ 1.24]. Futhermore, a multi-level Octree mesh has been reported in [1.25] and adopted in the CST microwave studio software [1.26]. Fig.1 (a) and (b) show the schematic of a multi-grid mesh and a multi-level Octree mesh, respectively. The commercial software FEKO adopts variable mesh densities in a single model to account for the multi-scale problems. Although these techniques maintain the computational efficiency to a certain extent, they have difficulties in dealing with power conservation at the interface between the fine and coarse mesh regions. Furthermore, the time step of the overall simulation is defined with respect to the smallest mesh size in the problem, still resulting in long run time.

The alternative method is to use the local solutions embedded in a uniform mesh [1.6]. Since the electromagnetic response of particular canonical features within a larger computational environment is often highly localised, a specialised model for such features can be developed in isolation which can

then be coupled to the rest of the simulation through a standardised interface, thus avoiding the need to discretise within the feature. The specialised model can achieve a significant reduction in computational costs, not only by eliminating discretisation within the fine feature but also by permitting a larger mesh size in the exterior region. The challenges of this technique lie in obtaining the local solutions and devising appropriate interfaces [1.6].

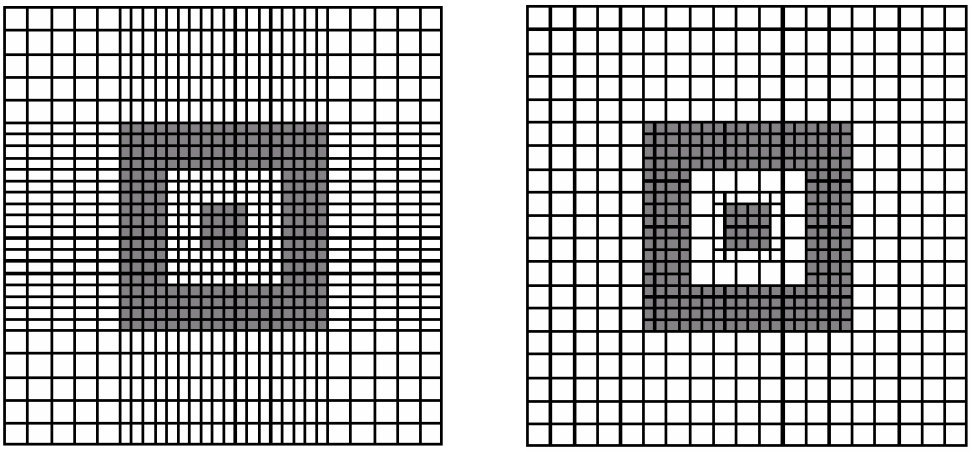

(a) (b)

Fig.1 (a) A multi-grid mesh and (b) a multi-level Octree mesh from [1.25]

The development of embedded models in both the FDTD and the TLM methods will be discussed in the next section.

1.2. Embedded Models in Numerical Methods

In this section, the development of embedded models in both the FDTD and the TLM methods is overviewed first. The major achievements of this thesis are then summarized.

In the FDTD method, several techniques have been used to obtain the local solutions in a uniform mesh, such as the surface impedance boundary conditions (SIBCs) [1.27], impedance network boundary conditions (INBCs) [1.28] and effective boundary conditions [1.29].

Surface impedance boundary conditions were first proposed by Leontovich in the 1940's [1.27] and were rigorously developed by Senior in 1960 [1.30]. This technique allows the replacement of lossy dielectric-coated objects or imperfect conductors with surface impedance boundary conditions, thus avoiding discretising the objects. It was firstly applied in a frequency domain analysis [1.31] and then adopted in the time domain method [1.29 ~ 1.38]. The SIBCs technique was introduced in the FDTD method in the 1990s. Maloney and Smith [1.32 ~ 1.33] deployed the SIBCs to replace lossy conductors for reducing the solution space and saving computational costs. It was efficiently implemented by using the recursive convolution of a series of exponential functions to obtain the time domain SIBCs. Beggs et al. [1.34] extended the constant SIBCs developed for a single frequency to a dispersive SIBCs applicable over a large frequency bandwidth. Kellaili et al. [1.35] implemented an oblique incident angle into the SIBCs for vertical or horizontal polarizations of locally plane waves. Oh et al. [1.36] presented an efficient implementation of SIBCs in the FDTD for a lossy dielectric half-space and a thin lossy dielectric medium. Higher order SIBCs [1.37 ~ 1.40] have also been developed for the FDTD method to account for 2D and 3D scattering problems involving a lossy medium. Recently, Santis et al. [1.41] approximated the surface impedance function of a lossy medium with a series of rational functions by using the vector fitting (VF) technique, which has the advantage of reducing the number of poles, thus reducing the order of the rational functions, for a limited frequency range while retaining the same order of accuracy.

Since SIBCs are only valid when the skin depth of the panel is much smaller than its thickness [1.34], the impedance network boundary conditions (INBCs) were proposed as an extension of SIBCs to account for the case where the thickness of the panel is comparable to, or smaller than, its skin depth. The implementation of the INBCs is based on the equivalence of the conductive shield to a transmission line, represented by a two-port network in terms of an impedance matrix in the frequency domain. The time domain procedures of INBCs are developed by algorithms of recursive convolutions. INBCs were introduced into the FDTD method by Feliziani et.al. [1.28] to analyse the electromagnetic field around penetrable shield structures. This technique was

then extended to analyse complex shielded problems in the 3D domain [1.42]. It was proven to be more efficient than the sub-cell technique [1.43] in the FDTD method. INBCs have also been applied in the FDTD method to analyse the effects of the electrostatic discharge (ESD) on conductive panels [1.44], avoiding the large space discretisation required by the standard FDTD method. Recently, Feliziani et.al. [1.45 ~ 1.46] further developed the INBCs to analyse the electromagnetic fields around non-perfectly conductive shields. In this new approach, a simple linear time-invariant (LTI) circuit was used to represent the frequency-domain admittance matrix of the shield. Its major advantage is that this circuit is directly analysed in the time domain without using convolution equations.

In order to model anisotropic carbon fibre composite materials, Sarto et al. [1.29, 1.47] introduced an effective boundary conditions technique into the FDTD method, excluding the material out of the discretisation region and thus saving the computational costs. Their approach was based on the transmission line formulation of the field propagation equations through the layer. The time domain formulations were computed from the frequency domain by using vector fitting procedures [1.48]. This technique is actually another extension of SIBCs.

In the TLM method, digital filter techniques have been used to obtain local solutions for a fine feature in a large problem. This technique is now overviewed.

In order to solve the multi-scale problems in the EMC area, Paul et al. [1.49 ~ 1.51] proposed a digital filter technique for the incorporation of fine features into the TLM method. In this technique, the fine features are represented by frequency-dependent external or internal boundary conditions. The frequency domain scattering functions of the boundary can be extracted from a set of data containing its analytical or measured scattering coefficients by using the Prony method [1.52]. Its time domain functions are obtained using the bilinear Z-transform and digital filter theory, which are then implemented in the TLM method. In the application of this technique, the implementation of the Prony method is a key part. Since the accuracy of the method depends on the number

of poles used for describing the transfer functions of the digital filters [1.51], the number of poles must be selected correctly to get an accurate approximation to a particular data set. The Prony method also involves the calculation of matrix inversion, which may increase the computation complexity and cause large computational overheads, especially for a large matrix [1.52].

Based on the above techniques, an embedded thin film model in the TLM method is presented in this thesis to address the multi-scale problems, e.g. thin films in a large problem space. In this technique, the thin film is excluded from the large problem and modelled locally without discretisation. It is equivalent to a section of transmission line, represented by a two-port network in terms of an admittance matrix. The frequency domain admittance matrix involves the calculation of cotangent and cosecant functions, which can be approximated by known analytical expansions in partial fractions. The time domain expressions are then obtained by using the bilinear Z transform and digital filter theory. The time domain TLM algorithm includes a scattering process and a connection process [1.4]. By modifying its connection process, the time domain expressions of the thin film are embedded into the TLM algorithm. Unlike other techniques discussed above, this technique does not involve the calculation of matrix inversion and the choice of the correct number of poles, which makes it more efficient. Furthermore, the frequency domain equations of the thin film come from the analytical equations based on the parameters of the film, not from an approximation based on known data sets, leading to accurate results.

In this thesis, the embedded thin film model has been applied within one-dimensional (1D) and two-dimensional (2D) TLM methods. In the 1D problem, the model is used to analyse the reflection and transmission properties of not only conductive panels, such as carbon fibre composite (CFC) panels and titanium panels, but also dielectric panels, such as antireflection coatings and fibre Bragg gratings. In the 2D problem, it is extended to analyse the shielding performance of CFC panels with finite length at arbitrary excitations. In addition, it is applied to investigate the resonant properties and shielding

performance of curved CFC structures. Its extension to three-dimensional (3D) problems is discussed in the future work.

1.3. Outline of the Thesis

The outline of the thesis is provided as follows.

Chapter 2 reviews the fundamentals of the Transmission Line Modelling (TLM) method for one-dimensional (1D), two-dimensional (2D) and three-dimensional (3D) problems. Stub technique and generalised condensed node are described as ways of modelling material parameters.

Chapter 3 presents detailed derivation of the embedded thin film model in the TLM algorithm. The embedded model for single layer thin films is introduced first. Its implementation starts with the analytical expansions of the cotangent and cosecant functions in the admittance matrix of the thin film, which are then transformed from the frequency domain to the time domain, using the inverse Z transform and general digital filter theory. The thin film model is embedded between TLM nodes by modifying the TLM's connection process. Based on the single layer thin films, an embedded model for multilayer thin films is derived. According to the admittance matrix of each layer, a linear matrix equation is formed to describe the scattering properties of the multilayer thin film, which is solved using a Gauss-Seidel method. Furthermore an anisotropic thin film model is introduced at the end of this chapter.

Chapter 4 demonstrates the applications of the 1D TLM method with embedded thin film model. Both lossy and lossless thin films are considered. As examples of lossy thin films, the reflection and transmission coefficients of several different CFC panels and titanium panels are calculated using the embedded model and compared to analytical results. Furthermore, the model is applied to investigate the shielding performance of CFC panels. As examples of lossless thin films, the reflection coefficients of an antireflection (AR) coating and the transmission coefficients of a fibre Bragg grating (FBG) are also computed using the embedded model and compared to the analytical

results. These examples are used to investigate the accuracy, stability, convergence and efficiency of the embedded thin film model in the 1D TLM method. Furthermore, the advantages of the embedded model over the conventional TLM method are elaborated by comparing the computational resources used by both methods.

Chapter 5 describes the embedded thin film model for arbitrary excitations in a 2D TLM method. The embedded model developed in Chapter 3 is first applied to model an infinitely long thin film at oblique incidence. Here the thin film is seen as 1D model embedded between 2D TLM nodes due to the introduction of a transverse impedance. The model is extended to include thin films with finite length at arbitrary excitations by using the plane wave decomposition theory. In order to simulate a plane wave propagating in an infinite space at oblique incidence, plane wave excitation methods for both TE- and TM- polarised waves are presented. After introducing the theory, the accuracy and convergence of the embedded model for arbitrary excitations are examined by calculating the reflection and transmission coefficients of infinitely long CFC panels with TE- and TM- polarised wave excitations at different angles of incidence over a wide frequency range. In the end, the embedded model is applied to model a CFC panel of finite length with a point source excitation. The effects of the finite dimensions of the CFC panel on the electromagnetic field propagation are discussed.

Chapter 6 extends the embedded model to the case of curved thin films in a 2D TLM method. Embedding of the curved thin films in the TLM algorithm is done firstly, by approximating the thin films using a piece-wise linearisation and secondly, embedding the linearised segments between adjacent nodes, where a three-layer stack is introduced to allow for arbitrary model placement between the nodes. The convergence and accuracy of the embedded curved thin film model are investigated by calculating the resonance frequencies of infinitely-long, hollow, CFC circular and elliptical resonators and comparing them with those of the equivalent metal circular and elliptical resonators. Furthermore, the model is applied to analyse the shielding performance of a

CFC airfoil with the profile of NACA2415 [1.53]. The impact of small gaps in the airfoil structure on its shielding performance is also investigated.

Chapter 7 provides the main conclusions of the thesis and discusses its possible applications in three dimensional (3D) problems for future development of this work.

References

[1.1] A. Taflove and S. C. Hagness, Computational Electrodynamics: the Finite Difference Time-Domain Method, 3rd ed. Norwood MA: Artech House, 2005.

[1.2] J. L. Volakis, A. Chaterjee, and L. C. Kempel, Finite Element Method for Electromagnetics. New York: IEEE Press, 1998.

[1.3] R. F. Harrington, Field Computation by Moment Methods. New York: McMillan, 1968.

[1.4] C. Christopoulos, The Transmission-Line Modeling Method TLM. IEEE Press, 1995.

[1.5] J. Paul, C. Christopoulos, and D. W. P. Thomas, "Generalized material models in TLM - part 3: materials with nonlinear properties," IEEE Transactions on Antennas and Propagation, vol. 50, no. 7, pp. 997–1004, 2002.

[1.6] C. Christopoulos, "Multi-scale modelling in time-domain electromagnetics," AEU - International Journal of Electronics and Communications, vol. 57, no. 2, pp. 100–110, 2003.

[1.7] A. Baker, S. Dutton, and D. Kelly, Composite Materials for Aircraft Structures, 2nd ed. Virginia: AIAA Education Series, 2004.

[1.8] M. Kalanchiam and M. Chinnasamy, "Advantages of composite materials in aircraft structures," World Academy of Science, Engineering and Technology, vol. 71, pp. 597–601, 2012.

[1.9] M. Apr, M. D. Amore, K. Gigliotti, M. S. Sarto, S. Member, and V. Volpi, "Lightning indirect effects certification of a transport aircraft by numerical simulation," IEEE Transactions on Electromagnetic Compatibility, vol. 50, no. 3, pp. 513–523, 2008.

[1.10] M. D'Amore and M. S. Sarto, "Theoretical and experimental characterization of the EMP-interaction with composite-metallic enclosures," IEEE Transactions on Electromagnetic Compatibility, vol. 42, no. 2, pp. 152–163, 2000.

[1.11] M. D'Amore and M. Sabrina Sarto, "Time-domain analysis of lightning interaction to aeronautical structures composite materials," in IEEE 1997 International Symposium on Electromagnetic Compatibility, pp. 397–402, 1997.

[1.12] S. J. Earl, "Some methods for modelling carbon fibre composites for the effects of lightning," in Challenges in the Modelling and Measurement of Electromagnetic Materials, The Institution of Engineering and technology Seminar on, pp. 33–38, 2006.

[1.13] K. Kunz and L. Simpson, "A Technique for increasing the resolution of finite-difference solutions of the Maxwell equation," IEEE Transactions on Electromagnetic Compatibility, vol. EMC-23, no. 4, pp. 419–422, 1981.

[1.14] M. J. White, Z. Yun, and M. F. Iskander, "A new 3D FDTD multigrid technique with dielectric traverse capabilities," IEEE Transactions on Microwave Theory and Techniques, vol. 49, no. 3, pp. 422–430, 2001.

[1.15] J. Gazave, A. Reineix, and J. P. Seaux, "3D space-time subgridding algorithm for FDTD," in 2007 IEEE Antennas and Propagation International Symposium, pp. 3065–3068, 2007.

[1.16] J.-P. Brenger, "A huygens subgridding for the FDTD method," IEEE Transactions on Antennas and Propagation, vol. 54, no. 12, pp. 3797–3804, 2006.

[1.17] Z. Huang, G. G. Pan, and K.-S. Chen, "A synchronized multigrid time domain method via huygens subgridding and implicit algorithms," IEEE Transactions on Antennas and Propagation, vol. 61, no. 5, pp. 2605–2614, 2013.

[1.18] J. L. Herring and C. Christopoulos, "Multigrid transmission-line modelling (TLM) method for solving electromagnetic field problems," Electronics Letters, vol. 27, no. 20, p. 1794, 1991.

[1.19] J. L. Herring and C. Christopoulos, "Solving electromagnetic field problems using a multiple grid transmission-line modeling method," IEEE Transactions on Antennas and Propagation, vol. 42, no. 12, pp. 1654–1658, 1994.

[1.20] M. Niediwiecki, A. Review, and J. Wlodarczyk, "New multigrid interface for the TLM method," Electronics Letters, vol. 32, no. 12, pp. 1111-1112, 1996.

[1.21] P. Sewell, J. Wykes, A. Vukovic, D. W. P. Thomas, T. M. Benson, and C. Christopoulos, "Multi-grid interface in computational electromagnetics," Electronics Letters, vol. 40, no. 3, pp. 162-163, 2004.

[1.22] S. Wright, "The application of transmisison-line modelling implicit and hybrid algorithms to electromagnetic problems," PhD thesis, University of Nottingham, 1988.

[1.23] R. Scaramuzza and A. J. Lowery, "Hybrid symmetrical condensed node for the TLM method," Electronics Letters, vol. 26, no. 23, pp. 1947-1949, 1990.

[1.24] V. Trenkic, C. Christopoulos, and T. M. Benson, "On the time step in hybrid symmetrical condensed TLM nodes," IEEE Transactions on Microwave Theory and Techniques, vol. 43, no. 9, pp. 2172–2174, 1995.

[1.25] P. S. Duxbury, a. J. Wlodarczyk, and R. a. Scaramuzza, "The implementation and benefits of octree staggered meshing in a TLM based 3D EM simulation package," 2004 RF and Microwave Conference (IEEE Cat. No.04EX924), pp. 199–203, 2004.

[1.26] "CST microwave studio TLM solver." [Online]. Available: https://www.cst.com/Products/CSTMWS/TLM-Solver.

[1.27] M. A. Leontovich, "On the approximate boundary conditions for electromagnetic fields on the surface of well conducting bodies," in Investigations of Propagation of Radio Waves, B.A. Vvedensky, Ed. Academy of Sciences USSR, pp. 5–20, 1948.

[1.28] M. Feliziani, F. Maradei, and G. Tribellini, "Field analysis of penetrable conductive shields by the finite-difference time-domain method with impedance network boundary conditions (INBCs)," IEEE Transactions on Electromagnetic Compatibility, vol. 41, no. 4, pp. 307–319, 1999.

[1.29] M. S. Sarto and C. L. Holloway, "Effective boundary conditions for the time-domain analysis of the EMC performances of fiber composites," 1999 IEEE International Symposium on Electromagnetic Compatability. Symposium Record (Cat. No.99CH36261), vol. 1, pp. 462–467, 1999.

[1.30] T. B. A. Senior, "Impedance boundary conditions for imperfectly conducting surfaces," Applied Scientific Research, Section B, vol. 8, no. 1, pp. 418–436, 1960.

[1.31] S. R. H. Hoole, K. Weeber, and N. R. G. Hoole, "The natural finite element formulation of the impedance boundary condition in shielding structures," Journal of Applied Physics, vol. 63, no. 8, pp. 3022–3024, 1988.

[1.32] J. G. Maloney and G. S. Smith, “Implementation of surface impedance concepts in the finite-difference time-domain (FD-TD) technique,” in International Symposium on Antennas and Propagation Society, *Merging Technologies for the 90’s*, pp. 1628–1631, 1990.

[1.33] J. G. Maloney and G. S. Smith, “The use of surface impedance concepts in the finite-difference time-domain method,” IEEE Transactions on Antennas and Propagation, vol. 40, no. 1, pp. 38–48, 1992.

[1.34] J. H. Beggs, R. J. Luebbers, K. S. Yee, and K. S. Kunz, “Finite-difference time-domain implementation of surface impedance boundary conditions,” IEEE Transactions on Antennas and Propagation, vol. 40, no. 1, pp. 49–56, 1992.

[1.35] S. Kellali, B. Jecko, and a. Reineix, “Implementation of a surface impedance formalism at oblique incidence in FDTD method,” IEEE Transactions on Electromagnetic Compatibility, vol. 35, no. 3, pp. 347–356, 1993.

[1.36] K. S. Oh and J. E. Schutt-Aine, “An efficient implementation of surface impedance boundary conditions for the finite-difference time-domain method,” IEEE Transactions on Antennas and Propagation, vol. 43, no. 7, pp. 660–666, 1995.

[1.37] N. Farahat, S. Yuferev, and N. Ida, “High order surface impedance boundary conditions for the FDTD method,” IEEE Transactions on Magnetics, vol. 37, no. 5, pp. 3242–3245, 2001.

[1.38] M. K. Karkkainen and S. A. Tretyakov, “Finite-difference time-domain model of interfaces with metals and semiconductors based on a higher order surface impedance boundary condition,” IEEE Transactions on Antennas and Propagation, vol. 51, no. 9, pp. 2448–2455, 2003.

[1.39] M. K. Karkkainen and S. A. Tretyakov, “A class of analytical absorbing boundary conditions originating from the exact surface impedance boundary condition,” IEEE Transactions on Microwave Theory and Techniques, vol. 51, no. 2, pp. 560–563, 2003.

[1.40] H. Zheng and K. W. Leung, “FDTD implementation and application of high order impedance boundary condition using rational functions,” IEEE Transactions on Antennas and Propagation, vol. 57, no. 8, pp. 2397–2408, 2009.

[1.41] V. De Santis, S. Cruciani, M. Feliziani, and M. Okoniewski, “Efficient low order approximation for surface impedance boundary Conditions in finite-difference time-domain Method,” IEEE Transactions on Magnetics, vol. 48, no. 2, pp. 271–274, 2012.

[1.42] M. Feliziani and F. Maradei, “Finite-difference time-domain modeling of thin shields,” System, vol. 36, no. 4, pp. 848–851, 2000.

[1.43] J. G. Maloney and G. S. Smith, “The efficient modeling of thin material shields in the finite-difference time-domain (FDTD) method,” IEEE Transactions on Antennas and Propagation, vol. 40, no. 3, pp. 323–330, 1992.

[1.44] F. Maradei and M. Raugi, “Analysis of upsets and failures due to ESD by the FDTD-INBCs method,” IEEE Transactions on Industry Applications, vol. 38, no. 4, pp. 1009–1017, 2002.

[1.45] M. Feliziani, “Subcell FDTD Modeling of Field Penetration Through Lossy Shields,” IEEE Transactions on Electromagnetic Compatibility, vol. 54, no. 2, pp. 299–307, 2012.

[1.46] M. Feliziani, S. Member, and S. Cruciani, “FDTD modeling of impedance boundary conditions by equivalent LTI circuits,” vol. 60, no. 12, pp. 3656–3666, 2012.

[1.47] M. S. Sarto, “A new model for the FDTD analysis of the shielding performances of thin composite structures,” IEEE Transactions on Electromagnetic Compatibility, vol. 41, no. 4, pp. 298–306, 1999.

[1.48] B. Gustavsen and A. Semlyen, “Rational approximation of frequency domain responses by vector fitting,” IEEE Transactions on Power Delivery, vol. 14, no. 3, pp. 1052–1061, 1999.

[1.49] J. Paul, V. Podlozny, and C. Christopoulos, “The use of digital filtering techniques for the simulation of fine features in emc problems solved in the time domain,” IEEE Transactions on Electromagnetic Compatibility, vol. 45, no. 2, pp. 238–244, 2003.

[1.50] V. Podlozny, C. Christopoulos, and J. Paul, “Efficient description of fine features using digital filters in time-domain computational electromagnetics,” in Proceedings of CEM 2002 - 4th International Conference on Computation in Electromagnetics, vol. 2002, no. 5, pp. 65–65, 2002.

[1.51] J. Paul, V. Podlozny, D. W. P. Thomas, and C. Christopoulos, “Time-domain simulation of thin material boundaries and thin panels using digital filters in TLM,” Turk. J. Elec. Engin, vol. 10, no. 2, pp. 185–198, 2002.

[1.52] J. N. Brittingham, E. K. Miller, and J. L. Willows, “Pole extraction from real-frequency information,” Proceedings of the IEEE, vol. 68, no. 2, pp. 263–273, 1980.

[1.53] E. N. Jacobs, K. E. Ward, and R. M. Pinkerton, “The characteritics of 78 related airfoil sections from tests in the variable-density wind tunnel,” NACA report No.460, 1933.

2.The Transmission Line Modelling (TLM) Method

2.1. Overview

This chapter presents the basis of the Transmission Line Modelling (TLM) method that is founded on the analogy between the propagation of the electromagnetic fields and circuit networks. The TLM method [2.1] is a time-domain numerical method that solves the differential form of Maxwell's equations. It has been widely used in microwave applications [2.1 ~ 2.4] and THz applications [2.5 ~ 2.6]. Its implementation for the one-dimensional (1D), two-dimensional (2D) and three-dimensional (3D) problems in free space is presented. This is followed by an overview of methods for modelling materials parameters different from free space by using (i) a stub technique and (ii) the condensed node model. These methods will be used in the thesis to model the background materials surrounding the thin films.

2.2. Analogy between EM Fields and Circuit Networks

All classical electromagnetic phenomena can be described by Maxwell's equations [2.7]:

$$\begin{aligned} \nabla \times \vec{E} &= -\frac{\partial \vec{B}}{\partial t}, \\ \nabla \times \vec{H} &= \vec{J} + \frac{\partial \vec{D}}{\partial t}, \\ \nabla \cdot \vec{D} &= \rho, \\ \nabla \cdot \vec{B} &= 0, \end{aligned} \tag{2-1}$$

where the symbols $\vec{E}, \vec{D}, \vec{H}, \vec{B}, \vec{J}$ represent the vectors of the electric field intensity, the electric flux density, the magnetic field intensity, the magnetic flux density and the current density, respectively, and ρ is the scalar electric charge density.

The following constitutive relations [2.7] are assumed,

$$\begin{aligned} \vec{D} &= \varepsilon \vec{E}, \\ \vec{B} &= \mu \vec{H}. \end{aligned} \tag{2-2}$$

where μ and ε are the permeability and permittivity of the medium.

In Cartesian coordinates, after expanding the vectors $\vec{E}$ and $\vec{H}$ using the above constitutive relations, the first two equations in (2-1) become:

$$\begin{aligned} \frac{\partial E_z}{\partial y} - \frac{\partial E_y}{\partial z} &= -\mu \frac{\partial H_x}{\partial t}, \\ \frac{\partial E_x}{\partial z} - \frac{\partial E_z}{\partial x} &= -\mu \frac{\partial H_y}{\partial t}, \\ \frac{\partial E_y}{\partial x} - \frac{\partial E_x}{\partial y} &= -\mu \frac{\partial H_z}{\partial t}, \end{aligned} \tag{2-3}$$

$$\begin{aligned} \frac{\partial H_z}{\partial y} - \frac{\partial H_y}{\partial z} &= J_x + \varepsilon \frac{\partial E_x}{\partial t}, \\ \frac{\partial H_x}{\partial z} - \frac{\partial H_z}{\partial x} &= J_y + \varepsilon \frac{\partial E_y}{\partial t}, \\ \frac{\partial H_y}{\partial x} - \frac{\partial H_x}{\partial y} &= J_z + \varepsilon \frac{\partial E_z}{\partial t}. \end{aligned} \tag{2-4}$$

If a one dimensional problem is considered ($\frac{\partial}{\partial x} = 0, \frac{\partial}{\partial y} = 0$), equations (2-3) and (2-4) reduce to,

$$-\frac{\partial E_y}{\partial z} = -\mu \frac{\partial H_x}{\partial t}, \tag{2-5}$$

$$\frac{\partial E_x}{\partial z} = -\mu \frac{\partial H_y}{\partial t}, \tag{2-6}$$

$$-\frac{\partial H_y}{\partial z} = J_x + \varepsilon \frac{\partial E_x}{\partial t}, \tag{2-7}$$

$$\frac{\partial H_x}{\partial z} = J_y + \varepsilon \frac{\partial E_y}{\partial t}. \tag{2-8}$$

Equations (2-5) and (2-8) have the same form as equations (2-6) and (2-7). The two pairs of equations are independent of each other, so here the solutions of (2-6) and (2-7) are considered.

Combining (2-6) and (2-7), the following equation is obtained,

$$\frac{\partial^2 E_x}{\partial z^2} = \mu\varepsilon \frac{\partial^2 E_x}{\partial t^2} + \mu \frac{\partial J_x}{\partial t}. \tag{2-9}$$

Applying Ohm's Law ($J_x = \sigma_e E_x$) [2.7] to equation (2-9), where σ_e is the electrical conductivity of the medium, gives,

$$\frac{\partial^2 E_x}{\partial z^2} = \mu\varepsilon \frac{\partial^2 E_x}{\partial t^2} + \mu\sigma_e \frac{\partial E_x}{\partial t}. \tag{2-10}$$

Equation (2-10) is the one-dimensional (1D) wave equation that describes the propagation of the electric field component E_x along one-dimension.

At high frequencies, propagation of the electromagnetic signals along the transmission line can be described using a transmission line model. In a transmission line model, the short length of the transmission line, dz, is developed using the circuit shown in Fig. 2-1, where R, G, L and C are the series resistance, shunt admittance, series inductance and shunt capacitance per section of length dz, respectively.

Applying Kirchhoff's voltage and current laws [2.8] to the circuits shown in Fig. 2-1, two equations are obtained as follows,

$$dz \frac{\partial v}{\partial z} = -L \frac{\partial i}{\partial t} - iR, \tag{2-11}$$

$$dz \frac{\partial i}{\partial z} = -C \frac{\partial v}{\partial t} - Gv, \tag{2-12}$$

where both transient voltage (v) and current (i) are functions of z.

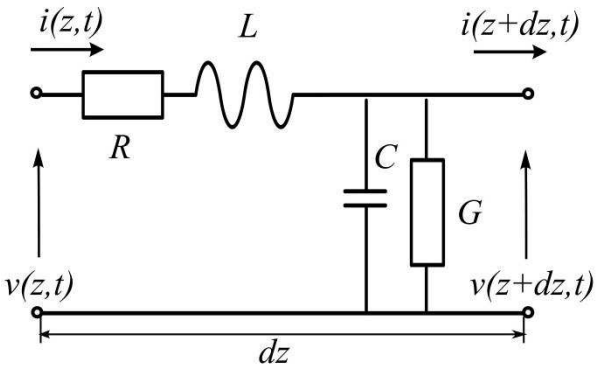

Fig. 2-1 Section of a transmission line.

When the current (i) is eliminated between equations (2-11) and (2-12), the equation for the voltage (v) is expressed as,

$$\frac{\partial^2 v}{\partial z^2} = \frac{GR}{(dz)^2} v + \frac{1}{(dz)^2}(GL + RC)\frac{\partial v}{\partial t} + \frac{LC}{(dz)^2}\frac{\partial^2 v}{\partial t^2}. \tag{2-13}$$

Similarly, when the voltage (v) is eliminated, the following equation for the current (i) is obtained,

$$\frac{\partial^2 i}{\partial z^2} = \frac{GR}{(dz)^2} i + \frac{1}{(dz)^2}(GL + RC)\frac{\partial i}{\partial t} + \frac{LC}{(dz)^2}\frac{\partial^2 i}{\partial t^2}. \tag{2-14}$$

Assuming $R = 0$, equation (2-13) becomes,

$$\frac{\partial^2 v}{\partial z^2} = \frac{GL}{(dz)^2}\frac{\partial v}{\partial t} + \frac{LC}{(dz)^2}\frac{\partial^2 v}{\partial t^2}. \tag{2-15}$$

Comparing equations (2-10) and (2-15), both of which are repeated below for convenience, it is found that they have the same form,

$$\frac{\partial^2 E_x}{\partial z^2} = \mu\varepsilon\frac{\partial^2 E_x}{\partial t^2} + \mu\sigma_e\frac{\partial E_x}{\partial t},$$

$$\frac{\partial^2 v}{\partial z^2} = \frac{LC}{(dz)^2}\frac{\partial^2 v}{\partial t^2} + \frac{GL}{(dz)^2}\frac{\partial v}{\partial t},$$

so that the following equivalences can be made,

$$v \leftrightarrow E_x,\ \ \frac{C}{dz} \leftrightarrow \varepsilon,\ \ \frac{L}{dz} \leftrightarrow \mu,\ \ \frac{G}{dz} \leftrightarrow \sigma_e.$$

Similarly, it is observed that the equations describing the behaviour of the magnetic field H_y and the current i have the same form and so the following equivalence exists,

$$i \leftrightarrow H_y.$$

These equivalences show that the wave propagation can be modelled using transmission line equivalent circuits, providing that a suitable mapping between line parameters and the propagation medium is made.

2.3. The Transmission Line Modelling (TLM) Method

As discussed in the previous section, the Transmission Line Modelling (TLM) method is based on the analogy between the propagation of the electromagnetic fields and the behaviour of voltages and currents on a transmission line. Unlike the Finite Difference Time Domain (FDTD) method, which is an approximation of derivative terms using finite differences in Maxwell's equations [2.9], the TLM method is a wave physical model, which propagates signals along a network of transmission lines. Another important difference is that the FDTD method has to satisfy the Courant condition for stability [2.10], whilst the TLM method is unconditionally stable.

The TLM method discretises the modelling space using a mesh of transmission lines, connected at nodes. The field is represented using voltage wave pulses which propagate and scatter through the mesh at every time step. Its implementation can be algorithmically separated into several stages namely: initialization, calculation of the voltages at all nodes, scattering and connection processes, and boundary conditions setup [2.1]. Initialization defines the sources and initial wave values; the scattering process determines the reflected voltage waves at all nodes and the connection process obtains the new values for the incident voltage waves at all nodes by exchanging the voltage waves

between adjacent nodes. Boundary conditions define the modelling space, for example, by providing conditions representing outgoing waves.

In the following sections, the implementations of the one-dimensional (1D), two-dimensional (2D) and three-dimensional (3D) TLM models are discussed separately in terms of the scattering and connection processes.

2.3.1. 1D TLM Model

Based on the equivalence between electromagnetic fields and electric circuits, as discussed in section 2.2, the parameters of free space are modelled by the inductance and capacitance of the transmission line as follows,

$$L = \mu_0 \cdot dz, C = \varepsilon_0 \cdot dz, \tag{2-16}$$

where μ_0 and ε_0 are the permeability and permittivity of free space, L and C are the inductance and capacitance per length of the transmission line, respectively, and dz is the mesh size. The modelling of material parameters different from free space is described in section 2.4.

The transmission line is characterised by the characteristic impedance as [2.1]

$$Z_0 = \sqrt{L/C}. \tag{2-17}$$

The time step, Δt , is the time the voltage takes to propagate through a section of transmission line of length dz. It is also related to the inductance and capacitance as follows,

$$\Delta t = \frac{dz}{c} = \sqrt{LC}, \tag{2-18}$$

where c is the velocity of the wave propagation in free space and is given by,

$$c = {1}\Big/{\sqrt{L/dz \cdot C/dz}} = {dz}\Big/{\sqrt{LC}}. \tag{2-19}$$

Fig. 2-2 shows two sections of transmission line connected at node n. In Fig. 2-2, V_n is the total nodal voltage at node n, ${VL_n}^i$ and ${VR_n}^i$ are the incident voltages from the left and right side of node n, respectively, and ${VL_n}^r$ and ${VR_n}^r$ are the reflected voltages from the left and the right side of node n, respectively.

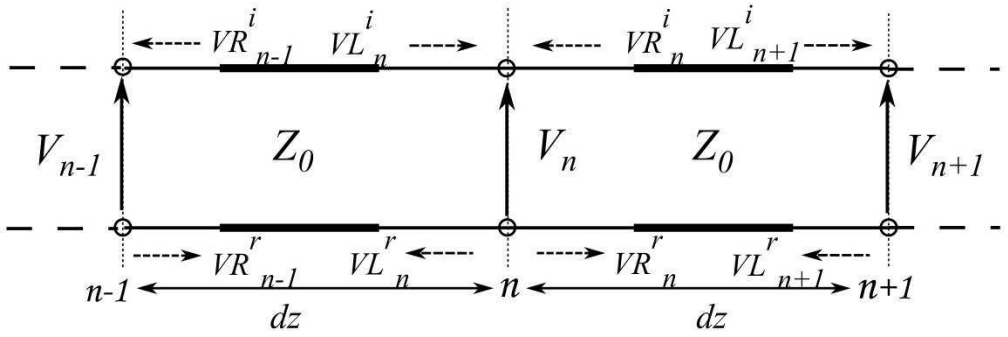

Fig. 2-2 Two sections of lossless transmission line connected at node n.

The total voltage at node n at the time step k is a sum of incident and reflected voltages calculated as,

$$ {}_kV_n = {}_kVL_n{}^i + {}_kVR_n{}^i. \tag{2-20}$$

In the scattering process, the reflected voltages at node n at the time step k are obtained from the incident voltages as,

$$\begin{aligned} {}_kVL_n{}^r &= {}_kV_n - {}_kVL_n{}^i, \\ {}_kVR_n{}^r &= {}_kV_n - {}_kVR_n{}^i. \end{aligned} \tag{2-21}$$

In the connection process, the reflected voltages from node n become incident voltages on the adjacent nodes at the next time step, k+1, as,

$$ {}_{k+1}VR_n{}^i = {}_kVL_{n+1}{}^r, \tag{2-22}$$

$$ {}_{k+1}VL_n{}^i = {}_kVR_{n-1}{}^r. \tag{2-23}$$

Following an initial excitation and imposing proper boundary conditions [2.1], these three processes are repeated at each node for the desired number of time steps.

2.3.2. 2D TLM Model

In the 2D TLM model, two different nodes are used to model free space [2.1]: the series node shown in Fig. 2-3 (a) and the shunt node shown in Fig. 2-3 (b). For the waves propagating in the z direction, the series node is used to model the TE modes with the field components E_x, E_y and H_z, while the shunt node is used to model the TM modes with the field components H_x, H_y and E_z.

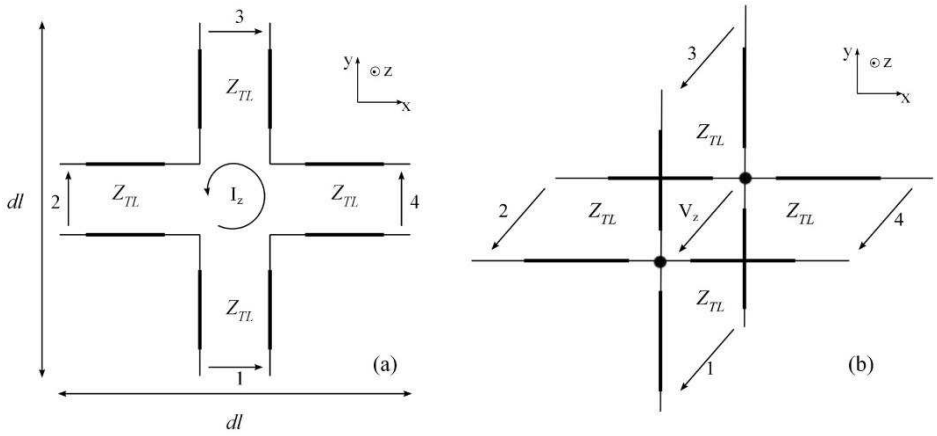

Fig. 2-3 (a) The 2D series TLM node and (b) the 2D shunt TLM node.

The 2D series TLM node

As shown in Fig. 2-3 (a), four sections of transmission lines of characteristic impedance Z_{TL} are connected in series [2.1]. The characteristic impedance Z_{TL} is $Z_{TL} = Z_0/\sqrt{2}$, and the time step is $\Delta t = dl/(\sqrt{2}c)$, where dl is the mesh size.

The voltages and currents at node (n_x, n_y), where $n_x = x/dl$, $n_y = y/dl$, at the time step k are calculated as,

$$
\begin{aligned}
{}_kI_z &= \frac{{}_kV_1^i + {}_kV_4^i - {}_kV_2^i - {}_kV_3^i}{2Z_{TL}}, \\
{}_kV_x &= \frac{{}_kV_1^i + {}_kV_3^i}{2}, \quad {}_kV_y = \frac{{}_kV_2^i + {}_kV_4^i}{2},
\end{aligned}
\tag{2-24}
$$

where ${}_kI_z$, ${}_kV_x$ and ${}_kV_y$ are the current in the z direction and the voltages in the x and y directions, respectively. Voltages ${}_kV_1^i$, ${}_kV_2^i$, ${}_kV_3^i$ and ${}_kV_4^i$ are the incident voltages at the ports 1, 2, 3 and 4 of node (n_x, n_y), respectively.

According to the voltages and currents at node (n_x, n_y), the corresponding electric and magnetic field components can be obtained as follows,

$$H_z = \frac{I_z}{dl}, E_x = -\frac{V_x}{dl}, \; E_y = -\frac{V_y}{dl}. \tag{2-25}$$

The scattering process calculates the reflected voltages at all nodes, which can be expressed in terms of a scattering matrix as,

$${}_k\underline{V}^r = \underline{\underline{S}} \cdot {}_k\underline{V}^i, \tag{2-26}$$

where

$$\begin{aligned} {}_k\underline{V}^i &= \left[{}_kV_1^i \;\; {}_kV_2^i \;\; {}_kV_3^i \;\; {}_kV_4^i \right]^T, \\ {}_k\underline{V}^r &= \left[{}_kV_1^r \;\; {}_kV_2^r \;\; {}_kV_3^r \;\; {}_kV_4^r \right]^T, \\ \underline{\underline{S}} &= 0.5 \cdot \begin{bmatrix} 1 & 1 & 1 & -1 \\ 1 & 1 & -1 & 1 \\ 1 & -1 & 1 & 1 \\ -1 & 1 & 1 & 1 \end{bmatrix}, \end{aligned} \tag{2-27}$$

and the superscript T indicates the transpose operator.

The connection process is an exchange of the voltages between the adjacent nodes, which is expressed as,

$${}_{k+1}V_1^i(n_x, n_y) = {}_kV_3^r(n_x, n_y - 1), \tag{2-28}$$

$${}_{k+1}V_3^i(n_x, n_y) = {}_kV_1^r(n_x, n_y + 1), \tag{2-29}$$

$${}_{k+1}V_2^i(n_x, n_y) = {}_kV_4^r(n_x - 1, n_y), \tag{2-30}$$

$${}_{k+1}V_4^i(n_x, n_y) = {}_kV_2^r(n_x + 1, n_y). \tag{2-31}$$

The 2D shunt TLM node

The shunt node is shown in Fig. 2-3 (b), where the characteristic impedance of each transmission line is expressed as $Z_{TL} = \sqrt{2}Z_0$ [2.1] and the time step $\Delta t = dl/(\sqrt{2}c)$.

In the shunt node, the voltages and currents at node (n_x, n_y) at the time step k are calculated as,

$$
\begin{aligned}
{}_kV_z &= \frac{{}_kV_1^i + {}_kV_2^i + {}_kV_3^i + {}_kV_4^i}{2}, \\
{}_kI_x = \frac{{}_kV_2^i - {}_kV_4^i}{Z_{TL}}, &\quad {}_kI_y = \frac{{}_kV_1^i - {}_kV_3^i}{Z_{TL}},
\end{aligned}
\tag{2-32}
$$

where ${}_kV_z$, ${}_kI_x$, and ${}_kI_y$, are the voltage in the z direction, the currents in the x and y directions, respectively.

According to the voltages and currents at node (n_x, n_y), the corresponding electric and magnetic field components can be obtained as,

$$
E_z = -\frac{V_z}{dl}, H_x = -\frac{I_y}{dl}, H_y = \frac{I_x}{dl}. \tag{2-33}
$$

The scattering process is similar to that for the series nodes as in equation (2-26), but with the scattering matrix $\underline{\underline{S}}$ of the form,

$$
\underline{\underline{S}} = 0.5 \cdot \begin{bmatrix} -1 & 1 & 1 & 1 \\ 1 & -1 & 1 & 1 \\ 1 & 1 & -1 & 1 \\ 1 & 1 & 1 & -1 \end{bmatrix}. \tag{2-34}
$$

The connection process for the shunt nodes is the same as that for the series node as in equations (2-28)-(2-31).

2.3.3. 3D TLM Model

The scheme of a 3D TLM node is shown in Fig. 2-4. The node is known as symmetrical condensed node (SCN), first described by Johns [2.11], and is a mixture of both series and shunt nodes representing both polarisations. The SCN node has 12 ports as shown in Fig. 2-4.

The characteristic impedance of each transmission line in the node is $Z_{TL} = Z_0$ and the time step is $\Delta t = dl/2c$.

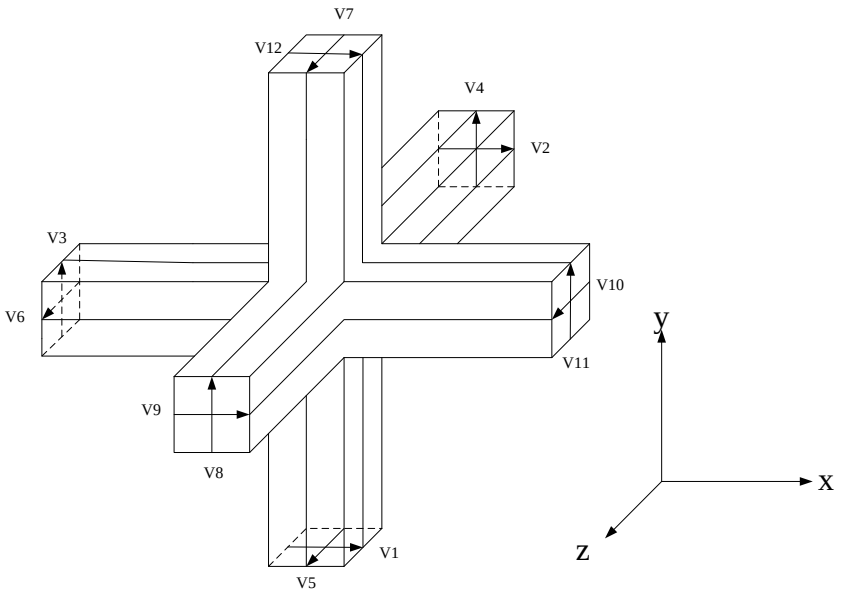

Fig. 2-4 A 3D symmetrical condensed node (SCN).

There are a total of 12 incident voltages and 12 reflected voltages, so the scattering matrix $\underline{\underline{S}}$ is a 12×12 matrix and is given by [2.1],

$$\underline{\underline{\mathbf{S}}} = \frac{1}{2}\begin{bmatrix} 0 & 1 & 1 & 0 & 0 & 0 & 0 & 0 & 1 & 0 & -1 & 0 \\ 1 & 0 & 0 & 0 & 0 & 1 & 0 & 0 & 0 & -1 & 0 & 1 \\ 1 & 0 & 0 & 1 & 0 & 0 & 0 & 1 & 0 & 0 & 0 & -1 \\ 0 & 0 & 1 & 0 & 1 & 0 & -1 & 0 & 0 & 0 & 1 & 0 \\ 0 & 0 & 0 & 1 & 0 & 1 & 0 & -1 & 0 & 1 & 0 & 0 \\ 0 & 1 & 0 & 0 & 1 & 0 & 1 & 0 & -1 & 0 & 0 & 0 \\ 0 & 0 & 0 & -1 & 0 & 1 & 0 & 1 & 0 & 1 & 0 & 0 \\ 0 & 0 & 1 & 0 & -1 & 0 & 1 & 0 & 0 & 0 & 1 & 0 \\ 1 & 0 & 0 & 0 & 0 & -1 & 0 & 0 & 0 & 1 & 0 & 1 \\ 0 & -1 & 0 & 0 & 1 & 0 & 1 & 0 & 1 & 0 & 0 & 0 \\ -1 & 0 & 0 & 1 & 0 & 0 & 0 & 1 & 0 & 0 & 0 & 1 \\ 0 & 1 & -1 & 0 & 0 & 0 & 0 & 0 & 1 & 0 & 1 & 0 \end{bmatrix} \tag{2-35}$$

As in the 1D and 2D models, the connection process assures TLM continuity. It builds the following relations between the neighbouring nodes,

$$_{k+1}V_2{}^{i}(n_x, n_y, n_z) = {}_{k}V_9{}^{r}(n_x, n_y, n_z - 1), \tag{2-36}$$

$$_{k+1}V_9{}^{i}(n_x, n_y, n_z) = {}_{k}V_2{}^{r}(n_x, n_y, n_z + 1), \tag{2-37}$$

$$_{k+1}V_4{}^{i}(n_x, n_y, n_z) = {}_{k}V_8{}^{r}(n_x, n_y, n_z - 1), \tag{2-38}$$

$$_{k+1}V_8{}^{i}(n_x, n_y, n_z) = {}_{k}V_4{}^{r}(n_x, n_y, n_z + 1), \tag{2-39}$$

$$_{k+1}V_1{}^{i}(n_x, n_y, n_z) = {}_{k}V_{12}{}^{r}(n_x, n_y - 1, n_z), \tag{2-40}$$

$$_{k+1}V_{12}{}^{i}(n_x, n_y, n_z) = {}_{k}V_1{}^{r}(n_x, n_y + 1, n_z), \tag{2-41}$$

$$_{k+1}V_5{}^{i}(n_x, n_y, n_z) = {}_{k}V_7{}^{r}(n_x, n_y - 1, n_z), \tag{2-42}$$

$$_{k+1}V_7{}^{i}(n_x, n_y, n_z) = {}_{k}V_5{}^{r}(n_x, n_y + 1, n_z), \tag{2-43}$$

$$_{k+1}V_3{}^{i}(n_x, n_y, n_z) = {}_{k}V_{11}{}^{r}(n_x - 1, n_y, n_z), \tag{2-44}$$

$$_{k+1}V_{11}{}^{i}(n_x, n_y, n_z) = {}_{k}V_3{}^{r}(n_x + 1, n_y, n_z), \tag{2-45}$$

$$_{k+1}V_6{}^{i}(n_x, n_y, n_z) = {}_{k}V_{10}{}^{r}(n_x - 1, n_y, n_z), \tag{2-46}$$

$$_{k+1}V_{10}{}^{i}(n_x, n_y, n_z) = {}_{k}V_6{}^{r}(n_x + 1, n_y, n_z). \tag{2-47}$$

The 1D and 2D TLM models will be used to model free space surrounding the embedded models of thin films that are developed in the work described in this thesis. The 3D model is shown here for completeness.

2.4. Modelling Material Properties in the TLM Method

Since the velocity of wave propagation depends on the medium parameters, it is impossible to model change in medium parameters in the same problem by simply adjusting the circuit parameters locally [2.1]. This is because all incident voltages have to arrive at nodes at the same time irrespective of medium they propagate in. Therefore it is necessary to maintain the same discretisation and the same time step throughout the problem. For this purpose, the stub technique [2.1] and the condensed node [2.12] have been developed to model the media with different material constituent properties.

In this section, the stub technique and the condensed node are introduced and their implementation in a 1D TLM method is described.

2.4.1. The Stub Technique

When modelling problems containing different media, extra inductance (representing permeability) and extra capacitance (representing permittivity) can be introduced in the form of a stub [2.1], in order to maintain both connectivity and synchronism.

For example, the dielectric medium can be modelled by adding an extra capacitance in the TLM model. Fig. 2-5 shows the extra capacitance C_s as an open circuit stub that is connected at node n in a 1D TLM model. The characteristic impedance of the capacitance, Z_c, is given by [2.1],

$$Z_c = \frac{\Delta t}{2C_s}. \tag{2-48}$$

Z_c can be expressed in terms of the characteristic impedance of free space, Z_0, as [2.6],

$$Z_c = \frac{Z_0}{2\chi_e}, \tag{2-49}$$

where $\chi_e = \varepsilon_r - 1$ is the electric susceptibility of the medium.

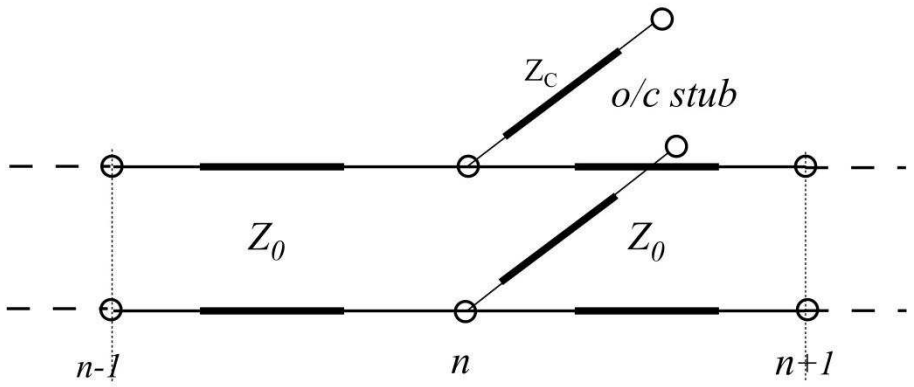

Fig. 2-5 A capacitive stub connected at node n in a 1D TLM model.

Due to the presence of the stub, the total nodal voltage of node n at the time step k is expressed as,

$${}_kV_n = \frac{{}_kVL_n{}^i + {}_kVR_n{}^i + 2\chi \cdot {}_kVC_n{}^i}{1 + \chi_e}, \tag{2-50}$$

where ${}_kVC_n{}^i$ represents the incident voltage at the time step k to the capacitive stub.

Then the scattering process is given by,

$$\begin{aligned} {}_kVL_n{}^r &= {}_kV_n - {}_kVL_n{}^i, \\ {}_kVR_n{}^r &= {}_kV_n - {}_kVR_n{}^i, \\ {}_kVC_n{}^r &= {}_kV_n - {}_kVC_n{}^i, \end{aligned} \tag{2-51}$$

where ${}_kVC_n{}^r$ represents the reflected voltage at the time step k from the capacitive stub.

The connection process for the node is the same as in equations (2-22) and (2-23), and the connection process for the stub is given as,

$$_{k+1}VC_n{}^{i} = {}_{k}VC_n{}^{r}, \tag{2-52}$$

since the capacitive stub is an open circuit stub.

This is the 1D implementation of the stub technique used to model the permittivity of the medium. A similar method can be used to model the permeability of the medium. This technique can also be extended to 2D and 3D TLM models. The details of the extensions can be found in [2.1].

Janyani [2.6] developed the stub technique to model instantaneous nonlinear materials by employing a Kerr model of nonlinearity for the 1D case. The stub technique was further developed to model the dispersive nonlinear dielectrics using a more physically based Duffing equation [2.6].

2.4.2. The Condensed Node

Paul [2.11] developed his condensed node to model material parameters different from free space. This model employs discrete signal processing techniques to incorporate Maxwell's curl equations and the constitutive relations into the TLM algorithm. This technique is intuitive, flexible and transparent [2.12].

Fig. 2-6 shows a 1D condensed node with two ports (V_4 and V_5) and two total field quantities (E_y and H_z). Noted here that Paul's port numbering system is adopted, which is different from that used in section 2.3. The space steps in the node are assumed to be the same $\Delta x = \Delta y = \Delta z = dl$. Its implementation is based on the field-circuit equivalence and normalization process.

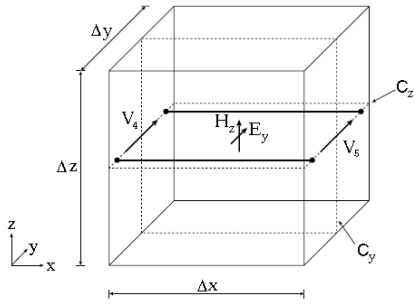

Fig. 2-6 A 1D condensed node describing propagation in x from [2.12].

The compact form of Maxwell equations described in [2.12] is as follows,

$$\begin{bmatrix} \nabla \times \vec{H} \\ -\nabla \times \vec{E} \end{bmatrix} - \begin{bmatrix} \overrightarrow{J_{ef}} \\ \overrightarrow{J_{mf}} \end{bmatrix} = \begin{bmatrix} \sigma_e * \vec{E} \\ \sigma_m * \vec{H} \end{bmatrix} + \frac{\partial}{\partial t} \begin{bmatrix} \varepsilon_0 \vec{E} + \varepsilon_0 \chi_e * \vec{E} \\ \mu_0 \vec{H} + \mu_0 \chi_m * \vec{H} \end{bmatrix}, \tag{2-53}$$

where $\overrightarrow{J_{ef}}$ and $\overrightarrow{J_{mf}}$ are the free electric current density and magnetic voltage density, σ_m is magnetic resistivity and χ_m is the magnetic susceptibility.

Equation (2-53) can be simplified in 1D as [2.12]

$$-\frac{\partial}{\partial x} \begin{bmatrix} H_z \\ E_y \end{bmatrix} - \begin{bmatrix} J_{efy} \\ J_{mfz} \end{bmatrix} = \begin{bmatrix} \sigma_e * E_y \\ \sigma_m * H_z \end{bmatrix} + \frac{\partial}{\partial t} \begin{bmatrix} \varepsilon_0 E_y + \varepsilon_0 \chi_e * E_y \\ \mu_0 H_z + \mu_0 \chi_m * H_z \end{bmatrix}, \tag{2-54}$$

where J_{efy} and J_{mfz} are the free electric current and magnetic voltage densities in y and z axis, respectively.

The quantities in equation (2-54) are normalized as

$$\begin{gathered} E_y = -\frac{V_y}{dl},\ H_z = -\frac{I_z}{dl} = -\frac{i_z}{dl \cdot Z_0}, \\ J_{efy} = -\frac{I_{fy}}{dl^2} = -\frac{i_{fy}}{dl^2 \cdot Z_0},\ \ J_{mfz} = -\frac{V_{fz}}{dl^2}, \\ \sigma_e = \frac{g_e}{dl \cdot Z_0}, \sigma_m = \frac{r_m \cdot Z_0}{dl}. \end{gathered} \tag{2-55}$$

By applying the field-circuit equivalence and the normalization process, the transmission line model of equation (2-54) is found as [2.12]

$$-\frac{\partial}{\partial \bar{x}}\begin{bmatrix} i_z \\ V_y \end{bmatrix} - \begin{bmatrix} i_{fy} \\ V_{fz} \end{bmatrix} = \begin{bmatrix} g_e \cdot V_y \\ r_m \cdot I_z \end{bmatrix} + \bar{s}\begin{bmatrix} V_y + \chi_e \cdot V_y \\ i_z + \chi_m \cdot i_z \end{bmatrix}, \tag{2-56}$$

where $\frac{\partial}{\partial \bar{x}} = \frac{\partial}{\partial x} \cdot dl$ and $\bar{s} = s \cdot dt$, with s being the Laplace variable.

Stokes' theorem is applied using the integration contours C_y and C_z indicated in Fig. 2-6, so equation (2-56) becomes,

$$\begin{bmatrix} V_4 + V_5 \\ V_4 - V_5 \end{bmatrix} - \begin{bmatrix} i_{fy} \\ V_{fz} \end{bmatrix} = \begin{bmatrix} g_e \cdot V_y \\ r_m \cdot I_z \end{bmatrix} + \bar{s}\begin{bmatrix} V_y + \chi_e \cdot V_y \\ i_z + \chi_m \cdot i_z \end{bmatrix}, \tag{2-57}$$

where V_4 and V_5 are the total voltages on both sides of the node.

Equation (2-57) is further converted to the travelling wave format as

$$2\begin{bmatrix} V_4 + V_5 \\ V_4 - V_5 \end{bmatrix}^i - \begin{bmatrix} i_{fy} \\ V_{fz} \end{bmatrix} = 2\begin{bmatrix} V_y \\ I_z \end{bmatrix} + \begin{bmatrix} g_e \cdot V_y \\ r_m \cdot I_z \end{bmatrix} + \bar{s}\begin{bmatrix} V_y + \chi_e \cdot V_y \\ i_z + \chi_m \cdot i_z \end{bmatrix}, \tag{2-58}$$

where V_4^i and V_5^i are the incident voltages on the both sides of the node.

The left side of equation (2-58) is seen as the external excitation of the node, which is defined as the reflected fields [2.12], so equation (2-58) becomes

$$2\begin{bmatrix} V_y \\ I_z \end{bmatrix}^r = 2\begin{bmatrix} V_y \\ I_z \end{bmatrix} + \begin{bmatrix} g_e \cdot V_y \\ r_m \cdot I_z \end{bmatrix} + \bar{s}\begin{bmatrix} V_y + \chi_e \cdot V_y \\ i_z + \chi_m \cdot i_z \end{bmatrix}. \tag{2-59}$$

By defining transmission coefficients $t_{ey} = 2/(2 + g_e + \bar{s}\chi_e)$ and $t_{mz} = 2/(2 + r_m + \bar{s}\chi_m)$, equation (2-59) becomes

$$\begin{bmatrix} V_y \\ i_z \end{bmatrix} = \begin{bmatrix} t_{ey} & 0 \\ 0 & t_{mz} \end{bmatrix}\begin{bmatrix} V_y^r \\ -i_z^r \end{bmatrix}. \tag{2-60}$$

If the material has constant parameters, equation (2-60) can be solved by introducing the Z-transform with s replaced by $\frac{2}{\Delta t} \cdot (1 - z^{-1})/(1 + z^{-1})$ as

$$\begin{bmatrix} V_y \\ i_z \end{bmatrix} = \begin{bmatrix} T_{ey} & 0 \\ 0 & T_{mz} \end{bmatrix}\left(2\begin{bmatrix} V_y^r \\ -i_z^r \end{bmatrix} + z^{-1}\begin{bmatrix} S_{ey} \\ S_{mz} \end{bmatrix}\right), \tag{2-61}$$

$$\begin{bmatrix} S_{ey} \\ S_{mz} \end{bmatrix} = 2\begin{bmatrix} V_y^r \\ -i_z^r \end{bmatrix} + \begin{bmatrix} \kappa_{ey} & 0 \\ 0 & \kappa_{mz} \end{bmatrix}\begin{bmatrix} V_y \\ i_z \end{bmatrix}, \tag{2-62}$$

where

$$T_{mz} = (2 + r_m + 2\chi_m)^{-1}, \kappa_{mz} = -(2 + r_m - 2\chi_m),$$
$$T_e = (2 + g_e + 2\chi_e)^{-1}, \kappa_{ey} = -(2 + g_e - 2\chi_m).$$

Fig. 2-7 shows the equivalent circuit of a 1D condensed node. Its scattering process can be expressed in terms of the voltage V_y and the current i_z,

$$\begin{bmatrix} V_4^r \\ V_5^r \end{bmatrix} = \begin{bmatrix} V_y - i_z - V_5^i \\ V_y + i_z - V_4^i \end{bmatrix}, \tag{2-63}$$

where $V_4^{i,r}$ and $V_5^{i,r}$ are the incident and reflected voltages from both sides of the node, which are corresponding to $VL_n^{i,r}$ and $VR_n^{i,r}$ in equation (2-21).

Its connection process is the same as in equations (2-22) and (2-23).

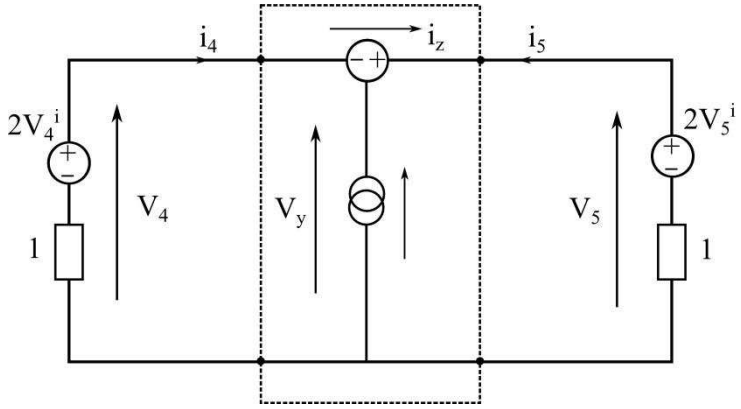

Fig. 2-7 The equivalent circuit of a 1D condensed TLM node.

The extensions of the condensed node in the 2D and 3D TLM can be found in [2.12]. Through modification of the transmission coefficients t_{ey} and t_{mz} in equation (2-60), the condensed node can be applied to model the frequency-dependent, nonlinear and anisotropic materials. The details are discussed in [2.13 ~ 2.15].

Both the stub technique and the condensed node are used in this thesis to model materials different from free space, which are surrounding the thin films.

2.5. Conclusions

This chapter introduced the Transmission Line Modelling (TLM) method. Based on the field-circuit equivalence, the procedures for modelling free space using the 1D, 2D and 3D TLM models were firstly described. Stub techniques and the condensed nodes were then overviewed as methods of modelling material parameters different from free space.

In the next chapter, the methodology for embedding single and multiple layers of thin film within the coarse TLM mesh is described.

References

[2.1] C. Christopoulos, The Transmission-Line Modeling Method TLM. IEEE Press, 1995.

[2.2] J. L. Herring and C. Christopoulos, "Multigrid transmission-line modelling (TLM) method for solving electromagnetic field problems," Electronics Letters, vol. 27, no. 20, pp. 1794-1795, 1991.

[2.3] J. L. Herring, "Developments in the Transmission-Line Modelling Method for electromagentic compatibility studies," PhD Thesis, University of Nottingham, 1993.

[2.4] C. Christopoulos, J. F. Dawson, L. Dawson, I. D. Flintoft, O. Hassan, a C. Marvin, K. Morgan, P. Sewell, C. J. Smartt, and Z. Q. Xie, "Characterization and modelling of electromagnetic interactions in aircraft," Proceedings of the Institution of Mechanical Engineers, Part G: Journal of Aerospace Engineering, vol. 224, no. 4, pp. 449–458, 2010.

[2.5] V. Janyani, J. D. Paul, A. Vukovic, T. M. Benson, and P. Sewell, "TLM modelling of nonlinear optical effects in fibre Bragg gratings," IEE Proceedings Optoelectronics, vol. 151, no. 4, pp. 185-192, 2004.

[2.6] V. Janyani, "Modelling of dispersive and nonlinear materials for optoelectronics using TLM," PhD thesis, University of Nottingham, 2005.

[2.7] S. Ramo, J. R. Whinnery, and T. Van Duzer, Fields and Waves in Communication Electronics, 3rd ed. John Wiley & Sons, Inc., 1997.

[2.8] S. A. Boctor, Electric Circuit Analysis. Englewood Cliffs: NJ: Prentice-Hall, 1987.

[2.9] M. N. O. Sadiku and A. F. Peterson, "A comparison of numerical methods for computing electromagnetic fields," in IEEE Proceedings on Southeastcon, pp. 42–47, 1990

[2.10] A. Taflove and S. C. Hagness, Computational Electrodynamics: the Finite Difference Time-Domain Method, 3rd ed. Norwood MA: Artech House, 2005.

[2.11] P. B. Johns, "New symmetrical condensed node for three-dimensional solution of electromagnetic-wave problems by TLM," Electronics Letters, vol. 22, no. 3, pp. 162-164, 1986.

[2.12] J. Paul, "The modelling of general electromagnetic materials in TLM," PhD thesis, University of Nottingham, 1998.

[2.13] J. Paul, C. Christopoulos, and D. W. P. Thomas, "Generalized material models in TLM — part I : materials with frequency-dependent properties," IEEE Transactions on Antennas and Propagation, vol. 47, no. 10, pp. 1528–1534, 1999.

[2.14] J. Paul, C. Christopoulos, and D. W. P. Thomas, "Generalized material models in TLM — part 2 : materials with anisotropic properties," IEEE Transactions on Antennas and Propagation, vol. 47, no. 10, pp. 1535–1542, 1999.

[2.15] J. Paul, C. Christopoulos, and D. W. P. Thomas, "Generalized material models in TLM - part 3: materials with nonlinear properties," IEEE Transactions on Antennas and Propagation, vol. 50, no. 7, pp. 997–1004, 2002.

3. Time Domain Embedded Thin Film Model

3.1. Overview

Thin films can be made of layers of a wide variety of materials including metals, insulators and semiconductors. They may be electrically conductive or non-conducting, optically transparent or opaque. The thickness of thin films is often much smaller than the wavelength of interest, ranging from fractions of a micrometre to several millimetres. Thin films have a wide range of applications in the optics [3.1 ~ 3.2] and Electromagnetic Compatibility (EMC) [3.3 ~ 3.6], as they can manipulate polarisation, reflection, transmission and absorption of light.

To successfully engineer and innovate products and technologies encompassing electromagnetic phenomena it is critical to deploy accurate and efficient simulation and design tools. As discussed in Chapter 2, the Transmission Line Modelling (TLM) [3.7] method, as a time domain simulation technique, provides a powerful and general technique upon which to base such design software.

In the TLM method, generating a suitable mesh is by no means a trivial task in its own right. Moreover the use of very small computational nodes results in a very large memory and run time overhead [3.7]. Because the thickness of the thin film is usually the smallest feature in the problem and much smaller than the wavelength of interest, the TLM mesh size needs to be significantly small to allow for at least one node within the film (as shown in Fig. 3-1 (a)). That not only increases the total number of nodes required, but also sets the maximum time step for the time-stepping evolution to become prohibitively small, which result in increasing of the total number of time steps needed to achieve a particular frequency resolution. In summary, the presence of a thin film generally leads to very fine mesh that needs to be run for more time steps. The use of non-uniform meshing [3.8], for example by means of multi-

gridding, alleviates this problem as it allows locally a fine mesh to be used only where they are truly needed, thus reducing the node count. However, the problem that the time step is determined by the smallest mesh size remains.

To overcome this problem it is expedient to recognise that the electromagnetic response of the thin film within a larger computational environment is highly localised. This means that a specialised model for such features can be developed in isolation, which can then be coupled to the rest of the simulation through a standardised interface, which avoids the need to discretise within the thin film.

One possible method for embedding thin films into the TLM algorithm is modifying its connection process. If, for example, a pair of nodes lies on opposite sides of a physical dielectric material boundary, the connection process is no longer a simple exchange of values, rather the reflection and transmission formulae for normal incidence on a dielectric interface come into play. It can be observed that the connection process described above in the case of a dielectric boundary is a simple illustration of how the known localised behaviour of a physical feature is embedded into the TLM algorithm. Indeed this inter-node connection behaves like a junction between two 1D transmission line circuit elements, each of whose parameters depends straightforwardly on the bulk material properties of the node from which it originates. This also provides a perfect opportunity to introduce thin film models: if the thin film is geometrically inserted between two layers of nodes it is only necessary to replace each one-dimensional (1D) transmission line junction, involving the dielectric interface reflection and transmission formulae, with those appropriate for the pair of lines joined through a circuit element whose response mimics the locally 1D behaviour of the thin layer. Thus the thin film need not be meshed as in Fig. 3-1 (b); it is now only defined by a section of transmission line. Its frequency dependent characteristics can be described by its admittance matrix, which connects the voltages and currents in both sides of the thin film. Since the TLM method operates in the time domain, the admittance matrix of the thin film should be transformed to the time domain in order to be embedded within the TLM algorithm. Therefore, an

inverse Z transform, general digital filter design and implementation techniques are adopted to transfer the frequency response of thin films to the time domain and then embed the time domain response within the mesh. Therefore the time step can be chosen according to the frequency of interest and not the restrictive fine features.

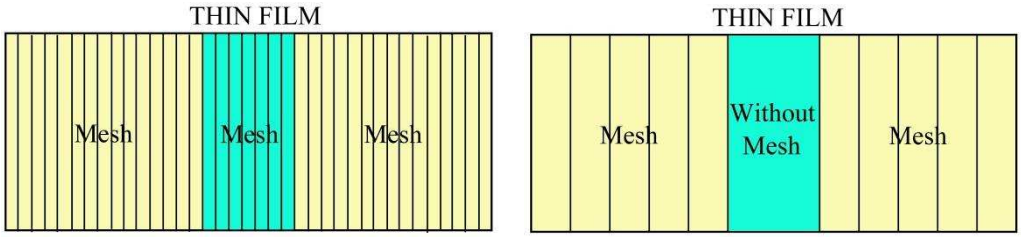

Fig. 3-1 (a) Modelling a thin film using conventional TLM (b) The embedded time domain thin film model.

In this chapter, the derivation of this specialised model for several thin film configurations, including a single-layer thin film model, a multilayer thin film model and an anisotropic thin film model, is demonstrated based on the inverse Z transform, general digital filter design and implementation techniques. The applications of these thin film models embedded between 1D and 2D TLM nodes will be discussed in the following chapters.

3.2. Single-Layer Thin Film Model

Consider a thin film which is assumed to be infinite in length and width, and of thickness of d. It can be viewed as a section of transmission line of length d. With the voltages and currents on the two sides of the film, it becomes a two-port network, as shown in Fig. 3-2.

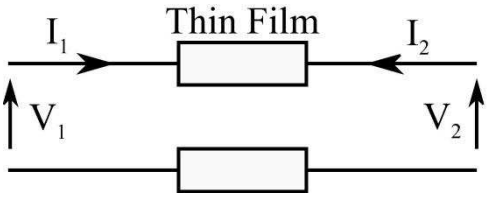

Fig. 3-2 Transmission Line Model of a thin film.

According to network theory [3.9], the admittance matrix of the film is given by,

$$\begin{pmatrix} I_1 \\ I_2 \end{pmatrix} = -j \begin{pmatrix} Ycot\theta & -Ycsc\theta \\ -Ycsc\theta & Ycot\theta \end{pmatrix} \begin{pmatrix} V_1 \\ V_2 \end{pmatrix}, \tag{3-1}$$

where Y is the characteristic admittance of the film and θ is the electrical length of the film which can be expressed as

$$\theta = \omega d\sqrt{LC},\ Y = \sqrt{C/L}, \tag{3-2}$$

where ω is the angular frequency and C and L are per unit length capacitance and inductance values of the thin film, respectively.

For general materials, L and C can be expressed by [3.7]

$$L = \mu + \frac{\sigma_m}{j\omega}, C = \varepsilon + \frac{\sigma_e}{j\omega}, \tag{3-3}$$

where $\mu, \varepsilon, \sigma_m$ and σ_e are the permeability, the permittivity, the magnetic resistivity and the electric conductivity of the material.

This two-port transmission line is initially considered to be embedded between two adjacent 1D TLM nodes, as shown in Fig. 3-3 (a).

In Fig. 3-3 (a), VR_n^i and VR_n^r are the incident and reflected voltages of the right side of the TLM node n, while VL_{n+1}^i and VL_{n+1}^r are the incident and reflected voltages from the left side of the TLM node (n+1), respectively. V_1^i and V_1^r are the incident and reflected voltages at port 1, while V_2^i and V_2^r are the incident and reflected voltages at port 2, respectively. The voltages of both ports have the following relations with the TLM nodes' incident and reflected voltages,

$$V_1{}^i = VR_n{}^r,\ V_1{}^r = VR_n{}^i,\ V_2{}^i = VL_{n+1}{}^r,\ V_2{}^r = VL_{n+1}{}^i.$$

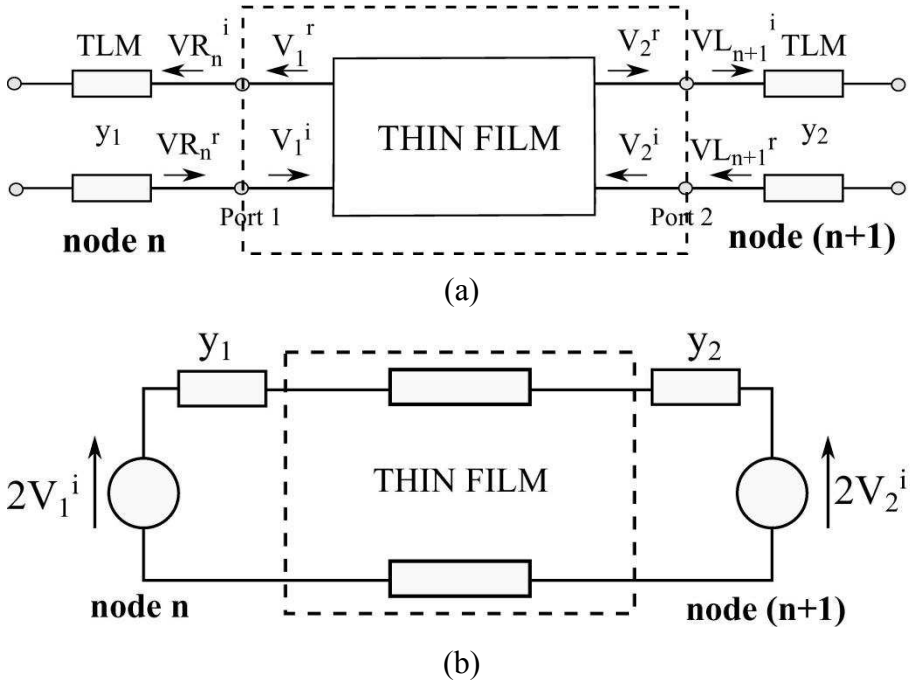

Fig. 3-3 (a) A thin film embedded between two 1D TLM nodes and (b) its Thevenin equivalent circuit.

From Fig. 3-3 (a), the reflection coefficient *R* and the transmission coefficient *T* of the thin film are defined in terms of the incident and reflected voltages as,

$$R = \frac{V_1^r}{V_1^i}, \tag{3-4}$$

$$T = \frac{V_2^r}{V_1^i}. \tag{3-5}$$

The embedding of the film requires that at each time step the reflected voltages on both ports need to be solved in terms of both the incident voltages from the adjacent TLM nodes and the film characteristics.

Because of the embedding of the film into two adjacent TLM nodes n and (n+1), the equation (2-22) for the node n and the equation (2-23) for the node (n+1) in the connection process should be modified.

Fig. 3-3 (b) shows the Thevenin equivalent circuits of the node n and (n+1) that are driving the thin film. Considering the admittance matrix of the film (equation (3-1)), the following relations are obtained,

$$\begin{pmatrix} 2y_1{V_1}^i \\ 2y_2{V_2}^i \end{pmatrix} = \begin{pmatrix} y_1 - jYcot\theta & jYcsc\theta \\ jYcsc\theta & y_2 - jYcot\theta \end{pmatrix} \begin{pmatrix} V_1 \\ V_2 \end{pmatrix} = [M] \begin{pmatrix} V_1 \\ V_2 \end{pmatrix}, \tag{3-6}$$

where y_1 and y_2 are the characteristic admittance of the TLM nodes on the left and right sides of the thin film, respectively, and the matrix [M] is defined for future convenience.

Multiplying the left and right sides of equation (3-6) with $[M]^{-1}$, the total voltages can be expressed by

$$\begin{aligned} &(y_1y_2 + YY - jY(y_1 + y_2)cot\theta) \begin{pmatrix} V_1 \\ V_2 \end{pmatrix} \\ &\qquad = \begin{pmatrix} y_2 - jYcot\theta & -jYcsc\theta \\ -jYcsc\theta & y_1 - jYcot\theta \end{pmatrix} \begin{pmatrix} 2y_1{V_1}^i \\ 2y_2{V_2}^i \end{pmatrix}. \end{aligned} \tag{3-7}$$

The aim is to solve V_1 and V_2 from equation (3-7). Then the reflected terms are given by

$$\begin{pmatrix} {V_1}^r \\ {V_2}^r \end{pmatrix} = \begin{pmatrix} V_1 \\ V_2 \end{pmatrix} - \begin{pmatrix} {V_1}^i \\ {V_2}^i \end{pmatrix}. \tag{3-8}$$

Equation (3-7) can be separated into two equations for V_1 and V_2, respectively.

$$\begin{aligned} &(y_1y_2 + YY - jY(y_1{+}y_2)cot\theta) \cdot V_1 \\ &\qquad = (2y_1y_2 - 2y_1jYcot\theta) \cdot V_1^i - 2y_2\, jYcsc\theta \cdot V_2^i, \end{aligned} \tag{3-9}$$

$$\begin{aligned} &(y_1y_2 + YY - jY(y_1{+}y_2)cot\theta) \cdot V_2 \\ &\qquad = -2y_1\, jYcsc\theta \cdot V_1^i + (2y_1y_2 - 2y_2jYcot\theta) \cdot V_2^i. \end{aligned} \tag{3-10}$$

In the above equations (3-9) and (3-10), all voltages are defined in the frequency domain whilst the TLM method is operating in the time domain. In order to connect the equations (3-9) and (3-10) with the TLM algorithm, they have to be transformed into the time domain. For this purpose an inverse Z-transform [3.10] is used.

It is noted that in equations (3-9) and (3-10), cotangent and cosecant functions are given in terms of frequency, which are difficult to be transformed directly to the time domain. Thus the expansions of the cotangent and cosecant functions in partial fractions are considered.

According to [3.11], the cotangent and cosecant functions can be expanded as infinite summations, so that the following equations are obtained,

$$jYcot\theta = j\sqrt{\frac{C}{L}}\left(\frac{1}{\theta} + 2\theta\sum_{k=1}^{N=\infty}\frac{1}{\theta^2 - k^2\pi^2}\right), \tag{3-11}$$

$$jYcsc\theta = j\sqrt{\frac{C}{L}}\left(\frac{1}{\theta} + 2\theta\sum_{k=1}^{N=\infty}\frac{(-1)^k}{\theta^2 - k^2\pi^2}\right). \tag{3-12}$$

Since $\theta = \omega d\sqrt{LC}$, the expansions (3-11) and (3-12) can be changed to the s-domain first, using $s = j\omega$,

$$jYcot\theta = -\frac{1}{sLd} - 2sCd\sum_{k=1}^{N=\infty}\frac{1}{s^2d^2LC + k^2\pi^2}, \tag{3-13}$$

$$jYcsc\theta = -\frac{1}{sLd} - 2sCd\sum_{k=1}^{N=\infty}\frac{(-1)^k}{s^2d^2LC + k^2\pi^2}. \tag{3-14}$$

Next, by setting

$$s = \frac{2}{\Delta t}\cdot\frac{1 - z^{-1}}{1 + z^{-1}}, \tag{3-15}$$

equations (3-13) and (3-14) are transferred to the Z-domain as required.

After replacing the cotangent and cosecant functions with the expansion summations (3-11) and (3-12) and transferring them to Z-domain, equations (3-9) and (3-10) have the form

$$\sum_i \frac{P_i(z)}{Q_i(z)}y(z) = \sum_i \frac{R_i(z)}{S_i(z)}x(z), \tag{3-16}$$

where $P_i(z), Q_i(z), R_i(z)$ and $S_i(z)$ are first-order or multiple-order polynomials in z, and $x(z)$ and $y(z)$ are the input and the output of the system, respectively.

For the right side of equation (3-16), each term $R_i(z)/S_i(z)$ can be seen as the transfer function of a digital filter. Assuming its output is $w_i(z)$, the digital filter can be expressed as,

$$w_i(z) = \frac{R_i(z)}{S_i(z)} \cdot x(z). \tag{3-17}$$

The summation of all the terms in the right side of equation (3-16) can be viewed as the parallel combination of a number of first- or multiple-order digital filters as shown in Fig.3-4, in which $w(z)$ is the overall output of the system.

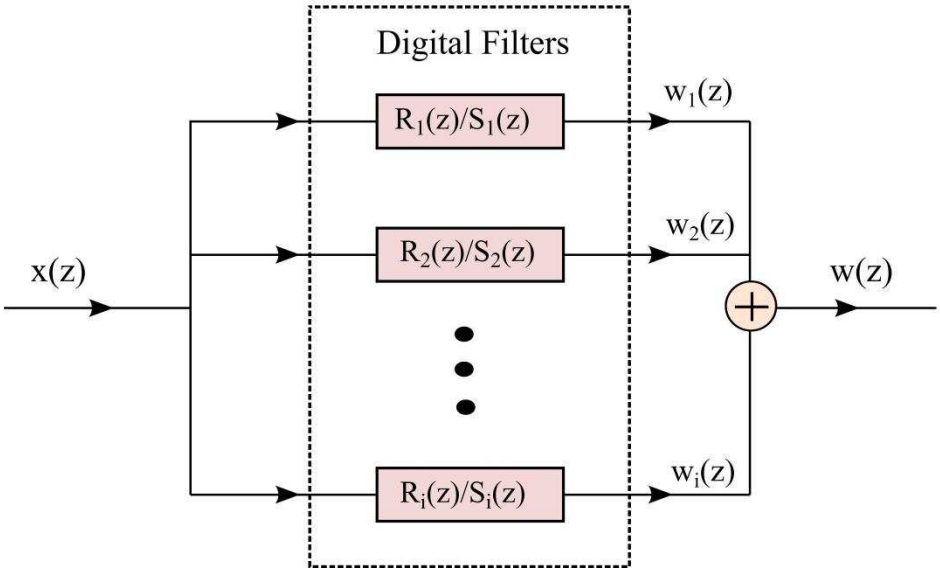

Fig.3-4 The parallel combination of a number of digital filters.

According to digital filter theory [3.12], the overall output of the parallel combination of digital filters equals the summation of the output from each filter. It can be expressed as,

$$w(z) = \sum_i w_i(z) = \sum_i \frac{R_i(z)}{S_i(z)} x(z). \tag{3-18}$$

Therefore, the output of the right side of the equation (3-16) can be obtained by calculating the output of each term first and then summing them together. For each term, an inverse Z transform is used to obtain the output in the time domain.

For example, a transfer function of the second order (Biquad) digital filter has the following form,

$$\frac{R_i(z)}{S_i(z)} = \frac{A_{i1} + A_{i2}z^{-1} + A_{i3}z^{-2}}{B_{i1} + B_{i2}z^{-1} + B_{i3}z^{-2}}, \tag{3-19}$$

where $A_{i1}, A_{i2}, A_{i3}, B_{i1}, B_{i2}$ and B_{i3} are known coefficients.

The output $w_i(z)$ of this filter in the Z domain is given by

$$w_i(z) = \frac{A_{i1} + A_{i2}z^{-1} + A_{i3}z^{-2}}{B_{i1} + B_{i2}z^{-1} + B_{i3}z^{-2}} \cdot x(z). \tag{3-20}$$

Using an inverse Z transform and considering its time shift properties [3.10], the output in the time domain $w_i(n\Delta t)$ can be found as,

$$\begin{aligned} w_i(n\Delta t) = [&A_{i1}x(n\Delta t) + A_{i2}x((n-1)\Delta t) + A_{i3}x((n-2)\Delta t) \\ &-B_{i2}w_i\big((n-1)\Delta t\big) - B_{i3}w_i((n-2)\Delta t)]/B_{i1}, \end{aligned} \tag{3-21}$$

where $x(n\Delta t)$ and $w_i(n\Delta t)$ are the input and output amplitudes at time $n\Delta t$, respectively.

The overall output of the right side of the equation (3-16), $w(n\Delta t)$, can be obtained through summing the output of each filter together,

$$w(n\Delta t) = \sum_i w_i(n\Delta t). \tag{3-22}$$

Therefore, equation (3-16) becomes,

$$\sum_i \frac{P_i(z)}{Q_i(z)} y(z) = w(z). \tag{3-23}$$

In equation (3-23), $Q_i(z) = Q_{i0} + z^{-1}Q_{i1} + z^{-2}Q_{i2} + \cdots$ where $Q_{i0},\ Q_{i1}, Q_{i2}, \cdots$ are constant values, and $P_i(z)$ is a general polynomial in z.

The left side of equation (3-23) represents the sum of a number of rational polynomials. The denominator $Q_i(z)$ is a polynomial in z which makes it difficult to solve for the output $y(z)$. In order to solve the output $y(z)$, a little mathematical trick is needed.

Assuming

$$u_i(z) = \frac{P_i(z)}{Q_i(z)} y(z), \tag{3-24}$$

and multiplying both sides of equation (3-24) by $Q_i(z)$ and then dividing by Q_{i0}, equation (3-24) becomes,

$$\frac{Q_i(z)}{Q_{i0}} \cdot u_i(z) = \frac{P_i(z)}{Q_{i0}} \cdot y(z). \tag{3-25}$$

After some transformation of equation (3-25) (adding and subtracting $u_i(z)$ on the left side), $u_i(z)$ is obtained as,

$$u_i(z) = \frac{P_i(z)}{Q_{i0}} y(z) - \left(\frac{Q_i(z)}{Q_{i0}} - 1 \right) u_i(z). \tag{3-26}$$

Summing both sides of equation (3-26) yields,

$$\sum_i u_i(z) = y(z) \sum_i \frac{P_i(z)}{Q_{i0}} - \sum_i \left(\frac{Q_i(z)}{Q_{i0}} - 1 \right) u_i(z). \tag{3-27}$$

Considering (3-24) and (3-23),

$$\sum_i u_i(z) = w(z),$$

and combining with (3-27), the final output in the Z-domain, $y(z)$, can be expressed by

$$y(z) \sum_i \frac{P_i(z)}{Q_{i0}} = \sum_i \left(\frac{Q_i(z)}{Q_{i0}} - 1 \right) u_i(z) + w(z). \tag{3-28}$$

In equation (3-28), since Q_{i0} is a constant value, both $P_i(z)/Q_{i0}$ and $Q_i(z)/Q_{i0}$ are general polynomials in z. After applying an inverse Z transform to both sides of (3-28), the final output in the time domain $y(n\Delta t)$ is easily obtained.

In order to make the above derivations more easily understood, a signal flow graph may be used to explain the solutions of equations (3-9) and (3-10). As

shown in Fig.3-5, equations (3-9) and (3-10) can be seen as a digital filter system with two inputs and two outputs.

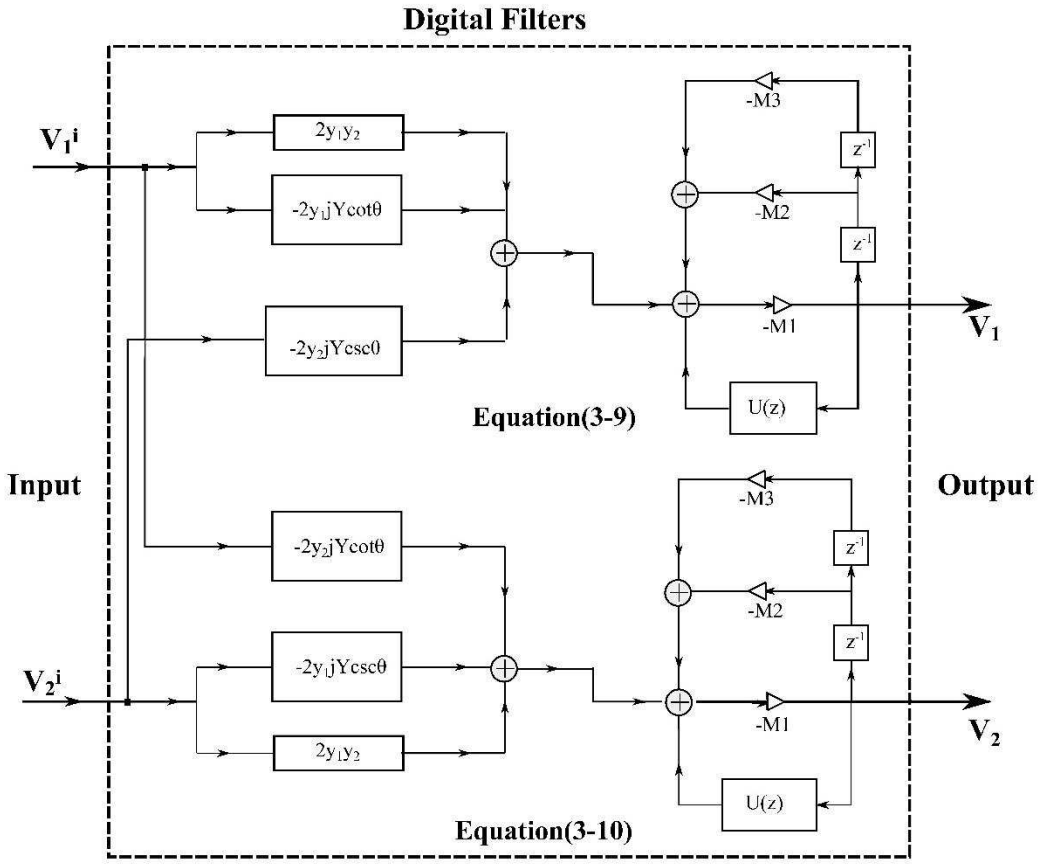

Fig.3-5 Signal flow graph of equations (3-9) and (3-10).

In this digital filter system, V_1^i and V_2^i are the input signals, while V_1 and V_2 are the output signals.

$jYcot\theta$ and $jYcsc\theta$ are parallel combinations of (N+1) first and second order digital filters, which can be written as

$$jYcot\theta = -\frac{\Delta t}{d}\cdot\frac{1+z^{-1}}{A_2+B_2z^{-1}} - \frac{2\Delta t}{d}\sum_{k=1}^{N=\infty}\frac{A_1+B_1z^{-1}+C_1z^{-2}}{A_k+B_kz^{-1}+C_kz^{-2}},$$

$$jYcsc\theta = -\frac{\Delta t}{d}\cdot\frac{1+z^{-1}}{A_2+B_2z^{-1}} \tag{3-29}$$

$$-\frac{2\Delta t}{d}\sum_{k=1}^{N=\infty}\frac{(-1)^k(A_1+B_1z^{-1}+C_1z^{-2})}{A_k+B_kz^{-1}+C_kz^{-2}},$$

where

$$A_1 = 2\varepsilon + \sigma_e \Delta t,\ B_1 = 2\sigma_e \Delta t,\ C_1 = \sigma_e \Delta t - 2\varepsilon,$$

$$A_2 = 2\mu + \sigma_m \Delta t,\ B_2 = \sigma_m \Delta t - 2\mu,$$

$$A_k = 4\mu\varepsilon + 2\Delta t(\mu\sigma_e + \varepsilon\sigma_m) + (\sigma_m\sigma_e + k^2\pi^2/d^2)\Delta t^2,$$

$$B_k = -8\mu\varepsilon + 2(\sigma_m\sigma_e + k^2\pi^2/d^2)\Delta t^2,$$

$$C_k = 4\mu\varepsilon - 2\Delta t(\mu\sigma_e + \varepsilon\sigma_m) + (\sigma_m\sigma_e + k^2\pi^2/d^2)\Delta t^2.$$

$U(z)$ is also the parallel combination of a number of first and second order digital filters,

$$U(z) = \frac{B_2}{A_2} z^{-1} u_2(z) + \frac{B_2}{A_2} z^{-1} u_3(z) + \sum_{k=1}^{N=\infty} \left(\frac{B_k}{A_k} z^{-1} + \frac{C_k}{A_k} z^{-2} \right) u_{4k}(z), \tag{3-30}$$

where

$$u_2(z) = \frac{A_1 + C_1 z^{-1}}{A_2 + B_2 z^{-1}},$$

$$u_3(z) = (y_1 + y_2) \cdot \frac{\Delta t}{d} \cdot \frac{1 + z^{-1}}{A_2 + B_2 z^{-1}},$$

$$u_{4k}(z) = (y_1 + y_2) \cdot \frac{2\Delta t}{d} \cdot \frac{A_1 + B_1 z^{-1} + C_1 z^{-2}}{A_k + B_k z^{-1} + C_k z^{-2}}.$$

$M1, M2$ and $M3$ are constant gain and expressed as,

$$M_1 = y_1 y_2 + \frac{A_1}{A_2} + (y_1 + y_2) \cdot \frac{\Delta t}{d \cdot A_2} + (y_1 + y_2) \cdot \frac{2\Delta t}{d} \cdot \sum_{k=1}^{N=\infty} \frac{A_1}{A_k},$$

$$M_2 = \frac{C_1}{A_2} + (y_1 + y_2) \cdot \frac{\Delta t}{d \cdot A_2} + (y_1 + y_2) \cdot \frac{2\Delta t}{d} \cdot \sum_{k=1}^{N=\infty} \frac{B_1}{A_k},$$

$$M_3 = (y_1 + y_2) \cdot \frac{2\Delta t}{d} \cdot \sum_{k=1}^{N=\infty} \frac{C_1}{A_k}.$$

Therefore, the thin film embedded in the TLM algorithm behaves like a complex digital filter system with two inputs and two outputs. The accuracy of the model depends on the number of terms, N, used in the expansions of equations (3-11) and (3-12). This will be analysed in Chapter 4. Through modifying the connection process of the TLM algorithm, the model is embedded between two adjacent TLM nodes without discretisation.

3.3. Multi-Layer Thin Film Model

The model developed in section 3.2 can be extended to model a multilayer thin film stack. The stack, as a whole, is embedded between two adjacent TLM nodes as an interface. Through modifying the connection process, the multilayer thin film model connects with the TLM algorithm.

In the single layer embedded model, its implementation starts with the admittance matrix of the layer. If using the same method of modelling the m-layer (m >= 2) film as that of single layer film, the overall admittance matrix of the m-layer film should be found. The admittance matrix of each layer is easily obtained, but the overall admittance matrix of the m-layer film is hard to get. Since the layers are cascaded together, the straightforward thinking is multiplying all the matrixes, but it is not applicable for the admittance matrix. Only ABCD matrices [3.9] could be multiplied together. Thus one possible way forward is transferring the admittance matrix of each layer to an ABCD matrix first, then multiplying them to get the overall ABCD matrix and at the end transferring the overall ABCD matrix back to admittance matrix. Although the overall admittance matrix of the m-layer film could be found using such a method, it is not efficient and also hard to implement the digital filters especially for a large number of layers.

Therefore, an efficient and easy way to implement digital filters method is presented in this section, which avoids calculating the overall admittance matrix. It starts with the admittance matrix of each layer. In the admittance matrix of the adjacent layers there are some common quantities, which can be cancelled and then combined together. After combining together, a linear matrix equation can be formed. The unknown quantities of the reflected voltages from the stack can be solved for using a Gauss-Seidel method. This method will be explained in detail in the following sub-sections.

Consider an m-layer (m >= 2) thin film, embedded between two TLM nodes as shown in Fig. 3-6. As in the single layer thin film model, each layer can be seen as a two-port transmission line with thickness $d_i (i = 1,2,\dots,m)$.

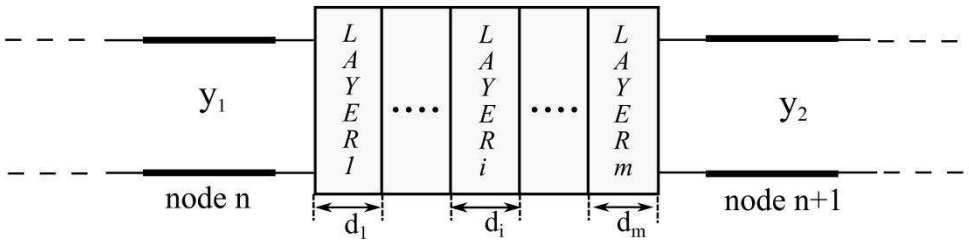

Fig. 3-6 An m-layer (m >= 2) thin film embedded between 1D TLM nodes.

In the general case, the materials in each layer of the m-layer thin film may have different electric and magnetic properties. Therefore, the equivalent capacitance and inductance of each layer can be expressed in terms of their electric and magnetic properties as follows:

$$C_i = \varepsilon_i + \frac{\sigma_{ei}}{j\omega}, L_i = \mu_i + \frac{\sigma_{mi}}{j\omega},$$

where the subscript i represents the particular layer ($i = 1,2,\dots,m$).

The characteristic admittance of each layer is given by

$$Y_i = \sqrt{\frac{C_i}{L_i}}, \quad i = 1,2,\dots,m.$$

In the following sections, a two-layer thin film model is presented first, and then a three-layer thin film model is derived. At the end, as a general case, a generalised thin film model is described.

3.3.1. Two-Layer (m = 2) Thin Film Model

Fig.3-7 (a) shows a two-layer thin film embedded between two adjacent 1D TLM nodes. Its transmission line model is shown in Fig.3-7 (b) with associated voltages and currents. There are two sections of transmission line.

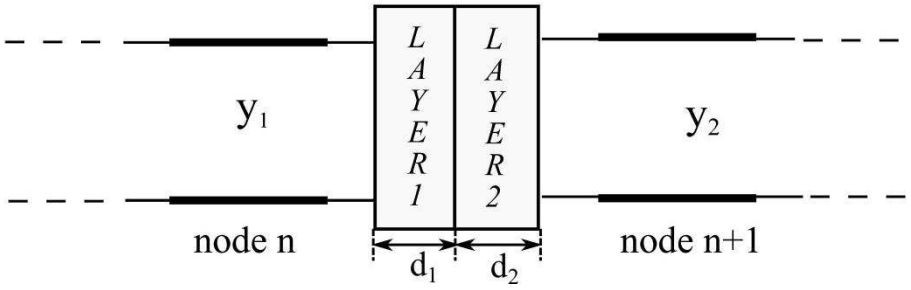

(a)

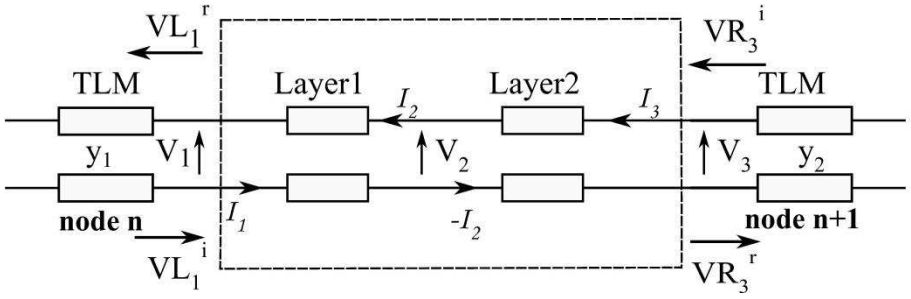

(b)

Fig.3-7 (a) A two-layer thin film embedded between 1D TLM nodes (b) the transmission line model of the two-layer thin film.

As shown in Fig.3-7 (b) the admittance matrix of each layer can be written as,

$$\begin{pmatrix} I_1 \\ I_2 \end{pmatrix} = \begin{pmatrix} y_1 - jY_1 cot\theta_1 & jY_1 csc\theta_1 \\ jY_1 csc\theta_1 & -jY_1 cot\theta_1 \end{pmatrix} \cdot \begin{pmatrix} V_1 \\ V_2 \end{pmatrix}, \tag{3-31}$$

$$\begin{pmatrix} -I_2 \\ I_3 \end{pmatrix} = \begin{pmatrix} -jY_2 cot\theta_2 & jY_2 csc\theta_2 \\ jY_2 csc\theta_2 & y_2 - jY_2 cot\theta_2 \end{pmatrix} \cdot \begin{pmatrix} V_2 \\ V_3 \end{pmatrix}. \tag{3-32}$$

Each matrix in the above equations, (3-31)-(3-32), can be separated into two equations.

From (3-31),

$$I_1 = (y_1 - jY_1 cot\theta_1) \cdot V_1 + jY_1 csc\theta_1 \cdot V_2, \tag{3-33}$$

$$I_2 = jY_1 csc\theta_1 \cdot V_1 + (-jY_1 cot\theta_1) \cdot V_2. \tag{3-34}$$

From (3-32),

$$-I_2 = -jY_2 cot\theta_2 \cdot V_2 + jY_2 csc\theta_2 \cdot V_3, \tag{3-35}$$

$$I_3 = jY_2 csc\theta_2 \cdot V_2 + (y_2 - jY_2 cot\theta_2) \cdot V_3. \tag{3-36}$$

Since equations (3-34) and (3-35) have common terms I_2 and V_2, by summing these two equations, I_2 can be eliminated as follows,

$$0 = jY_1 csc\theta_1 \cdot V_1 + (-jY_1 cot\theta_1 - jY_2 cot\theta_2) \cdot V_2 + jY_2 csc\theta_2 \cdot V_3. \tag{3-37}$$

Considering equations (3-33), (3-37) and (3-36), the following linear matrix equation can be obtained,

$$\begin{pmatrix} I_1 \\ 0 \\ I_3 \end{pmatrix} = \begin{pmatrix} y_1 - jY_1 cot\theta_1 & jY_1 csc\theta_1 & 0 \\ jY_1 csc\theta_1 & -jY_1 cot\theta_1 - jY_2 cot\theta_2 & 0 \\ 0 & jY_2 csc\theta_2 & y_2 - jY_2 cot\theta_2 \end{pmatrix} \begin{pmatrix} V_1 \\ V_2 \\ V_3 \end{pmatrix}. \tag{3-38}$$

When the thin film is embedded between two 1D TLM nodes, as in Fig.3-7 (b), the following relations exist,

$$I_1 = 2y_1 \cdot {VL_1}^i,$$
$$I_3 = 2y_2 \cdot {VR_3}^i,$$
$$V_1 = {VL_1}^i + {VL_1}^r,$$
$$V_3 = {VR_3}^i + {VR_3}^r,$$

where ${VL_1}^i$ and ${VL_1}^r$ are the incident and reflected voltages on the left side of the two-layer film, and ${VR_3}^i$ and ${VR_3}^r$ are the incident and reflected voltages on the right side of the two-layer film.

Applying the above relations in equation (3-38), the following linear equations are obtained,

$$\begin{pmatrix} 2y_1 \cdot {VL_1}^i \\ 0 \\ 2y_2 \cdot {VR_3}^i \end{pmatrix} = \begin{pmatrix} y_1 - jY_1 cot\theta_1 & jY_1 csc\theta_1 & 0 \\ jY_1 csc\theta_1 & -jY_1 cot\theta_1 - jY_2 cot\theta_2 & 0 \\ 0 & jY_2 csc\theta_2 & y_2 - jY_2 cot\theta_2 \end{pmatrix} \begin{pmatrix} {VL_1}^i + {VL_1}^r \\ V_2 \\ {VR_3}^i + {VR_3}^r \end{pmatrix} \quad (3\text{-}39)$$

In equation (3-39), the incident voltages from the left side and the right side of the film are known, while the reflected voltages and intermediate voltages are unknowns. That means that equation (3-39) has the form $[\boldsymbol{b}] = [\boldsymbol{A}][\boldsymbol{x}]$, where $[\boldsymbol{A}]$ is a square matrix.

The straightforward method for solving equation with the from $[\boldsymbol{b}] = [\boldsymbol{A}][\boldsymbol{x}]$ is to multiply both sides of the equation with the inverse of matrix $[\boldsymbol{A}]$**,** i.e. $[\boldsymbol{A}]^{-1}$. However, the matrix $[\boldsymbol{A}]^{-1}$ in equation (3-39) is difficult to obtain considering that cotangent and cosecant functions exist in the matrix. In order to avoid calculating $[\boldsymbol{A}]^{-1}$, the Gauss-Seidel method [3.13] based on an iterative matrix solver is used to solve equation (3-39).

The initial values were chosen to be 0,

$${VL_1}^{r(0)} = 0,\ {V_2}^{(0)} = 0,\ {VR_3}^{r(0)} = 0.$$

Then, the iteration process is as follows,

$${VL_1}^i + {VL_1}^{r(k+1)} = -\frac{1}{y_1 - jY_1 cot\theta_1} \cdot \left(jY_1 csc\theta_1 \cdot {V_2}^{(k)} - 2y \cdot {VL_1}^i\right),$$

$${V_2}^{(k+1)} = -\frac{1}{-jY_1 cot\theta_1 - jY_2 cot\theta_2} \cdot \left(jY_1 csc\theta_1 \cdot \left({VL_1}^i + {VL_1}^{r(k+1)}\right) + jY_2 csc\theta_2 \cdot {VR_3}^{r(k)}\right),$$

$${VR_3}^i + {VR_3}^{r(k+1)} = -\frac{1}{y - jY_2 cot\theta_2} \cdot \left(jY_2 csc\theta_2 \cdot {V_2}^{(k+1)} - 2y_2 \cdot {VR_3}^i\right).$$

Rearranging the above equations so that all the unknown values are on the left hand side, the iteration process turns into:

$$(y_1 - jY_1 cot\theta_1) \cdot {VL_1}^{r(k+1)} = -jY_1 csc\theta_1 \cdot {V_2}^{(k)} + (y_1 + jY_1 cot\theta_1) \cdot {VL_1}^{i},$$

$$(-jY_1 cot\theta_1 - jY_2 cot\theta_2) \cdot {V_2}^{(k+1)}$$
$$= -jY_1 csc\theta_1 \cdot {VL_1}^{i} - jY_1 csc\theta_1 \cdot {VL_1}^{r(k+1)} - jY_2 csc\theta_2 \cdot {VR_3}^{r(k)},$$

$$(y_2 - jY_2 cot\theta_2) \cdot {VR_3}^{r(k+1)}$$
$$= -jY_2 csc\theta_2 \cdot {V_2}^{(k+1)} + (y_2 + jY_2 cot\theta_2) \cdot {VR_3}^{i}.$$

It is noted that the Gauss-Seidel method solves for unknown values in a sequential manner within one iteration, whereby voltage ${VL_1}^{r(k+1)}$ is obtained first and then used to obtain voltage ${V_2}^{(k+1)}$. ${V_2}^{(k+1)}$ is used to obtain ${VR_3}^{r(k+1)}$.

Each equation in the above procedure has a similar form to equation (3-9) described in section 3.2. They can be solved through inverse Z transform and digital filter theory as demonstrated in section 3.2. When the required tolerances on all unknown values are achieved, the iteration procedure is "terminated".

3.3.2. Three-Layer (m = 3) Thin Film Model

Fig.3-8 (a) shows a three-layer thin film embedded between two adjacent 1D TLM nodes. Its transmission line model is shown in Fig.3-8 (b).

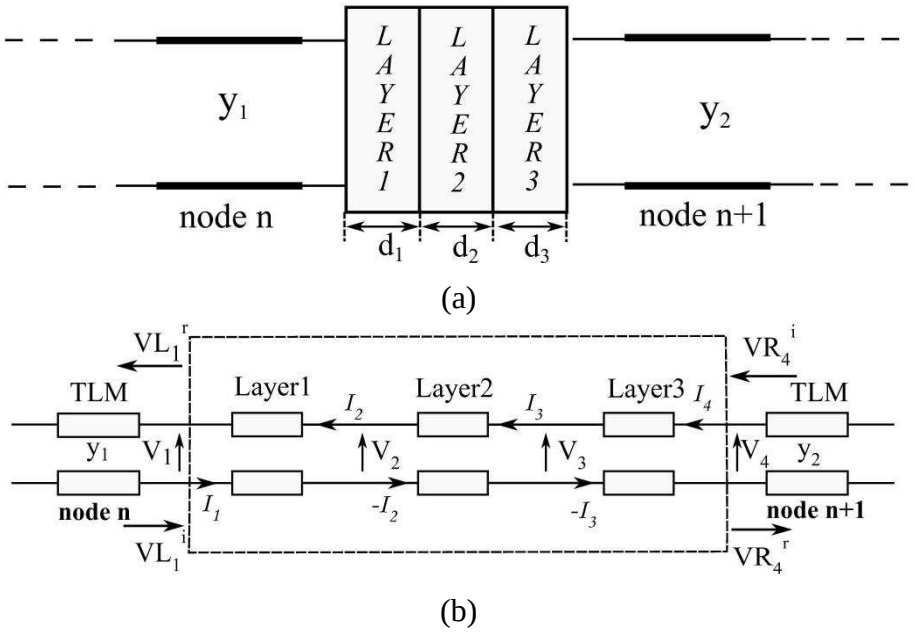

Fig.3-8 (a) A three-layer thin film embedded between 1D TLM nodes (b) the transmission line model of the three-layer thin film.

As shown in Fig.3-8 (b) the admittance matrix of each layer can be written as,

$$\begin{pmatrix} I_1 \\ I_2 \end{pmatrix} = \begin{pmatrix} y_1 - jY_1 cot\theta_1 & jY_1 csc\theta_1 \\ jY_1 csc\theta_1 & -jY_1 cot\theta_1 \end{pmatrix} \cdot \begin{pmatrix} V_1 \\ V_2 \end{pmatrix}, \tag{3-40}$$

$$\begin{pmatrix} -I_2 \\ I_3 \end{pmatrix} = \begin{pmatrix} -jY_2 cot\theta_2 & jY_2 csc\theta_2 \\ jY_2 csc\theta_2 & -jY_2 cot\theta_2 \end{pmatrix} \cdot \begin{pmatrix} V_2 \\ V_3 \end{pmatrix}, \tag{3-41}$$

$$\begin{pmatrix} -I_3 \\ I_4 \end{pmatrix} = \begin{pmatrix} -jY_3 cot\theta_3 & jY_3 csc\theta_3 \\ jY_3 csc\theta_3 & y_2 - jY_3 cot\theta_3 \end{pmatrix} \cdot \begin{pmatrix} V_3 \\ V_4 \end{pmatrix}. \tag{3-42}$$

Each matrix in the above equations (3-40)-(3-42) can be separated into two equations. After combination as in the two-layer thin film model, the following linear matrix equations can be obtained,

$$\begin{pmatrix} I_1 \\ 0 \\ 0 \\ I_4 \end{pmatrix} = \begin{pmatrix} y_1 - jY_1 cot\theta_1 & jY_1 csc\theta_1 & 0 & 0 \\ jY_1 csc\theta_1 & -jY_1 cot\theta_1 - jY_2 cot\theta_2 & jY_2 csc\theta_2 & 0 \\ 0 & jY_2 csc\theta_2 & -jY_2 cot\theta_2 - jY_3 cot\theta_3 & jY_3 csc\theta_3 \\ 0 & 0 & jY_3 csc\theta_3 & y_2 - jY_3 cot\theta_3 \end{pmatrix} \cdot \begin{pmatrix} V_1 \\ V_2 \\ V_3 \\ V_4 \end{pmatrix}. \tag{3-43}$$

When the thin film is embedded between two 1D TLM nodes, as in Fig.3-8 (b), the following relations exist,

$$I_1 = 2y_1 \cdot {VL_1}^i,$$
$$I_4 = 2y_2 \cdot {VR_4}^i,$$

$$V_1 = {VL_1}^i + {VL_1}^r,$$
$$V_4 = {VR_4}^i + {VR_4}^r,$$

where ${VL_1}^i$ and ${VL_1}^r$ are the incident and reflected voltages on the left side of the multi-layer film, and ${VR_4}^i$ and ${VR_4}^r$ are the incident and reflected voltages on the right side of the multi-layer film.

Applying the above relations into equation (3-43), the following linear equations are obtained,

$$\begin{pmatrix} 2y_1 \cdot {VL_1}^i \\ 0 \\ 0 \\ 2y_2 \cdot {VR_4}^i \end{pmatrix} = \begin{pmatrix} y_1 - jY_1 cot\theta_1 & jY_1 csc\theta_1 & 0 & 0 \\ jY_1 csc\theta_1 & -jY_1 cot\theta_1 - jY_2 cot\theta_2 & jY_2 csc\theta_2 & 0 \\ 0 & jY_2 csc\theta_2 & -jY_2 cot\theta_2 - jY_3 cot\theta_3 & jY_3 csc\theta_3 \\ 0 & 0 & jY_3 csc\theta_3 & y_2 - jY_3 cot\theta_3 \end{pmatrix} \cdot \begin{pmatrix} {VL_1}^i + {VL_1}^r \\ V_2 \\ V_3 \\ {VR_4}^i + {VR_4}^r \end{pmatrix}. \quad (3\text{-}44)$$

Equation (3-44) can be solved using the Gauss-Seidel method [3.13].

The initial values were chosen to be 0,

${VL_1}^{r(0)} = 0, {V_2}^{(0)} = 0, {V_3}^{(0)} = 0, {VR_4}^{r(0)} = 0.$

Then, the iteration process is as follows,

$$(y_1 - jY_1 cot\theta_1) \cdot {VL_1}^{r(k+1)} = -jY_1 csc\theta_1 \cdot {V_2}^{(k)} + (y_1 + jY_1 cot\theta_1) \cdot {VL_1}^i,$$

$$(-jY_1 cot\theta_1 - jY_2 cot\theta_2) \cdot {V_2}^{(k+1)} = -jY_1 csc\theta_1 \cdot {VL_1}^i - jY_1 csc\theta_1 \cdot {VL_1}^{r(k+1)} - jY_2 csc\theta_2 \cdot {V_3}^{(k)},$$

$$(-jY_3 cot\theta_3 - jY_2 cot\theta_2) \cdot {V_3}^{(k+1)} = -jY_2 csc\theta_2 \cdot {V_2}^{(k+1)} - jY_3 csc\theta_3 \cdot {VR_4}^i - jY_3 csc\theta_3 \cdot {VR_4}^{r(k)},$$

$$(y_2 - jY_3 cot\theta_3) \cdot {VR_4}^{r(k+1)} = -jY_3 csc\theta_3 \cdot {V_4}^{(k+1)} + (y_2 + jY_3 cot\theta_3) \cdot {VR_4}^i.$$

Each equation in the above procedure has a similar form to equation (3-9) described in section 3.2. They can be solved through inverse Z transform and digital filter theory as demonstrated in section 3.2. When the required

tolerances on all unknown values are achieved, the iteration process is complete.

3.3.3. Generalised Multi-layer (m >= 4) Thin Film Model

For thin films with m (m >= 4) layers, there are m admittance matrix equations like (3-40). After some mathematical manipulations, equations like (3-44) can be obtained, resulting in a square matrix of order (m+1) with (m+1) unknowns.

For thin films with four or more layers (m >= 4), the linear matrix equation like (3-44) can be written as,

$$\begin{pmatrix} 2y \cdot {VL_1}^i \\ 0 \\ 0 \\ \vdots \\ 0 \\ 0 \\ 2y \cdot {VR_{m+1}}^i \end{pmatrix} =$$

$$\begin{pmatrix} y - jY_1 cot\theta_1 & jY_1 csc\theta_1 & 0 & 0 & 0 & 0 & \cdots & 0 \\ jY_1 csc\theta_1 & -jY_1 cot\theta_1 - jY_2 cot\theta_2 & jY_2 csc\theta_2 & 0 & 0 & 0 & \cdots & 0 \\ 0 & jY_2 csc\theta_2 & -jY_2 cot\theta_2 - jY_3 cot\theta_3 & jY_2 csc\theta_2 & 0 & 0 & \cdots & 0 \\ & & & \vdots & & & & \\ 0 \cdots 0 & 0 & jY_{m-2} csc\theta_{m-2} & -jY_{m-2} cot\theta_{m-2} - jY_{m-1} cot\theta_{m-1} & jY_{m-1} csc\theta_{m-1} & & 0 & \\ 0 \cdots 0 & 0 & 0 & jY_{m-1} csc\theta_{m-1} & -jY_{m-1} cot\theta_{m-1} - jY_m cot\theta_m & & jY_m csc\theta_m & \\ 0 \cdots 0 & 0 & 0 & 0 & jY_m csc\theta_m & & y_2 - jY_m cot\theta_m & \end{pmatrix}$$

$$\cdot \begin{pmatrix} {VL_1}^i + {VL_1}^r \\ V_2 \\ V_3 \\ \vdots \\ V_{m-1} \\ V_m \\ {VR_{m+1}}^i + {VR_{m+1}}^r \end{pmatrix}.$$

(3-45)

Its solution is given using Gauss-Seidel method by the following iteration process,

$$(y - jY_1 cot\theta_1) \cdot {VL_1}^{r(k+1)} = -jY_1 csc\theta_1 \cdot {V_2}^{(k)} + (y + jY_1 cot\theta_1) \cdot {VL_1}^i,$$

$$(-jY_1 cot\theta_1 - jY_2 cot\theta_2)\cdot {V_2}^{(k+1)} = -jY_1 csc\theta_1 \cdot {VL_1}^{i} - jY_1 csc\theta_1 \cdot {VL_1}^{r(k+1)} - jY_2 csc\theta_2 \cdot {V_3}^{(k)},$$

$$(-jY_{i-1} cot\theta_{i-1} - jY_i cot\theta_i)\cdot {V_i}^{(k+1)} = -jY_{i-1} csc\theta_{i-1} \cdot {V_{i-1}}^{(k+1)} - jY_i csc\theta_i \cdot {V_{i+1}}^{(k)}, \quad (3 \le i \le m-2),$$

$$(-jY_{m-1} cot\theta_{m-1} - jY_m cot\theta_m)\cdot {V_m}^{(k+1)} = -jY_{m-1} csc\theta_{m-1} \cdot {V_{m-1}}^{(k+1)} - jY_m csc\theta_m \cdot {VR_{m+1}}^{i} - jY_m csc\theta_m \cdot {VR_{m+1}}^{r(k)},$$

$$(y - jY_m cot\theta_m)\cdot {VR_{m+1}}^{r(k+1)} = -jY_m csc\theta_m \cdot {V_m}^{(k+1)} + (y + jY_m csc\theta_m)\cdot {VR_{m+1}}^{i}.$$

When the required tolerances on all unknown values are achieved, the iteration process is "terminated".

Therefore, the model for the multilayer thin film is integrated into the TLM algorithm. After one run of the TLM, the reflected and transmitted voltages from the film are obtained in the time domain.

3.4. Anisotropic Thin Film Model

The electric and magnetic properties of anisotropic materials vary in different directions [3.14]. In this section, only non-magnetic materials with electric anisotropy are considered. The materials are assumed to be anisotropic in two-dimensional (2D) so they can be modelled using two 1D models.

Assume that an anisotropic thin film has the following electric properties:

$$\varepsilon = \begin{pmatrix} \varepsilon_x & 0 \\ 0 & \varepsilon_y \end{pmatrix},\ \sigma_e = \begin{pmatrix} \sigma_{ex} & 0 \\ 0 & \sigma_{ey} \end{pmatrix}. \tag{3-46}$$

Consider a plane electric field $\vec{E}^i$ propagating in the z direction. It has two components, E_x and E_y. They satisfy the following relations:

$$\vec{E}^i = E_x\hat{\boldsymbol{x}} + E_y\hat{\boldsymbol{y}} = \left|E^i\right|cos\varphi \cdot \hat{\boldsymbol{x}} + \left|E^i\right|sin\varphi \cdot \hat{\boldsymbol{y}},$$

where φ is the angle between the electric field $\vec{E}^i$ and the x axis, and $\hat{\boldsymbol{x}}$ and $\hat{\boldsymbol{y}}$ are the unit vectors in the x and y direction, respectively.

When the electric field $\vec{E}^i$ is normally incident upon the anisotropic thin film, the thin film will have different responses in the x and y directions, as shown in Fig. 3-9.

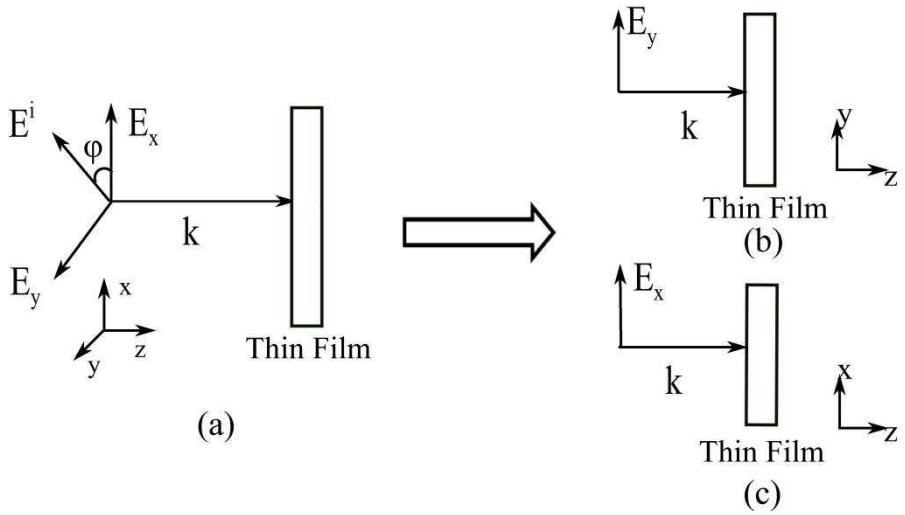

Fig. 3-9 (a)The electric field E^i incident upon an anisotropic thin film can be decomposed into x and y field components (b) E_y field component incident on a thin film (c) E_x field component incident on a thin film.

The E_x component of $\vec{E}^i$ has effects on the film in the x direction which has the properties of ε_x and σ_{ex} for the permittivity and conductivity. The E_y component has effects on the film in the y direction which has the properties of ε_y and σ_{ey}.

The responses of the film to the electric fields in the two directions are independent of each other. Therefore, they can be analysed by performing two separate simulations with incident fields shown in Fig. 3-9 (b, c). For each

direction, the thin film can be modelled using the embedded thin film TLM model.

In the x direction, the reflected and transmitted electric fields from the thin film are obtained as E_x^r and E_x^t, respectively. In the y direction, the reflected and transmitted electric fields from the thin film are obtained as E_y^r and E_y^t, respectively. Therefore, the overall reflected and transmitted electric fields from the anisotropic thin film can be acquired as,

$$\begin{aligned} \vec{E}^r &= E_x^r cos\varphi \cdot \hat{x} + E_y^r sin\varphi \cdot \hat{y}, \\ \vec{E}^t &= E_x^t cos\varphi \cdot \hat{x} + E_y^t sin\varphi \cdot \hat{y}. \end{aligned} \tag{3-47}$$

Examples will be given in the next chapter to test this model.

3.5. Conclusions

In this chapter, time domain thin film models, including single-layer and multilayer thin film models, have been developed for embedding in the TLM method. The case of a 1D anisotropic thin film is also discussed. In these models, the thin films are not discretised, but act as a kind of interface between the adjacent TLM nodes. Their frequency responses are transformed to the time domain using digital filter theory and the inverse Z transform, and then added to the TLM algorithm. Since these embedded models do not require discretisation, they have the potential to reduce the total simulation time and save memory usage. The only control parameter that affects the accuracy of the model is the number of terms in cotangent and cosecant expansions; this will be analysed in the next chapter.

The applications of these models in 1D TLM algorithms are investigated in the following chapter, through which the accuracy, stability, convergence and efficiency of the time domain embedded thin film model are also discussed.

The further applications of these models in 2D TLM algorithms will be studied in Chapter 5 and 6. Some modifications to these models will be discussed there too.

References

[3.1] A. Vukovic, "Fourier transform analysis of optoelectronic components and circuits," PhD thesis, Universtiy of Nottingham, 2000.

[3.2] C. Giles, "Lightwave applications of fiber Bragg gratings," J. Light. Technol., vol. 15, no. 8, pp. 1391–1404, 1997.

[3.3] M. Apr, M. D. Amore, K. Gigliotti, M. S. Sarto, S. Member, and V. Volpi, "Lightning Indirect Effects Certification of a Transport Aircraft by Numerical Simulation," IEEE Trans. Electromagn. Compat., vol. 50, no. 3, pp. 513–523, 2008.

[3.4] C. L. Holloway, M. S. Sarto, and M. Johansson, "Analyzing Carbon-Fiber Composite Materials With Equivalent-Layer Models," IEEE Trans. Electromagn. Compat., vol. 47, no. 4, pp. 833–844, 2005.

[3.5] M. Parise and M. S. Sarto, "Efficient formulation of high-order boundary conditions for the high-frequency modeling of multilayer composite slab," 2003 IEEE Symp. Electromagn. Compat. Symp. Rec. (Cat. No.03CH37446), vol. 2, pp. 753–758, 2003.

[3.6] M. S. Sarto, "A new model for the FDTD analysis of the shielding performances of thin composite structures," IEEE Trans. Electromagn. Compat., vol. 41, no. 4, pp. 298–306, 1999.

[3.7] C. Christopoulos, The Transmission-Line Modeling Method TLM. IEEE Press, 1995.

[3.8] O. V. Vasilyev, "High Order Finite Difference Schemes on Non-uniform Meshes with Good Conservation Properties," J. Comput. Phys., vol. 157, no. 2, pp. 746–761, 2000.

[3.9] D. M. Pozar, Microwave engineering. Wiley. com, 2009.

[3.10] S. K. Mirta and J. F. Kaiser, Handbook for digital signal processing. John Wiley & Sons, Inc., 1993.

[3.11] M. Abramowitz and I. A. Stegun, Handbook of Mathematical Functions with Formulas, Graphs, and Mathematical Tables, The 10th. Washington, D.C.: Government printing office, 1972.

[3.12] J. O. Smith, Introduction to Digital Filters with Audio Applications. W3K Publishing, 2007.

[3.13] Press, H., A. Teukolsky, T. Vetterling, and P. Flannery, Numerical Recipes in C++. The Art of Computer Programming. Cambridge University Press, 2002.

[3.14] M. Lin, C. H. Chen, and S. Member, “Plane-wave shielding characteristics of anisotropic laminated composites,” IEEE Trans. Electromagn. Compat., vol. 35, no. 1, pp. 21–27, 1993.

4.Embedded Thin Film Model in the One-Dimensional TLM Method

4.1. Overview

The embedded thin film model described in Chapter 3 is a universal model and can be used to model thin films composed of either lossless or lossy materials. Depending on the thin film parameters, thin films can be transparent to electromagnetic (EM) waves at the desired frequency range, while others may present highly reflective properties. In this chapter, the frequency responses of both lossless and lossy thin films are explored using the proposed embedded model. According to the results, the accuracy, stability, convergence and efficiency of the embedded model are also examined.

The accuracy of the embedded thin film model is compared against the results obtained from the analytical methods for calculating the thin film's reflection and transmission coefficients. The analytical methods are overviewed in section 4.2.

In section 4.3, the frequency responses of lossy thin films are investigated using the embedded model. As examples of lossy thin films, the reflection and transmission properties of several different carbon fibre composite (CFC) panels and titanium panels are studied. The results calculated using the conventional TLM approach are shown for comparison. In addition, anisotropic CFC panels are also investigated.

In section 4.4, the frequency responses of lossless thin films are investigated using the embedded model developed. Examples of lossless thin films, including antireflection (AR) coatings and fibre Bragg gratings (FBG), are explored. The reflection coefficients of AR coatings are first calculated using the embedded model. To improve the efficiency, a modified thin film model is also presented to model single-layer AR coatings. Also, the transmission

properties of FBG are demonstrated using the embedded model and compared against the conventional TLM approach.

4.2. Analytical Methods for Analysing Thin Films

This section overviews two analytical approaches for analysing thin films mainly: the transfer matrix method [4.1] and the even/odd mode method [4.2].

4.2.1. Transfer Matrix Method

The general case of a multi-layer thin film with arbitrary thicknesses is shown in Fig.4-1. Each layer is characterised with characteristic impedance Z_i, thickness d_i and wavenumber k_i.

The incident and reflected fields are considered at the left of each interface. The overall reflection response, $R_1 = E_{1-}/E_{1+}$, can be obtained recursively by the propagation of the reflection responses.

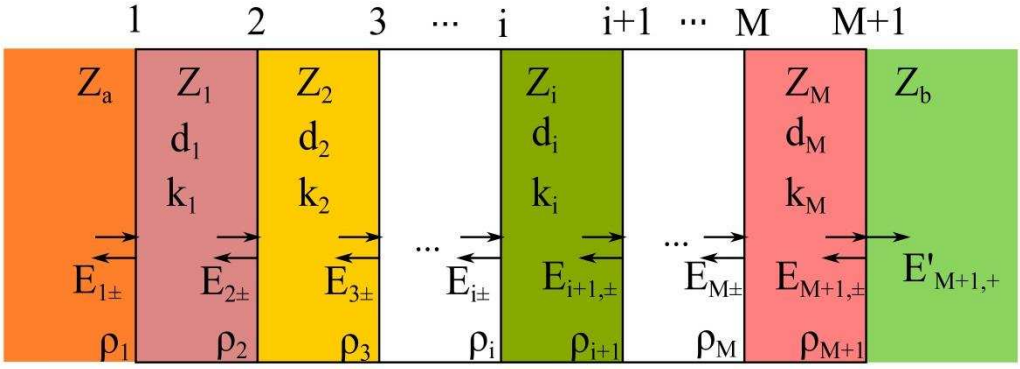

Fig.4-1 Multilayer thin film structure.

The reflection coefficients ρ_i from the left of each interface are defined in terms of characteristic impedance as follows [4.1]:

$$\rho_i = \frac{Z_i - Z_{i-1}}{Z_i + Z_{i-1}}, i = 1,2, \dots \dots, M+1. \tag{4-1}$$

The conventions $Z_0 = Z_a$ and $Z_{M+1} = Z_b$ are used, so that

$$\rho_1 = \frac{Z_1 - Z_a}{Z_1 + Z_a}, \rho_{M+1} = \frac{Z_b - Z_M}{Z_b + Z_M}. \tag{4-2}$$

The forward/backward fields at the left of interface i are related to those at the left of interface i+1 by [4.1]:

$$\begin{bmatrix} E_{i+} \\ E_{i-} \end{bmatrix} = \frac{1}{\tau_i} \begin{bmatrix} e^{jk_i d_i} & \rho_i e^{-jk_i d_i} \\ \rho_i e^{jk_i d_i} & e^{-jk_i d_i} \end{bmatrix} \begin{bmatrix} E_{i+1,+} \\ E_{i+1,-} \end{bmatrix}, i = M, M-1, \dots \dots, 1. \tag{4-3}$$

In equation (4-3), at the interface $\tau_i = 1 + \rho_i$ and $k_i d_i$ is the electrical length of the ith layer, where $k_i = 2\pi n_i / \lambda_0$, and λ_0 is the operating wavelength.

Then, the reflection coefficients at interface i are expressed as,

$$R_i = \frac{E_{i-}}{E_{i+}} = \frac{\rho_i + R_{i+1} e^{-2jk_i d_i}}{1 + \rho_i R_{i+1} e^{-2jk_i d_i}}, i = M, M-1, \dots \dots, 1 \tag{4-4}$$

and initialized by R_M.

Assuming no waves coming from the right-most medium, the recursions are initialized at the (M+1)th interface as follows:

$$\begin{bmatrix} E_{M+1,+} \\ E_{M+1,-} \end{bmatrix} = \frac{1}{\tau_{M+1}} \begin{bmatrix} 1 & \rho_{M+1} \\ \rho_{M+1} & 1 \end{bmatrix} \begin{bmatrix} E'_{M+1,+} \\ 0 \end{bmatrix} = \frac{1}{\tau_{M+1}} \begin{bmatrix} 1 \\ \rho_{M+1} \end{bmatrix} E'_{M+1,+}. \tag{4-5}$$

Thus, $R_M = \rho_{M+1}$.

Therefore, the reflection responses of the multilayer thin film satisfy the recursions:

$$R_i = \frac{E_{i-}}{E_{i+}} = \frac{\rho_i + R_{i+1} e^{-2jk_i d_i}}{1 + \rho_i R_{i+1} e^{-2jk_i d_i}}, i = M, M-1, \dots \dots, 1 \tag{4-6}$$

and initialized by $R_M = \rho_{M+1}$.

4.2.2. Even/Odd Mode Method

The even/odd mode approach is only applicable to symmetric networks for S parameter analysis [4.2].

Considering a two port network shown in Fig. 4-2, where both sides are excited using voltages V_1^+, V_2^+, respectively.

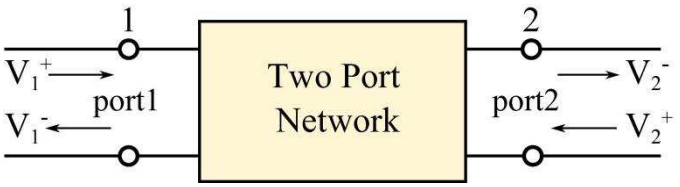

Fig. 4-2 Two port network.

This two port network has the following relations [4.3]:

$$\begin{bmatrix} V_1^- \\ V_2^- \end{bmatrix} = \begin{bmatrix} S_{11} & S_{12} \\ S_{21} & S_{22} \end{bmatrix} \begin{bmatrix} V_1^+ \\ V_2^+ \end{bmatrix}. \tag{4-7}$$

The coefficients, S_{11}, S_{12}, S_{21}, and S_{22}, are known as the scattering coefficients or scattering parameters.

If the network is symmetric, the analysis can be simplified by analysing only half of the network and placing even and odd boundary conditions on the symmetric plane.

For a symmetric network, $S_{11} = S_{22}$, and $S_{12} = S_{21}$.

In the even mode, the following equations are satisfied,

$$V_1^+ = V_2^+ = a, V_1^- = V_2^- = b. \tag{4-8}$$

Replacing the voltages in equation (4-7) with equation (4-8), it is found that,

$$b = (S_{11} + S_{12})a. \tag{4-9}$$

Therefore, the reflection coefficients Γ_e for the even mode can be expressed as:

$$\Gamma_e = \frac{b}{a} = S_{11} + S_{12}. \tag{4-10}$$

In the odd mode, the following relations are satisfied,

$$V_1^+ = -V_2^+ = a, V_1^- = -V_2^- = b. \tag{4-11}$$

Then replacing the voltages in equation (4-7) with equation (4-11), it is found that,

$$b = (S_{11} - S_{12})a. \tag{4-12}$$

Therefore, the reflection coefficients Γ_o for the odd mode may be expressed as:

$$\Gamma_o = \frac{b}{a} = S_{11} - S_{12}. \tag{4-13}$$

Based on equations (4-10) and (4-13), the S parameters can be expressed as,

$$\begin{aligned} S_{11} = S_{22} &= (\Gamma_e + \Gamma_o)/2, \\ S_{12} = S_{21} &= (\Gamma_e - \Gamma_o)/2. \end{aligned} \tag{4-14}$$

For example, consider that the electric field is incident upon a uniform thin film from free space and then transmitted into free space. Its transmission line model is shown in Fig. 4-3.

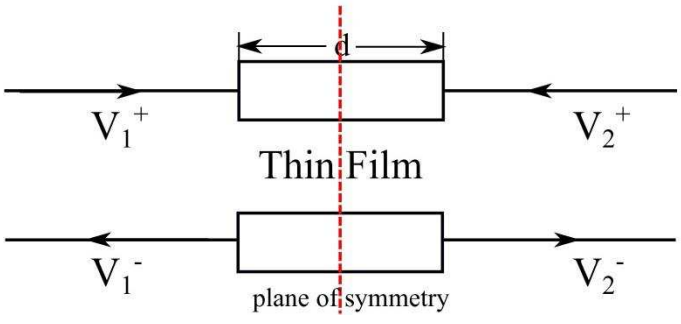

Fig. 4-3 The transmission line model of a thin film.

Assume that the thin film has a thickness d and its characteristic impedance $Z_c = \sqrt{L/C}$.

Since free space is on both sides of the thin layer, the whole structure can be seen as a symmetric two port network, whose plane of symmetry lies in the middle of the thin layer.

The even mode is equivalent to having a magnetic wall, i.e. open circuit, in the symmetry plane, shown in Fig. 4-4.

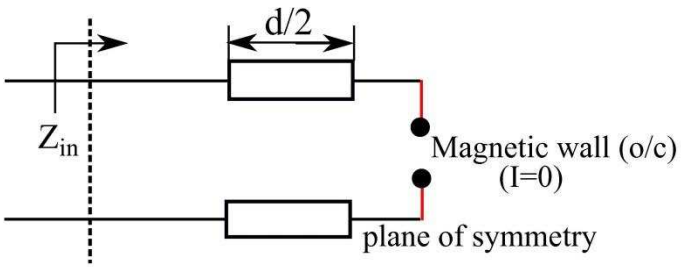

Fig. 4-4 The even mode network of the thin film.

From Fig. 4-4, its input impedance is

$$Z_{ine} = Z_C \frac{Z_L + jZ_C tan(\frac{kd}{2})}{Z_C + jZ_L tan(\frac{kd}{2})} = \frac{Z_C}{jtan(\frac{kd}{2})}, \tag{4-15}$$

where Z_L is the load impedance (in this case equal to infinity) and k is the wavenumber.

Its reflection coefficient for the even mode is given by,

$$\Gamma_e = \frac{Z_{ine} - Z_0}{Z_{ine} + Z_0}, \tag{4-16}$$

where load impedance $Z_L = \infty$ and Z_0 is the characteristic impedance of free space.

For the odd mode, it is like an electric wall in the symmetry plane, as shown in Fig. 4-5.

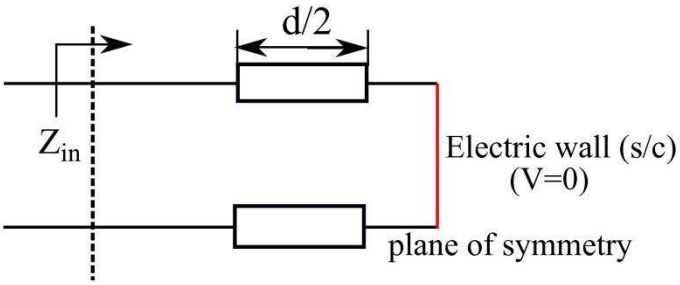

Fig. 4-5 The odd mode network of the thin film.

From Fig. 4-5, load impedance $Z_L = 0$ and the input impedance Z_{ino} is

$$Z_{ino} = Z_C \frac{Z_L + jZ_C tan(\frac{kd}{2})}{Z_C + jZ_L tan(\frac{kd}{2})} = jZ_C tan\left(\frac{kd}{2}\right). \tag{4-17}$$

The reflection coefficient for the odd mode is given by

$$\Gamma_o = \frac{Z_{ino} - Z_0}{Z_{ino} + Z_0}. \tag{4-18}$$

Therefore, the reflection and transmission coefficients of the thin film are calculated from equations (4-16) and (4-18) as

$$\begin{aligned} R = S_{11} = S_{22} &= \frac{\Gamma_e + \Gamma_o}{2}, \\ T = S_{21} = S_{12} &= \frac{\Gamma_e - \Gamma_o}{2}. \end{aligned} \tag{4-19}$$

4.3. Applications of Embedded Model to Lossy Films

In this section lossy non-magnetic materials are considered. For lossy non-magnetic materials, the permeability is a real number, but the permittivity is a frequency dependent complex number [4.1]. The equivalent inductance and capacitance, L and C, can be expressed by

$$L = \mu = \mu_0 \mu_r,$$
$$C = \varepsilon + \frac{\sigma_e}{j\omega} = \varepsilon_0 \varepsilon_r + \frac{\sigma_e}{j\omega}, \tag{4-20}$$

where $\mu_0 = 1.26 \times 10^{-6}$ Hm^{-1} is the permeability of free space, $\varepsilon_0 = 8.85 \times 10^{-12}$ Fm^{-1} is the permittivity of free space, μ_r and ε_r are the relative permeability and permittivity of the material, σ_e is the conductivity of the material, and ω is the angular frequency.

In this section, carbon fibre composite (CFC) panels and titanium panels are used as examples of lossy materials and investigated to test the embedded time domain thin film model in 1D TLM method.

Results obtained using the numerical method (R_N) will be compared against with those of the analytical method (R_A). For that purpose, the following percentage error is used,

$$percentage\ error = \frac{|R_N - R_A|}{|R_A|} \cdot 100\%. \tag{4-21}$$

It is noted that in the following examples, when the percentage errors are within 2%, it is assumed that the required accuracy of the numerical results is achieved, although in reality bigger percentage errors may be allowed.

4.3.1. Carbon Fibre Composite (CFC) Panels

Carbon fibre composite (CFC) materials have received considerable attention [4.4 ~ 4.7] due to their high strength-to-weight ratio and ease of fabrication. As replacement of metals, they have been used in many areas, such as spacecraft and aircraft structures [4.4], avionics systems [4.8], and Radio-Frequency Identification (RFID) [4.9]. However, due to their lower conductivity, CFC materials have lower shielding effectiveness compared to that of metals. In order to analyse and improve their shielding effectiveness, a variety of CFC materials have been studied using either numerical or analytical methods [4.4 ~ 4.7].

In this section, the CFC panels are considered as a one dimensional (1D) problem and analysed using the embedded model in the 1D TLM method. The reflection and transmission coefficients of single and multiple layer CFC panels are calculated to test the accuracy, stability, convergence and efficiency of the embedded model. For comparison purposes, the conventional TLM method is also used to model these panels. The embedded model is then applied to analyse the shielding effectiveness of CFC panels. Anisotropic CFC panels are also investigated.

Carbon fibre composite materials are inhomogeneous materials which consist of continuous carbon fibres embedded in an epoxy matrix [4.10]. In this section the CFC panels are modelled as a homogeneous medium using the equivalent-layer model [4.5]. As this equivalent-layer model is valid up to several GHz [4.5], the highest frequency discussed in this section was chosen to be 1GHz.

4.3.1.1. Single Layer CFC Panels

Fig.4-6 shows the normally incident electric fields E^i, reflected fields E^r and transmitted fields E^t from a CFC panel. The CFC panel is assumed to be surrounded by free space.

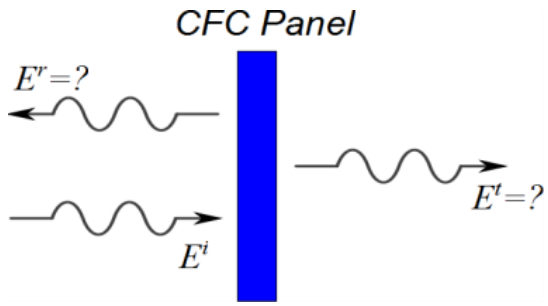

Fig.4-6 Incident electric fields E^i, reflected fields E^r and transmitted fields E^t from a CFC panel.

The reflection and transmission coefficients are defined as

$$R = \frac{E^r}{E^i}, T = \frac{E^t}{E^i}. \tag{4-22}$$

The shielding effectiveness (SE) is defined as the ratio of the amplitude of the incident field to that of the transmitted field. It is typically described in decibels (dB) as follows,

$$SE = 20 \cdot log_{10}\left(\frac{E^i}{E^t}\right) (dB). \tag{4-23}$$

The parameters of the CFC panel used in this section were chosen as: thickness of 1 mm, effective permittivity $\varepsilon_r = 2$ and conductivity $\sigma_e = 10^4$ Sm^{-1} as in [4.4].

In the 1D TLM model, the length of free space on each side of the panel was chosen to be 0.1 m, and matched boundaries [4.11] were set at the ends of free space regions to simulate the infinite free space. Free space on each side of the panel was discretised using 1D TLM nodes. The CFC panel was modelled using the time domain thin film model proposed in Chapter 3 and embedded between two adjacent 1D TLM nodes. A delta pulse was used to excite the TLM nodes. The reflected and transmitted fields were calculated in the time domain first and then a Fast Fourier Transform (FFT) was used to transfer them to the frequency domain to obtain the reflection and transmission coefficients.

The TLM mesh size is typically set as less than one tenth of the smallest wavelength [4.11]. In order to obtain the discretisation errors, the reflection and transmission coefficients of the CFC panel were calculated at 1 GHz using the embedded model for N = 100 with different mesh size, dz. The results obtained were compared to the analytical results calculated using the even/odd mode method described in section 4.2. The percentage errors (calculated using equation (4-21)) in the reflection and transmission coefficients at 1 GHz are shown in Fig.4-7 against the mesh size, represented by λ/dz. Fig.4-7 shows that as the mesh size decreases, the percentage errors in both reflection and transmission coefficients decrease. Although the CFC panel is not discretised, the discretisation errors come from the modelling of the fields outside the panel using the TLM method. In the following calculations, the mesh size was chosen to be 0.01 m ($\lambda/dz = 30$), in order to minimize discretisation errors.

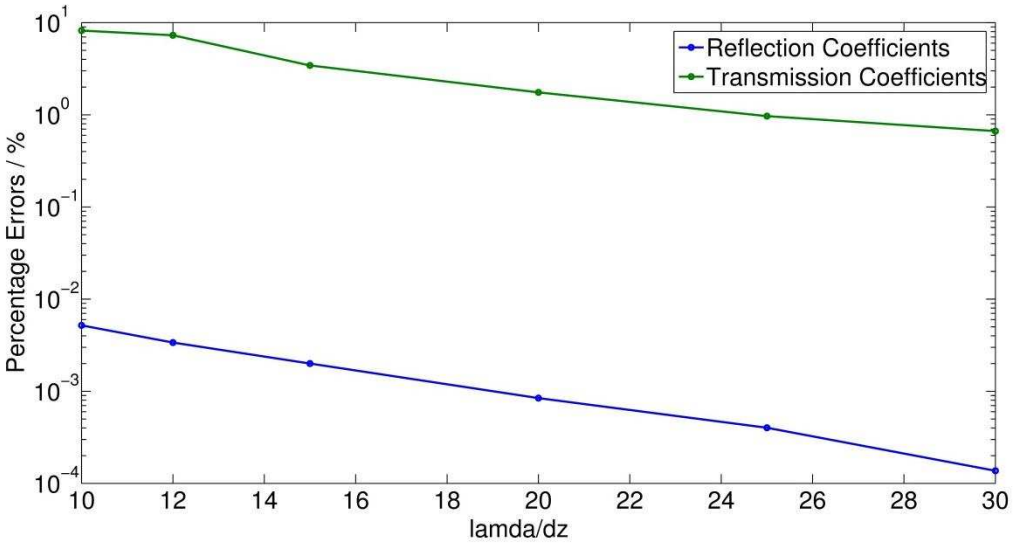

Fig.4-7 Percentage errors in the reflection and transmission coefficients of the CFC panel at 1 GHz calculated using the embedded model for N =100, with different mesh size, dz.

Using a mesh size of 0.01 m, the stability of the embedded model is discussed. A number of digital filters were used in the time domain model for the CFC panel, as described in section 3.2. From Fig. 3-5, the transfer functions of these digital filters are derived from the expansions of cotangent and cosecant functions. Since the stability of digital filters is dependent on the poles of their transfer functions [4.12], the poles of the expansions of cotangent and cosecant functions are investigated.

In equation (3-29), there are (N+1) transfer functions for each expansion. The poles of these transfer functions are the values of z at which their denominator equals to zero. They are the roots of the following denominator polynomials,

$$\begin{aligned} A_2 + B_2 z^{-1} &= 0, \\ A_k + B_k z^{-1} + C_k z^{-2} &= 0. \end{aligned} \tag{4-24}$$

For the CFC panel, the above coefficients of equations (3-29) are calculated as follows,

$A_2 = 2\mu + \sigma_m \Delta t = 2.51 \times 10^{-6}$ (Hm^{-1}),

$B_2 = \sigma_m \Delta t - 2\mu = -2.51 \times 10^{-6}$ (Hm^{-1}),

$$A_k = 4\mu\varepsilon + 2\Delta t(\mu\sigma_e + \varepsilon\sigma_m) + (\sigma_m\sigma_e + k^2\pi^2/d^2)\Delta t^2$$
$$= 8.38 \times 10^{-13} + 1.10 \times 10^{-14} \cdot k^2 \ (\mathrm{S^2m^{-2}}), \qquad k = 1,2,\cdots,N$$

$$B_k = -8\mu\varepsilon + 2\left(\sigma_m\sigma_e + \frac{k^2\pi^2}{d^2}\right)\Delta t^2$$
$$= -1.78 \times 10^{-16} + 1.10 \times 10^{-14} \cdot k^2 \ (\mathrm{S^2m^{-2}}), \qquad k = 1,2,\cdots,N$$

$$C_k = 4\mu\varepsilon - 2\Delta t(\mu\sigma_e + \varepsilon\sigma_m) + \left(\sigma_m\sigma_e + \frac{k^2\pi^2}{d^2}\right)\Delta t^2$$
$$= -8.38 \times 10^{-13} + 1.10 \times 10^{-14} \cdot k^2 \ (\mathrm{S^2m^{-2}}). \qquad k = 1,2,\cdots,N$$

According to these values, the values for z in equation (4-24) can be obtained, which are the poles of the transfer functions in the expansions. All these poles are within the unit circle indicating that the time domain CFC model is stable. To date, it has been found that only when the materials are with gain, the embedded model becomes unstable.

Since the expansions used in equations (3-11) and (3-12) include infinite terms, they must be truncated for computational purposes. In order to investigate the errors from truncating the expansions, the percentage errors (calculated using equation (4-21)) in the reflection and transmission coefficients of the CFC panel at 1 GHz were calculated using the embedded model for different number of terms, N, shown in Fig.4-8. It can be seen that the percentage errors in the transmission coefficients decrease as the number of expansion terms increases. Fig.4-8 also shows the percentage errors in the reflection coefficients decrease until N = 20 and then converge to some point as the number of terms, N, increases.

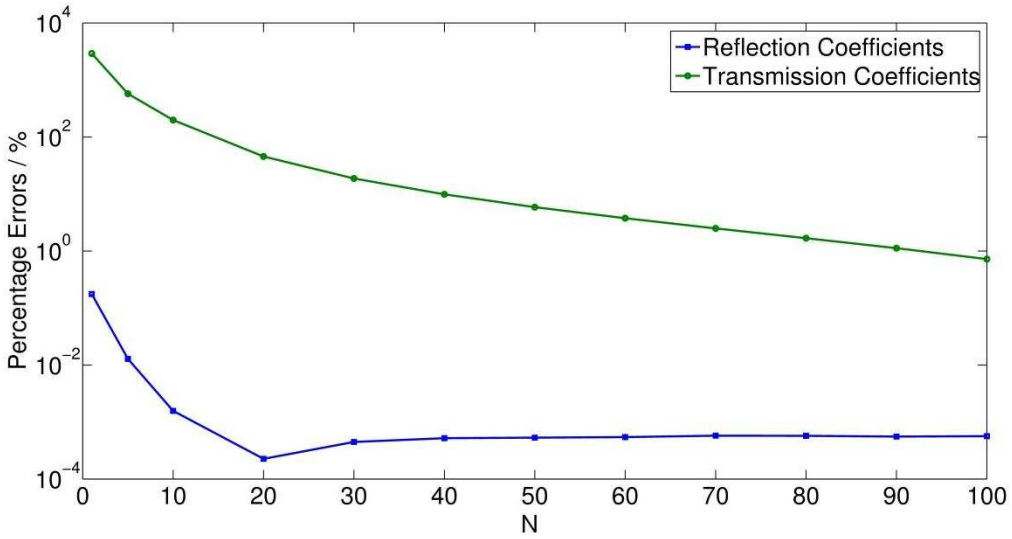

Fig.4-8 Percentage errors in the reflection and transmission coefficients of the CFC panel at 1 GHz calculated using the embedded model for dz = 0.01 m, with different number of expansion terms, N.

After investigating the errors from discretisation and truncation in the expansion terms, the reflection and transmission coefficients of the CFC panel were calculated in the frequency range from 0 to 1 GHz using the embedded model with a mesh size of 0.01 m. Fig.4-9 shows the reflection and transmission coefficients of the single layer CFC panel in the frequency range from 0 to 1 GHz for different number of expansion terms, N, and compares them with the analytical ones obtained using the even/odd mode method described in section 4.2. It can be seen that the agreement between numerical and analytical results for the reflection coefficients is excellent regardless of the number of expansion terms. The calculated transmission coefficients decrease with the number of expansion terms especially in the high frequency region. When N = 100, the numerical results of both reflection and transmission coefficients are virtually indistinguishable from the analytical ones over a wide frequency span.

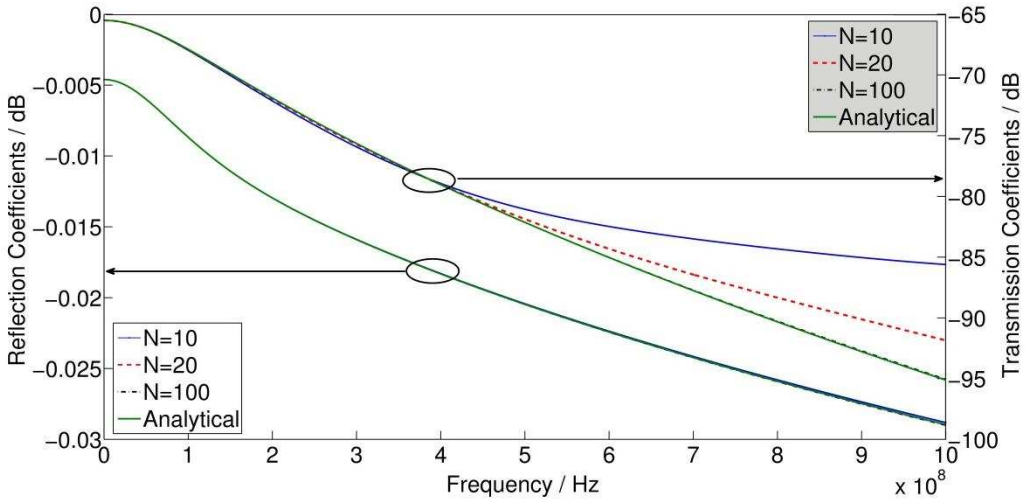

Fig.4-9 Reflection and transmission coefficients of a single layer CFC panel with 1 mm thickness and $\varepsilon_r = 2, \sigma_e = 10^4$ Sm^{-1}, calculated using the embedded model for different number of expansion terms N (N = 10, 20 and 100) and analytical method.

Fig.4-10 (a, b) shows the percentage errors (defined in equation (4-21)) in the reflection and transmission coefficients calculated using the embedded model compared to the analytical ones. From Fig.4-10 (a, b), it can be seen that the errors in both reflection and transmission coefficients become very small with the increase of the expansion order, N. When N = 100, the reflection coefficients errors are less than 0.0006% and the transmission coefficients errors are less than 0.8% in the frequency range from 0 to 1 GHz.

In reality, the high accuracy (0.0006% error in the reflection coefficients) may not be needed. Here in order to make sure the percentage errors in the transmission coefficients are less than 2%, the percentage errors in the reflection coefficients are very small. In the following examples, similar high accuracy in the reflection coefficients exists, due to the same reason.

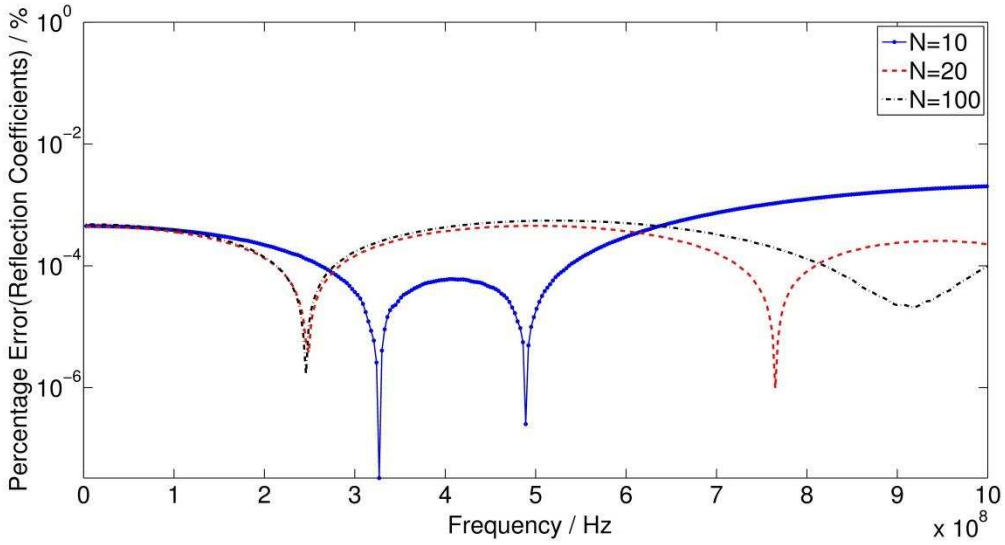

(a)

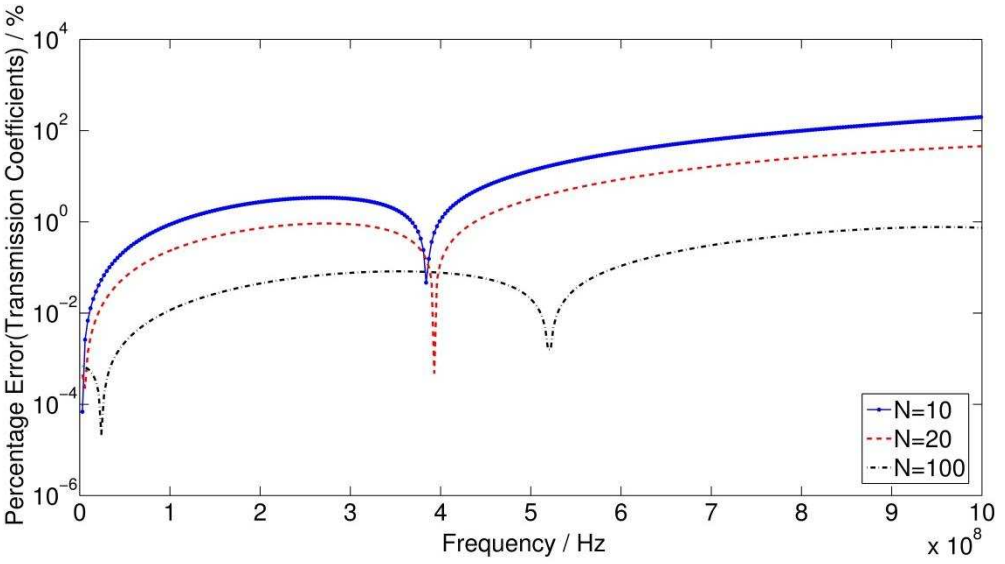

(b)

Fig.4-10 Percentage errors in the (a) reflection coefficients and (b) transmission coefficients calculated using the embedded model with different number of terms, N (N = 10, 20, and 100).

In the conventional TLM method, both free space and the CFC panel need to be discretised. Since the thickness of this CFC panel is 1 mm, the mesh size dz must be smaller than 1 mm in order to have at least one node for the panel in the mesh. For a conductive panel, the mesh size inside it is generally chosen as less than its skin depth δ [4.13] in order to analyse the field penetrating the panel accurately,

$$dx \ll \delta = 1/\sqrt{\pi f_{max} \mu \sigma} \tag{4-25}$$

where f_{max} is the maximum frequency of interest. For this CFC panel, since the maximum frequency of interest is 1 GHz, the skin depth of the panel is 0.16 mm. Therefore, the mesh sizes for the conventional TLM method should be chosen as less than 0.16 mm.

In order to investigate the discretisation errors of the conventional TLM method, the reflection and transmission coefficients of the CFC panel were calculated at 1 GHz using the conventional TLM method for different mesh size, dz. Results obtained were compared with the analytical results. The percentage errors in the reflection and transmission coefficients at 1 GHz are shown in Fig.4-11 against the mesh size, represented by d/dz, where d is the thickness of the panel. It can be seen that when the panel is discretised using 40 nodes ($dz = 0.025\,mm$), the percentage errors in the transmission coefficients are around 1.02% and the percentage errors in the reflection coefficients are around 0.002%.

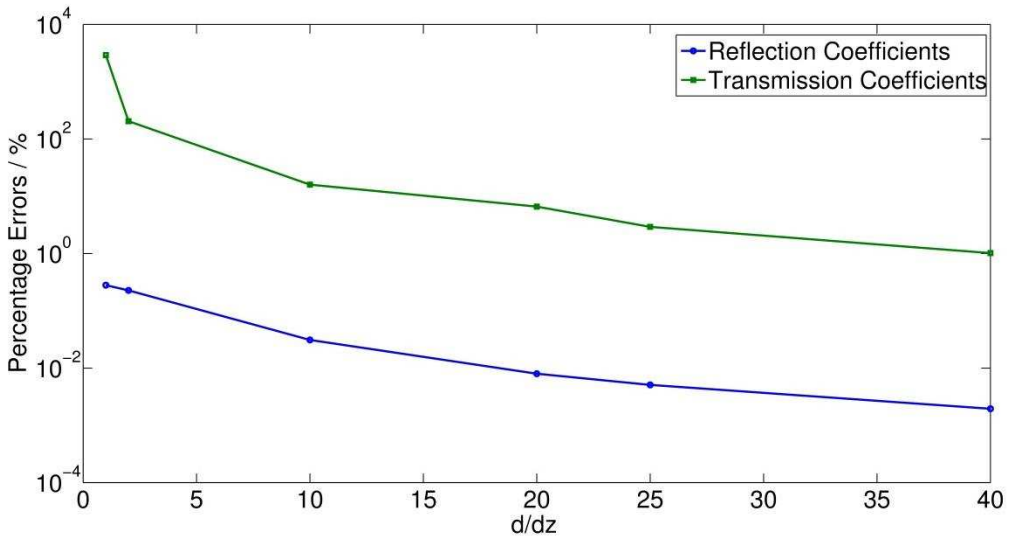

Fig.4-11 Percentage errors in the reflection and transmission coefficients of a single layer CFC panel at 1 GHz using the conventional TLM method for different mesh size, dz.

For comparison purposes, the reflection and transmission coefficients of the CFC panel in the frequency range from 0 to 1 GHz were calculated using the

conventional TLM method with the mesh size of 0.025 mm. Fig.4-12 shows the percentage errors (defined in equation (4-21)) in the reflection and transmission coefficients calculated using the conventional TLM method compared to the analytical ones. It can be seen that when the mesh size $dz = 0.025$ mm, the errors in the reflection coefficients are less than 0.001% and the errors in the transmission coefficients are less than 1% in the frequency range from 0 to 1 GHz, which is comparable to the corresponding errors calculated using the embedded model with a mesh size of 0.01 m.

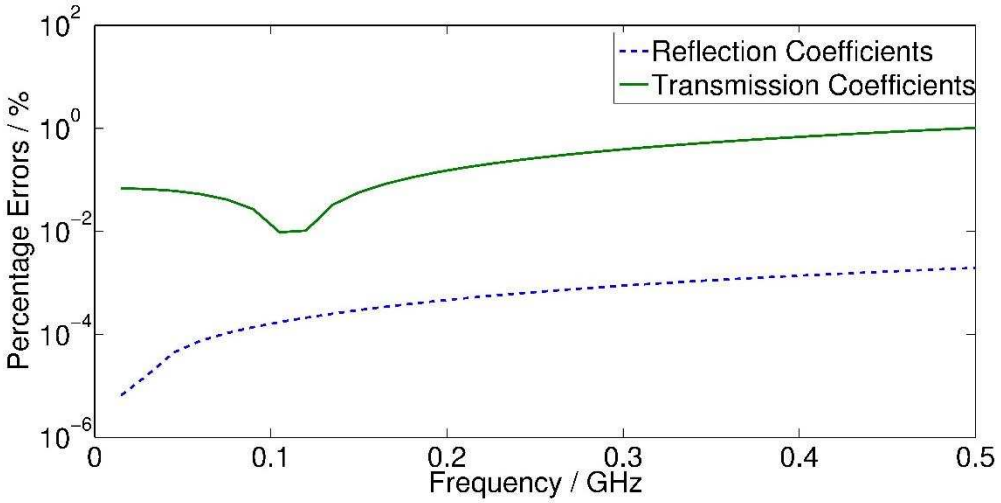

Fig.4-12 Percentage errors in the reflection coefficients and transmission coefficients calculated using the conventional TLM method with a mesh size of 0.025 mm.

Therefore, to get the results of the same accuracy as the embedded model, the conventional TLM method should use a mesh size of 0.025 mm (approximate one sixth of its skin depth at the highest frequency of interest). The free space on each side of the CFC panel is discretised into 4000 nodes. The CFC panel is discretised into 40 nodes. In total there are 8040 nodes using the conventional TLM method. Compared to the embedded model, there are only 20 nodes with a mesh size of 0.01 m since the CFC panel is not discretised. Furthermore, to get the same frequency resolution as that in the embedded model, the number of time steps needed in the conventional TLM is 4×10^5, while the number of time steps needed in the embedded model is 1000. In other words, the smaller mesh size in the conventional TLM results in 420 times bigger memory storage

for the nodes and 400 times the number of iterations compared to those in the embedded model, as shown in Table 4-1.

Table 4-1 Comparison between the conventional TLM model and the embedded model for the single layer CFC panel

Model	Mesh size (mm)	Number of nodes	Number of time steps	Run time (s) *
Conventional TLM	0.025	8040	4×10^5	82
Embedded model	10	20	1000	0.188

(* the run time is based on a PC with an Intel Core 2 Duo CPU 3GHz processor and 4GB memory)

In summary, the mesh size in the conventional TLM is dependent on the thickness of the CFC panel, while the mesh size in the embedded model is determined by the highest frequency of interest since the embedded model eliminates the need for discretisation of the panel. The condition determined by the thickness of thin films is generally much more restrictive than that determined by the highest frequency for the choice of mesh size. Thus, compared to the conventional TLM method, the embedded model can achieve the same or better accuracy using a larger mesh size. Therefore, the embedded model has the advantages of saving memory storage and reducing computational requirements for simulation.

As an application of the verified embedded model, four kinds of single layer CFC panels with different conductivities and thicknesses were studied to analyse their shielding effectiveness.

The parameters of these four CFC panels are as follows,

Panel 1: $\varepsilon_r = 2, \sigma_e = 10^4\ \mathrm{Sm}^{-1}, d = 1\ \mathrm{mm}$,

Panel 2: $\varepsilon_r = 2, \sigma_e = 10^4\ \mathrm{Sm}^{-1}, d = 1.2\ \mathrm{mm}$,

Panel 3: $\varepsilon_r = 2, \sigma_e = 8000\ \mathrm{Sm}^{-1}, d = 1\ \mathrm{mm}$,

Panel 4: $\varepsilon_r = 2, \sigma_e = 8000\ \mathrm{Sm}^{-1}, d = 1.2\ \mathrm{mm}$.

Panel 1 has the same parameters as the previous example. To analyse the effects of the conductivity and thickness on the shielding effectiveness, these four panels have the same permittivity but different conductivities and thicknesses. Panel 2 has the same conductivity as panel 1, but it is thicker than panel1. Panel 3 has the same thickness as panel 1, but its conductivity is lower. Panel 4 has the same conductivity as panel 3, but it is thicker than panel 3.

Fig.4-13 shows the shielding effectiveness of these four single layer CFC panels. It can be seen that they all show good shielding properties, especially in the high frequency range. Panel 2 shows better shielding effectiveness than panel 1 because of its greater thickness. It also presents better shielding effectiveness than panel 4 due to its higher conductivity. Overall panel 2 with its greater thickness and higher conductivity provides best shielding effectiveness. These results show that thicker panels with higher conductivity provide better shielding effectiveness.

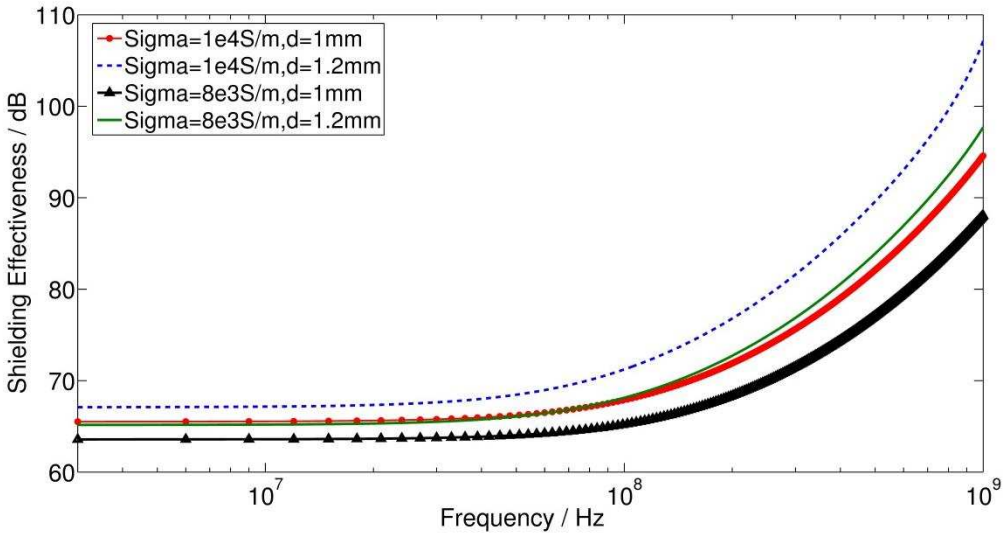

Fig.4-13 The shielding effectiveness of four different single layer CFC panels calculated using the embedded model.

4.3.1.2. Anisotropic Panel

For the anisotropic CFC panel, the electrical properties are considered for electric field components in the x and y directions. In the x direction they are given by $\varepsilon_{rx} = 2$ and $\sigma_{ex} = 10^4$ Sm^{-1} from [4.4], and it is assumed that in the y direction they are given by $\varepsilon_{ry} = 3$ and $\sigma_{ey} = 10^3$ Sm^{-1}. The thickness of the panel is 1 mm.

As shown in Fig. 3-9, the electric field $\vec{E}^i$ is normally incident to the panel along the z axis. It can be decomposed into E_x and E_y components as

$$\vec{E}^i = E_x\hat{\boldsymbol{x}} + E_y\hat{\boldsymbol{y}} = \left|E^i\right|cos\varphi \cdot \hat{\boldsymbol{x}} + \left|E^i\right|sin\varphi \cdot \hat{\boldsymbol{y}},$$

where φ is the angle between the electric field and the x axis, and $\hat{\boldsymbol{x}}$ and $\hat{\boldsymbol{y}}$ are the unit vectors in the x and y direction, respectively.

As demonstrated in section 3.4, the anisotropic thin film has different independent responses for the two x and y directions components. Two models were built for the x and y directions using the embedded single layer thin film model. For each one, the reflected and transmitted electric fields were obtained through the model. Then combining these two components as in the equation (3-47), the overall reflected and transmitted electric fields were acquired.

The mesh size was chosen to be 0.01 m as in section 4.3.1.1.

Fig.4-14 shows the (a) reflection and (b) transmission coefficients of this anisotropic CFC panel as a function of the angle between the electric field and the x axis at 1 GHz. The order of the expansions, N, is 100, which was found to be sufficient to produce results virtually indistinguishable with the analytical ones on the figure.

It should be noted that when the electric field $\vec{E}^i$ is parallel to the x axis, i.e. the angle $\varphi = 0°$ or $\varphi = 180°$, it only has effects on the thin film along the x axis. Thus the thin film presents itself as an isotropic film with the parameters of $\varepsilon_{rx} = 2$ and $\sigma_{ex} = 10^4$ Sm^{-1}. Its reflection and transmission coefficients should be the same as those shown in Fig.4-9 when N = 100 at 1 GHz.

Similarly, when the angle φ equals 90°, the electric field $\vec{E}^i$ is parallel to the y axis so that only the thin film along the y axis has response to the field. Its reflection and transmission coefficients come from the thin film with the parameters of $\varepsilon_{ry} = 3$ and $\sigma_{ey} = 10^3$ Sm^{-1}. When the angle φ is between 0° and 90° or between 90° and 180°, the thin film along both x and y directions has responses to the electric field. That is why the shapes of its reflection and transmission coefficients against the angle are the ones shown in Fig.4-14.

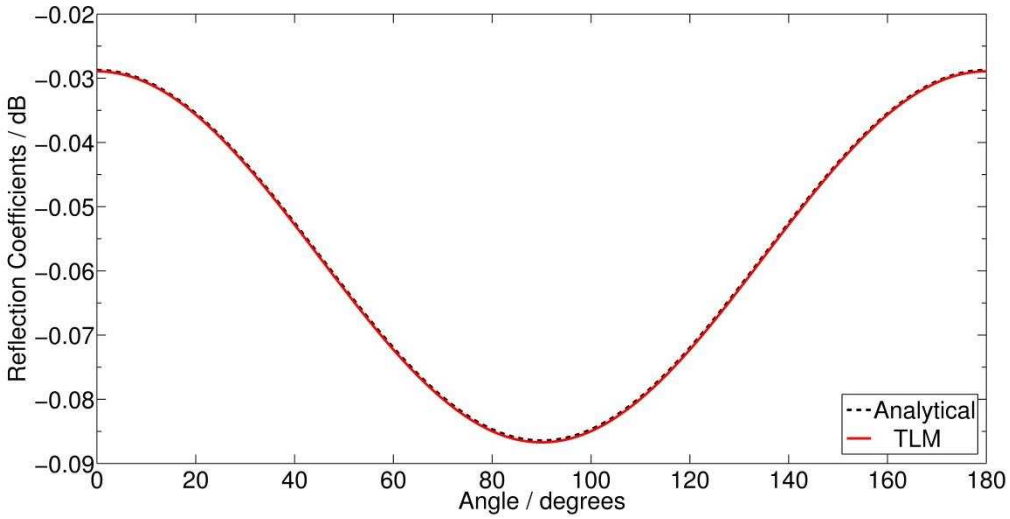

(a)

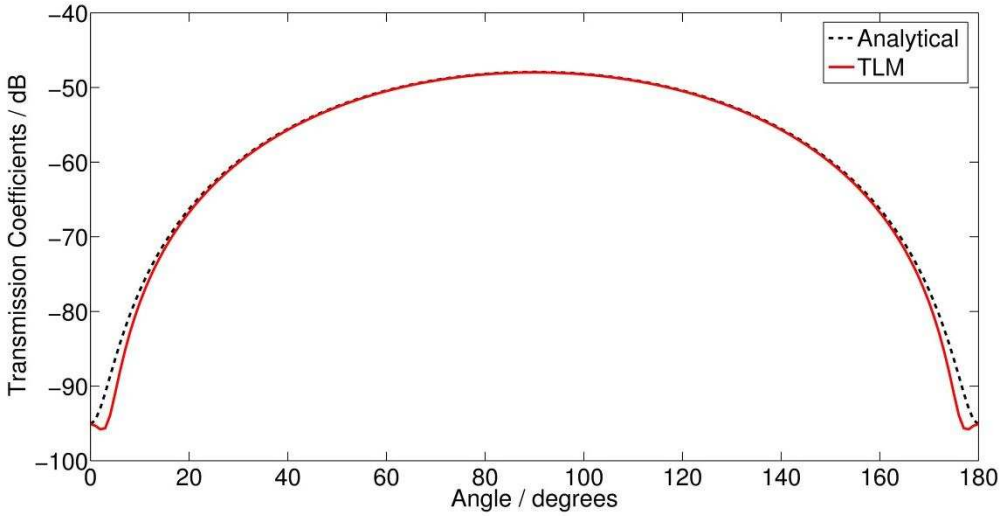

(b)

Fig.4-14 (a) Reflection coefficients and (b) transmission coefficients of an anisotropic CFC panel against the angle between the incident field with x axis at 1 GHz.

4.3.1.3. Multi-Layer CFC Panels

The first example to test the accuracy of the multilayer CFC model was chosen to be a symmetric three-layer CFC panel. The material in the middle layer was chosen to have the same parameters as in the example for single layer CFC panel, with $\varepsilon_r = 2, \sigma_e = 1 \times 10^4$ Sm^{-1} [4.4] .The first and third layers of this panel were assumed to have the same electric properties as $\varepsilon_r = 4, \sigma_e = 5 \times 10^3$ Sm^{-1}. All layers have the same thickness of 0.6 mm.

As before, free space on each side of this panel was discretised using 1D TLM nodes. The three-layer CFC panel, as a whole, was modelled using the multilayer time domain model proposed in section 3.3.2 and then embedded between two adjacent 1D TLM nodes. A delta pulse was chosen to be the excitation of the simulation. The reflected and transmitted electric fields were firstly obtained in the time domain and then a FFT was used to transform them into the frequency domain in order to get the reflection and transmission coefficients.

In order to investigate the discretisation errors of the embedded model, the reflection and transmission coefficients of the three-layer CFC panel at 1 GHz were calculated using the embedded model for N = 100 with different mesh size, dz. Results obtained were compared to the analytical ones calculated using the even/odd mode method described in section 4.2.2. Fig.4-15 shows the percentage errors in the reflection and transmission coefficients at 1 GHz against the mesh size, represented by λ/dz . Fig.4-15 shows that the discretisation errors decrease as the mesh size decreases. Therefore, in the following calculations, the mesh size was chosen to be 0.01 m ($\lambda/dz = 30$), in order to minimise the discretisation errors.

The errors from the truncation of the cotangent and cosecant function expansions are also investigated. Fig.4-16 shows the percentage errors in the reflection and transmission coefficients of the three-layer CFC panel at 1 GHz calculated using the embedded model for different number of terms, N, compared with the analytical ones. It can be seen that as the number of terms

increases, the percentage errors in the transmission coefficients decrease, while the percentage errors in the reflection coefficients converge much faster.

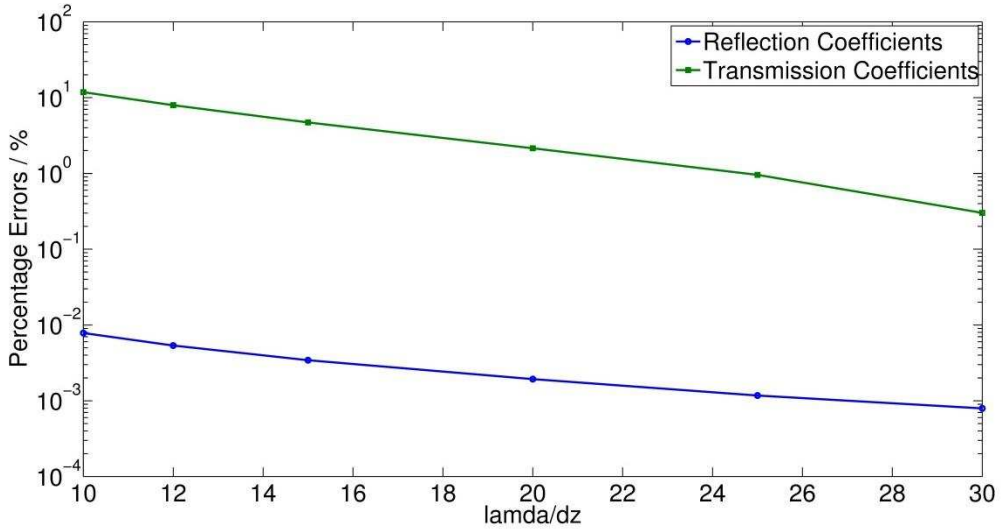

Fig.4-15 Percentage errors in the reflection and transmission coefficients of a symmetric three-layer CFC panel at 1 GHz calculated using the embedded model for N = 100, with different mesh size, dz.

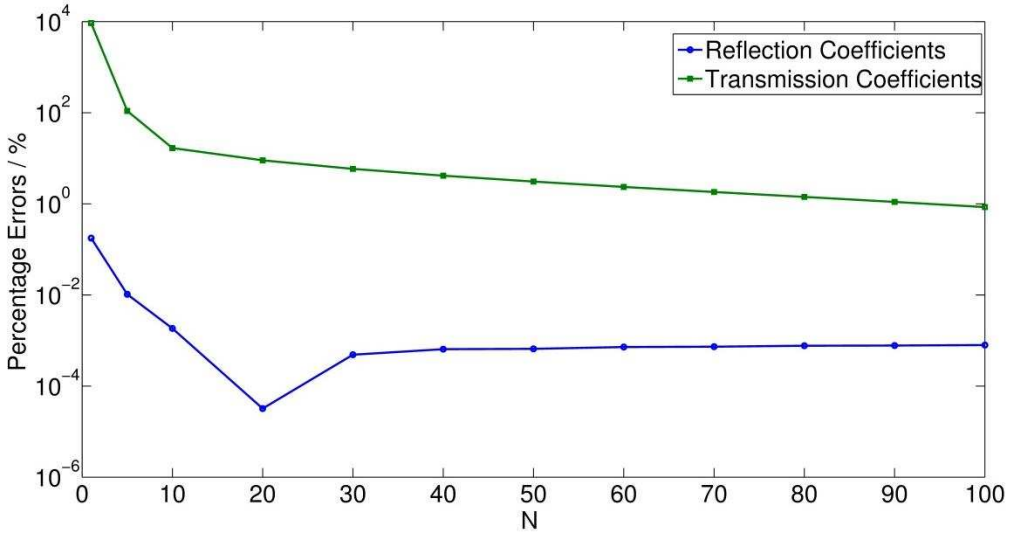

Fig.4-16 Percentage errors in the reflection and transmission coefficients of a symmetric three-layer CFC panel at 1 GHz calculated using the embedded model for dz = 0.01 m, with different number of terms, N.

After investigating the discretisation errors and truncation errors, the reflection and transmission coefficients of the three-layer CFC panel were calculated in the frequency range from 0 to 1 GHz, using the embedded model with a mesh

size of 0.01 m. Fig.4-17 shows the reflection and transmission coefficients of the three-layer CFC panel as a function of frequency. The numerical results obtained using different expansion terms N (N = 10, 20 and 100) are compared with the analytical ones obtained from the even/odd mode method mentioned in section 4.2. It can be seen that all the numerical results show good agreement with the analytical ones, with the agreement becoming closer when more terms are used to approximate the infinite series in equations (3-11) and (3-12).

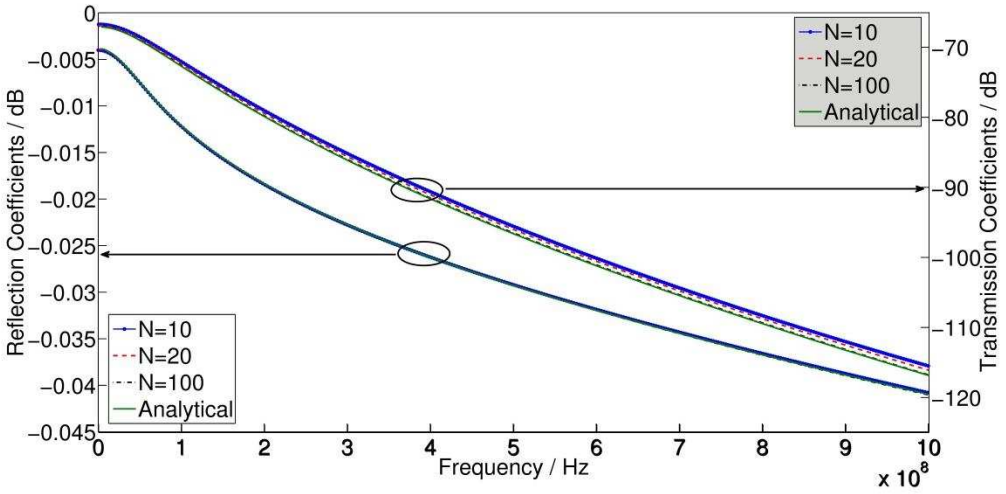

Fig.4-17 Reflection and transmission coefficients of a symmetric three-layer CFC panel calculated using the embedded model for N = 10, 20 and 100 and the analytical method.

Fig.4-18 (a, b) show the percentage errors (defined in equation (4-21)) in the reflection and transmission coefficients calculated using the embedded model compared to the analytical ones. It can be seen that the errors decrease with an increase in the number of expansion terms, N. When N = 100, the errors for the reflection coefficients are less than 0.001% and the errors for the transmission coefficients are less than 1.5%.

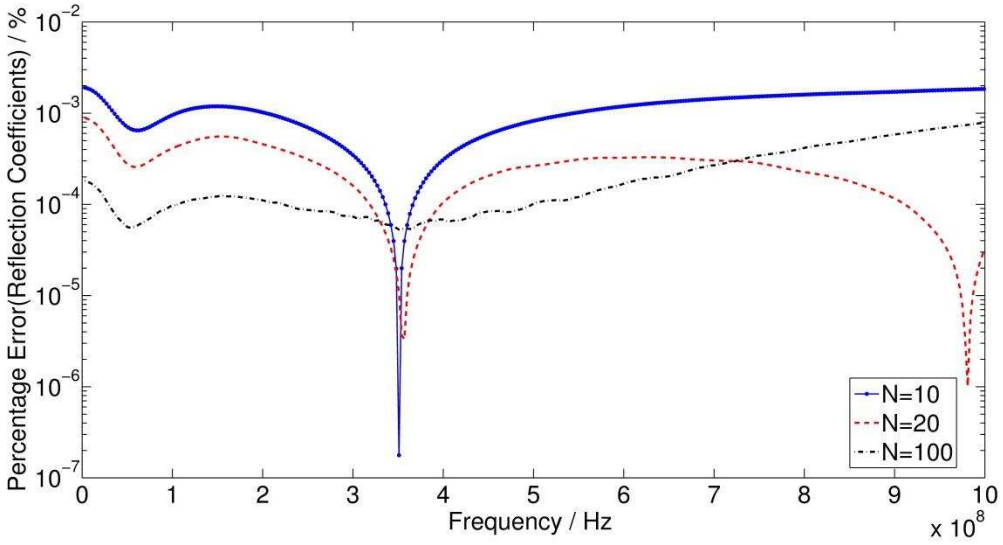

(a)

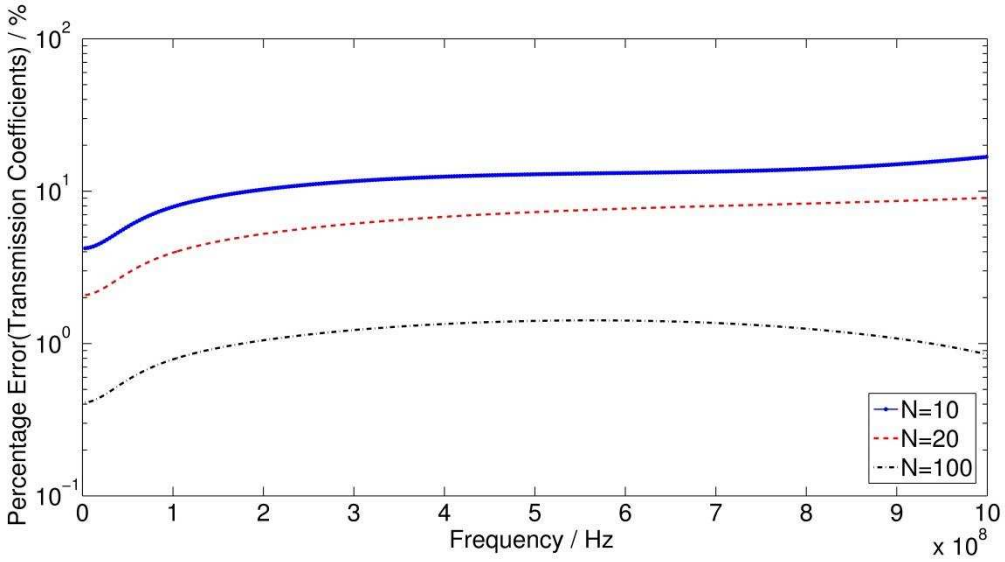

(b)

Fig.4-18 Percentage errors in the (a) reflection coefficients and (b) transmission coefficients calculated using the embedded model with different number of terms, N (N = 10, 20 and 100).

The three-layer CFC panel was also modelled using the conventional TLM method for comparison. Since the CFC panel needs to be discretised, the mesh size must be smaller than its skin depth at the highest frequency of interest. The discretisation errors of the conventional TLM method were first investigated. Fig.4-19 shows the percentage errors in the reflection and transmission coefficients of the three-layer CFC panel at 1 GHz calculated using the conventional TLM method with different mesh size, represented by

d/dz, where d is the thickness of the three-layer panel (1.8 mm), compared to the analytical ones. It can be seen that when the mesh size $dz = 0.025\,mm$ ($d/dz = 72$), the percentage errors in the reflection coefficients are around 0.002% and the percentage errors in the transmission coefficients are around 1%.

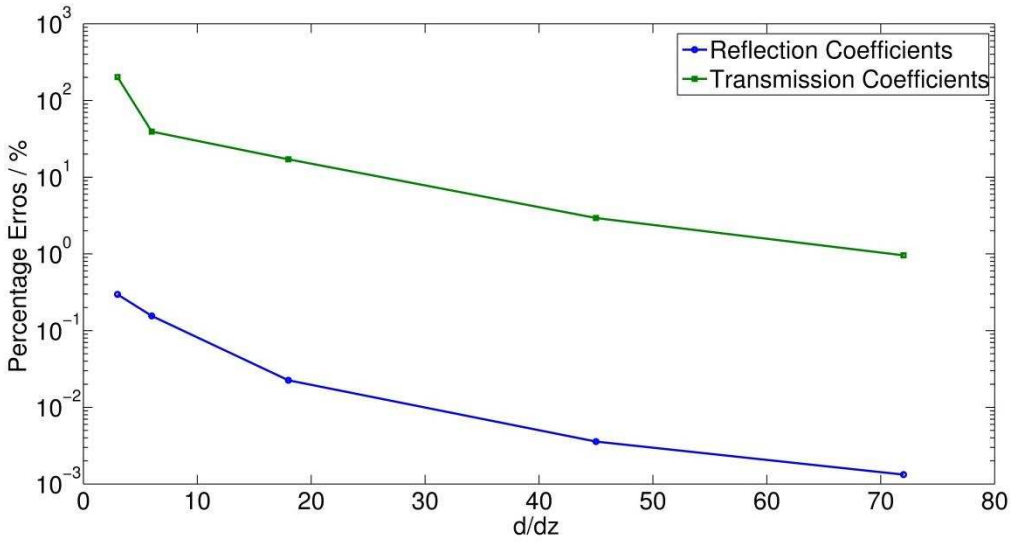

Fig.4-19 Percentage errors in the reflection and transmission coefficients of a symmetric three-layer CFC panel at 1 GHz calculated using the conventional TLM method for different mesh size, dz.

For comparison purposes, the reflection and transmission coefficients of the three-layer CFC panel in the frequency range from 0 to 1 GHz were calculated using the conventional TLM method with a mesh size of 0.025 mm. Fig.4-20 shows the percentage errors in the reflection and transmission coefficients calculated using the conventional TLM method compared to the analytical results. It can be seen that in the frequency range from 0 to 1 GHz, the errors in reflection coefficients are less than 0.002% and the errors in transmission coefficients are less than 1%, which is comparable to the corresponding errors calculated using the embedded model with a mesh size of 0.01 m.

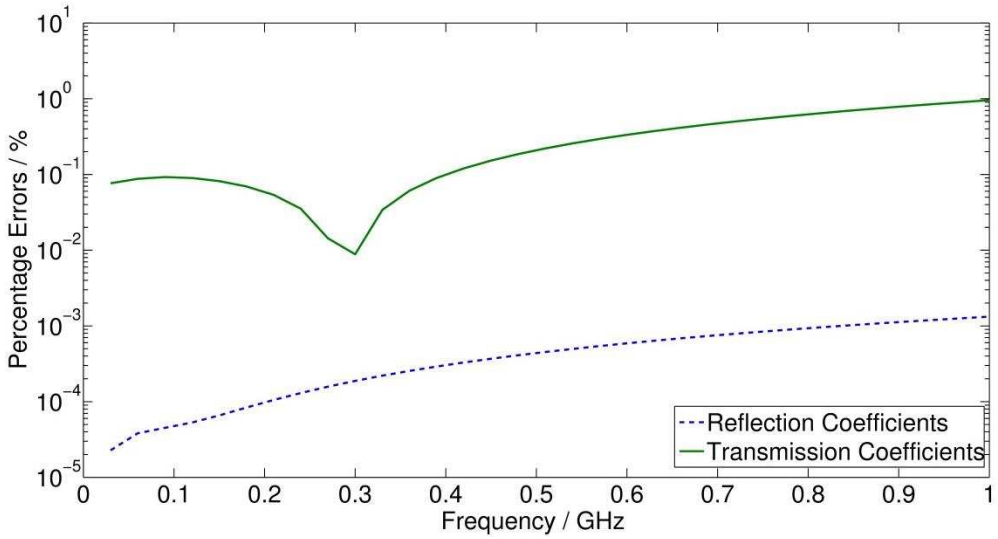

Fig.4-20 Percentage errors in the reflection coefficients and transmission coefficients calculated using the conventional TLM method with a mesh size of 0.025 mm.

With a mesh size of 0.025 mm in the conventional TLM model, there are 4000 nodes for free space (0.1 m) on each side of the three-layer CFC panel and 72 nodes for the three-layer CFC panel. In total, there are 8072 nodes in the mesh. Compared to the embedded model, there are only 20 nodes with the mesh size of 10 mm since the three-layer CFC panel is not discretised. Furthermore, the number of time steps needed in the conventional TLM model and the embedded model is 4×10^5 and 1000, respectively. Therefore, the embedded model saves 403.6 times memory storage for nodes and 400 times the number of iterations than those of the conventional TLM model, as shown in Table 4-2.

Table 4-2 Comparison between the conventional TLM model and the embedded model for the three layer CFC panel

Model	Mesh size (mm)	Number of nodes	Number of time steps	Run time (s) *
Conventional TLM	0.025	8072	4×10^5	83
Embedded model	10	20	1000	0.28

(* the run time is based on a PC with an Intel Core 2 Duo CPU 3GHz processor and 4GB memory)

In summary, the multi-layer embedded model can achieve the same accuracy as the conventional TLM model by using a larger mesh size, thus saving memory storage and reducing the number of time steps.

As a further application, the multilayer CFC model was used to calculate the shielding effectiveness (SE) of four CFC panels with different layers, which were originally studied in [4.4].

The properties of four CFC panels studied are given in Table 4-3 [4.4].

Table 4-3 Composition of multi-layer panels: number of layers, layer conductivity, relative permittivity and thickness

Panel	No. of layers	Layer conductivity(Sm^{-1})	Layer relative permittivity	Layer thickness(mm)
A	1	$\sigma_1 = 10^4$	$\varepsilon_{r1} = 2$	$d_1 = 1$
B	3	$\sigma_1 = 10^4$ $\sigma_2 = 50$ $\sigma_3 = 10^3$	$\varepsilon_{r1} = 2$ $\varepsilon_{r2} = 4$ $\varepsilon_{r3} = 3$	$d_1 = 0.6$ $d_2 = 0.6$ $d_3 = 0.6$
C	5	$\sigma_1 = \sigma_3 = 10^4$ $\sigma_2 = \sigma_4 = 50$ $\sigma_5 = 10^3$	$\varepsilon_{r1} = \varepsilon_{r3} = 2$ $\varepsilon_{r2} = \varepsilon_{r4} = 4$ $\varepsilon_{r5} = 3$	$d_1 = d_3 = 0.2$ $d_2 = d_4 = 0.2$ $d_5 = 0.2$
D	9	$\sigma_1 = \sigma_3 = \sigma_8 = 10^4$ $\sigma_2 = \sigma_4 = \sigma_6 = 50$ $\sigma_5 = \sigma_7 = \sigma_9 = 10^3$	$\varepsilon_{r1} = \varepsilon_{r3} = \varepsilon_{r8} = 2$ $\varepsilon_{r2} = \varepsilon_{r4} = \varepsilon_{r6} = 4$ $\varepsilon_{r5} = \varepsilon_{r7} = \varepsilon_{r9} = 3$	$d_1 = d_3 = d_8 = 0.2$ $d_2 = d_4 = d_6 = 0.2$ $d_5 = d_7 = d_9 = 0.2$

Panel A is modelled using a single layer time domain embedded model developed in section 3.2. Panel B is modelled using the three-layer time domain embedded model as demonstrated in section 3.3.2. Panels C and D are modelled using the generalised multi-layer thin film model introduced in section 3.3.3.

For panel C with 5 layers, equations like (3-45) are obtained, in which there is a square matrix of the order 6 and 6 unknowns.

For panel D with 9 layers, equations like (3-45) are obtained, in which there is a square matrix of the order 10 and 10 unknowns.

Fig. 4-21 shows the shielding performances of these four panels as a function of frequency calculated using the embedded TLM model compared to those calculated using the FDTD method from [4.4]. It can be concluded that the results show excellent agreements with those from [4.4].

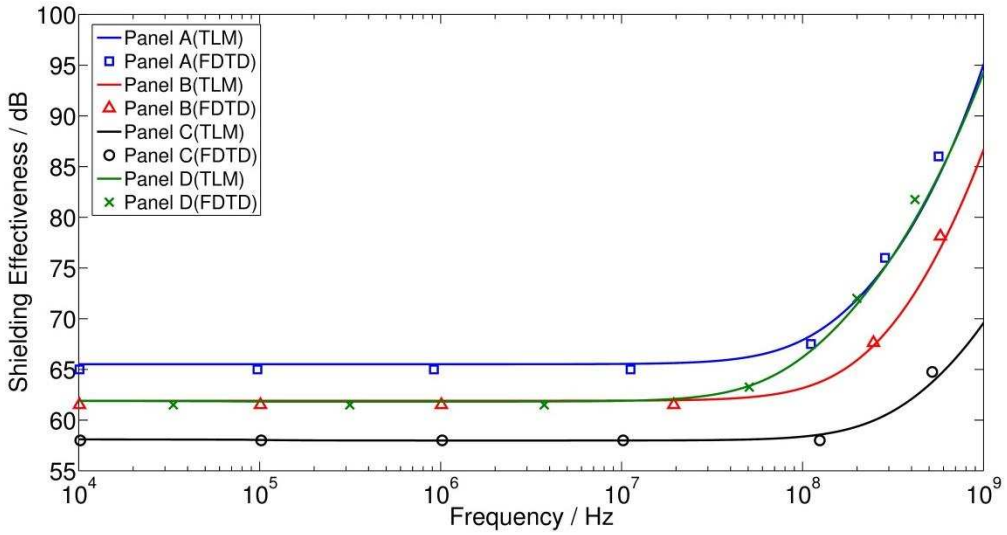

Fig.4-21 Shielding performances of the panels in Table I calculated using the embedded TLM model compared to those calculated using the FDTD method from [4.4].

From Fig. 4-21, it can be seen that panel A provides the best SE performance, which is composed of only one layer of CFC with thickness of 1 mm and conductivity of 10^4 Sm^{-1}. With the same total thickness as panel A, panel C has the lower SE since only two layers of the whole panel is made of the materials with conductivity 10^4 Sm^{-1}. Panels B and D have the same thickness and volume composition so they have the same SE performance in the lower frequency up to 10 MHz, where the reflection phenomenon dominates. At higher frequencies, due to the lamination effect, the SE of panel D increases dramatically and becomes much better than panel B, which is nearly equal to the one of panel A.

4.3.2. Titanium Panels

Titanium materials are excellent candidates for applications in aerospace industries because of their high strength-to-weight ratio, high operating temperature and excellent corrosion resistance [4.14].

To further prove the embedded model, the reflection and transmission properties of a titanium panel are studied in this section. The frequency range is chosen to be up to the highest lightning frequency (0 ~ 10 MHz) [4.6]. For comparison, the conventional TLM method is also used to model titanium panels.

A titanium panel used in C-27J aircraft [4.6] is taken as an example with parameters $\varepsilon_r = 1, \sigma_e = 5.88 \times 10^5$ Sm^{-1} and thickness of 1.2 mm.

The electric field is normally incident to the panel. The length of free space in each side of the titanium panel was chosen to be 10 m and the matched boundaries were used at the both ends to simulate the infinite space. Free space was discretised using 1D TLM nodes and the titanium panel was modelled using the embedded model. A delta pulse was used as the excitation of the simulation.

Since the highest frequency was chosen to be 10 MHz, the corresponding smallest wavelength is 30 m. The discretisation errors were firstly investigated. The reflection and transmission coefficients of the titanium panel at 10 MHz were calculated using the embedded model for N = 100 with different mesh size, dz. Results obtained were compared with the analytical ones calculated using the even/odd mode method described in section 4.2.2. Fig.4-22 shows the percentage errors in the reflection and transmission coefficients at 10 MHz against the mesh size, represented by λ/dz. It can be seen that the discretisation errors decrease with a decrease in the mesh size. In order to minimize the discretisation errors, the mesh size was chosen to be 1 m ($\lambda/dz = 30$) in the following calculations.

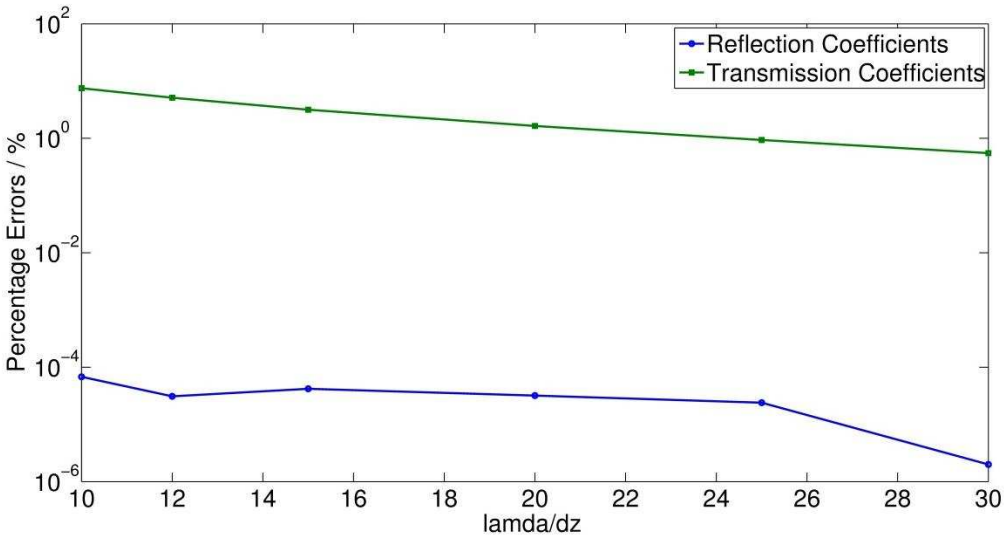

Fig.4-22 Percentage errors in the reflection and transmission coefficients of the titanium panel at 10 MHz calculated using the embedded model for N =100, with different mesh size, dz.

Using a mesh size of 1 m, the stability of the embedded model is investigated. In the embedded titanium model, the stability coefficients used in equation (4-24) are calculated as follows,

$$A_2 = 2\mu + \sigma_m \Delta t = 2.51 \times 10^{-6}\ (\mathrm{Hm^{-1}}),$$

$$B_2 = \sigma_m \Delta t - 2\mu = -2.51 \times 10^{-6}\ (\mathrm{Hm^{-1}}),$$

$$A_k = 4\mu\varepsilon + 2\Delta t(\mu\sigma_e + \varepsilon\sigma_m) + (\sigma_m\sigma_e + k^2\pi^2/d^2)\Delta t^2$$
$$= 4.93 \times 10^{-9} + 7.62 \times 10^{-11} \cdot k^2\ (\mathrm{S^2m^{-2}}), \qquad k = 1,2,\cdots,N$$

$$B_k = -8\mu\varepsilon + 2\left(\sigma_m\sigma_e + \frac{k^2\pi^2}{d^2}\right)\Delta t^2$$
$$= -8.89 \times 10^{-17} + 7.62 \times 10^{-11} \cdot k^2\ (\mathrm{S^2m^{-2}}), \qquad k = 1,2,\cdots,N$$

$$C_k = 4\mu\varepsilon - 2\Delta t(\mu\sigma_e + \varepsilon\sigma_m) + \left(\sigma_m\sigma_e + \frac{k^2\pi^2}{d^2}\right)\Delta t^2$$
$$= -4.93 \times 10^{-9} + 7.62 \times 10^{-11} \cdot k^2\ (\mathrm{S^2m^{-2}}). \qquad k = 1,2,\cdots,N$$

According to these values, the poles of the transfer functions of all the digital filters used in this titanium model are within the unit circle indicating that the model is stable.

The truncation errors from the approximation of the cotangent and cosecant functions using the expansions (equations (3-11) and (3-12)) are also investigated as before. Fig.4-23 shows the percentage errors in the reflection and transmission coefficients of the titanium panel at 10 MHz calculated using the embedded model for different number of terms, N, compared to the analytical ones. It can be seen that when N = 100, the percentage errors in the transmission coefficients are less than 1% while the percentage errors in the reflection coefficients are less than 0.0001%.

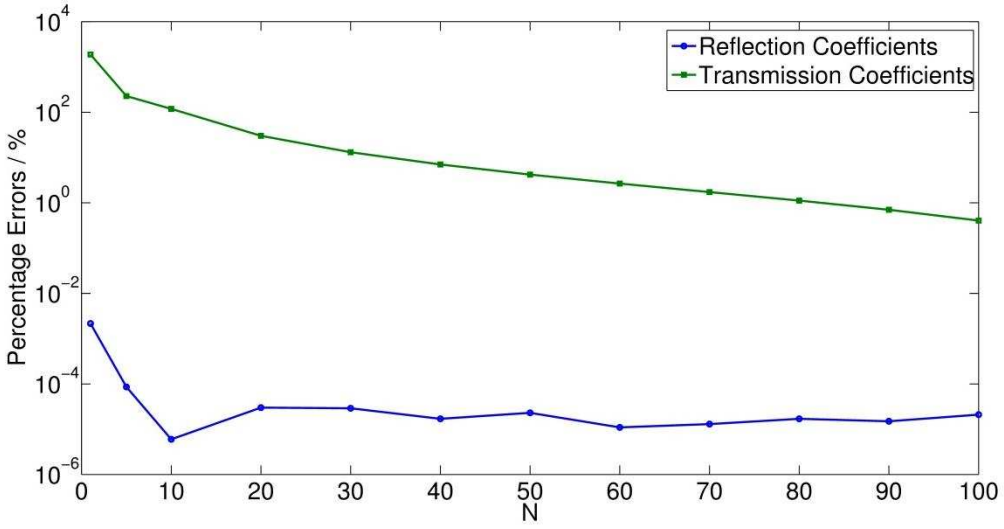

Fig.4-23 Percentage errors in the reflection and transmission coefficients of the titanium panel at 10 MHz calculating using the embedded model for dz = 1 m, with different number of expansion terms, N.

In order to maintain minimum discretisation errors, the reflection and transmission coefficients of the titanium panel were calculated in the frequency range from 0 to 10 MHz, using the embedded model with a mesh size of 1 m. Fig.4-24 shows the reflection and transmission coefficients of the titanium panel in the frequency range from 0 to 10 MHz, for different number of expansion terms, N, compared to the analytical results obtained using the even/odd mode method introduced in section 4.2.2. As expected, with an increase in the order of expansions, N, the numerical results in the frequency range from 0 to 10 MHz converge to the analytical ones. The reflection and transmission coefficients show that almost all the waves from 0 to 10 MHz

(larger than 99.99%) incident upon the titanium panel are reflected, indicating a very good shielding performance.

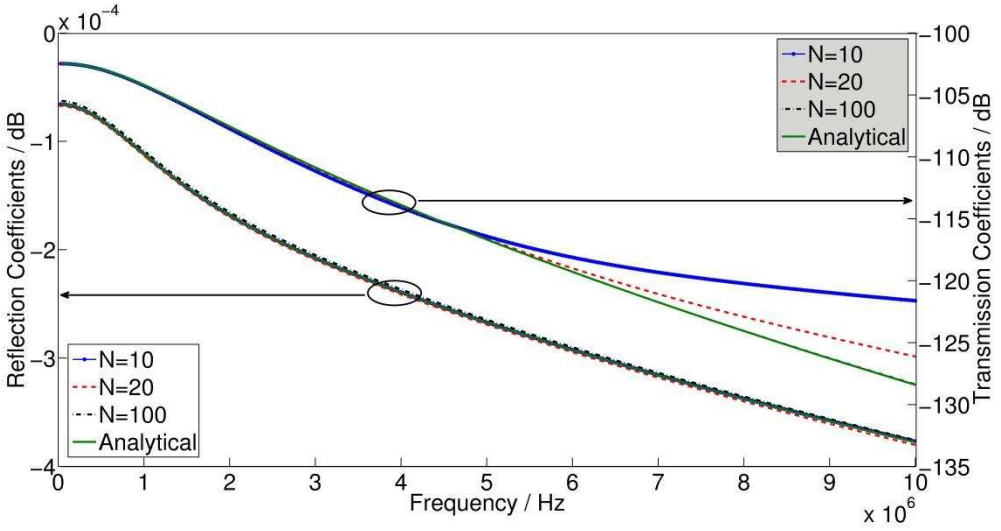

Fig.4-24 Reflection and transmission coefficients of a 1.2 mm titanium panel with $\varepsilon_r = 1, \sigma_e = 5.88 \times 10^5$ Sm^{-1} calculated using the embedded model for different number of terms, N, and analytical method.

Fig.4-25 (a, b) show the percentage errors (defined in equation (4-21)) in the reflection and transmission coefficients of the titanium panel compared to the analytical results. It can be seen that when N = 100, the errors for the reflection coefficients are less than 0.00003% and the errors for the transmission coefficients are less than 0.4% in the frequency range from 0 to 10 MHz.

For comparison purposes, the titanium panel was also modelled using the conventional TLM method. Since in the conventional TLM method the titanium panel needs to be discretised, the mesh size should be less than the skin depth of the panel at 10 MHz, which is 0.2 mm. Fig.4-26 shows the percentage errors in the reflection and transmission coefficients of the titanium panel at 10 MHz calculated using the conventional TLM method for different mesh size, represented by d/dz, where d is the thickness of the panel, compared to the analytical ones. It can be seen that when the mesh size is 0.025 mm ($d/dz = 48$), the errors in the reflection coefficients are less than 0.0002% while the errors in the transmission coefficients are less than 0.5%.

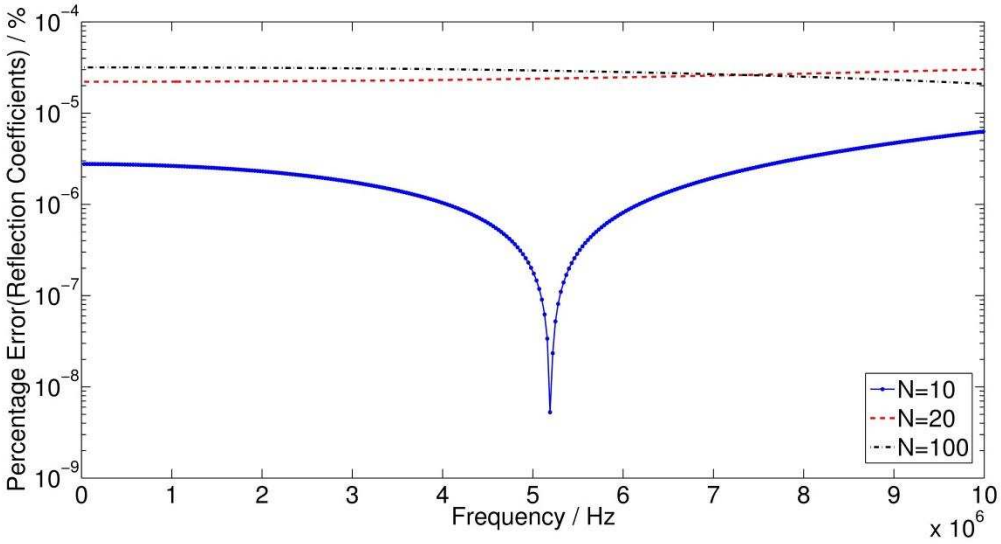

(a)

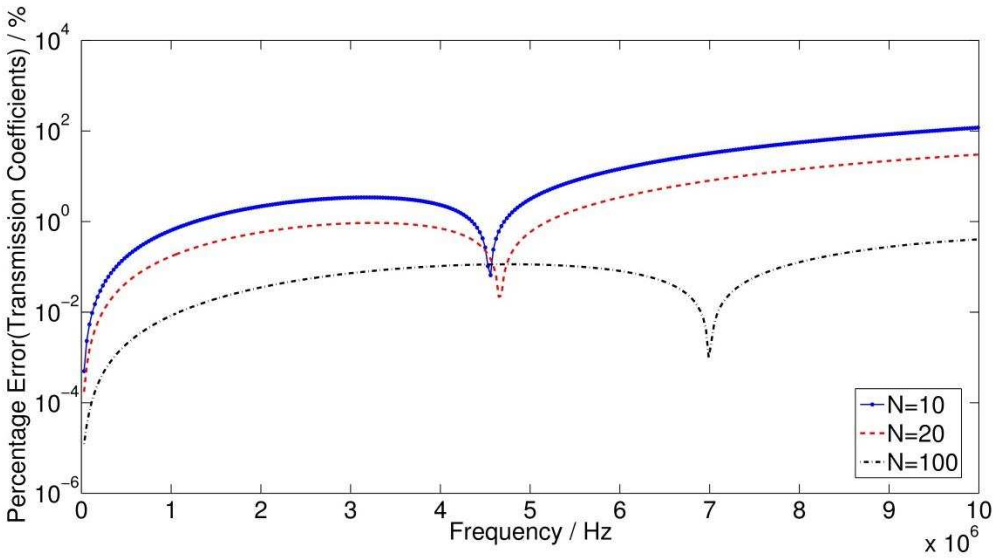

(b)

Fig.4-25 Percentage errors in the (a) reflection coefficients and (b) transmission coefficients calculated using the embedded model with different number of terms, N (N =10, 20 and 100).

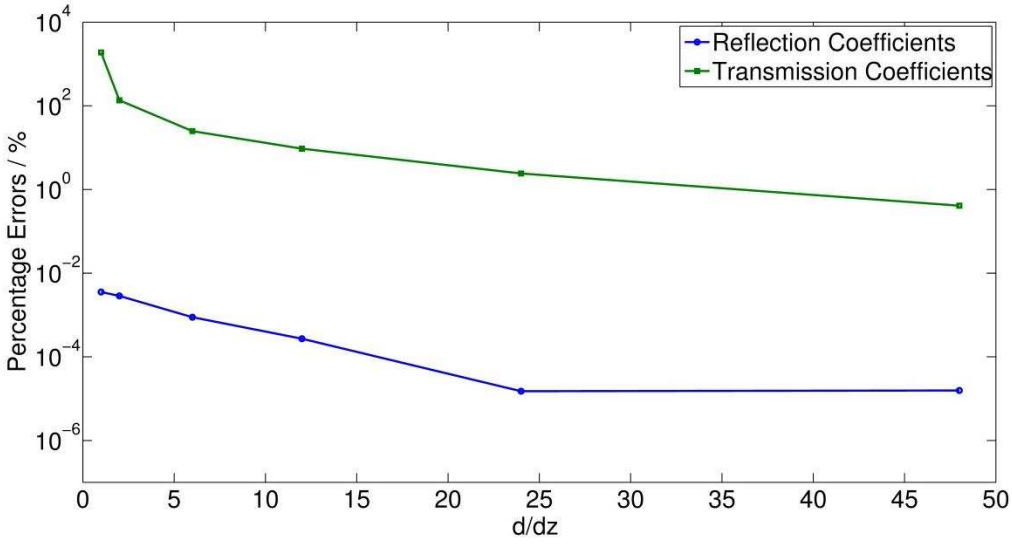

Fig.4-26 Percentage errors in the reflection and transmission coefficients of the titanium panel at 10 MHz calculated using the conventional TLM method for different mesh size, dz.

For comparison purposes, the reflection and transmission coefficients of the titanium panel were calculated in the frequency range from 0 to 10 MHz, using the conventional TLM method with a mesh size of 0.025 mm. Fig. 4-27 shows the percentage errors in the reflection and transmission coefficients calculating using the conventional TLM method compared to the analytical results. It is shown that in the frequency range from 0 to 10 MHz, the errors in the reflection coefficients are less than 0.00002% and the errors in the transmission coefficients are less than 0.5%, comparable to the corresponding errors calculated using the embedded model with a mesh size of 1 m.

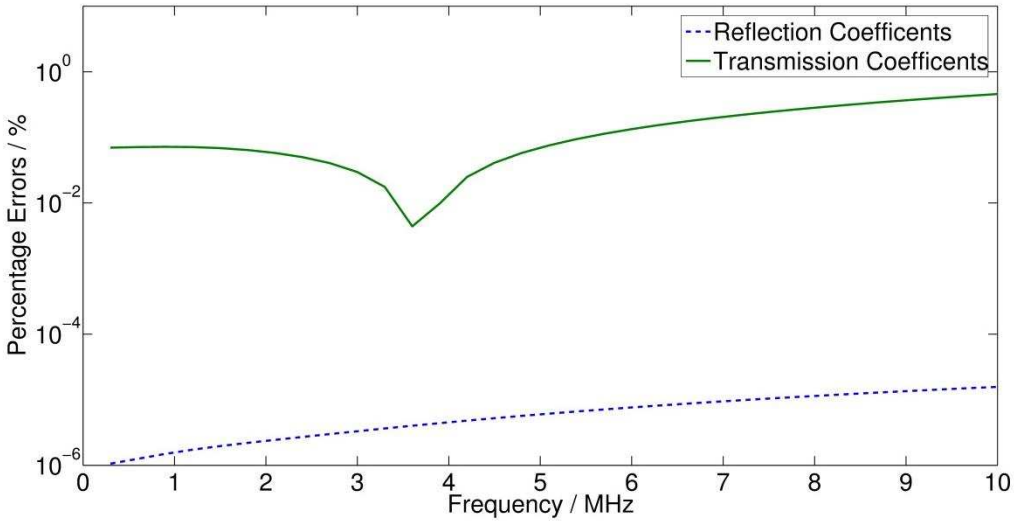

Fig. 4-27 Percentage errors in the reflection coefficients and transmission coefficients calculated using the conventional TLM method with a mesh size of 0.025 mm.

However, the number of nodes and the number of time steps needed in the conventional TLM model are huge, as shown in Table 4-4.

Table 4-4 Comparison between the conventional TLM model and the embedded model for the single layer titanium panel

Model	Mesh size	Number of nodes	Number of time steps	Run time *
Conventional TLM	0.025 mm	400048	4×10^7	>4hours
Embedded model	1 m	20	1000	0.39s

(* the run time is based on a PC with an Intel Core 2 Duo CPU 3GHz processor and 4GB memory)

In the conventional TLM method, the mesh size was chosen to be 0.025 mm in order to include more details of the panel into the mesh so that accurate results were obtained. In the embedded model, the mesh size depends on the smallest wavelength regardless of the thickness of the panel. Therefore, the mesh size used in the embedded model is 40000 times bigger than that used in the conventional TLM method.

In conclusion, the titanium embedded model once again shows that the embedded model can achieve the same accuracy as the conventional TLM method using a larger mesh size, resulting in saving memory storage and reducing the number of time steps thus saving the computational overheads.

4.4. Applications of Embedded Model to Dielectric Films

As examples of dielectric films, anti-reflection (AR) coatings and fibre Bragg gratings (FBG) are utilized to examine the embedded model proposed in Chapter 3.

For the isotropic and lossless dielectric materials, the equivalent inductance and capacitance, L and C, can be expressed by

$$\begin{aligned} L &= \mu = \mu_0 \mu_r, \\ C &= \varepsilon = \varepsilon_0 \varepsilon_r. \end{aligned} \tag{4-26}$$

A modified embedded thin film model is also presented to model single layer dielectric thin films.

4.4.1. Antireflection (AR) Coatings

AR coatings are used in optical amplifiers, couplers and switches [4.15] to reduce the reflection and enhance transmission.

In this section, the reflection coefficients of one quarter-wavelength AR coating are calculated using the embedded model proposed in Chapter 3. For comparison, the conventional TLM method is also used to model the AR coating.

The AR coating is assumed to be infinite in length and width, but only have finite thickness. As shown in Fig.4-28, the electric field is normally incident

from free space with refractive index n_a on to the film with refractive index n_1 and then emerges into a substrate with refractive index n_b.

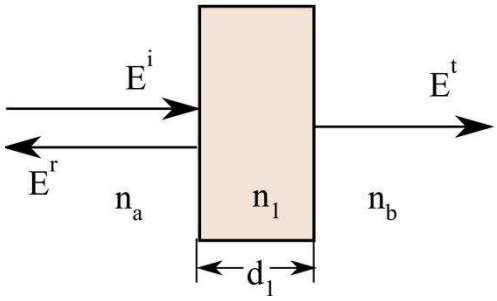

Fig.4-28 The electric field is normally incident to a quarter-wavelength film on a substrate.

The AR coating studied is taken from [4.1]. It has a refractive index $n_1 = 1.22$ and a quarter-wavelength thickness $d_1 = \frac{\lambda_0}{4n_1} = 112.7$ nm at $\lambda_0 = 550$ nm. The glass substrate has refractive index $n_b = 1.5$.

When analysing the reflection coefficients of the AR coating, the background materials (free space and glass substrate) were assumed to be infinite. In the simulation, the lengths of free space and glass substrate regions were chosen to be the same as 100 nm, and at both ends matched boundaries [4.11] were used to simulate the infinite space. The background materials were discretised using 1D TLM nodes, while the coating was modelled by the embedded model proposed in Chapter 3. The excitation was placed in the first node using a delta pulse. The incident field to and the reflected field from the AR coating were calculated in the time domain and then a Fast Fourier Transform (FFT) was taken to get the reflection coefficients of the AR coating.

In order to choose an appropriate mesh size, the discretisation errors were investigated first. The reflection coefficients of the AR coating at 550 nm were calculated using the embedded model with different mesh size, dz. Results obtained were compared with the analytical ones calculated using the transfer matrix method described in section 4.2.1. Fig.4-29 shows the percentage errors in the reflection coefficients of the AR coating at 550 nm calculated using the embedded model with different mesh size, represented by $\lambda/(n_b \cdot dz)$,

compared to the analytical ones. It can be seen that when the mesh size $dz = 1$ nm ($\lambda/(n_b \cdot dz) = 366.7$), the errors in the reflection coefficients are less than 1%. In the following calculations, the mesh size was chosen to be 1 nm to minimize the discretisation errors.

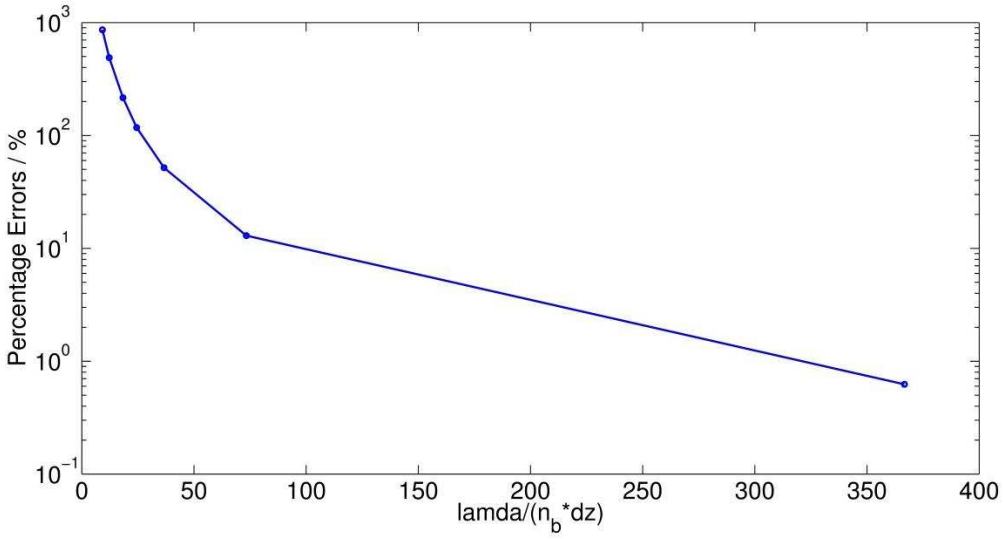

Fig.4-29 Percentage errors in the reflection coefficients of the AR coating at 550 nm calculated using the embedded model with different mesh size, dz.

Using a mesh size of 1 nm, the stability of the embedded model is investigated. For the time domain model of this AR coating connecting with the TLM algorithm, the key is to solve equations (3-9) and (3-10). According to section 3.2, these two equations can be seen as a complex digital filter system. The stability of the system depends on the poles of the transfer functions of all the digital filters.

According to the parameters of the AR coating, the stability coefficients used in equation (4-24) are calculated as follows ($\sigma_e = 0$ and $\sigma_m = 0$),

$$A_2 = 2\mu = 2.51 \times 10^{-6}\ (\mathrm{Hm^{-1}}),$$

$$B_2 = -2\mu = -2.51 \times 10^{-6}\ (\mathrm{Hm^{-1}}),$$

$$A_k = 4\mu\varepsilon + k^2\pi^2/d^2\Delta t^2$$
$$= 6.615 \times 10^{-17} + 8.634 \times 10^{-21} \cdot k^2\ (\mathrm{S^2m^{-2}}), \qquad k = 1,2,\cdots,N$$

$$B_k = -8\mu\varepsilon + 2\frac{k^2\pi^2}{d^2}\Delta t^2$$
$$= -13.23 \times 10^{-17} + 8.634 \times 10^{-21} \cdot k^2 \ (\mathrm{S^2 m^{-2}}), \qquad k = 1,2,\cdots,N$$

$$C_k = 4\mu\varepsilon + \frac{k^2\pi^2}{d^2}\Delta t^2$$
$$= 6.615 \times 10^{-17} + 8.634 \times 10^{-21} \cdot k^2 \ (\mathrm{S^2 m^{-2}}), \qquad k = 1,2,\cdots,N$$

From these values, it can be seen that for all the digital filters used in this system, the poles of their transfer functions are within the unit circle indicating that the AR model is stable [4.12].

Using the stable embedded model, the reflection coefficients of the AR coating were calculated in the wavelength range from 450 nm to 550 nm. Fig.4-30 shows the reflection coefficients of the AR coating as a function of wavelength for different number of terms, N (used in equations (3-11) and (3-12)), together with the analytical ones calculated using the transfer matrix method described in section 4.2. It shows that with an increase in the number of terms, N, the numerical results converge to the analytical ones. The convergence is best at the operating wavelength $\lambda_0 = 550$ nm.

Fig.4-31 shows the percentage errors (defined in equation (4-21)) in the reflection coefficients calculated using the embedded model and the analytical results. When N = 400, the errors are less than 2% in the wavelength range from 450 nm to 650 nm.

The runtime for N = 400 was 45s using a PC with an Intel Core 2 Duo CPU 3GHz processor and 4GB memory.

It is noticed that the results for the AR coating with $n_1 = 1.22$ show the slow convergence with the number of terms, N. 400 terms are needed to get results with errors less than 2%, which increases the computational costs. Thus it is desirable to obtain a more efficient implementation. The development of a modified embedded model is the subject of the following section.

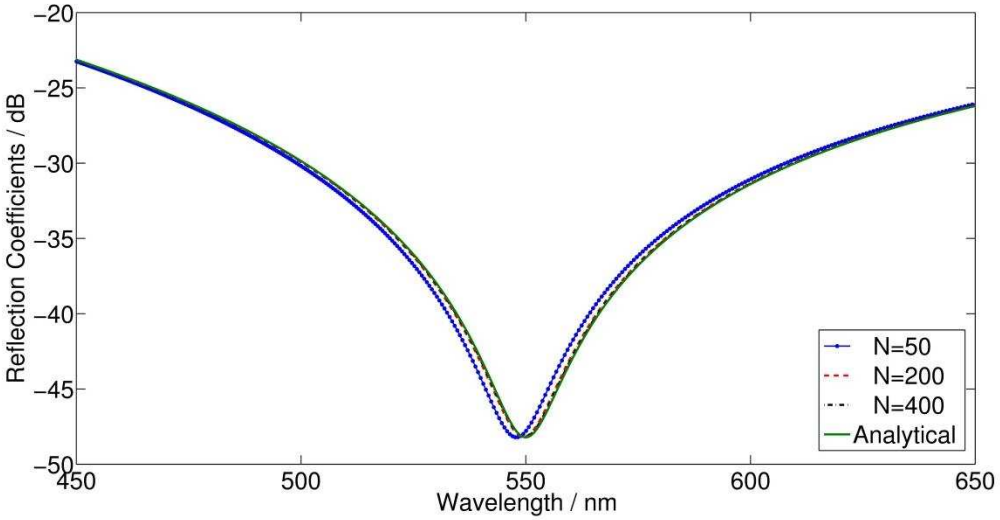

Fig.4-30 Reflection coefficients of the AR coating with $n_1 = 1.22$ calculated using the embedded model for different number of terms, N.

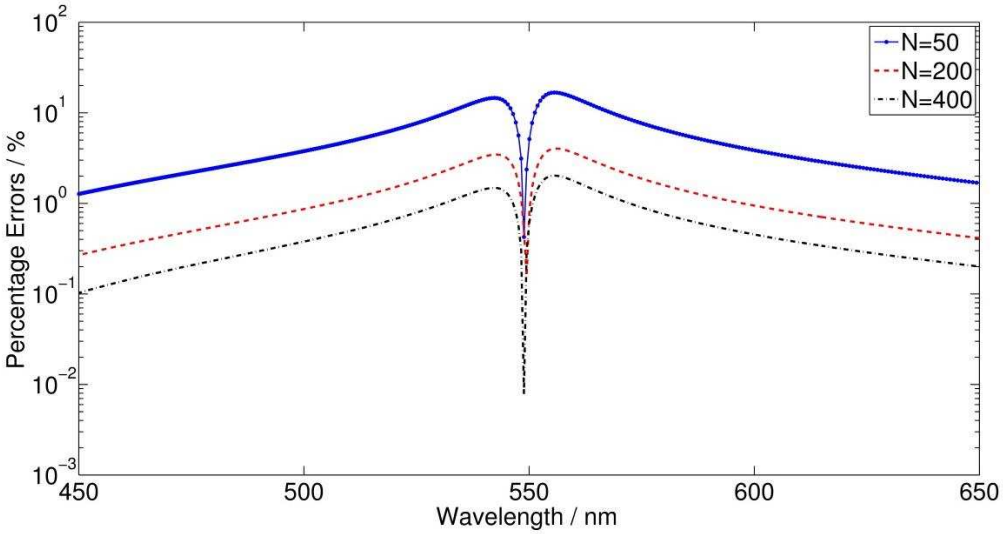

Fig.4-31 The percentage errors in the reflection coefficients calculated using the embedded model for different number of terms, N (N = 50, 200 and 400).

4.4.2. Modified Embedded Model for Single-layer Dielectric Films

From the previous examples, it can be seen that for single-layer AR coatings, 400 or more expansion terms are needed in cotangent and cosecant function expansions (equations (3-11) and (3-12)) to get good convergence to analytical results. This increases the computational costs. In this section, a modified embedded model for single-layer dielectric films is presented, which can reduce the number of expansion terms for convergence. This model is tested using the AR coating example studied in section 4.4.1.

The expansions for the cotangent and cosecant functions given in equations (3-11) and (3-12), are repeated here for convenience.

$$jYcot\theta = j\sqrt{\frac{C}{L}}\left(\frac{1}{\theta} + 2\theta\sum_{k=1}^{N=\infty}\frac{1}{\theta^2 - k^2\pi^2}\right),$$

$$jYcsc\theta = j\sqrt{\frac{C}{L}}\left(\frac{1}{\theta} + 2\theta\sum_{k=1}^{N=\infty}\frac{(-1)^k}{\theta^2 - k^2\pi^2}\right).$$

The above two equations converge rapidly when $\theta = 0$, that is at zero frequency for any thin thickness film. This means that accurate results for low frequencies could be obtained even using only a few terms. However, for very high frequencies, such as in the visible part of the electromagnetic spectrum, to get the accurate results, many more terms are needed to approximate the infinite series.

The above equations can be manipulated so that they converge faster at the specific frequency f_0.

For the cotangent function, the specific electrical length θ_0 is introduced as

$$cot\theta = cot(\theta - \theta_0 + \theta_0) = \frac{cos(\theta - \theta_0 + \theta_0)}{sin(\theta - \theta_0 + \theta_0)}$$

$$= \frac{cos(\theta - \theta_0)\,cos\theta_0 - sin(\theta - \theta_0)\,sin\theta_0}{sin(\theta - \theta_0)\,cos\theta_0 + cos(\theta - \theta_0)\,sin\theta_0}.$$

By dividing both the numerator and the denominator by $sin(\theta-\theta_0)\,sin\theta_0$, one can obtain,

$$cot\theta = \frac{cot(\theta-\theta_0)-tan\theta_0}{1+cot(\theta-\theta_0)\,tan\theta_0}, \tag{4-27}$$

where $cot\theta$ is replaced by $cot(\theta-\theta_0)$.

Similarly, $csc\theta$ can be expressed by

$$csc\theta = \frac{csc(\theta-\theta_0)/cos\theta_0}{1+cot(\theta-\theta_0)\,tan\theta_0}. \tag{4-28}$$

After replacing $cot\theta$ and $csc\theta$ in equations (3-11) and (3-12) with equations (4-27) and (4-28), they become

$$\begin{aligned}&\big((y_1y_2+YY+jY(y_1{+}y_2)tan\theta_0)+(y_1y_2+YY)tan\theta_0\,cot(\theta-\theta_0)\\&\qquad -Y(y_1{+}y_2)\,jcot(\theta-\theta_0)\big)\cdot V_1\\=\ &\big((2y_1y_2+2y_1jYtan\theta_0)+2y_1y_2tan\theta_0\,cot(\theta-\theta_0)-2y_1Y\\&\qquad \cdot jcot(\theta-\theta_0)\big)\cdot V_1^i-2y_2\,Y\frac{j\,csc(\theta-\theta_0)}{cos\theta_0}\cdot V_2^i,\end{aligned} \tag{4-29}$$

$$\begin{aligned}&\big((y_1y_2+YY+jY(y_1{+}y_2)tan\theta_0)+(y_1y_2+YY)tan\theta_0\,cot(\theta-\theta_0)\\&\qquad -Y(y_1{+}y_2)\,jcot(\theta-\theta_0)\big)\cdot V_2\\=\ &-2y_1\,Y\frac{j\,csc(\theta-\theta_0)}{cos\theta_0}\cdot V_1^i\\&\qquad +\big((2y_1y_2+2y_1jYtan\theta_0)+2y_1y_2tan\theta_0\,cot(\theta-\theta_0)-2y_2Y\\&\qquad \cdot jcot(\theta-\theta_0)\big)\cdot V_2^i.\end{aligned} \tag{4-30}$$

Equations (4-29) and (4-30) now involve $cot(\theta-\theta_0)$ and $csc(\theta-\theta_0)$ which converge faster at θ_0, which corresponds to the frequency f_0 defined as $\theta_0 = 2\pi f_0 d\sqrt{LC}$.

In equations (4-27) and (4-28), $tan\theta_0$ is a known value given a specific f_0, and $cot(\theta-\theta_0)$ and $csc(\theta-\theta_0)$ are expanded using the same expansion technique as in equation (3-11) and (3-12), as follows,

$$\begin{aligned} cot(\theta-\theta_0) &= \frac{1}{\theta-\theta_0} + 2(\theta-\theta_0)\sum_{k=1}^{N=\infty}\frac{1}{(\theta-\theta_0)^2-k^2\pi^2}, \\ csc(\theta-\theta_0) &= \frac{1}{\theta-\theta_0} + 2(\theta-\theta_0)\sum_{k=1}^{N=\infty}\frac{(-1)^k}{(\theta-\theta_0)^2-k^2\pi^2}. \end{aligned} \tag{4-31}$$

Equation (4-31) converges rapidly when $\theta=\theta_0$, which means that fewer terms are needed to get accurate results at the given frequency f_0.

After substituting equation (4-31) in equations (4-29) and (4-30) and then transferring them into Z domain, the solutions are obtained using the same method as described in section 3.2.

Since

$$\theta = \omega d\sqrt{LC}, \qquad \theta_0 = \omega_0 d\sqrt{LC} = 2\pi f_0\sqrt{LC},$$

then equation (4-31) in the Z domain becomes

$$\begin{aligned} cot(\theta-\theta_0) &= -m_1\frac{1+z^{-1}}{AA_2+CC_2z^{-1}} \\ &\quad - 2m_1\sum\frac{AA_2+BB_2z^{-1}+CC_2z^{-2}}{AA_k+BB_kz^{-1}+CC_kz^{-2}}, \\ csc(\theta-\theta_0) &= -m_1\frac{1+z^{-1}}{AA_2+CC_2z^{-1}} \\ &\quad - 2m_1(-1)^k\sum\frac{AA_2+BB_2z^{-1}+CC_2z^{-2}}{AA_k+BB_kz^{-1}+CC_kz^{-2}}. \end{aligned} \tag{4-32}$$

Parameters in equation (4-32) are given by:

$AA_2 = \omega_0\Delta t + 2j,$

$BB_2 = 2\omega_0\Delta t,$

$CC_2 = \omega_0\Delta t - 2j,$

$$m_1 = \frac{\Delta t}{d\sqrt{\mu\varepsilon}},$$

$$AA_k = -4 + 4j\omega_0\Delta t + \Delta t^2\left(\omega_0^2 - \frac{k^2\pi^2}{d^2\mu\varepsilon}\right),$$

$$BB_k = 8 + 2\Delta t^2\left(\omega_0^2 - \frac{k^2\pi^2}{d^2\mu\varepsilon}\right),$$

$$CC_k = -4 - 4j\omega_0\Delta t + \Delta t^2\left(\omega_0^2 - \frac{k^2\pi^2}{d^2\mu\varepsilon}\right).$$

This modified embedded model can only work well for single layer dielectric films since this model involves an electrical length shifting procedure. For multilayer films, there are two or more electrical lengths which was found to result in not only no savings in computational resource but also stability problems in practice.

In order to test the modified embedded model, the AR coating studied in section 4.4.1 is used as an example.

The AR coating studied in [4.1] has a refractive $n_1 = 1.22$ and has a quarter-wavelength thickness $d_1 = \frac{\lambda_0}{4n_1} = 112.7$ nm at $\lambda_0 = 550$ nm. The glass substrate has refractive index $n_b = 1.5$.

Since the centre wavelength is $\lambda_0 = 550$ nm, the frequency at which the operating of the coating is optimized is $f_0 = c/\lambda_0 = 545$ THz. According to the described model the cotangent and cosecant functions are now shifted to frequency f_0 for which they converge faster.

The TLM mesh size was chosen to be 1 nm as before.

Fig.4-32 (a) shows the reflection coefficients of the AR coating calculated using the modified embedded model for different number of terms N (N = 5, 10 and 20), together with the analytical results. It can be seen that numerical results indistinguishable from the analytical ones are obtained using only 20 terms. This is in contrast to Fig.4-30 where 400 terms are used and convergence is only achieved at resonant wavelength.

Fig.4-32 (b) shows the percentage errors (defined in equation (4-21)) in the reflection coefficients calculated using the modified embedded model for different number of terms, N, and compared to the analytical ones. It can be seen that when N = 20, the errors in the wavelength range from 450 nm to 650 nm are less than 3%. Compared to the embedded model proposed in Chapter 3, the modified model achieves similar accuracy in the desired wavelength range, even using only 20 terms.

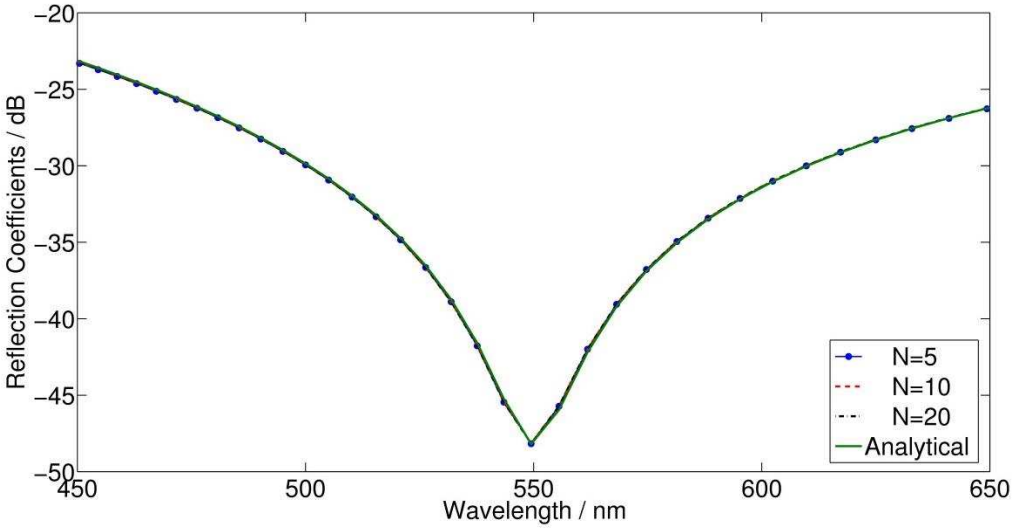

(a)

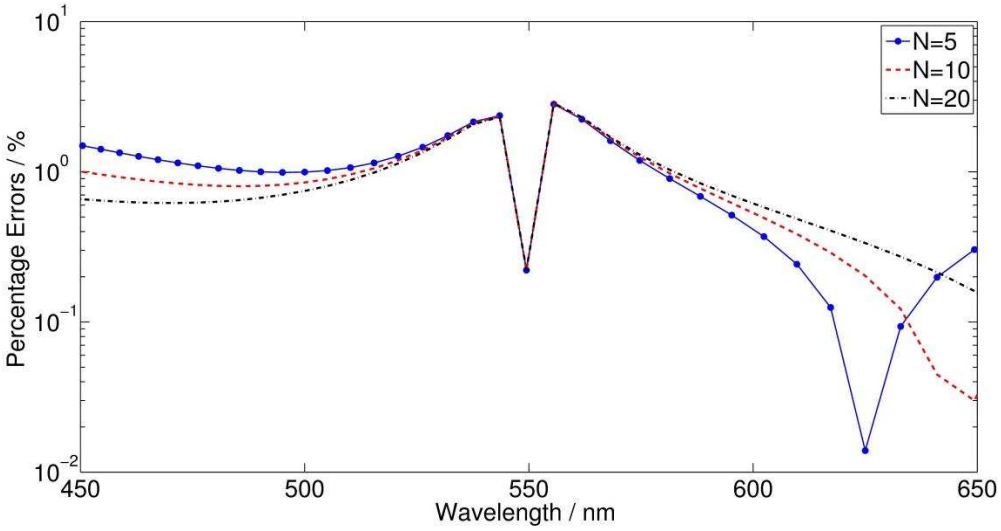

(b)

Fig.4-32 (a) Reflection coefficients of the AR coating with $n_1 = 1.22$ (b) percentage errors in the reflection coefficients, calculated using the modified model for different number of terms N (N = 5, 10 and 20).

Therefore, the number of terms used in the modified model is reduced by twenty times over that in the embedded model proposed in Chapter 3, and this improves the efficiency of the simulation.

For comparison purposes, the conventional TLM method is also used to model the AR coating. The discretisation errors were firstly investigated, in order to choose an appropriate mesh size. Fig.4-33 shows the percentage errors in the reflection coefficients of the AR coating at 550 nm calculated using the conventional TLM method for different mesh size, dz, represented by d/dz, where d is the thickness of the coating, compared to the analytical ones. It can be seen that when $dz = 0.2\ nm$ ($d/dz = 563.5$), the errors in the reflection coefficients are around 0.2%.

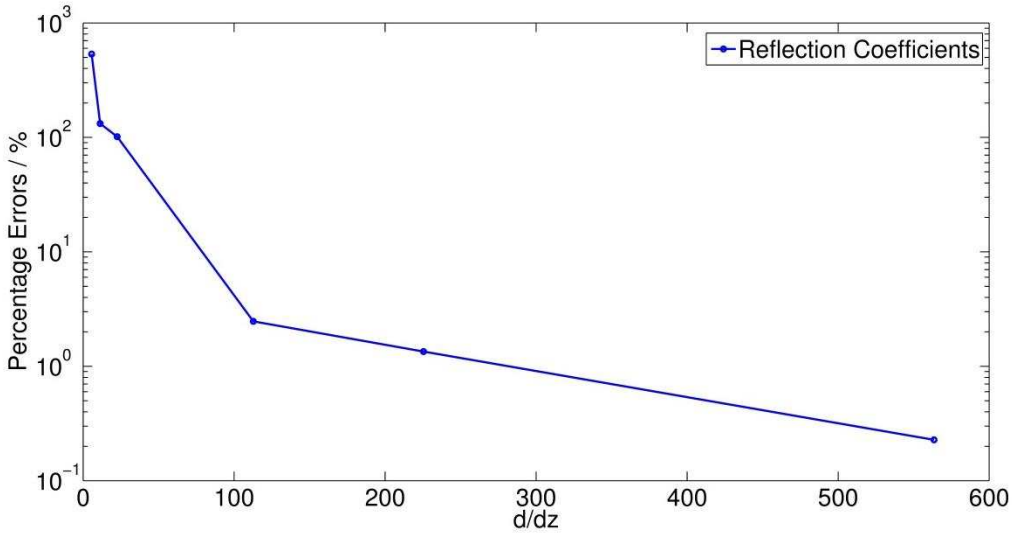

Fig.4-33 Percentage errors in the reflection coefficients of the AR coating with $n = 1.22$ calculated using the conventional TLM method with different mesh size, dz.

For comparison purposes, the reflection coefficients of the AR coating were calculated in the wavelength range from 450 nm to 650 nm using the conventional TLM method with the mesh size of 1 nm and 0.2 nm. Fig. 4-34 shows the percentage errors in the reflection coefficients calculated using the conventional TLM method with different discretisations $dz = 1$ nm and 0.2 nm. It can be seen that when the mesh size is 1 nm, the errors in the reflection coefficients are less than 10% in the wavelength range from 450 nm to 650 nm;

when the mesh size is 0.2 nm, the errors are below 4% in the wavelength range from 450 nm to 650 nm, comparable with the results from the embedded model with a mesh size of 1 nm.

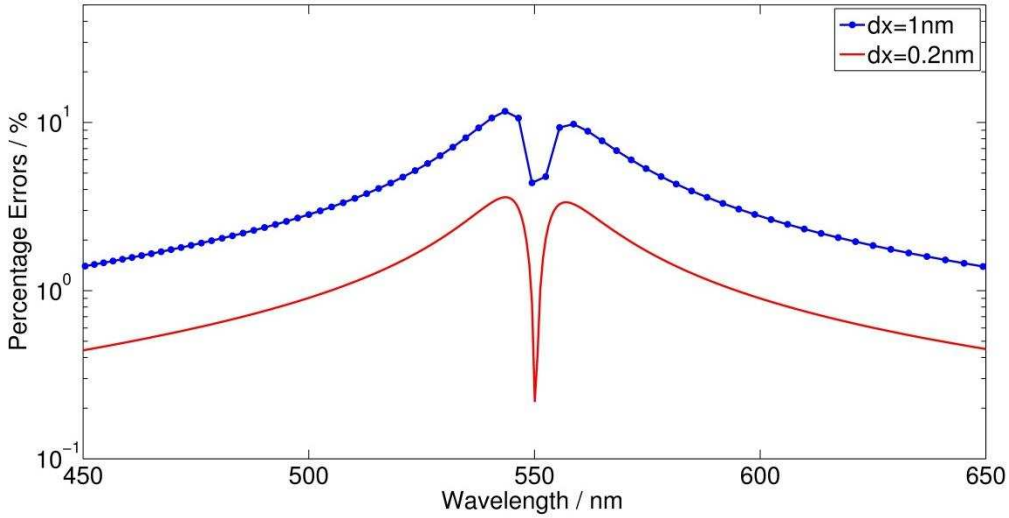

Fig. 4-34 The percentage errors in the reflection coefficients calculated using the conventional TLM method compared with the analytical ones for two different discretisation $dz = 1$ nm and 0.2 nm.

Table 4-5 shows the comparison in the compuational consumptions for the conventional TLM model and the modified embedded model. It can be seen that for the conventional TLM method, smaller mesh size is needed to capture the details of the AR coating, which leads to bigger memory storage for the nodes and a larger number of time steps in the simulation.

Table 4-5 Comparison between the conventional TLM model and the modified embedded model for the AR coating with $n_1 = 1.22$

Model	Mesh size (nm)	Number of nodes	Number of time steps	Run time(s) *
Conventional TLM	0.2	1564	2.5×10^6	137
Modified Embedded model	1	200	5×10^5	25

(* the run time is based on a PC with an Intel Core 2 Duo CPU 3GHz processor and 4GB memory)

4.4.3. Fibre Bragg Gratings (FBG)

Fibre Bragg gratings (FBG) have been the subject of intense investigation in recent years, driven by applications such as filters, fibre lasers, dispersion compensators and wavelength converters [4.17 ~ 4.18]. They operate through reflecting light over a narrow frequency range and transmitting at all other frequencies [4.19].

In this section, the filter property of a linear Bragg grating structure [4.20] is tested using the embedded model. The structure shown in Fig.4-35 consists of 68 alternating layers of refractive indices $n_1 = 2.05$ and $n_2 = 1.95$. The thickness of each layer is chosen to be a quarter wavelength at the Bragg (centre) wavelength of $\lambda_0 = 1\mu m$. Thus the thicknesses of each layer are $d_1 = \frac{\lambda_0}{4n_1} = 112.95$ nm and $d_2 = \frac{\lambda_0}{4n_2} = 128.20$ nm, respectively. The length of the free space region on each side of the grating in the model is chosen to be 1000 nm and matched boundaries [4.11] were used at both ends to simulate the infinite space.

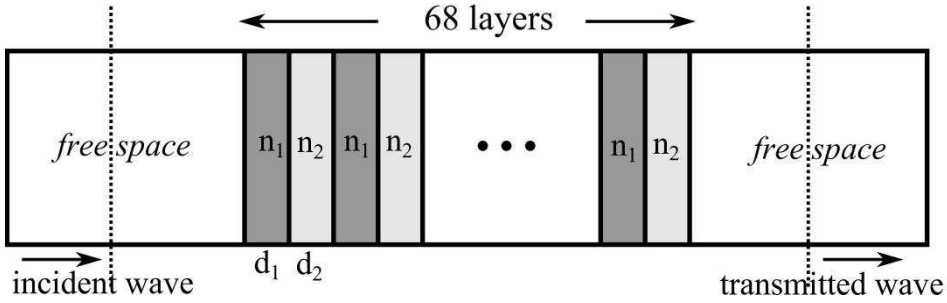

Fig.4-35 Fibre Bragg grating structure having 68 alternating layers of refractive indices $n_1 = 2.05$ and $n_2 = 1.95$. The thicknesses at the centre wavelength of 1 μm are: $d_1 = 112.95$ nm and $d_2 = 128.20$ nm.

To calculate the transmission coefficients of this FBG structure, free space on both sides of this structure was discretised using 1D TLM nodes. The FBG structure was embedded between two adjacent 1D TLM nodes using the time domain embedded multilayer thin film model introduced in Chapter 3.

The FBG structure has two different dielectric materials. Therefore, their capacitance and inductance are expressed as,

$$L1 = \mu_0\mu_r = \mu_0,\ C1 = \varepsilon_0\varepsilon_r = 4.2025\varepsilon_0,$$

$$L2 = \mu_0\mu_r = \mu_0,\ C2 = \varepsilon_0\varepsilon_r = 3.8025\varepsilon_0,$$

and their characteristic admittances are given by

$$Y1 = \sqrt{\frac{C1}{L1}} = 0.0054\ \text{S},$$

$$Y2 = \sqrt{\frac{C1}{L1}} = 0.0052\ \text{S}.$$

The 68-layer FBG embedded between two adjacent TLM nodes is shown in Fig. 4-36.

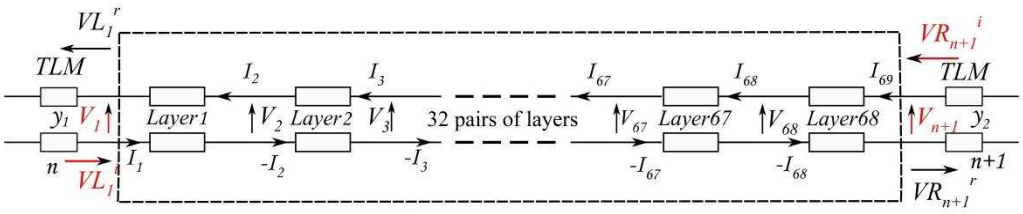

Fig. 4-36 68 layer fibre Bragg grating embedded between two adjacent 1D TLM nodes.

Since the FBG structure has 68 layers, there are 68 admittance matrix equations with the form given in equation (3-31). Equations like (3-45) can be obtained, in which there is a square matrix of the order 69 and 69 unknowns. Its solution is obtained by the Gauss-Seidel method described in section 3.3.3.

The discretisation errors were firstly investigated in order to choose an appropriate mesh size. Fig.4-37 shows the percentage errors in the transmission coefficients of the FBG structure at 1 μm calculated using the embedded model for different mesh size, represented by λ/dz, compared to the analytical ones. It can be seen that when the mesh size is 10 nm ($\lambda/dz = 100$), the errors are around 0.01%. In the following calculation, the mesh size was chosen to be 10 nm in order to minimize the discretisation errors in the frequency range from 280 THz to 320 THz.

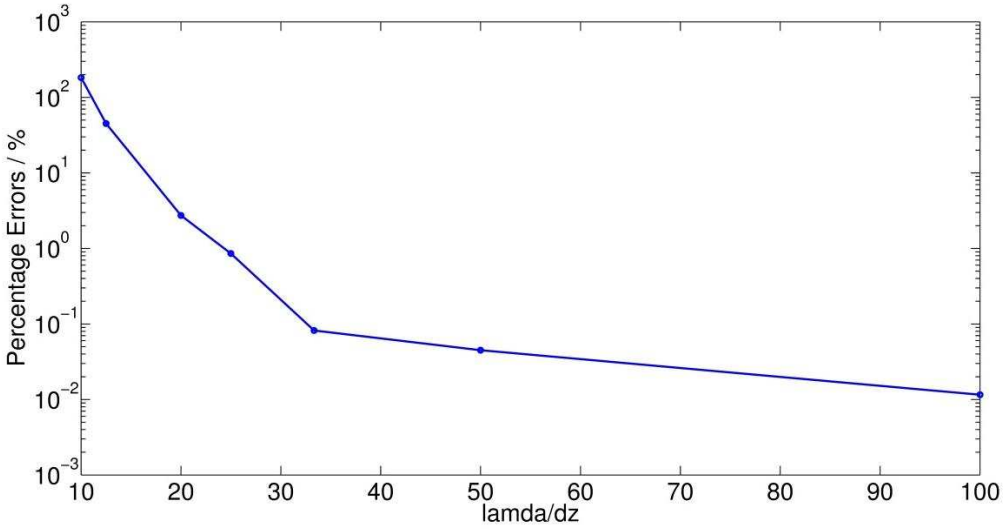

Fig.4-37 Percentage errors in the transmission coefficients of the FBG structure at 1 μm calculated using the embedded model for different mesh size, dz.

Fig.4-38 (a) shows the transmission coefficients of the FBG structure with different expansion terms N, namely N = 50, 100 and 200, compared to the analytical one calculated using a transfer matrix method as described in section 4.2.2. When N = 200, the numerical results are virtually indistinguishable from the analytical ones. The percentage errors (defined in equation (4-21)) in the transmission coefficients of the FBG compared with the analytical results are shown in Fig.4-38 (b). It can be seen that when N = 200, the errors are below 0.2% from 280 THz to 320 THz.

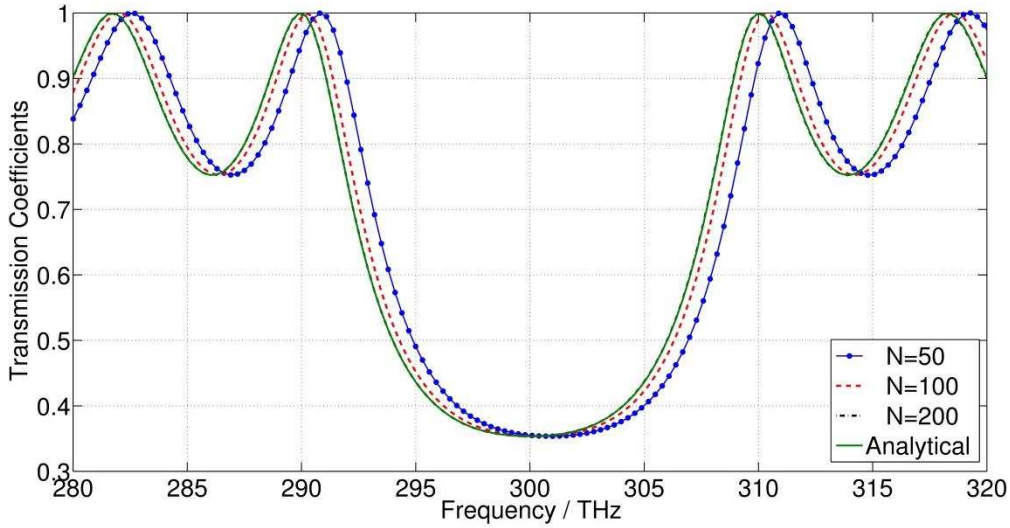

(a)

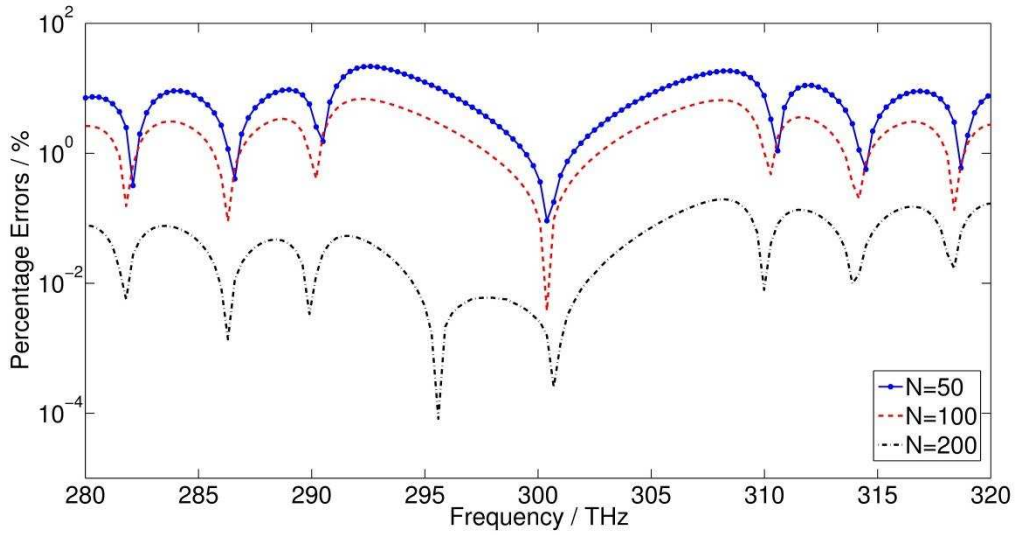

(b)

Fig.4-38 (a) The transmission coefficients of the FBG and (b) the percentage errors in transmission coefficients obtained using the embedded model for different number of terms N (N = 50, 100 and 200).

For comparison purposes, the FBG structure was also modelled using the conventional TLM method with a discretisation $dz = 10$ nm and $dz = 1$ nm. Fig.4-39 shows the percentage errors in the transmission coefficients obtained from the conventional TLM method in comparison to the analytical results. It can be seen that when the mesh size is 10 nm the errors are below 20%, while for a mesh size of 1 nm, the errors are below 0.8%, comparable with the ones calculated using the embedded model with a mesh size of 10 nm.

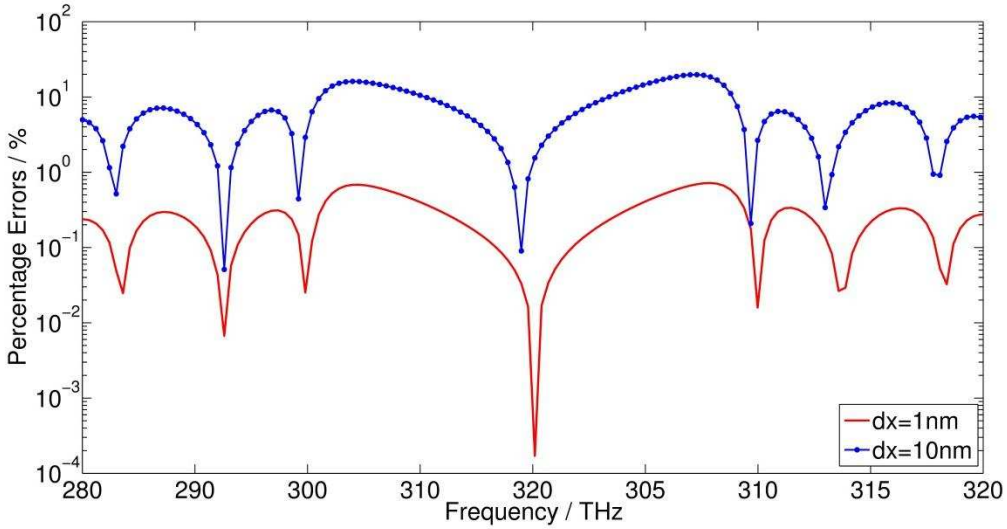

Fig.4-39 The percentage errors in transmission coefficients obtained using the conventional TLM method for mesh size 1 nm and 10 nm.

Table 4-6 shows the comparison in the computational costs for the conventional TLM model and the embedded model for the FBG structure. It can be seen that since the mesh size for the embedded model is bigger, a smaller number of nodes and time steps are needed, leading to a saving in memory storage for the nodes and a saving in the number of time steps. The total run time is longer for the embedded model because there are 68 layers of films, for each of which at least 200 digital filters are used. The large number of digital filters used may also take up large memory storage.

Table 4-6 Comparison between the conventional TLM model and the embedded model for the FBG structure

Model	Mesh size (nm)	Number of nodes	Number of time steps	Run time (s) *
Conventional TLM	1	14500	1×10^6	180
Embedded model	10	300	1×10^5	450

(* the run time is based on a PC with an Intel Core 2 Duo CPU 3GHz processor and 4GB memory)

In this example, there is no saving in the run time and total memory storage for the embedded model due to the large number of layers, but a relative large mesh size is used, resulting in a saving in the number of time steps.

4.5. Conclusions

In this chapter, the frequency responses of lossy, anisotropic and lossless thin films were investigated using the embedded thin film model proposed in Chapter 3. A variety of applications was studied, such as CFC panels and a titanium panel for EMC, and AR coatings and FBG for photonics.

For lossy materials, CFC panels and titanium panel were used as examples. Both single and multiple layer CFC panels were studied using the embedded model. For a single layer CFC panel, the errors in reflection coefficients are less than 0.0006% while the errors in transmission coefficients are less than 0.8%. For multilayer CFC panel the errors in the reflection coefficients are less than 0.001% while the errors in the transmission coefficients are less than 1.5%. As further applications, the shielding effectiveness of CFC panels was also discussed. It was shown that thicker panels with higher conductivity provide better shielding effectiveness. For titanium panels, the errors in the reflection coefficients are less than 0.00003% while the errors in its transmission coefficients are less than 0.4%. The high accuracy in the reflection coefficients is due to the requirement that the percentage errors in the transmission coefficients are less than 2%.

For lossless materials, antireflection coatings and fibre Bragg gratings were taken as examples to test the embedded thin film model. For a single layer AR coating in the visible spectrum, the errors in reflection coefficients compared with the analytical ones are less than 2% when N = 400. It was shown that the embedded thin film model has slow convergence in the case of lossless thin films with large electrical length. To alleviate this, the cotangent and cosecant expansions used were manipulated so that they converged faster at a desired frequency. By doing this, the number of terms needed to approximate the

infinite expansions is reduced by 20 times at a given frequency. However, the downside of this modified model is that it works well only for single layer films. For the fibre Bragg gratings, the transmission coefficients were calculated using the embedded model. The errors in FBG transmission coefficients are less than 0.2% in the desired wavelength range.

All examples considered proved the accuracy, stability and convergence of the embedded thin film model.

All models were compared against the conventional TLM method that requires discretisation of the panel. The embedded model shows great advantages over the conventional TLM method for lossy materials operating at microwave frequencies. Since a larger mesh size is used in the embedded model, considerable memory storage is saved and the number of time steps is reduced. However, in the case of a multi-layer stack with a large number of layers working in the optical frequency, the embedded model does not show much advantage over the conventional TLM method due to the fact that a large number of digital filters is needed.

The next two chapters will consider the embedded model in the two-dimensional (2D) TLM method, in which its applications in arbitrary excitations and curve structures will be elaborated.

References

[4.1] S. J. Orfanidis, “Electromangetic Waves and Antennas,” [Online]. Available: http://www.ece.rutgers.edu/~orfanidi/ewa/, 1996.

[4.2] K. C. Gupta, Microwaves. New Age international (p) Ltd., 1983.

[4.3] F. A. Benson and T. M. Benson, Fields, Waves and Transmission Lines. Chapman & Hall, 1991.

[4.4] M. S. Sarto, “A new model for the FDTD analysis of the shielding performances of thin composite structures,” IEEE Trans. Electromagn. Compat., vol. 41, no. 4, pp. 298–306, 1999.

[4.5] C. L. Holloway, M. S. Sarto, and M. Johansson, "Analyzing Carbon-Fiber Composite Materials With Equivalent-Layer Models," IEEE Trans. Electromagn. Compat., vol. 47, no. 4, pp. 833–844, 2005.

[4.6] M. Apr, M. D. Amore, K. Gigliotti, M. S. Sarto, S. Member, and V. Volpi, "Lightning indirect effects certification of a transport aircraft by numerical simulation," IEEE Trans. Electromagn. Compat., vol. 50, no. 3, pp. 513–523, 2008.

[4.7] M. Parise and M. S. Sarto, "Efficient formulation of high-order boundary conditions for the high-frequency modeling of multilayer composite slab," 2003 IEEE Symp. Electromagn. Compat. Symp. Rec. (Cat. No.03CH37446), vol. 2, pp. 753–758, 2003.

[4.8] S. Rea, D. Linton, E. Orr, and J. Mcconnell, "Electromagnetic Shielding Properties of Carbon Fibre Composites in Avionic Systems," Microw. Rev., vol. 11, no. 1, pp. 29–32, 2005.

[4.9] A. Mehdipour, C. W. Trueman, A. R. Sebak, and S. V. Hoa, "Carbon-fiber composite T-match folded bow-tie antenna for RFID applications," in 2009 IEEE Antennas and Propagation Society International Symposium, pp. 1–4, 2009.

[4.10] M. H. N. Alsadi, "Modelling of electromagnetic materials properties at microwave frequencies," PhD thesis, University of Nottingham, 2012.

[4.11] C. Christopoulos, The Transmission-Line Modeling Method TLM. IEEE Press, 1995.

[4.12] J. O. Smith, Introduction to Digital Filters with Audio Applications. W3K Publishing, 2007.

[4.13] M. Feliziani, F. Maradei, and G. Tribellini, "Field analysis of penetrable conductive shields by the finite-difference time-domain method with impedance network boundary conditions (INBCs)," IEEE Trans. Electromagn. Compat., vol. 41, no. 4, pp. 307–319, 1999.

[4.14] R. R. Boyer, "An overview on the use of titanium in the aerospace industry," Mater. Sci. Eng. A, vol. 213, no. 1–2, pp. 103–114, 1996.

[4.15] A. Vukovic, "Fourier transform analysis of optoelectronic components and circuits," PhD thesis, University of Nottingham, 2000.

[4.16] V. Janyani, "Modelling of dispersive and nonlinear materials for optoelectronics using TLM," PhD thesis, University of Nottingham, 2005.

[4.17] C. Giles, "Lightwave applications of fiber Bragg gratings," J. Light. Technol., vol. 15, no. 8, pp. 1391–1404, 1997.

[4.18] N. M. Litchinitser, B. J. Eggleton, and D. B. Patterson, “Fiber Bragg gratings for dispersion compensation in transmission: theoretical model and design criteria for nearly ideal pulse recompression,” J. Light. Technol., vol. 15, no. 8, pp. 1303–1313, 1997.

[4.19] T. Tamir, Integrated optics, 2nd ed. Springer, 1979.

[4.20] V. Janyani, J. D. Paul, A. Vukovic, T. M. Benson, and P. Sewell, “TLM modelling of nonlinear optical effects in fibre Bragg gratings,” IEE Proc. Optoelectron., vol. 151, no. 4, pp. 185-192, 2004.

5.Embedded Thin Film Model for Arbitrary Excitations in the Two-Dimensional TLM method

5.1. Overview

In this chapter, the embedded model developed in Chapter 3 is first applied to model the reflection and transmission from a thin film of infinite length at oblique incidence, in which the thin film is represented by a one-dimensional (1D) model embedded between two-dimensional (2D) TLM nodes. It is then extended to model a thin film of finite length subject to arbitrary excitations by using the plane wave decomposition theory. Its accuracy and convergence are verified using examples of infinitely long CFC panels excited at oblique incidence. Finally it is applied to model CFC panels of finite length with a point source excitation.

5.2. Analytical Method for Analysing Oblique Incidence onto a Thin Film

At oblique incidence, the reflection and transmission coefficients of the thin film can be calculated using the transfer matrix method or the even/odd mode method derived in section 4.2. However, the impedances in these methods should be replaced by transverse impedances [5.1] in the case of oblique incidence. Thus, the concept of transverse impedance at oblique incidence is introduced first.

When a plane wave is incident onto a thin film at an arbitrary angle, the discussion can be separated into two cases [5.1]: polarisation with the electric field normal to the plane of incidence, referred to as the transverse electric (TE) polarisation and polarisation with the electric field in the plane of incidence,

referred to as the transverse magnetic (TM) polarisation. Other cases may be considered as a superposition of these two.

Fig. 5-1 depicts a plane wave incident from free space onto a thin film at an angle of φ, and the subsequent reflection and transmission into free space, for (a) the TE and (b) the TM polarisations.

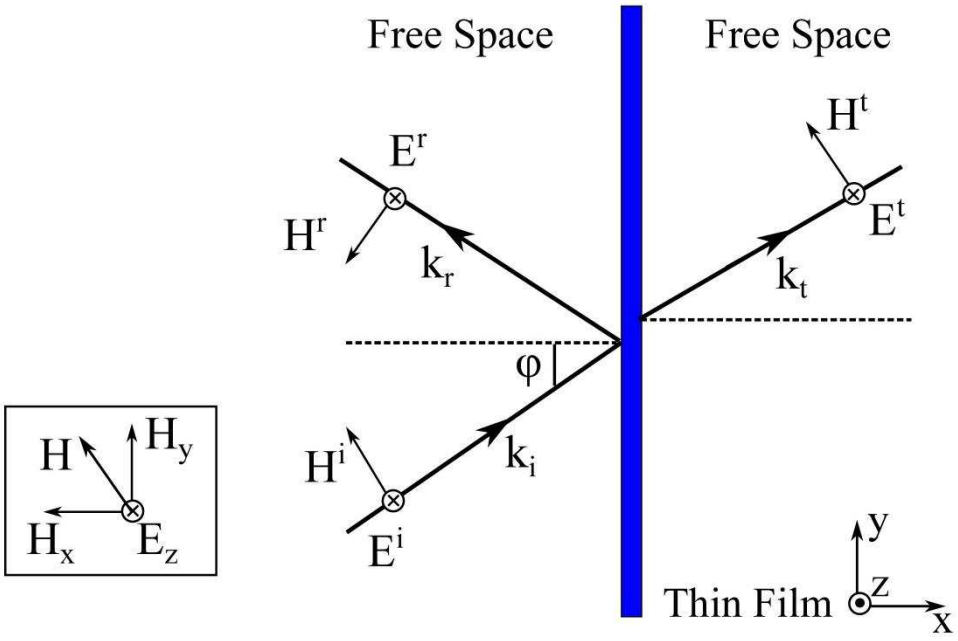

(a)

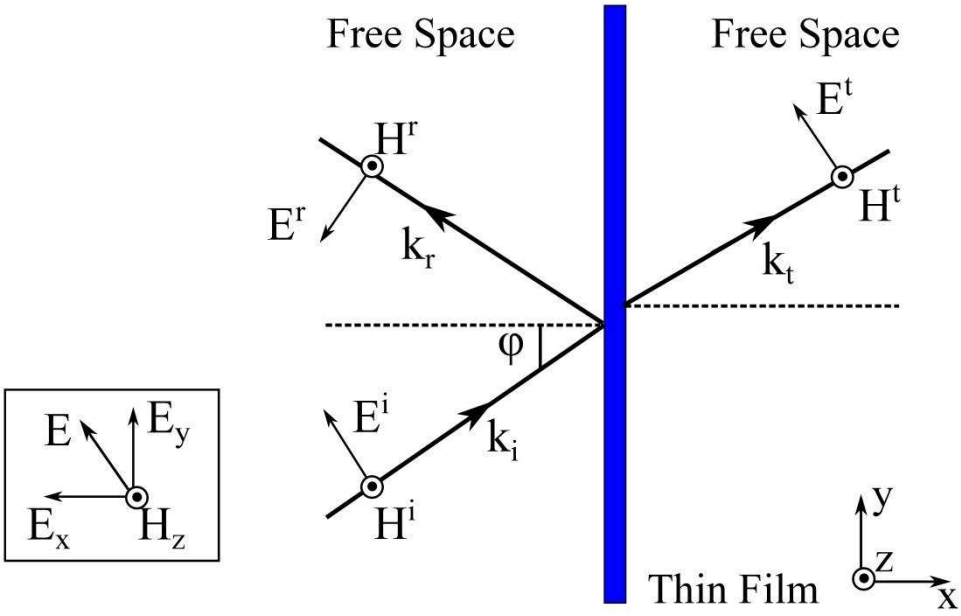

(b)

Fig. 5-1 Oblique incidence onto a thin film for (a) TE-polarised and (b) TM-polarised waves.

As in Fig. 5-1 (a), the existing field components in the TE-polarised wave are H_x, H_y and E_z, while the components in the TM-polarised wave are E_x, E_y and H_z as in Fig. 5-1 (b). The transverse impedance [5.1] is defined as the ratio of the electric to magnetic field components in the plane parallel to the boundary. For TE-polarised wave, the transverse impedance is calculated as E_z/H_y; for TM-polarised wave, the transverse impedance is calculated as E_y/H_z.

Considering that $H_y = Hcos\varphi$ for the TE polarisation and $E_y = Ecos\varphi$ for the TM polarisation, the transverse impedances in free space for both polarisations, Z_{TE} for TE-polarised wave and Z_{TM} for TM-polarised wave, are given in terms of the incident angle as [5.1],

$$\begin{aligned} Z_{TE} &= \frac{Z_0}{cos\varphi}, \\ Z_{TM} &= Z_0 cos\varphi, \end{aligned} \tag{5-1}$$

where Z_0 is the characteristic impedance of free space and φ is the incident angle with respect to the x-axis in free space.

The transverse impedance in a thin film can also be expressed in terms of the refraction angle with the same form as equation (5-1). However, if the thin film is composed of lossy materials, the wavenumber in the thin film is complex-valued and so the angle of refraction may also become complex-valued. In equation (5-1), the calculation of the transverse impedance needs to deal with the cosine of the angle, which is difficult to calculate for a complex-valued angle. To avoid the need for such a calculation, it is convenient to express the transverse impedance in terms of the wavenumber in the medium as follows [5.2].

In the case of oblique incidence, the wavenumber in the given medium k_i has two components k_{xi} and k_{yi}, whose relations are $k_{xi} = k_i cos\varphi_i$ with $cos\varphi_i = k_{xi}/k_i$ and $k_{yi} = k_i sin\varphi_i$.

Since $k_i = \omega\sqrt{\mu_i\varepsilon_i}$ and $Z_i = \sqrt{\mu_i/\varepsilon_i}$, then $k_i Z_i = \omega\mu_i$ and $k_i/Z_i = \omega\varepsilon_i$.

Therefore, the transverse impedance for both polarisations may be re-expressed in terms of the wavenumber in the medium as [5.2]:

$$Z_{iTE} = \frac{Z_i}{cos\varphi_i} = \frac{Z_i \cdot k_i}{k_{xi}} = \frac{\omega\mu_i}{k_{xi}},$$
$$Z_{iTM} = Z_i cos\varphi_i = \frac{Z_i \cdot k_{xi}}{k_i} = \frac{k_{xi}}{\omega\varepsilon_i}, \tag{5-2}$$

where Z_i is the characteristic impedance of the medium and φ_i is the propagation angle with respect to the x-axis in the medium.

After introducing the transverse impedance, the reflection and transmission coefficients of thin films are calculated using the transfer matrix method as follows.

As discussed in section 4.2, the panel is assumed to consist of M layers. At oblique incidence, the characteristic impedance of each layer in equation (4-1) is replaced by its transverse impedance given by equation (5-1) or (5-2). The reflection coefficients of each interface for both polarisations are,

$$\rho_i^{TE} = \frac{Z_{TE}^i - Z_{TE}^{i-1}}{Z_{TE}^i + Z_{TE}^{i-1}},$$
$$\rho_i^{TM} = \frac{Z_{TM}^i - Z_{TM}^{i-1}}{Z_{TM}^i + Z_{TM}^{i-1}}, \tag{5-3}$$

where $i = 1,2,\cdots,M+1$.

Therefore as in equation (4-6), the reflection coefficients of the thin film are given by,

$$R_i = \frac{E_{i-}}{E_{i+}} = \frac{\rho_i + R_{i+1}e^{-2jk_i d_i cos\varphi_i}}{1 + \rho_i R_{i+1} e^{-2jk_i d_i cos\varphi_i}}, \qquad i = M, M-1, \ldots\ldots, 1$$

and initialized by $R_M = \rho_{M+1}$.

5.3. Embedded Model for Thin Films at Arbitrary Excitations

In this section, the simple two-dimensional (2D) case of an infinitely long thin film with a plane wave impinging at oblique incidence is studied. Based on this simple case, a more complicated situation of a thin film of finite length subject to arbitrary excitations is also studied.

5.3.1. Infinitely Long Thin Film at Oblique Incidence

Consider a plane wave obliquely incident upon an infinitely long thin film at an angle φ, as shown in Fig. 5-2.

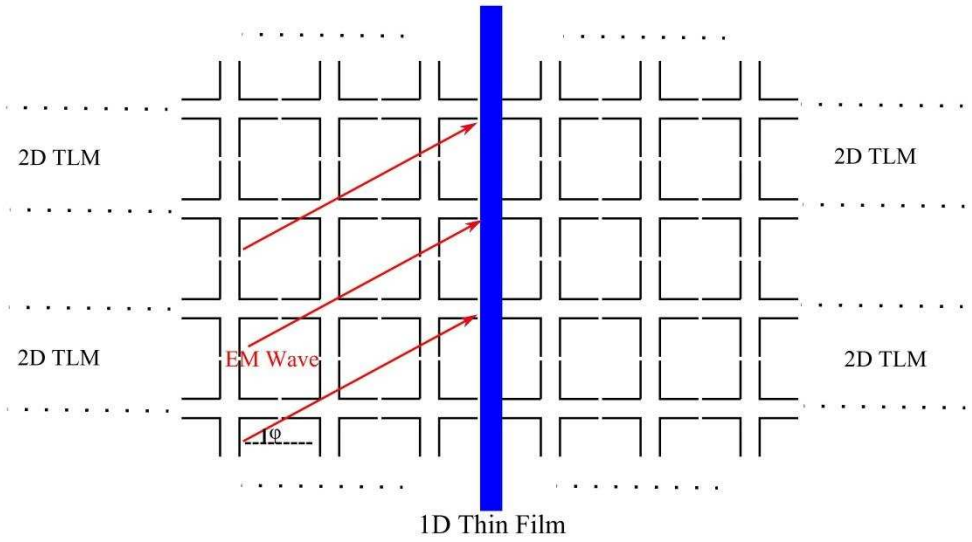

Fig. 5-2 A plane wave is incident upon a one-dimensional (1D) thin film model, embedded between 2D series nodes in the TLM, at oblique incidence.

In Fig. 5-2, the thin film is considered to be 1D and embedded in a 2D TLM mesh. As discussed in the previous section, at oblique incidence, the study of the reflection and transmission properties of the thin film is reduced to a 1D problem due to the introduction of the transverse impedance. Thus, the thin film can be seen as a section of 1D transmission line with the appropriate transverse impedance and then embedded between the adjacent 2D TLM nodes.

In order to embed the frequency responses of the thin film at oblique incidence into the time domain 2D TLM algorithm, the same technique can be used as was discussed for the normal incidence case in Chapter 3. Assume the infinitely long thin film is placed between the nodes (n_x, n_y) and $(n_x + 1, n_y)$, where n_x and n_y are the indices of the TLM node along the x and y axis, respectively. For each pair of nodes (n_x, n_y) and $(n_x + 1, n_y)$ in the modelling space, the equation (2-31) for the node (n_x, n_y) and the equation (2-30) for the node $(n_x + 1, n_y)$ in the connection process are modified because of the embedding of the thin film; in Chapter 3, they were replaced by equations (3-9) and (3-10) for the normal incidence case. In the case of oblique incidence, the impedances in equations (3-9) and (3-10) should be changed to the corresponding transverse impedances. The details of the modification are now discussed for both TE and TM polarisations.

As shown in Fig. 5-1 (a), the field components for the TE polarised wave are H_x, H_y and E_z. Therefore, the background material is modelled using the 2D shunt TLM nodes, as shown in Chapter 2.

In the case of oblique incidence, y_1 and y_2 in equations (3-9) and (3-10) are corresponding to the characteristic admittances of the 2D shunt nodes on both sides of the film, which are given by,

$$y_1 = y_2 = \frac{1}{Z_{TL}} = \frac{1}{\sqrt{2}Z_0}. \tag{5-4}$$

The admittance of the thin film is replaced by its transverse admittance Y_{TE} for the case of oblique incidence, which can be expressed in terms of the wavenumber as,

$$Y_{TE} = \frac{1}{Z_{TE}} = \frac{k_{xm}}{\omega\mu_m}. \tag{5-5}$$

where k_{xm} is the x component of the wavenumber in the thin film, given by $k_{xm}^2 = k_m^2 - k_{ym}^2$.

According to the Snell's law,

$$k_{ym} = k_{yb} = k_b sin\varphi, \tag{5-6}$$

where k_b is the wavenumber in the background material and k_{yb} is the y component of the k_b, and φ is the incident angle with respect to the x axis.

Thus,

$$k_{xm}^2 = k_m^2 - k_{ym}^2 = k_m^2 - (k_b sin\varphi)^2. \tag{5-7}$$

Therefore, the square of the admittance of the thin film in equations (3-9) and (3-10) is written as,

$$Y_{TE}Y_{TE} = \frac{k_{xm}^2}{\omega^2\mu_m^2} = \frac{k_m^2 - (k_b sin\varphi)^2}{\omega^2\mu_m^2}. \tag{5-8}$$

Furthermore, the electrical length of the thin film, θ_{TE}, is replaced by,

$$\theta_{TE} = k_{xm}d = d\sqrt{k_m^2 - (k_b sin\varphi)^2}. \tag{5-9}$$

Finally, $jYcot\theta$ and $jYcsc\theta$ in equations (3-9) and (3-10) are expanded for the case of oblique incidence as

$$\begin{aligned} jY_{TE}cot\theta_{TE} &= jY_{TE}\left(\frac{1}{\theta_{TE}} + 2\theta_{TE}\sum_{k=1}^{N=\infty}\frac{1}{\theta_{TE}^2 - k^2\pi^2}\right), \\ jY_{TE}csc\theta_{TE} &= jY_{TE}\left(\frac{1}{\theta_{TE}} + 2\theta_{TE}\sum_{k=1}^{N=\infty}\frac{(-1)^k}{\theta_{TE}^2 - k^2\pi^2}\right). \end{aligned} \tag{5-10}$$

For the TM polarised wave, Fig. 5-1 (b) shows that the field components are E_x, E_y and H_z, so the background material is modelled using the 2D series nodes as shown in Chapter 2.

In order to embed the thin film into 2D TLM nodes for TM-polarised wave at oblique incidence, the modification of the equations (3-9) and (3-10) for the normal incidence is similar to that just described for the TE polarisation; the only difference is that the transverse admittance of the thin film is now replaced by,

$$Y_{TM} = \frac{1}{Z_{TM}} = \frac{\omega \varepsilon_m}{k_{xm}}. \tag{5-11}$$

After these modifications, similar procedures to those described for the normal incidence case in section 3.2 are followed in order to embed the thin film model into the TLM algorithm for the case of oblique incidence.

5.3.2. Thin Film of Finite Length with Arbitrary Excitations

Consider a thin film of finite length in the 2D space. An arbitrary source, for example a point source, excites the nodes in the space as shown in Fig. 5-3. When the waves hit the thin film, they are incident onto the thin film at many different angles. In such a case, the above embedded model for a fixed angle of incidence needs extending.

In this section, an embedded model for a thin film of finite length with arbitrary excitations is introduced, based on the plane wave decomposition theory [5.3].

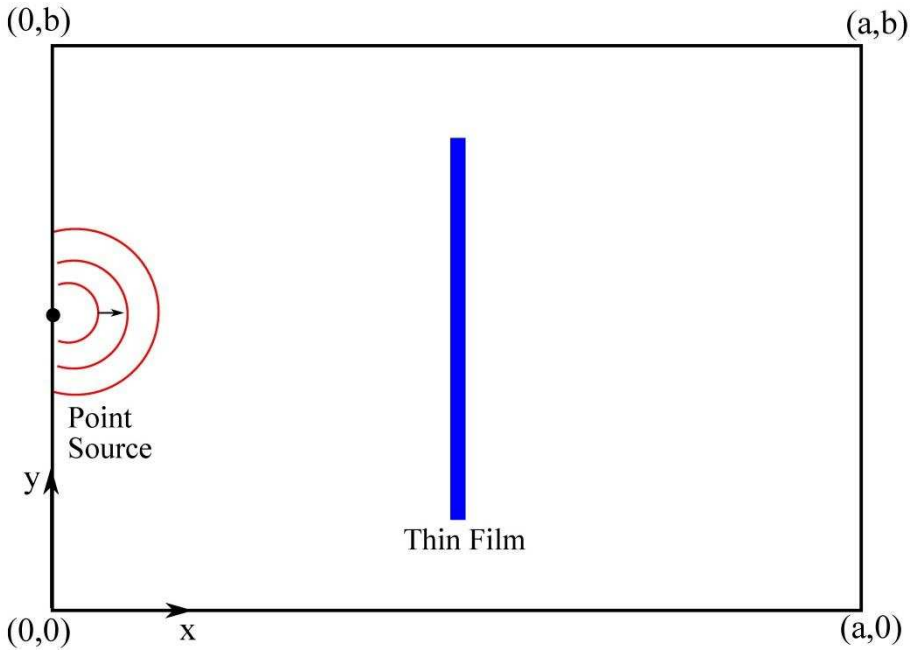

Fig. 5-3 The excitation from a point source hits a thin film of finite length.

The plane wave decomposition theory is introduced first.

The plane wave decomposition theory, also known as the angular spectrum representation of fields [5.3], says that an arbitrary field can be expanded as a series of plane waves and evanescent waves, which are physically solutions of Maxwell equations. In the following, the TE polarisation is considered to demonstrate the theory. The TM polarisation can be treated in a similar manner.

Assume that the electric field at x=0 is expressed as $E_z(0,y)$, which propagates towards the + x direction.

It is well known that a function in the time domain can be decomposed into a series of oscillations with different frequencies, different amplitudes and different phases using the Fourier transform [5.4]. Based on the same principle, the field $E_z(0,y)$ can be decomposed into a number of parts using a Fourier transform.

The Fourier transform of $E_z(0,y)$ can be expressed as,

$$E_z(0,y) = \frac{1}{2\pi}\int_{-\infty}^{\infty} \tilde{E}(s)e^{jsy}ds, \tag{5-12}$$

where $\tilde{E}(s)$ is the Fourier transform of $E_z(0,y)$, which is given by

$$\tilde{E}(s) = \int_{-\infty}^{\infty} E_z(0,y)e^{-jsy}dy, \tag{5-13}$$

where s is the Fourier transform variable.

If the field propagates in an infinite homogeneous space, the total field must satisfy the wave equation [5.1],

$$\left(\frac{d^2}{dx^2}+\frac{d^2}{dy^2}+k^2\right)E_z(x,y) = 0. \tag{5-14}$$

Therefore, it can be predicted that

$$E_z(x,y) = \frac{1}{2\pi}\int_{-\infty}^{\infty} \tilde{E}(s)e^{jsy}e^{-j\sqrt{k^2-s^2}x}ds, \tag{5-15}$$

since, if x=0, equation (5-15) becomes equation (5-12) and for each value of s, $e^{-j\sqrt{k^2-s^2}x}$ is the only x dependent term.

In order to gain some understanding, equation (5-15) can be written as

$$E_z(x,y) = \frac{1}{2\pi}\int_{-\infty}^{\infty} \tilde{E}(s)P(s;x,y)ds, \tag{5-16}$$

where $P(s;x,y) = e^{jsy}e^{-j\sqrt{k^2-s^2}x}$.

If $P(s;x,y)$ is the field of a plane wave propagating at an arbitrary direction, equation (5-15) expresses a general arbitrary field $E_z(x,y)$ as a superposition of the simpler fields $P(s;x,y)$, each of which has a weighting amplitude $\tilde{E}(s)$ and can propagate independently as each $P(s;x,y)$ satisfies the wave equation on its own.

In the following, it will be shown that $P(s;x,y)$ can represent a plane wave propagating in an arbitrary direction.

The definition of a plane wave heading along the x axis (Fig.5-4 (a)) is

$$E_z(plane\ wave) = P(s=0;x,y) = e^{-jkx}. \tag{5-17}$$

If a plane wave propagates at an angle φ to the x axis as shown in Fig.5-4 (b), the coordinate rotation principle is applied

$$\begin{pmatrix} x' \\ y' \end{pmatrix} = \begin{pmatrix} cos\varphi & -sin\varphi \\ sin\varphi & cos\varphi \end{pmatrix}\begin{pmatrix} x \\ y \end{pmatrix}, \tag{5-18}$$

so that

$$P(s=0;x',y') = e^{-jk(xcos\varphi - ysin\varphi)} = e^{-jkxcos\varphi}e^{jkysin\varphi}. \tag{5-19}$$

In equation (5-17), if $s = ksin\varphi$ is chosen, then $P(s=ksin\varphi;x,y) = e^{jsy}e^{-j\sqrt{k^2-s^2}x}$, which is the same as equation (5-19).

In other words, a plane wave propagating at an angle φ to the x axis has a field $P(s=ksin\varphi;x,y)$. Reversing the logic, a field $P(s=ksin\varphi;x,y)$ can be

interpreted as that of a plane wave heading at an angle $\varphi = \sin^{-1}(s/k)$ to the x axis.

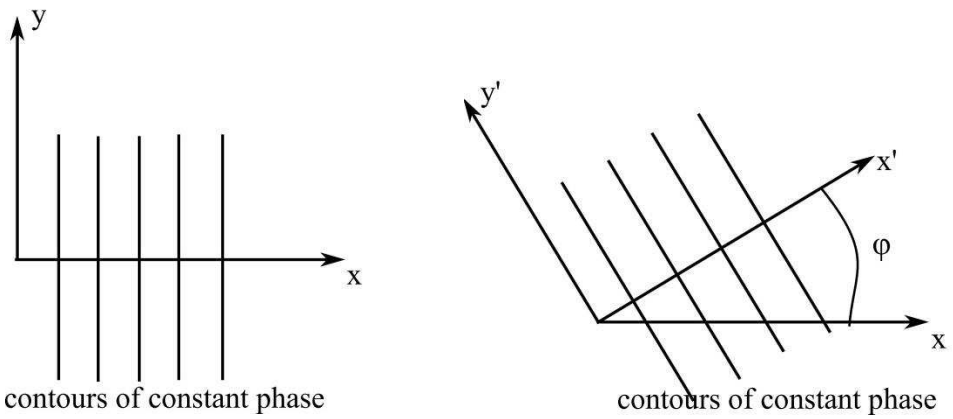

(a) (b)

Fig.5-4 (a) A plane wave propagates in the x direction (b) a plane wave propagates at an angle φ to the x axis.

However, it should be noted that if $k^2 < s^2$, $P(s = ksin\varphi; x, y) = e^{jsy}e^{\sqrt{s^2-k^2}x}$, which is an exponentially decaying function representing evanescent waves, where the angle φ is a complex number.

Therefore, equation (5-15) shows that a general field $E_z(x, y)$ can be expressed as a superposition of plane waves, each of which has a different angle of propagation φ and a different amplitude $\tilde{E}(s)$, and evanescent waves with decaying factors.

Based on the idea of the plane wave decomposition theory, an embedded model for a thin film of finite length with arbitrary excitations is developed.

According to the plane wave decomposition theory, the field incident from TLM nodes onto the film can be decomposed into a series of plane waves with different incident angles and evanescent waves with decaying factors. Each wave in the decomposition is independently incident upon the film at its own angle or decaying factor. At the excitation of each wave, the previous embedded model for the fixed incident angle can be applied to solve the reflection and transmission of the film. In the end, these fields are combined together and reflect back to the TLM nodes.

This is the first time that the plane wave decomposition theory is adopted for use in the TLM algorithm. Its implementation is given below for further clarification.

Assume the thin film, with length l, is placed between the nodes (n_x, n_y) and $(n_x + 1, n_y)$.

In the model, the voltages incident onto the thin film from both sides, ${V_L}^i(n_x, n_y)$ and ${V_R}^i(n_x + 1, n_y)$, can be obtained through the TLM algorithm. According to the plane wave decomposition theory, the incident voltages can be decomposed by using a Fourier transform into a superposition of waves, $V_L^i(\varphi)$ and $V_R^i(\varphi)$ as shown in Fig. 5-5, each of which is incident onto the thin film at a fixed angle φ_i (complex values represent evanescent waves). The response of the thin film to each of the waves can be obtained using the embedded model for the fixed angle of incidence. Thus the reflected voltages from the thin film, $V_L^r(\varphi)$ and $V_R^r(\varphi)$, are obtained for each incidence angle. In the end, an inverse Fourier transform is used to transform the reflected voltages from the angle domain, $V_L^r(\varphi)$ and $V_R^r(\varphi)$, to the space domain, ${V_L}^r(n_x, n_y)$ and ${V_R}^r(n_x + 1, n_y)$.

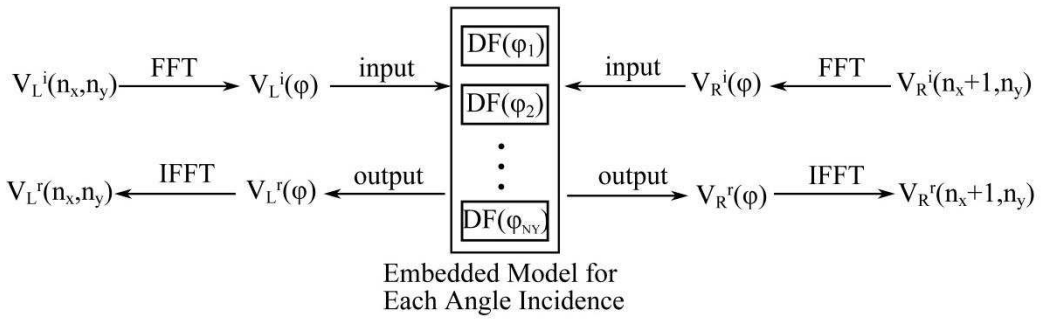

Fig. 5-5 The flow chart of the embedded thin film model for arbitrary excitations.

5.4. Plane Wave Excitations

At normal incidence, as discussed in Chapter 3, the periodic and matched boundary conditions were used to yield suitable problem boundary conditions

at the edge of the computational window in order to simulate a plane wave propagating in infinite space using the TLM method. However, those boundary conditions are not applicable for oblique incidence. In this section, the plane wave excitations are introduced within the TLM method to model a plane wave propagating in the infinite space at an arbitrary incident angle, φ. Furthermore, excitations for an infinitely long thin film are also described.

5.4.1. Excitations for Infinite Free Space

Consider a finite 2D TLM space in the x-y plane, $0 \leq x \leq a$ and $0 \leq y \leq b$ where a and b are dimensions in metres. In order to simulate a plane wave propagating in the infinite space, the excitations and boundaries should be properly set.

When a plane wave propagates in infinite free space, the electric and magnetic fields at each point can be evaluated using the plane wave propagation theory [5.1]. Thus, the fields at the boundaries of the finite region can be obtained and then converted to the voltages and currents in the TLM nodes, acting as excitations of the finite region.

In the following sub-sections, the plane wave excitations with TE polarisation and TM polarisation are elaborated separately.

5.4.1.1. TE-Polarised Wave Excitations

Consider a TE-polarised plane wave propagating in free space at an angle φ to the x axis, as shown in Fig. 5-6. The four nodes in Fig. 5-6 represent arbitrary shunt nodes on each of the four boundaries.

In Fig. 5-6, I_x, I_y and V_z are the currents and voltage at the given boundaries $(x, 0), (x, b), (0, y)$ and (a, y), respectively. They can be calculated as follows. Based on the plane wave propagation theory, it is assumed that

$$
\begin{aligned}
E_z &= -sin(\omega_0 t - (kcos\varphi \cdot x + ksin\varphi \cdot y)),\\
H_x = Hsin\varphi &= -y_0 sin\varphi \cdot sin(\omega_0 t - (kcos\varphi \cdot x + ksin\varphi \cdot y)),\\
H_y = Hcos\varphi &= y_0 cos\varphi \cdot sin(\omega_0 t - (kcos\varphi \cdot x + ksin\varphi \cdot y)),
\end{aligned}
\tag{5-20}
$$

where ω_0 is the angular frequency of the plane wave, y_0 is the admittance of free space and k is the wavenumber.

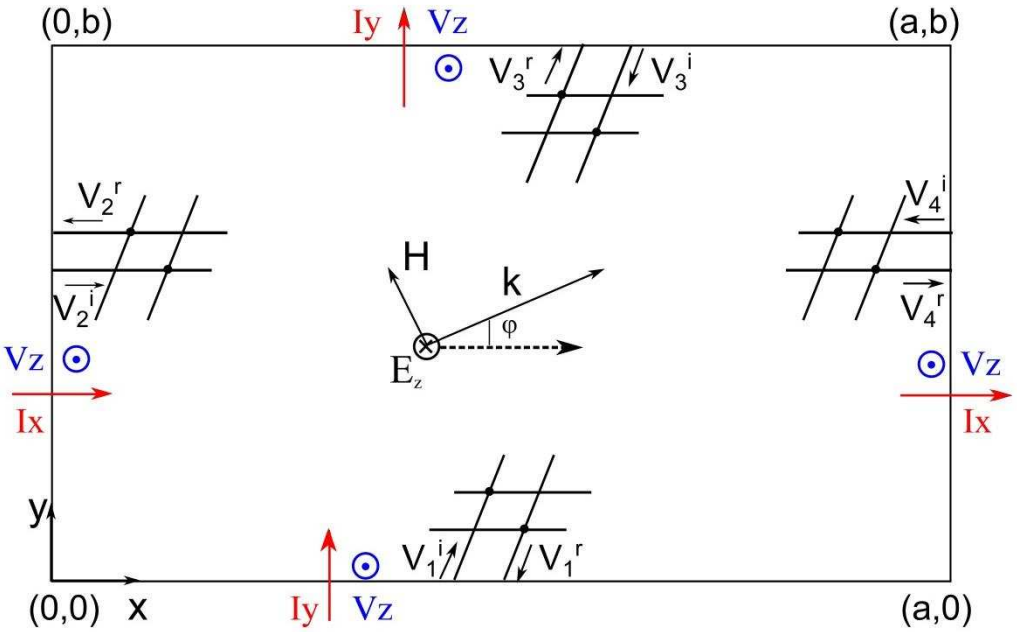

Fig. 5-6 A TE polarised plane wave propagates in the x-y plane at an angle φ to the x axis.

The corresponding voltage and currents at the boundaries of the 2D TLM space are given by [5.5]

$$
\begin{aligned}
V_z &= -E_z \cdot dl\,,\\
I_x = H_y \cdot dl\,, &\qquad I_y = -H_x \cdot dl\,,
\end{aligned}
\tag{5-21}
$$

where dl is the mesh size.

According to network theory [5.6], the incident and reflected voltages of the nodes at the boundaries can be calculated from the known currents and voltages, i.e. I_x, I_y and V_z.

For the boundary $y = 0$, the following relations exist,

$$\begin{cases} V_1^i + V_1^r = V_z \\ y_{TL}\left(V_1^i - V_1^r\right) = I_y \end{cases}. \tag{5-22}$$

Substituting equation (5-21) into equation (5-22), the incident and reflected voltages at the boundary $y = 0$ are calculated as,

$$\begin{cases} V_1^i = \dfrac{1}{2y_{TL}}(y_{TL} + y_0 sin\varphi)V_z \\ V_1^r = \dfrac{1}{2y_{TL}}(y_{TL} - y_0 sin\varphi)V_z \end{cases}. \tag{5-23}$$

Similarly, for the boundary $x = 0$,

$$\begin{cases} V_2^i = \dfrac{1}{2y_{TL}}(y_{TL} + y_0 cos\varphi)V_z \\ V_2^r = \dfrac{1}{2y_{TL}}(y_{TL} - y_0 cos\varphi)V_z \end{cases}. \tag{5-24}$$

For the boundary $y = b$,

$$\begin{cases} V_3^i = \dfrac{1}{2y_{TL}}(y_{TL} - y_0 sin\varphi)V_z \\ V_3^r = \dfrac{1}{2y_{TL}}(y_{TL} + y_0 sin\varphi)V_z \end{cases}. \tag{5-25}$$

For the boundary $x = a$,

$$\begin{cases} V_4^i = \dfrac{1}{2y_{TL}}(y_{TL} - y_0 cos\varphi)V_z \\ V_4^r = \dfrac{1}{2y_{TL}}(y_{TL} + y_0 cos\varphi)V_z \end{cases}. \tag{5-26}$$

Therefore, the incident and reflected voltages at the four boundaries of the 2D TLM region are calculated, which are the excitations of the whole region.

After the derivation of the excitations of the finite region, the boundary conditions are discussed as follows.

The voltages in a shunt node at the boundary may be expressed as in Fig. 5-7, where V_{TLM}^i and V_{TLM}^r are the incident and reflected voltages from TLM nodes,

respectively, and V^i and V^r are the plane wave excitations obtained from the above derivations.

From Fig. 5-7, it can be seen that, except for the excitation, matched boundaries [5.5] should also be set at the four boundaries in order to simulate the infinite space.

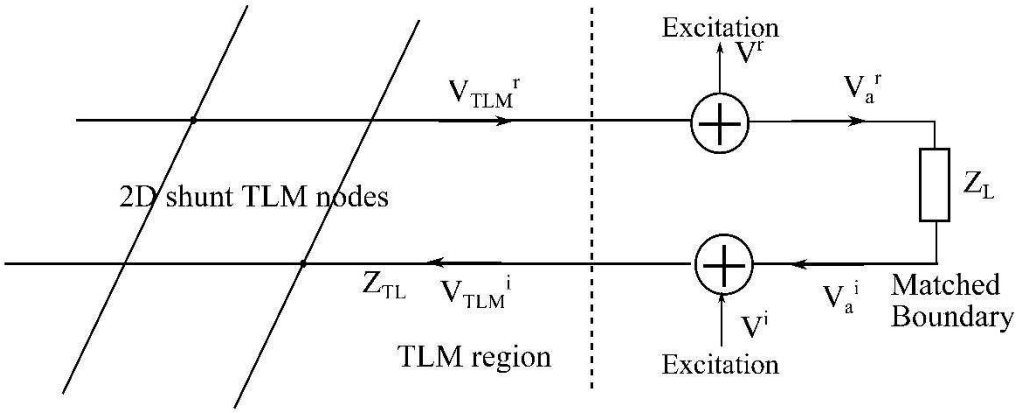

Fig. 5-7 The excitations in a node at the boundary.

From equation (5-1), the load impedance $Z_L = Z_0/cos\varphi$, so the reflection coefficient from the boundary is expressed as,

$$R = \frac{Z_L - Z_{TL}}{Z_L + Z_{TL}}. \tag{5-27}$$

Therefore, the incident voltage for the TLM nodes can be obtained as

$$V_{TLM}^i = V^i + R \cdot (V_{TLM}^r - V^r). \tag{5-28}$$

5.4.1.2. TM-Polarised Wave Excitations

Consider a TM-polarised plane wave propagating in the x-y plane at an angle φ to the x axis as shown in Fig. 5-8.

As shown in Fig. 5-8, the voltages, V_x and V_y, and the current I_z on the boundaries are the excitations of the region. They are calculated as follows.

According to the plane wave propagation theory, it is assumed that

$$E = sin(\omega t - kxcos\varphi - kysin\varphi), \tag{5-29}$$

then

$$E_x = -Esin\varphi, \qquad E_y = Ecos\varphi, \qquad H_z = y_0 E. \tag{5-30}$$

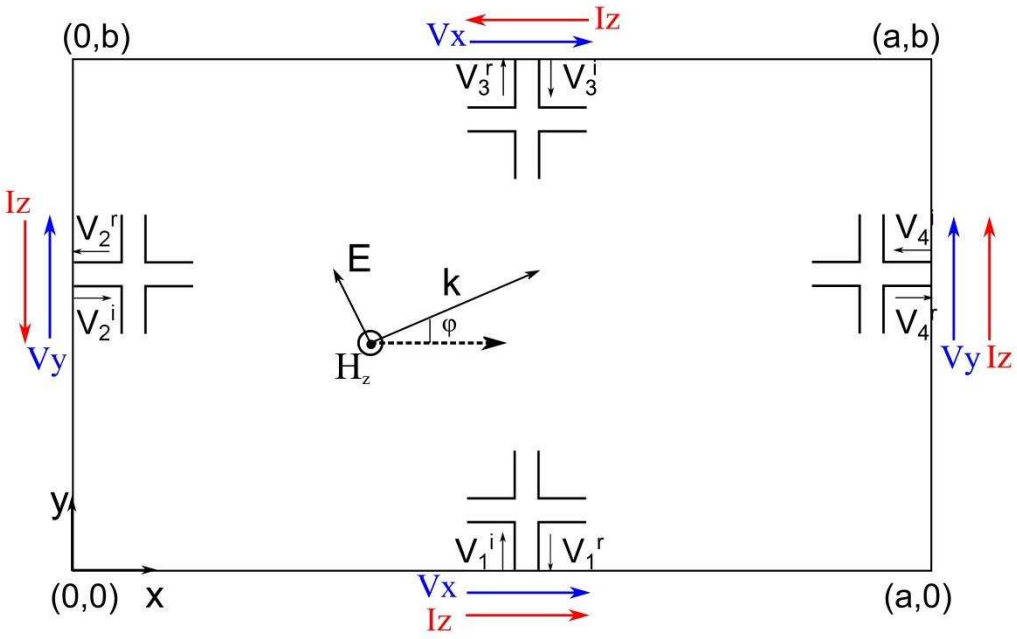

Fig. 5-8 A plane wave with TM polarisation propagates in the x-y plane at an angle φ to the x axis.

According to these fields, the voltages and currents at the boundaries are given as follows [5.5],

$$V_x = -E_x \cdot dl, \qquad V_y = -E_y \cdot dl, \qquad I_z = H_z \cdot dl. \tag{5-31}$$

Therefore, the incident and reflected voltages at the boundaries can be calculated based on the network theory as in the TE polarisation case.

For the boundary $y = 0$,

$$\begin{cases} V_1^i + V_1^r = V_x \\ y_{TL}\left(V_1^i - V_1^r\right) = I_z \end{cases}, \tag{5-32}$$

then

$$\begin{cases} V_1^i = \dfrac{dl}{2y_{TL}}(y_{TL}sin\varphi + y_0)E \\ V_1^r = \dfrac{dl}{2y_{TL}}(y_{TL}sin\varphi - y_0)E \end{cases}. \tag{5-33}$$

For the boundary $x = 0$,

$$\begin{cases} V_2^i = \dfrac{dl}{2y_{TL}}(-y_{TL}cos\varphi - y_0)E \\ V_2^r = \dfrac{dl}{2y_{TL}}(-y_{TL}cos\varphi + y_0)E \end{cases}. \tag{5-34}$$

For the boundary $y = b$,

$$\begin{cases} V_3^i = \dfrac{dl}{2y_{TL}}(y_{TL}sin\varphi - y_0)E \\ V_3^r = \dfrac{dl}{2y_{TL}}(y_{TL}sin\varphi + y_0)E \end{cases}. \tag{5-35}$$

For the boundary $x = a$,

$$\begin{cases} V_4^i = \dfrac{dl}{2y_{TL}}(-y_{TL}cos\varphi + y_0)E \\ V_4^r = \dfrac{dl}{2y_{TL}}(-y_{TL}cos\varphi - y_0)E \end{cases}. \tag{5-36}$$

Finally, the incident and reflected voltages at the boundary nodes are obtained, which are the excitations of the region.

The matched boundary conditions should also be used to simulate the infinite space, which can be expressed as equation (5-28). The difference from the TE case is that the load impedance $Z_L = Z_0 \cdot cos\varphi$.

5.4.2. Excitations for Infinitely Long Thin Film

When an infinitely long thin film is placed in free space, the distribution of the electromagnetic fields in the space is changed. In this section, the field distribution in the space is shown for TE- and TM- polarised wave excitations.

The same procedure as that introduced in section 5.4.1 for the infinite free space can be used to set the excitations of the TLM space.

As shown in Fig.5-9 for the case of the TE polarised wave, a thin film is positioned at $x = a/2$, which separates the space into the left and right parts. The plane wave is incident onto the film from the left at an angle φ to the x axis.

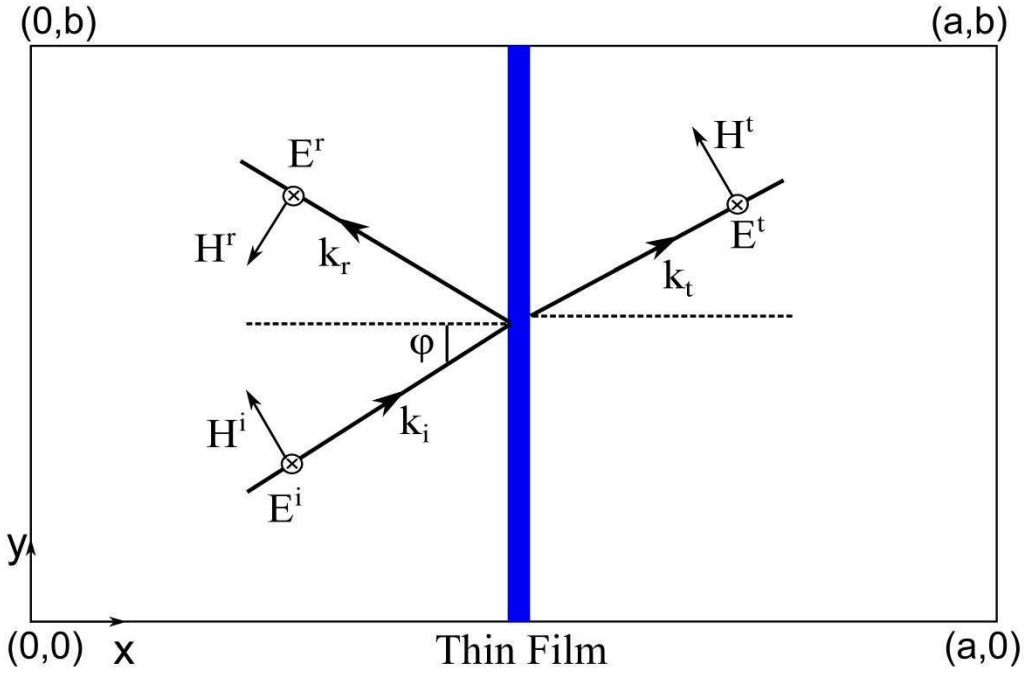

Fig.5-9 A plane wave with TE polarisation is obliquely incident onto a thin film at an angle φ in a 2D TLM space.

For the left part, the fields are composed of the incident wave and the reflected wave; for the right part, the fields are composed of the transmitted wave only.

According to plane wave propagation theory, it is assumed that

$$E^i = -sin(\omega_0 t - k \cdot xcos\varphi - k \cdot ysin\varphi), \qquad H^i = y_0 \cdot E^i. \tag{5-37}$$

The reflected fields and the transmitted fields are then expressed as

$$E^r = R \cdot E^i, \quad H^r = y_0 \cdot E^r, \qquad E^t = T \cdot E^i, \quad H^t = y_0 \cdot E^t, \tag{5-38}$$

where R and T are the reflection and transmission coefficients of the thin film at the angular frequency ω_0, respectively.

Therefore, the fields in the left part are expressed as

$$E_{zL} = E^i + E^r,$$
$$H_{xL} = H^i sin\varphi + H^r sin\varphi, \qquad H_{yL} = -H^i cos\varphi + H^r cos\varphi. \tag{5-39}$$

The fields in the right part are expressed as

$$E_{zR} = E^t, \qquad H_{xR} = H^t \sin\varphi, \qquad H_{yR} = -H^t cos\varphi. \tag{5-40}$$

For the TM-polarised wave, the field distribution can be calculated similarly. Fig.5-10 shows a thin film positioned at $x = a/2$. The TM polarised wave is obliquely incident onto the thin film from the left at an angle φ.

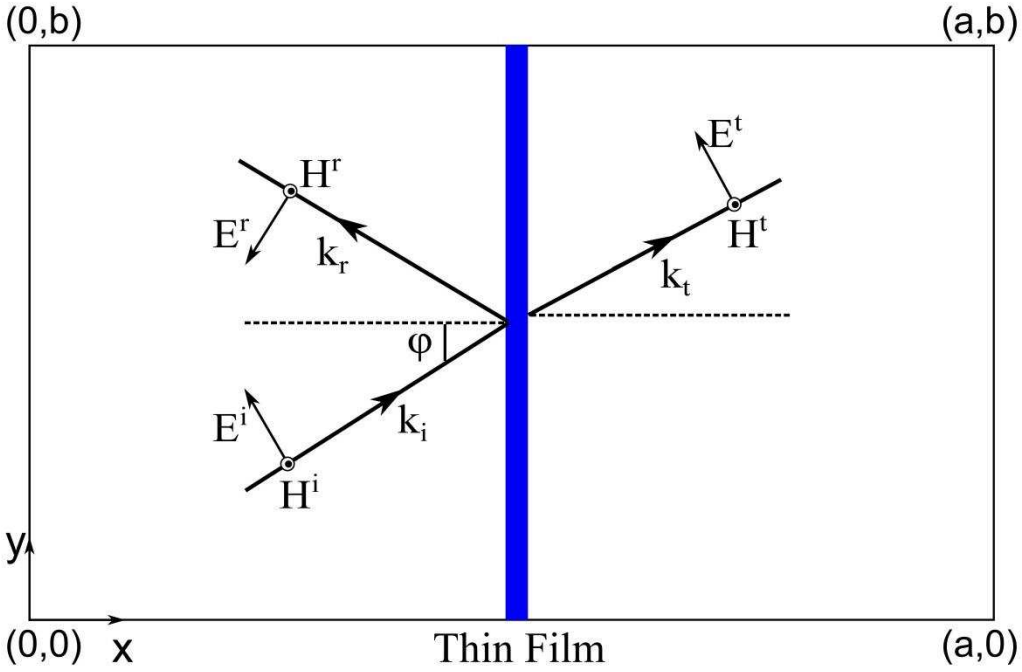

Fig.5-10 A TM polarised plane wave is obliquely incident to a thin film at an angle φ in a 2D TLM space.

According to the plane wave propagation theory, it is assumed that

$$E^i = sin(\omega_0 t - kxcos\varphi - kysin\varphi),$$
$$H^i = y_0 \cdot E^i. \tag{5-41}$$

The reflected and transmitted fields are expressed as in equation (5-38). Therefore, the fields in the left part are obtained as

$$E_{xL} = -E^i \cdot sin\varphi - E^r \cdot sin\varphi, \qquad E_{yL} = E^i \cdot cos\varphi - E^r \cdot cos\varphi,$$
$$H_{zL} = H^i + H^r. \tag{5-42}$$

The fields in the right part are obtained as

$$E_{xR} = -E^t \cdot sin\varphi, \qquad E_{yR} = E^t \cdot cos\varphi, \qquad H_{zR} = H^t. \tag{5-43}$$

According to the calculated distribution of the fields in the space, the excitations of the TLM space can be evaluated using the procedure described in section 5.4.1 for the infinite free space.

5.5. Validations

In this section, the embedded model for arbitrary excitations is validated using infinitely long CFC panels. A TE- or TM- polarised plane wave is obliquely incident onto the panel and its reflection and transmission coefficients are calculated using the embedded model and compared to the analytical results.

In order to examine its convergence and accuracy over a wide frequency range and for various incident angles, the reflection and transmission coefficients of the infinitely long CFC at 30° incidence are first calculated over the frequency range from 0 to 1 GHz. Reflection and transmission coefficients are then calculated at 1 GHz for several angles of incidence.

The parameters of the CFC panel were chosen as in section 4.3.1: effective permittivity $\varepsilon_r = 2$, conductivity $\sigma_e = 10^4$ S/m and thickness $d = 1$ mm.

Plane wave excitations and matched boundaries were used to represent the infinite space.

Percentage errors are used in this section for comparison purposes, which are defined using equation (4-21). The size of the whole 2D problem space was assumed to be 0.3 m $\times$ 0.394 m.

5.5.1. TE-Polarised Wave

The embedded model for an arbitrary excitation is firstly used to model the TE-polarised plane wave obliquely incident onto an infinitely long CFC panel at an angle of 30°.

In this example, 2D shunt nodes were used to model free space. The CFC panel was placed in the middle of the computational space, at $x = 0.15$ m.

In order to calculate the reflection and transmission coefficients of the CFC panel, two models were built. First, the plane wave propagating into free space at 30° to the x-axis was modelled in the 2D TLM space. The voltages at the nodal line $n_x = 0.15/dl$, where dl is the mesh size, were calculated as incident voltages V_{in}. The infinite CFC panel in free space was then modelled using the TE-polarised wave excitation, as described in section 5.4.2. The voltages at the nodal lines $n_x = 0.15/dl$ and $n_x = \frac{0.15}{dl} + 1$ were calculated as V_R and V_T, respectively. Finally, the reflection and transmission coefficients were obtained as $R = (V_R - V_{in})/V_{in}$ and $T = V_T/V_{in}$, respectively.

In order to evaluate the appropriate mesh size dl, the reflection and transmission coefficients of the CFC panel were calculated using different mesh sizes and compared to the analytical results. The TE-polarised wave has an assumed frequency of 1 GHz and is obliquely incident upon the panel at 30° to the x axis. Fig. 5-11 shows the percentage errors in the reflection and transmission coefficients of the CFC panel, calculated using the embedded model, against the mesh size, represented by λ/dl. The comparisons were made against results from the analytical method. It can be seen that as the mesh

size decreases, the percentage errors for both reflection and transmission coefficients become very small for sufficiently small dl, i.e. large λ/dl. It is noticed that when the mesh size $dl = 6$ mm ($\frac{\lambda}{dl} = 50$), the errors in the reflection and transmission coefficients are below 1%.

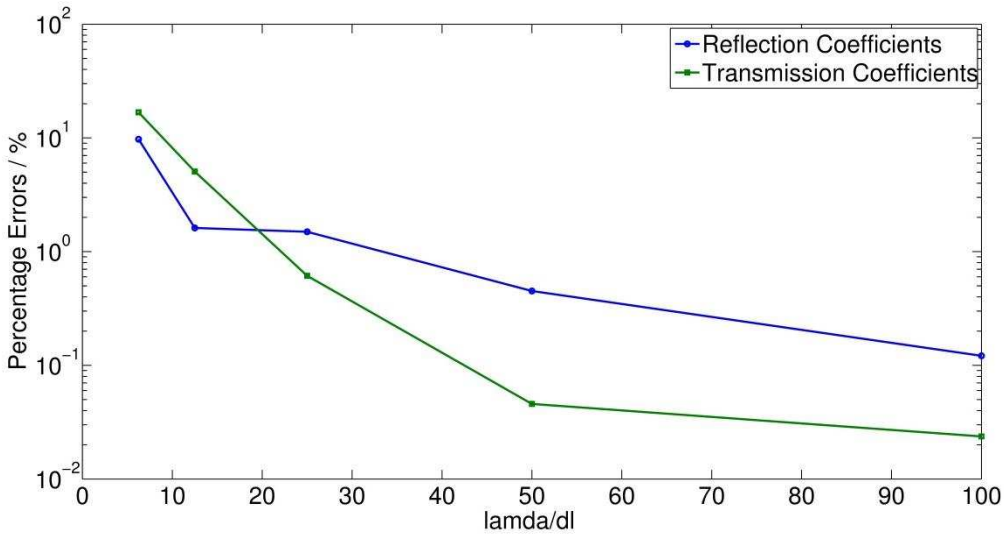

Fig. 5-11 Percentage errors in the reflection coefficients and transmission coefficients of the CFC panels calculated using the embedded model and the analytical method against λ/dl when the TE-polarised wave at 1 GHz is obliquely incident onto the panel at 30°.

In order to get good accuracy, the embedded model with a mesh size of 6 mm was used to calculate the reflection and transmission coefficients of the CFC panel in the frequency range from 0 to 1 GHz. Fig. 5-12 (a) shows the reflection coefficients of the CFC panel calculated using the embedded model for N = 10, 20 and 100 and the analytical method, when the TE-polarised wave is obliquely incident onto the panel at 30°. It can be seen that the reflection coefficients calculated using the embedded model have a small difference (around 0.02 dB) with those calculated using the analytical method in the frequency range from 0 to 1 GHz, although a gap between the numerical results and analytical results is observed in the figure. To clarify this, Fig. 5-12 (b) shows the percentage errors in the reflection coefficients calculated using the embedded model and the analytical method. Fig. 5-12 (b) indicates that the errors are very small and within 0.258% in the frequency range from 0 to 1 GHz.

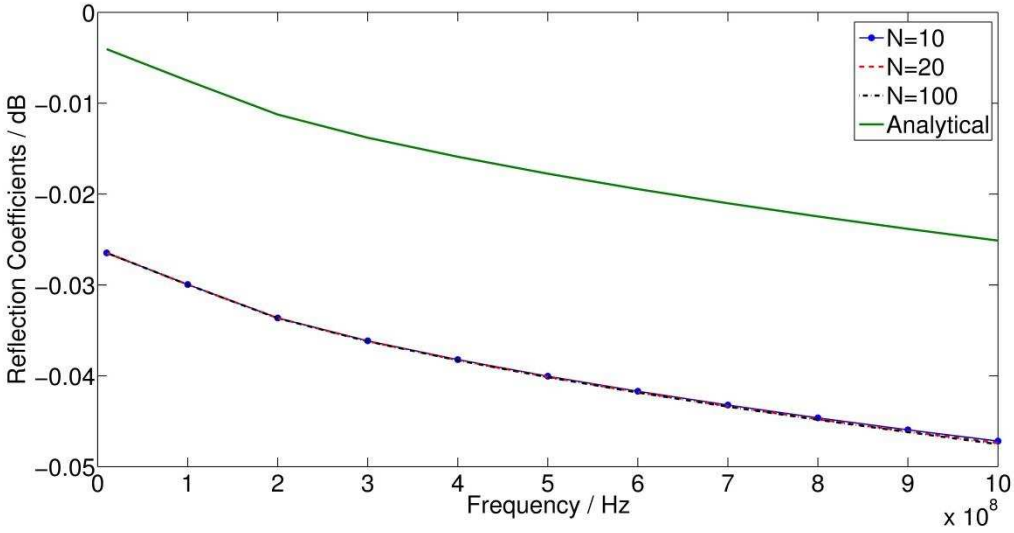

(a)

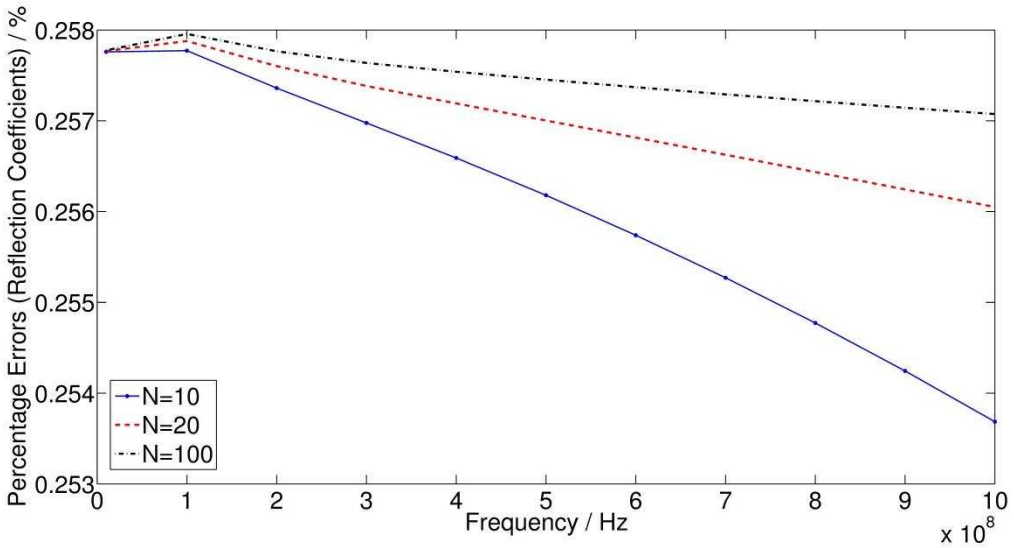

(b)

Fig. 5-12 (a) The reflection coefficients of the CFC panel when the TE-polarised plane wave is obliquely incident onto the panel at 30° and (b) the percentage errors in the reflection coefficients calculated using the embedded model with different N (N = 10, 20 and 100) compared to the analytical results. The TLM mesh size $dl = 6$ mm.

Fig. 5-13 (a) shows the transmission coefficients of the CFC panel calculated using the embedded model for N = 10, 20 and 100 and the analytical method, when the TE polarised wave is obliquely incident onto the panel at 30°. When N = 100, the numerical results are very close to the analytical ones in the frequency range from 0 to 1 GHz. The percentage errors in the transmission

coefficients are shown in Fig. 5-13(b), from which it can be seen that when N = 100 the errors are within 1% in the frequency range from 0 to 1 GHz.

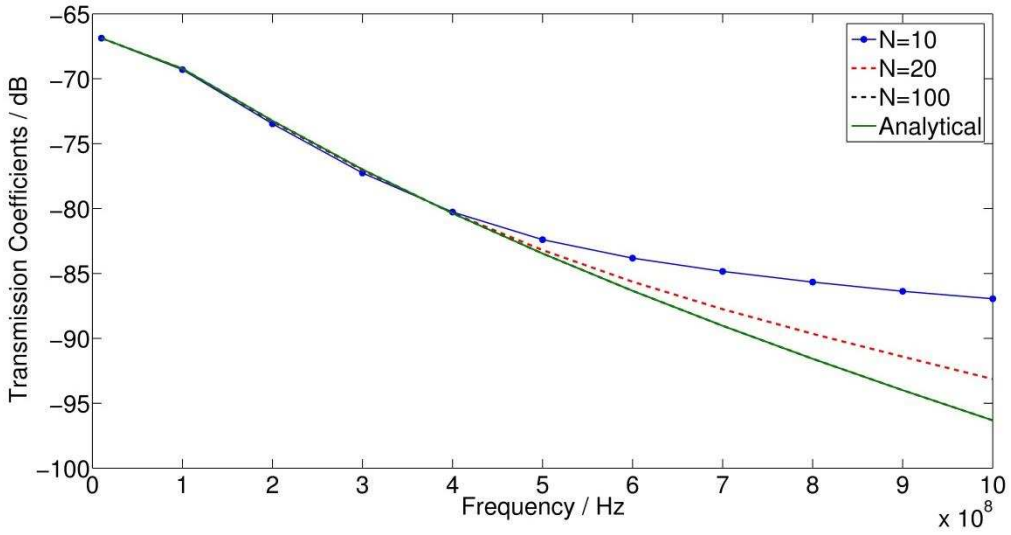

(a)

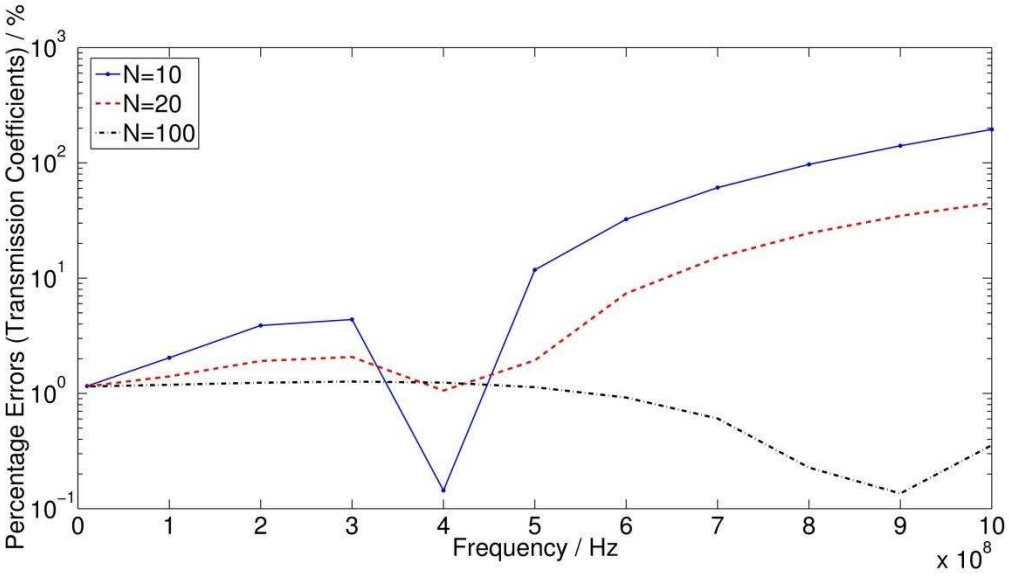

(b)

Fig. 5-13 (a) The transmission coefficients of the CFC panel when the TE-polarised plane wave is obliquely incident onto the panel at 30°(b) the percentage errors in the transmission coefficients calculated using the embedded model with different N (N = 10, 20 and 100) compared to the analytical results. The TLM mesh size $dl = 6$ mm.

From these results, it can be concluded that very good agreement between the results from the embedded model and the analytical method is achieved over a wide frequency range at one fixed angle of incidence.

If a conventional TLM method is used to simulate the CFC panel at oblique incidence, a much smaller mesh size should be used. According to the results from Chapter 4, the mesh size should be chosen as 0.025 mm to account for the existence of the 1 mm CFC panel. In such case, the number of nodes used in the simulation would be 12000×15360 to model the space with the size of $0.3\ \text{m} \times 0.384\ \text{m}$, i.e. 120 times higher in each direction than used in the embedded model (100×128). To store these nodes, the memory required would be very large. At the same time, the run time needed for the conventional TLM method would be much longer. From this point of view, the use of the proposed embedded model in the 2D TLM method reduces the usage of memory and run time significantly.

To further validate the accuracy of the embedded model, the reflection and transmission coefficients of the CFC panel at different angles of incidence are calculated at 1 GHz. Several angles of incident were selected from 0° (normal incidence) to approaching 90° (grazing incidence) as examples. The mesh size here was chosen to be 3 mm in order to get good accuracy for all the angles.

Fig. 5-14 (a) shows the reflection coefficients of the CFC panel at 1 GHz calculated using the embedded model for N = 10, 20 and 100 and the analytical method against the incident angle. It is seen that the numerical results have small differences with the analytical ones and they oscillate on both sides of the analytical results for different angles. In order to observe the differences, Fig. 5-14 (b) shows the percentage errors in the reflection coefficients calculated using the embedded model when compared to those from the analytical method. The errors are within 0.22% for the incident angles from 0° to 85°.

It is noticed that at 84° of incidence, the reflection coefficient is larger than 1. Although the error is small (around 0.2%), it is not practical. This can be improved by using a smaller mesh size. Fig.5-15 shows the reflection coefficients of the CFC panel against the incident angle calculated using the embedded model for different discretisations. It can be seen that as the mesh size decreases, the errors in the reflection coefficients for different angles of

incidence become smaller. For the large angle of incidence and for fine discretisation the reflection coefficient is less than 1.

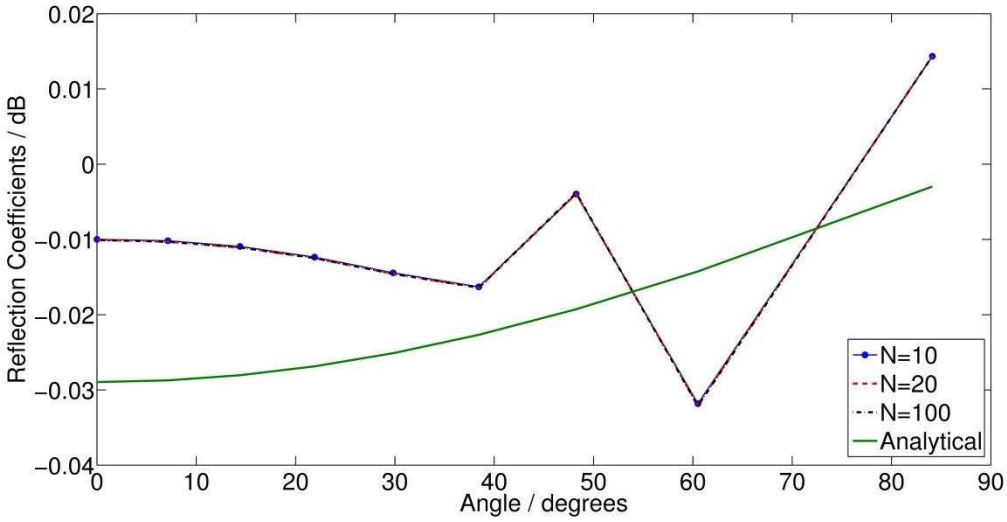

(a)

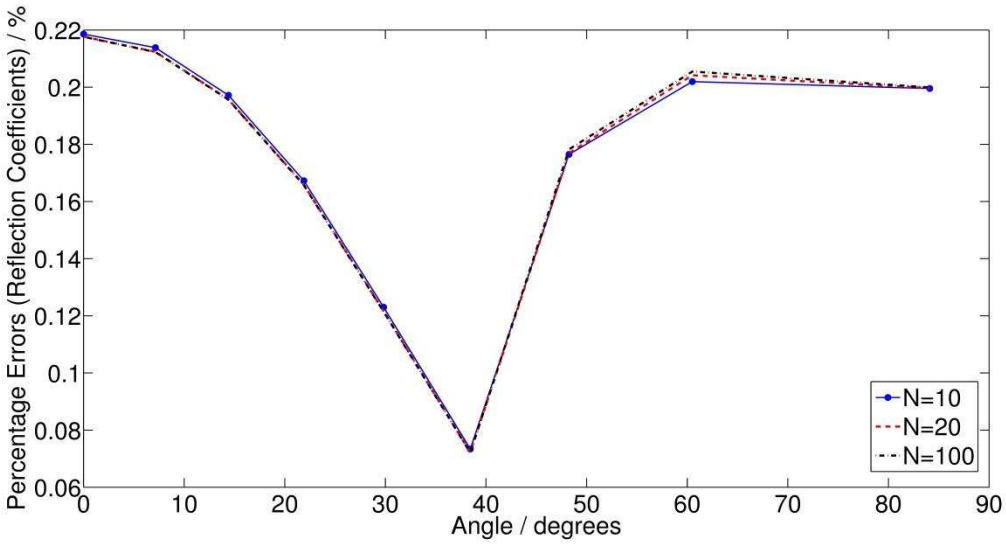

(b)

Fig. 5-14 (a) The reflection coefficients of the thin CFC panel against the incident angle φ at the frequency $f_0 = 1$ GHz for TE polarisation (b) the percentage errors in the reflection coefficients calculated using the embedded model for N = 10, 20 and 100 compared to the analytical results against the angle of incident. The TLM mesh size $dl = 3$ mm.

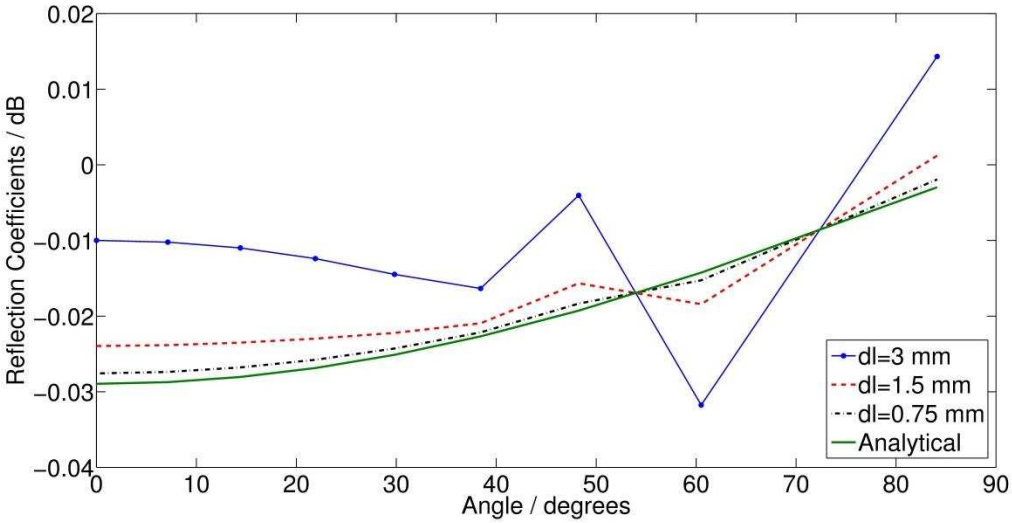

Fig.5-15 The reflection coefficients of the CFC panel against the angle of incidence at the frequency $f_0 = 1$ GHz for TE polarisation obtained using the embedded model and different discretisation dl.

Fig. 5-16 (a) shows the transmission coefficients of the CFC panel at 1GHz using the embedded model for N = 10, 20 and 100 and the analytical method against the incident angle. When N = 100, the numerical results converge to the analytical results. Fig. 5-16 (b) shows the percentage errors in the transmission coefficients calculating using the embedded model as a function of the incident angle. When N = 100 the errors are within 2% for the incident angles less than 40° and within 10% from 40° to 85°. Considering that the transmission coefficients at larger angles are very small, i.e. less than -95 dB, 10% error is deemed an acceptable error.

Fig. 5-14 (a) and Fig. 5-16 (a) show that, for the TE-polarised wave, as the angle of incident increases the reflection coefficients of the panel become bigger, while its transmission coefficients become smaller.

In summary, the results calculated using the embedded model show very good agreement with the analytical results. Thus the convergence and accuracy of the embedded model for the TE-polarised wave with arbitrary excitations is verified over a wide frequency range and for various angles of incidence.

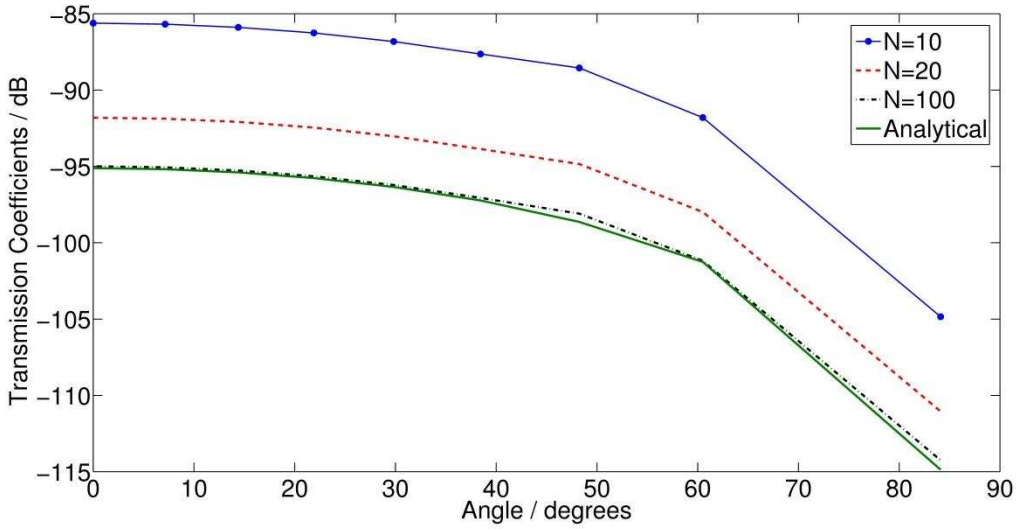

(a)

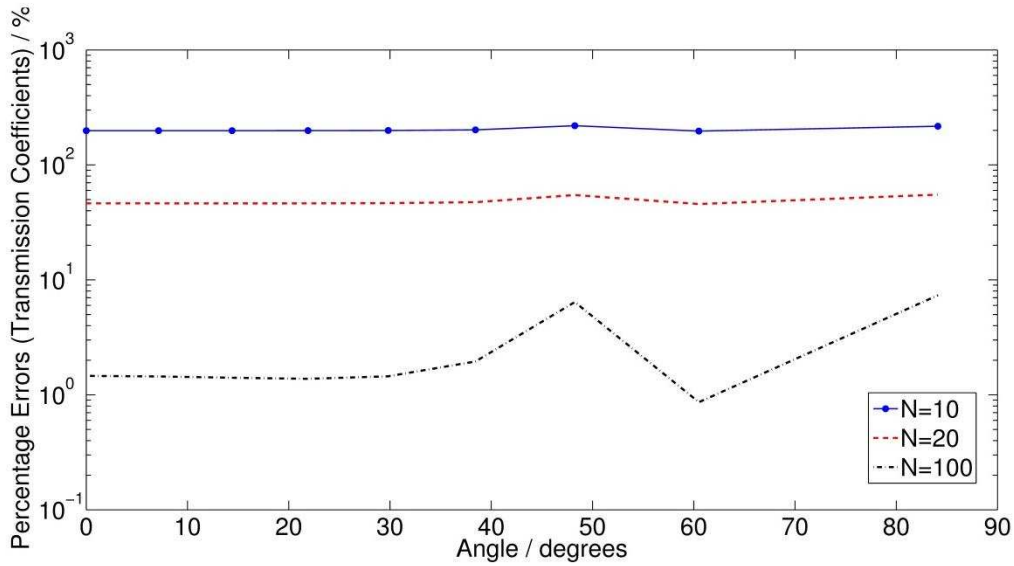

(b)

Fig. 5-16 (a) The transmission coefficients of the thin CFC panel against the incident angle φ at the frequency $f_0 = 1$ GHz for TE polarisation (b) the percentage errors in the transmission coefficients calculated using the embedded model for N = 10, 20 and 100 compared to the analytical results against the incident angle. The TLM mesh size $dl = 3$ mm.

5.5.2. TM-Polarised Wave

As in the case of the TE-polarised wave, the embedded model for arbitrary excitations is firstly used to model the reflection and transmission of TM-polarised waves obliquely incident upon an infinitely long CFC panel at an angle of 30°.

In this example, 2D series nodes were used to model free space. The CFC panel was placed in the middle of the computational space, at $x = 0.15$ m. The reflection and transmission coefficients of the CFC panel were calculated using the same method as that for the TE polarised wave case. The mesh size was chosen to be 6 mm as in the TE-polarised case.

Fig. 5-17 (a) shows the reflection coefficients of the CFC panel calculated using the embedded model for N = 10, 20 and 100 and the analytical method, when the TM polarised wave is obliquely incident onto the panel at 30°. It can be seen that the numerical results converge to the analytical ones in the frequency range from 0 to 1 GHz. Fig. 5-17 (b) shows the percentage errors in the reflection coefficients calculated using the embedded model when compared to those from the analytical method. The errors are within 0.002%, indicating the accuracy of the model.

Fig. 5-18(a) shows the transmission coefficients of the CFC panel calculated using the embedded model for N = 10, 20 and 100 and the analytical method, when the TM polarised wave is obliquely incident upon the panel at 30°. It can be seen that the numerical results become closer and closer to the analytical ones as the number of terms N increases. The percentage errors in the transmission coefficients of the CFC panel are shown in Fig. 5-18 (b), from which it can be seen that the errors are within 3% in the frequency range from 0 to 1 GHz.

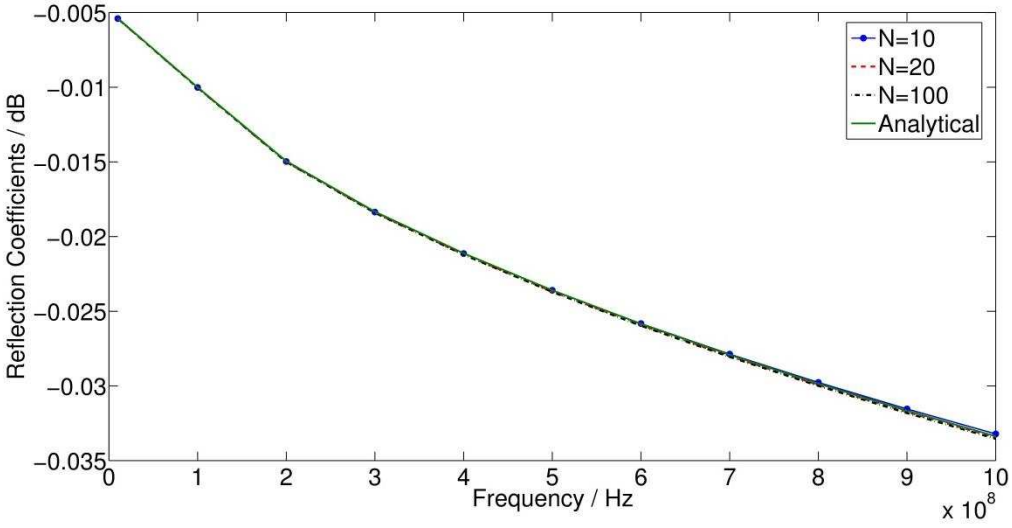

(a)

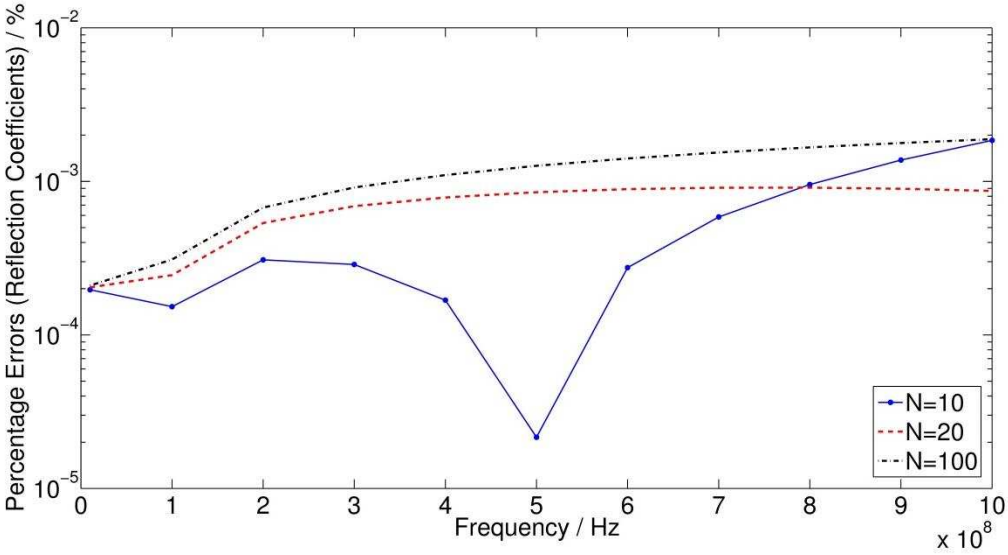

(b)

Fig. 5-17 (a) The reflection coefficients of the CFC panel when the TM-polarised plane wave is obliquely incident onto the panel at 30° (b) the percentage errors in the reflection coefficients calculated using the embedded model with different N (N = 10, 20 and 100) compared to the analytical results. The TLM mesh size $dl = 6$ mm.

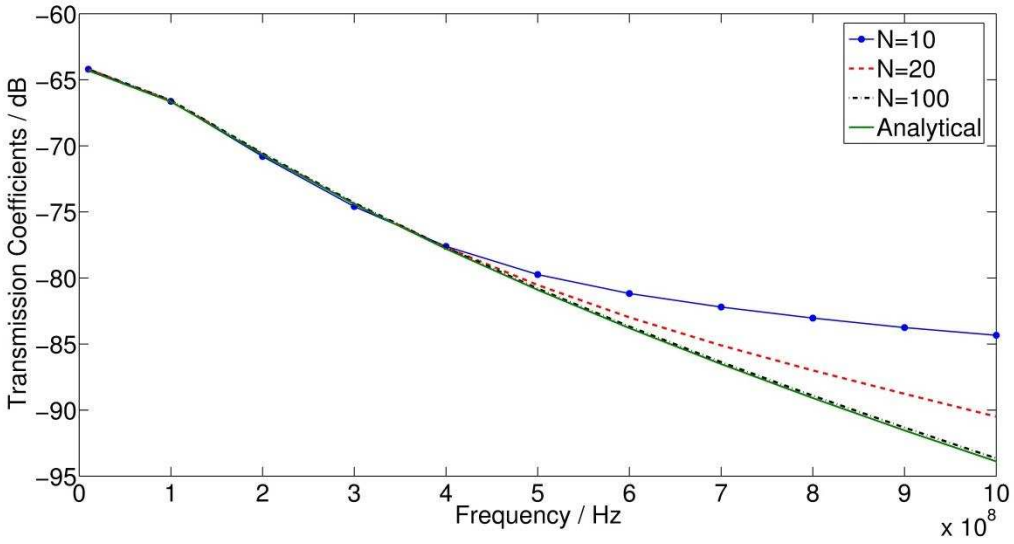

(a)

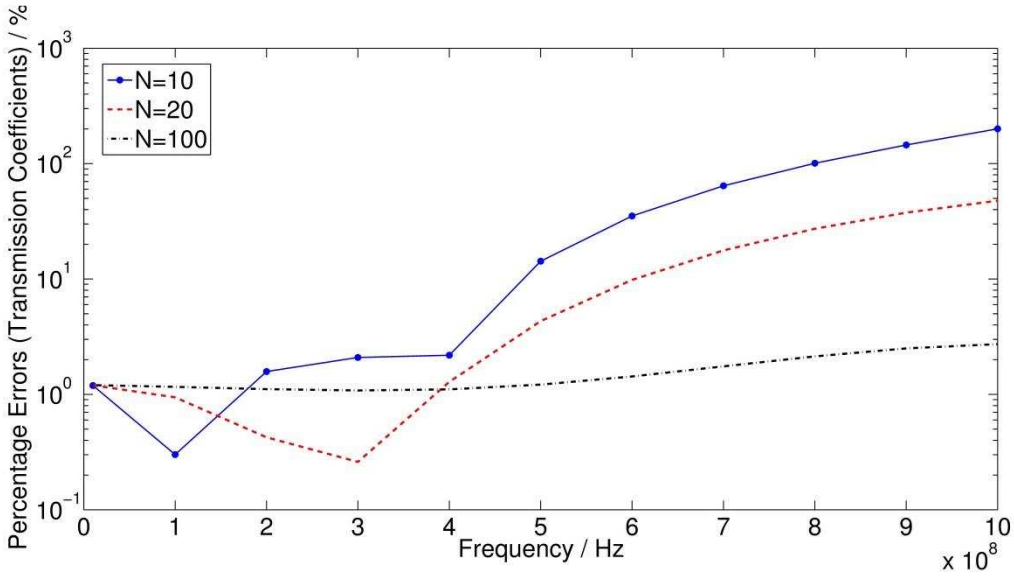

(b)

Fig. 5-18 (a) The transmission coefficients of the CFC panel when the TM-polarised plane wave is obliquely incident onto the panel at 30° (b) the percentage errors in the transmission coefficients calculated using the embedded model with different N (N = 10, 20 and 100) compared to the analytical results. The TLM mesh size $dl = 6$ mm

In summary, the accuracy and convergence of the embedded model for arbitrary excitations is verified over a wide frequency range by calculating the reflection and transmission coefficients of the CFC panel when the TM-polarised wave is obliquely incident onto the panel at 30°.

As was done for the TE case in section 5.4.1, to further validate the accuracy of the embedded model for arbitrary excitations, the reflection and transmission coefficients of the CFC panel at different angles of incidence were calculated at 1 GHz. Several angles of incidence were selected from 0° to approaching 90° as examples. The mesh size here was chosen to be 3 mm in order to get good accuracy for all the angles.

Fig. 5-19 (a) shows the reflection coefficients of the CFC panel at 1 GHz calculated using the embedded model for N = 10, 20 and 100 and the analytical method when the incident angles vary for the TM polarisation. Fig. 5-19(b) shows the percentage errors in the reflection coefficients calculated using the embedded model in comparison to those from the analytical method. It is seen that the numerical results converge as the number of terms, N, increases. The numerical results have excellent agreement with the analytical ones when the angle is less than 60°. The errors are within 0.3% for the incident angles from 0° to 60°. When the angle is larger than 60°, the error becomes big, i.e. the error is around 10% at 84° of incidence.

The accuracy for the large incident angle can be improved by using a smaller mesh size. Fig. 5-20 shows the reflection coefficients of the CFC panel against the angle of incidence calculated using the embedded model for different mesh size, dl. It is shown that as the mesh size decreases, the numerical results become closer to the analytical ones. Especially at large angle of incidence, the differences between the numerical results and the analytical ones are very small for a fine mesh size.

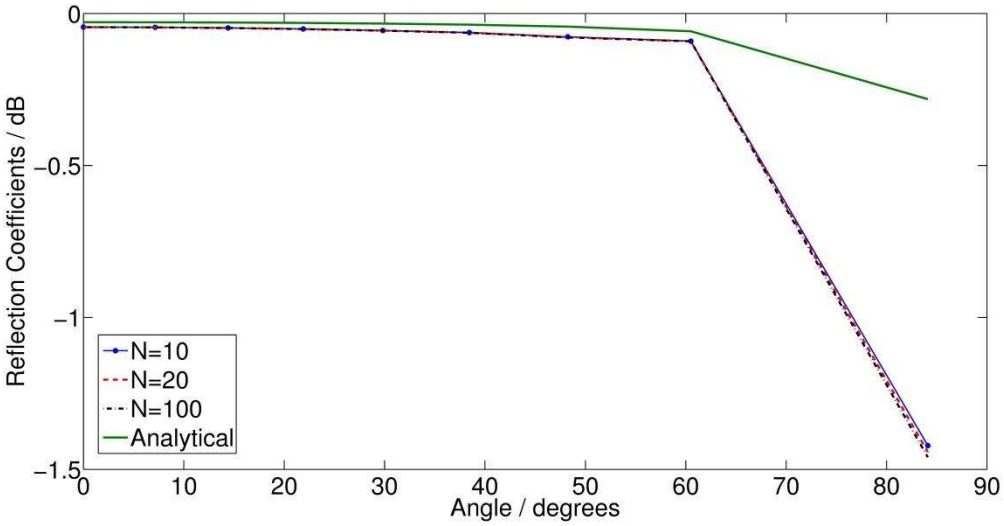

(a)

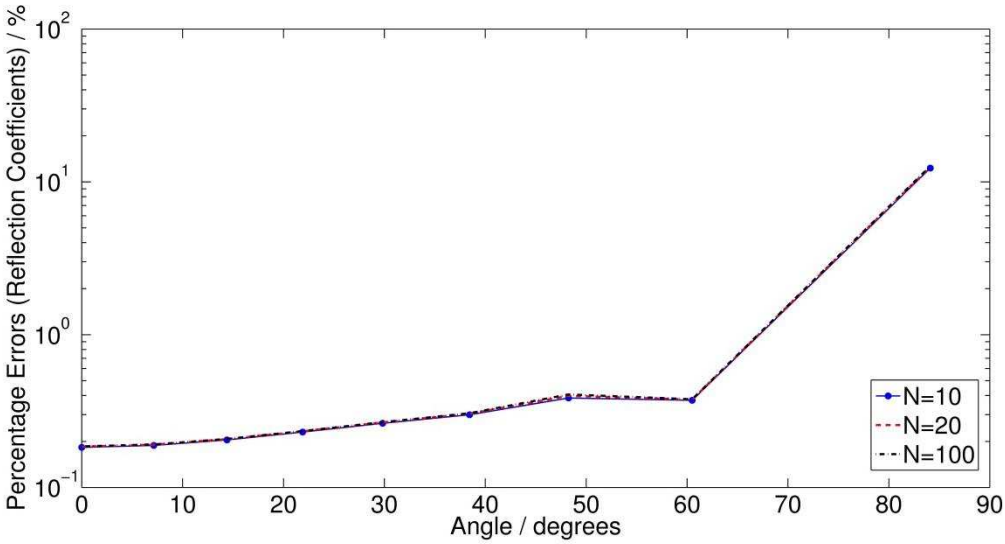

(b)

Fig. 5-19 (a) The reflection coefficients of the thin CFC panel against the incident angle φ at the frequency $f_0 = 1$ GHz for TM polarisation; (b) the percentage errors in the reflection coefficients calculated using the embedded model for N = 10, 20 and 100 compared to the analytical results against the incident angle. The TLM mesh size $dl = 3$ mm.

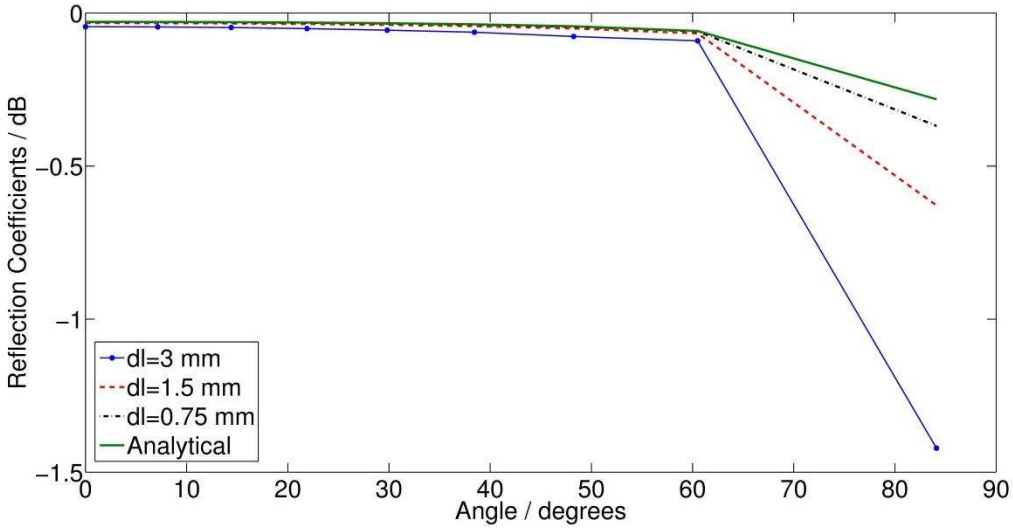

Fig.5-20 The reflection coefficients of the CFC panel against the incident angle at 1 GHz for the TM polarisation, obtained using the embedded model with different discretisation, dl.

Fig. 5-21 (a) shows the transmission coefficients of the CFC panel at 1 GHz using the embedded model for N = 10, 20 and 100 and the analytical method against the incident angle for the TM polarisation. When N = 100, the numerical results are very close to the analytical results. Fig. 5-21 (b) shows the percentage errors in the transmission coefficients against the incident angle. When N = 100, the errors are within 2% for the incident angle from 0° to 60° and the error for 84° is around 10%.

Fig. 5-19 (a) and Fig. 5-21 (a) exhibit that as the angle of incident increases for the TM-polarised wave, the reflection coefficients of the panel decrease and its transmission coefficients increase. This behaviour of the panel in the TM-polarised wave excitations differs from that observed for the TE-polarised wave excitations.

In summary, the convergence and accuracy of the embedded model for the TM polarised wave with arbitrary excitations are verified over a wide frequency range and for different angles of incidence.

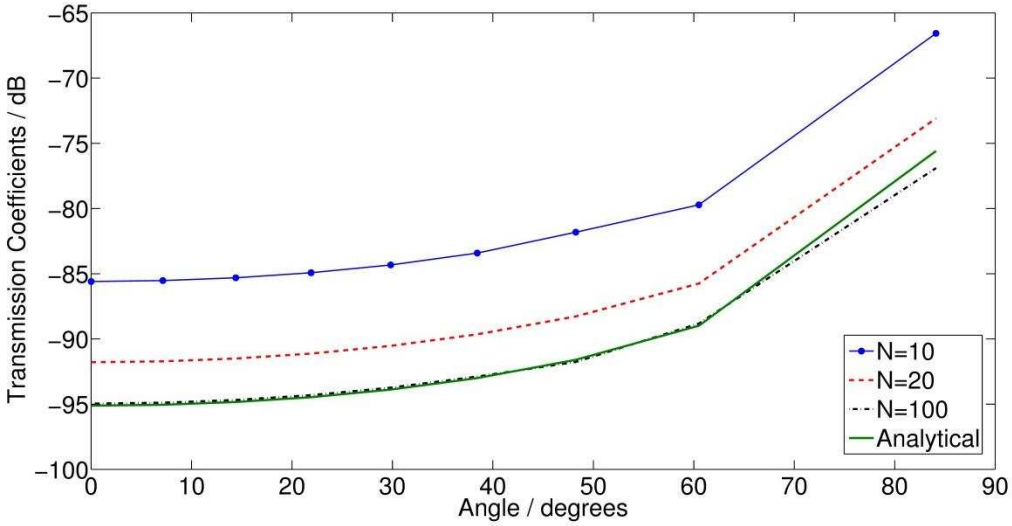

(a)

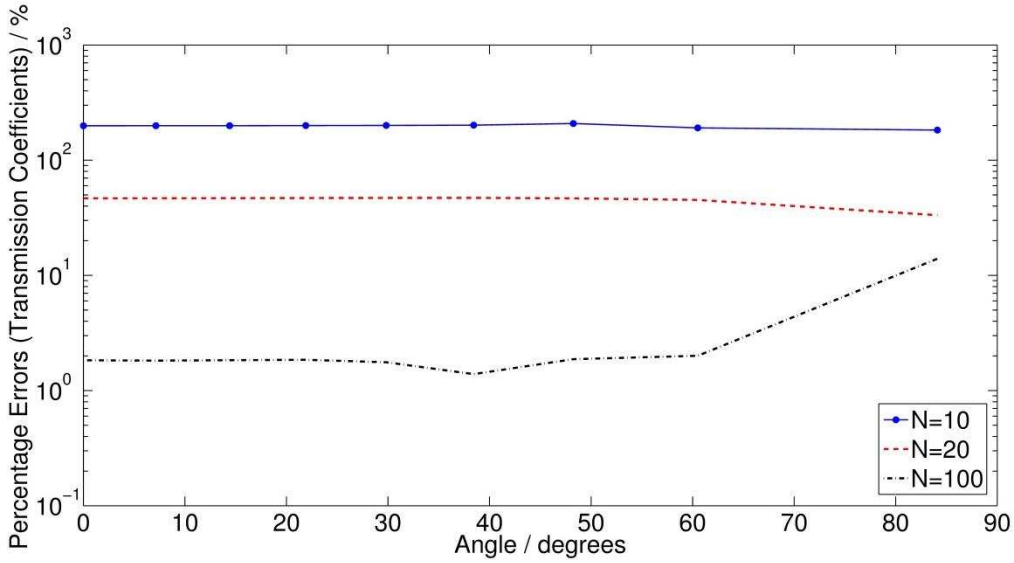

(b)

Fig. 5-21 (a) The transmission coefficients of the thin CFC panel against the incident angle φ at the frequency $f_0 = 1$ GHz for TM polarisation; (b) the percentage errors in the transmission coefficients calculated using the embedded model for N = 10, 20 and 100 compared to the analytical results against the incident angle. The TLM mesh size $dl = 3$ mm.

5.6. Applications

In the previous section, the embedded model has been verified for plane waves obliquely incident upon infinitely long CFC panels at fixed angles. In this section, it is applied to investigate the effects of a CFC panel having finite dimensions on the TE- and TM- polarised fields.

Consider a CFC panel with finite thickness in the x direction, finite length in the y direction, and infinite in the $\pm z$ directions. The parameters of the CFC panel were chosen as in section 4.3.1: effective permittivity $\varepsilon_r = 2$, conductivity $\sigma_e = 10^4$ Sm^{-1}, and thickness $d = 1$ mm.

As shown in Fig. 5-3, the CFC panel was placed in a 2D space, which was excited by a point source. As a demonstration, the 2D space was chosen to be 1.2 m × 0.9 m and matched boundaries [5] were used at the four problem-space boundaries. The dimension of the panel in the y direction was chosen to be 0.384 m. It was assumed that the panel was parallel to the y axis and located at $x = 0.6$ m. A point source was chosen to be the input signal. It was placed at the point (0, 0.45 m), and was taken to have the form of a sine wave with a frequency of 1 GHz.

The 2D shunt and series nodes were used to model the TE-polarised and the TM-polarised waves, respectively. In both cases, the fields from the TLM nodes near the panel are decomposed into a series of plane waves and evanescent waves, each of which is incident upon the panel independently at its own angle. As shown in Fig. 5-5, a Fourier transform was used to transfer the voltages in the space domain to the angle domain. If the indices of the voltage in the space domain are $0, dl, 2 \cdot dl, \dots, i \cdot dl, \dots,$ and $NN \cdot dl$, where NN is a real positive number, the s indices of the voltages in the angle domain are $0, \frac{1}{NN \cdot dl}, \frac{2}{NN \cdot dl}, \dots, \frac{i}{NN \cdot dl}, \dots, \frac{1}{dl}$. Since $s = ksin\varphi$ (equation (5-19)), the angle φ_i corresponding to a certain s index i is

$$\varphi_i = \arcsin(i/(2 \cdot pi \cdot l/\lambda_0)), \tag{5-44}$$

where l is the length of the thin film and λ_0 is the operating wavelength. From the equation (5-44), it can be seen that the angles of incidence depend on the ratio of the film's length to the operating wavelength.

For this example, the mesh size was chosen to be 3 mm as discussed before. Since the length of the thin film was 38.4 cm, the total number of nodes $NN = \frac{38.4\ cm}{0.3\ cm} = 128$. According to the equation (5-44), there are 9 real angles of incidence, $0°, 7.14°, 14.4^{\circ}, 21.90°, 29.83^{\circ}, 38.44°, 48.25^{\circ}, 60.5°$ and 84.11°, contributing to plane waves, and 119 complex angles, contributing to the evanescent waves.

Fig.5-22 shows the field intensity distribution of (a) the electric field component E_z and the magnetic field components (b) H_x and (c) H_y of the TE-polarised wave at 50,000 time steps. Fig.5-23 shows the field intensity of (a) the magnetic field component H_z and the electric field components (b) E_x and (c) E_y of the TM-polarised wave at 50,000 time steps. From Fig.5-22 and Fig.5-23, it can be seen that the field intensities of all the components exhibit symmetry about y = 0.45 m. Because of the point source, the field is locally propagating in a radial direction until it hits the CFC panel. When the fields hit the CFC panel, their direct propagation is blocked by the panel, but a part of the fields reaches the right side around the top and bottom of the panel.

In summary, for both TE and TM polarisations, the presence of the panel disturbs the electromagnetic field distributions in the 2D space. Due to the finite length of the panel, it cannot block all the fields, some of which reaches the side of the panel remote from the source, around its top and bottom. As the distance from the panel increases, more waves reach the right side over the panel and thus the shielding performance of the panel decreases rapidly.

It should also be noted that in contrast to the infinitely long panel case, the electric field shielding effectiveness is no longer equal to the magnetic field shielding effectiveness at each point on the side of the panel remote from the source. This is because of the different influence the finite dimension of the panel has on the electric and magnetic fields.

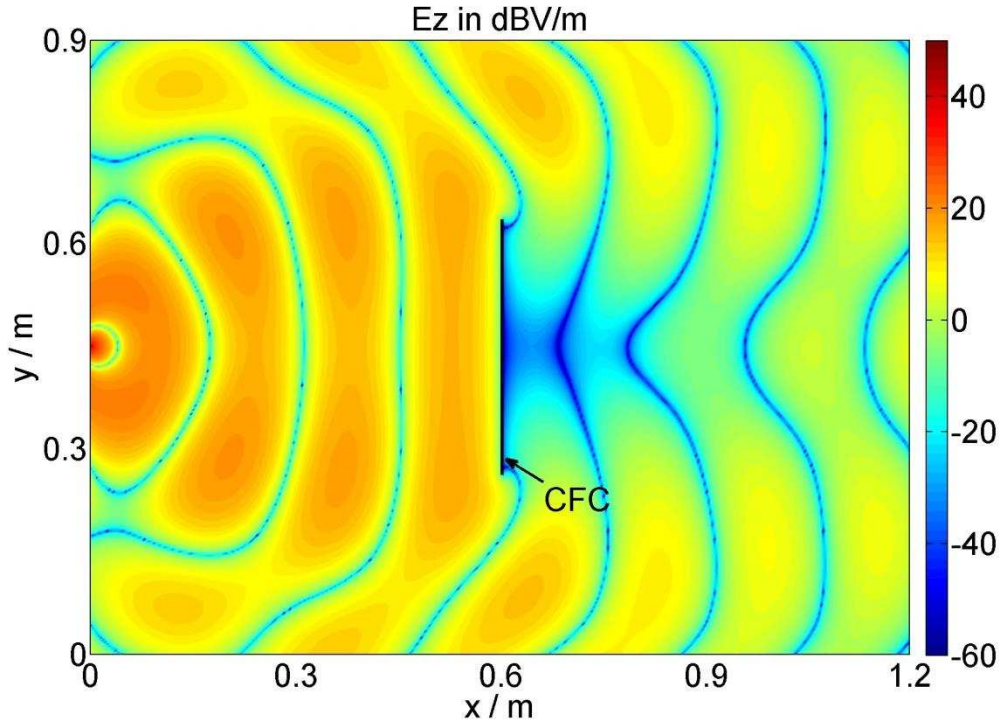
Ez in dBV/m
0.9
0.6
0.3
0
y / m
0
0.3
0.6
0.9
1.2
x / m
CFC
40
20
0
-20
-40
-60

(a)

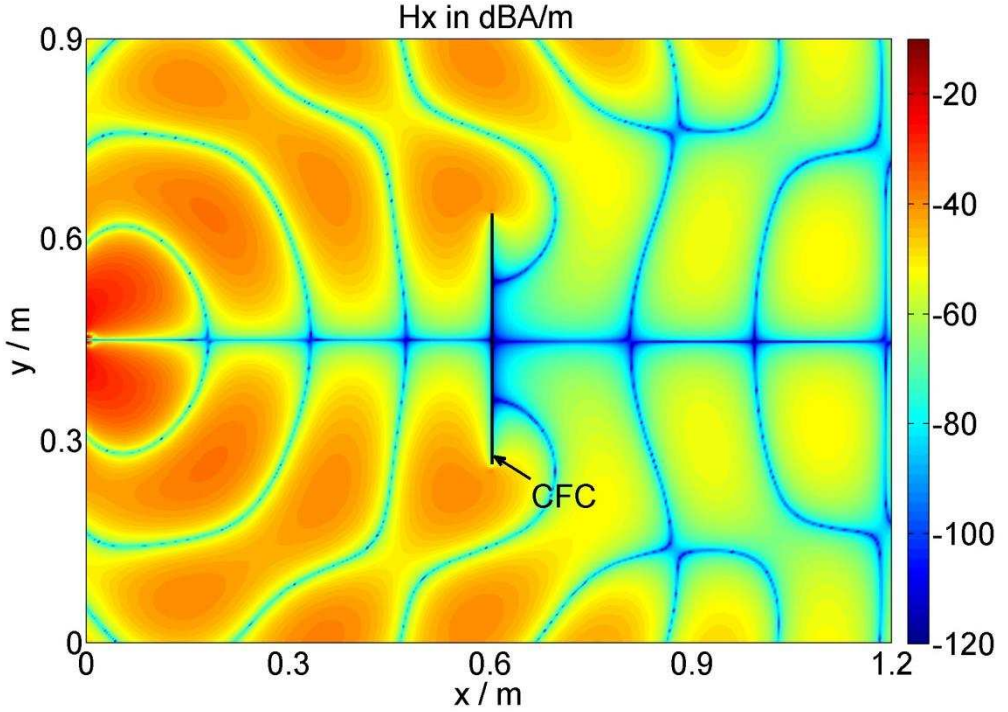
Hx in dBA/m
0.9
0.6
0.3
0
y / m
0
0.3
0.6
0.9
1.2
x / m
CFC
-20
-40
-60
-80
-100
-120

(b)

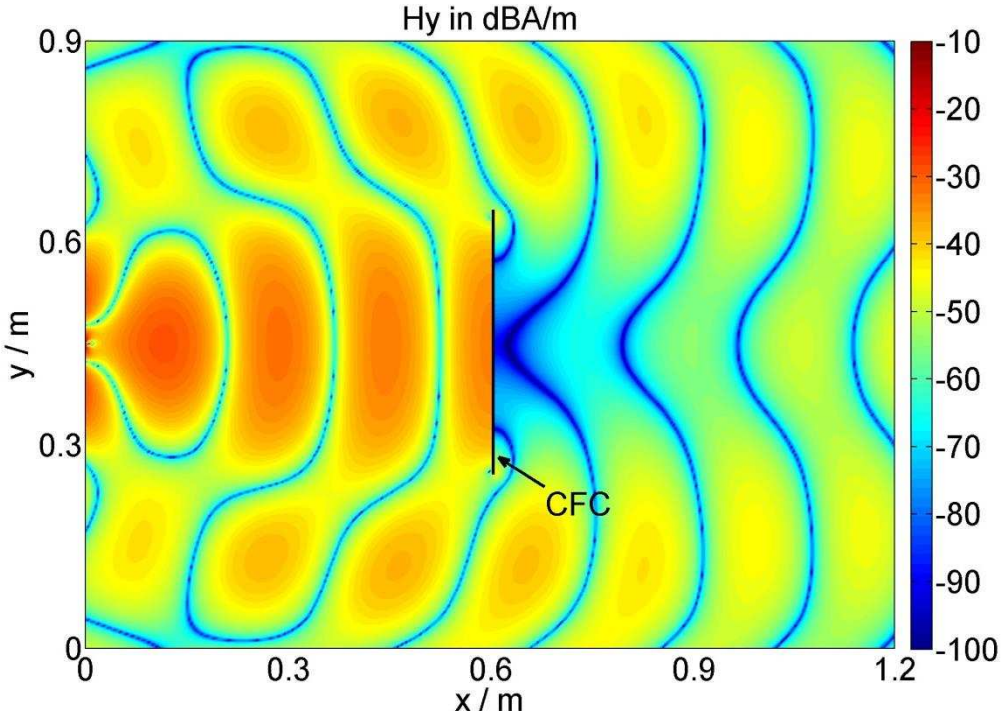

(c)

Fig.5-22 The field intensity distribution of (a) E_z (b) H_x and (c) H_y components in the 2D space when the TE-polarised wave is incident onto a 0.384 m long CFC panel.

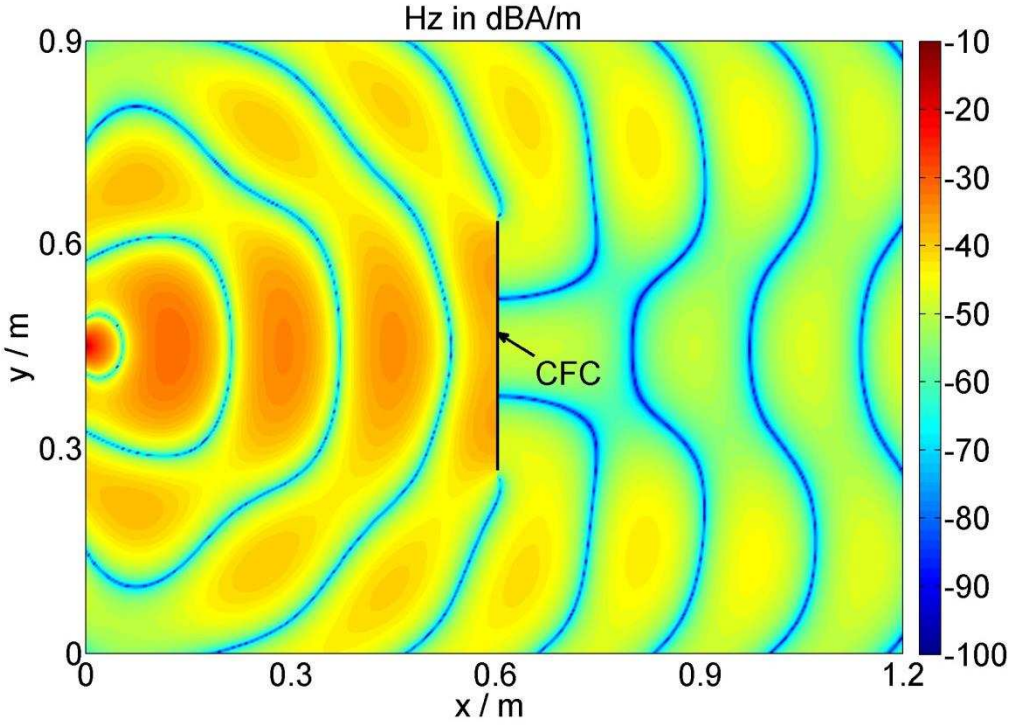
Hz in dBA/m
0.9
0.6
0.3
0
y / m
CFC
0
0.3
0.6
0.9
1.2
x / m
-10
-20
-30
-40
-50
-60
-70
-80
-90
-100

(a)

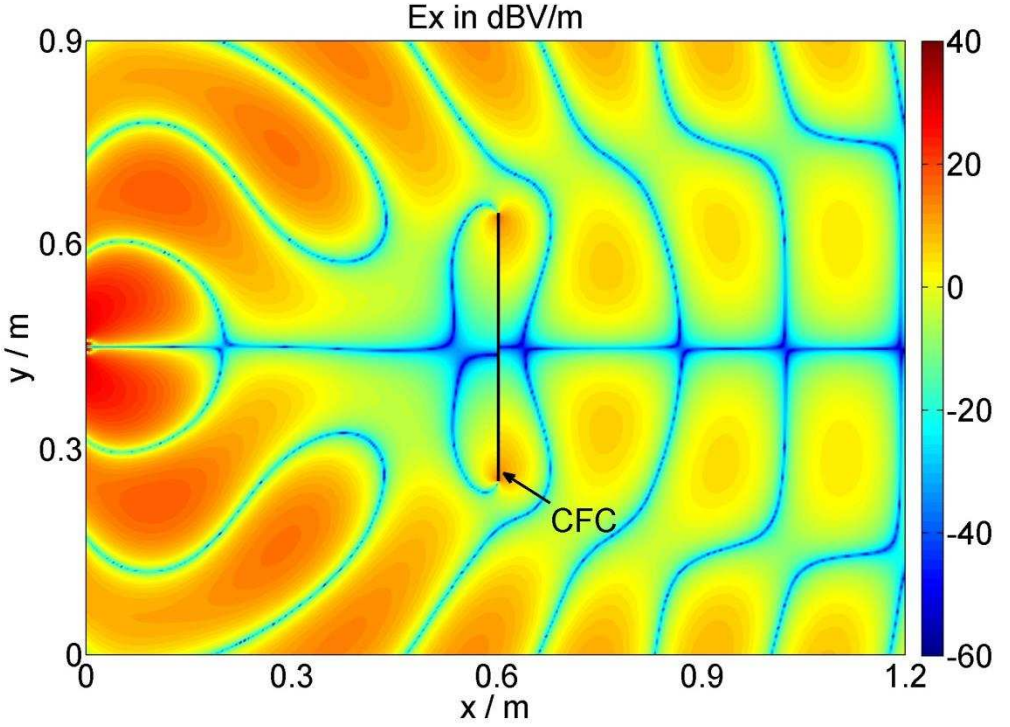
Ex in dBV/m
0.9
0.6
0.3
0
y / m
CFC
0
0.3
0.6
0.9
1.2
x / m
40
20
0
-20
-40
-60

(b)

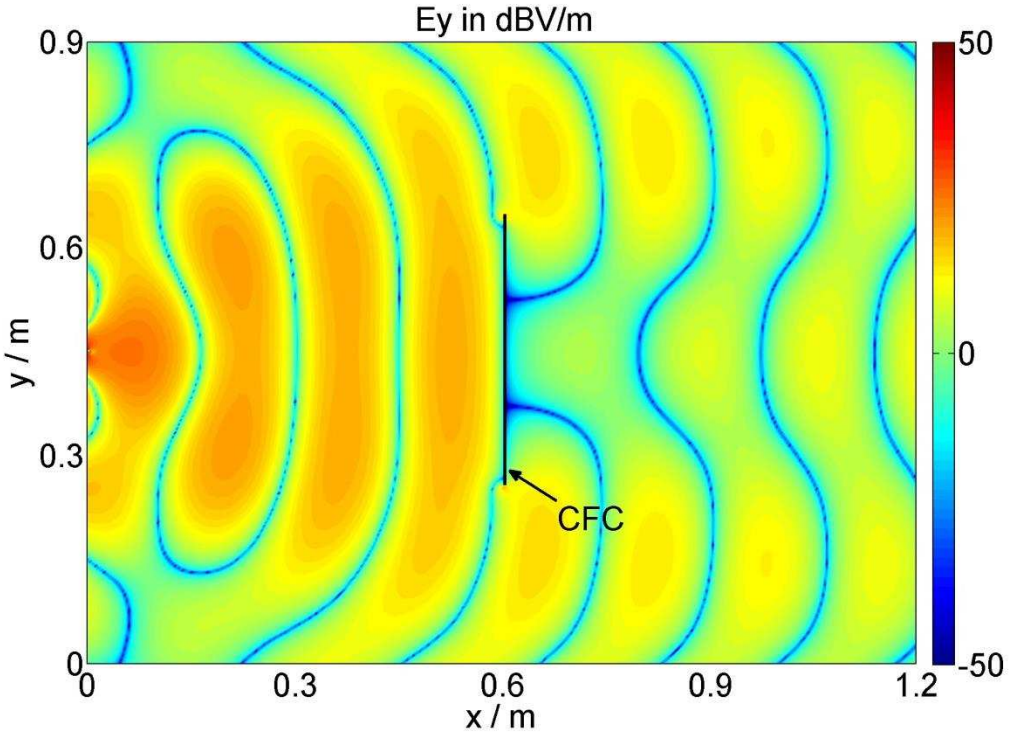

(c)

Fig.5-23 The field intensity distribution of (a) H_z, (b) E_x and (c) E_y components in the 2D space when the TM-polarised wave is incident onto a 0.384 m long CFC panel.

If the conventional TLM method is used to simulate the effects of the finite length CFC panel on the TE- and TM- polarised fields, the mesh size should be chosen as 0.025 mm as discussed in Chapter 4. The number of nodes needed to represent the $1.2\text{ m} \times 0.9\text{ m}$ region would be $48{,}000 \times 36{,}000$ and the number of nodes needed to represent the CFC panel would be 40×15360. In total, there would be $48{,}040 \times 36{,}000$ nodes needed in the conventional TLM method, compared to 400×300 nodes needed in the embedded model. From this point of view, the embedded model can save the memory storage significantly. Besides, since the mesh size needed in the conventional TLM method is 120 times bigger than that needed in the embedded model, the number of time steps needed in the conventional TLM method is 120 times bigger than that needed in the embedded model, in order to achieve the same frequency accuracy. Therefore, the embedded model for arbitrary excitations can save the memory storage and number of time steps significantly compared to the conventional TLM method.

In order to prove the results shown in Fig.5-22 and Fig.5-23, the straightforward thinking would be doing the same simulation using the conventional TLM method. However, considering the large memory storage and the number of time steps needed to simulate the finite length CFC panel, a simulation of the finite length zero thickness PEC boundary using the conventional TLM method is considered. Since the CFC materials have very high conductivity, the finite CFC panel should have similar responses to the fields as the PEC boundary.

In the simulation, the finite length CFC panel was replaced by the same length zero thickness PEC boundary, which has reflection coefficients of -1 and transmission coefficients of 0. Fig.5-24 shows the field intensity distribution of (a) the electric field component E_z and the magnetic field components (b) H_x and (c) H_y of the TE-polarised wave in the presence of the finite length zero thickness PEC boundary at $50{,}000$ time steps. Fig.5-25 shows the field intensity of (a) the magnetic field component H_z and the electric field components (b) E_x and (c) E_y of the TM-polarised wave in the presence of the finite length zero thickness PEC boundary at $50{,}000$ time steps.

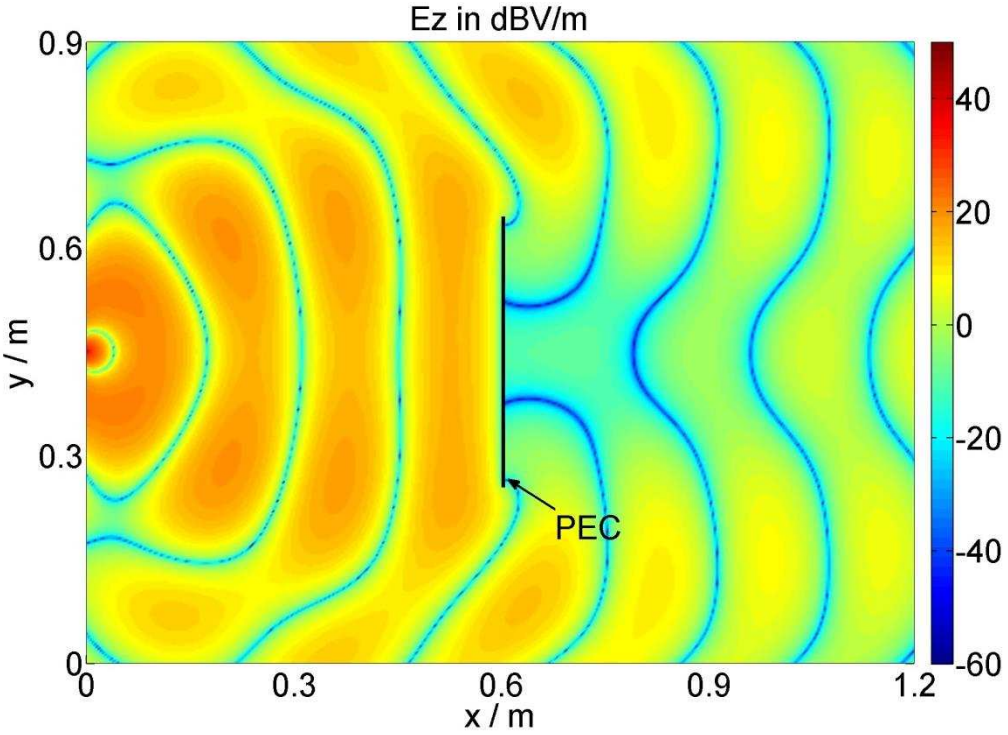
Ez in dBV/m
0.9
0.6
0.3
0
y / m
PEC
40
20
0
-20
-40
-60
0
0.3
0.6
0.9
1.2
x / m

(a)

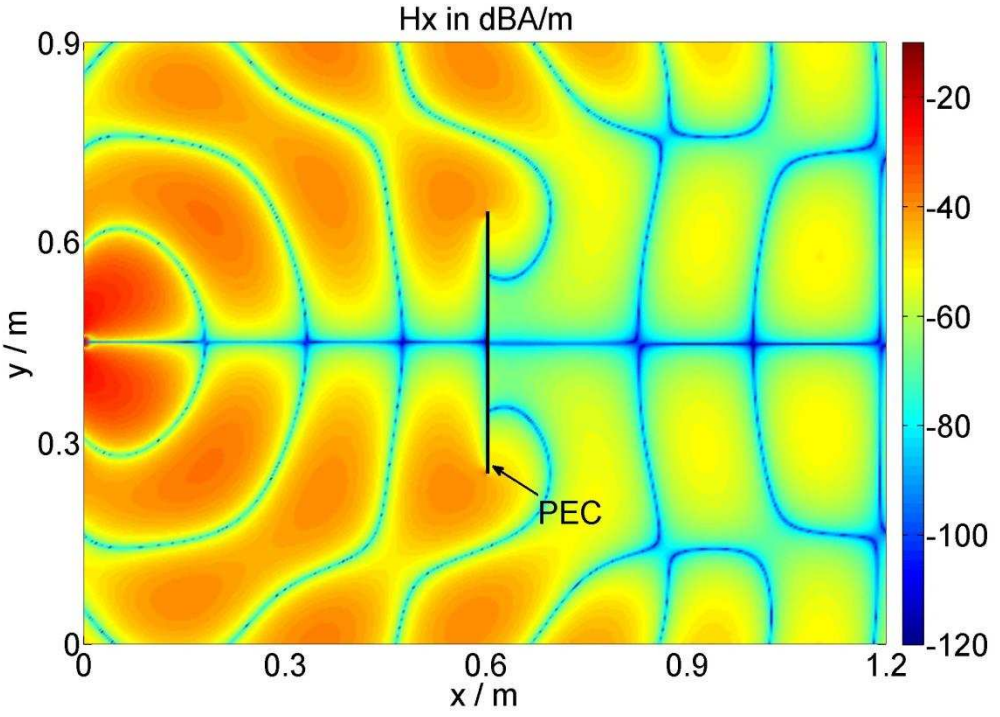
Hx in dBA/m
0.9
0.6
0.3
0
y / m
PEC
-20
-40
-60
-80
-100
-120
0
0.3
0.6
0.9
1.2
x / m

(b)

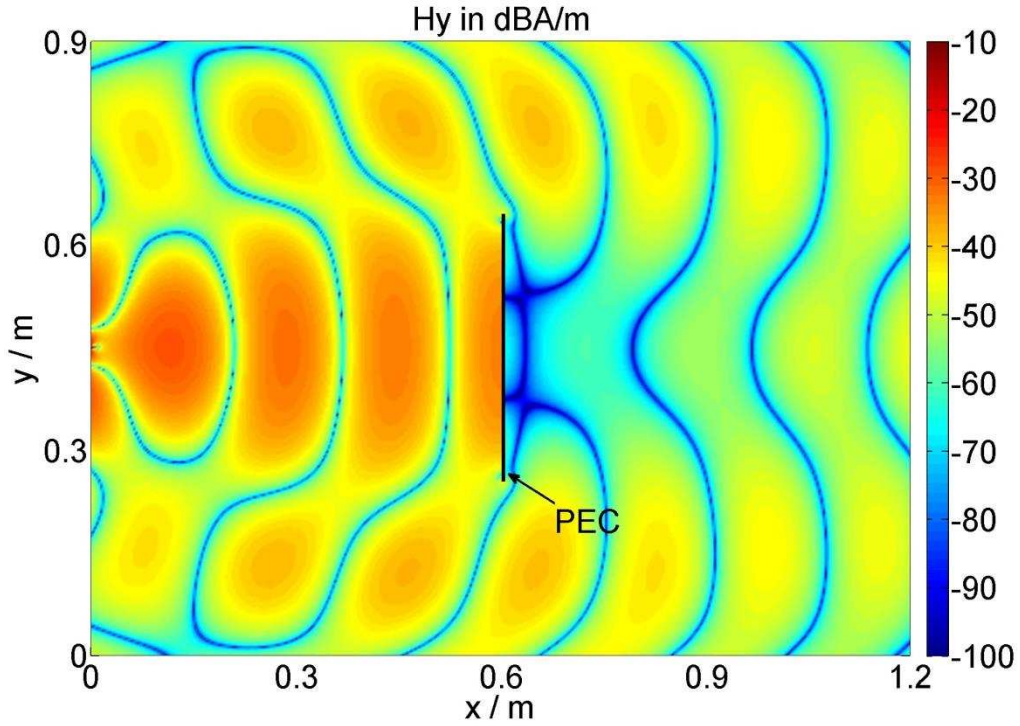

(c)

Fig.5-24 The field intensity distribution of (a) E_z (b) H_x and (c) H_y components in the 2D space when the TE-polarised wave is incident onto the 0.384m long zero thickness PEC.

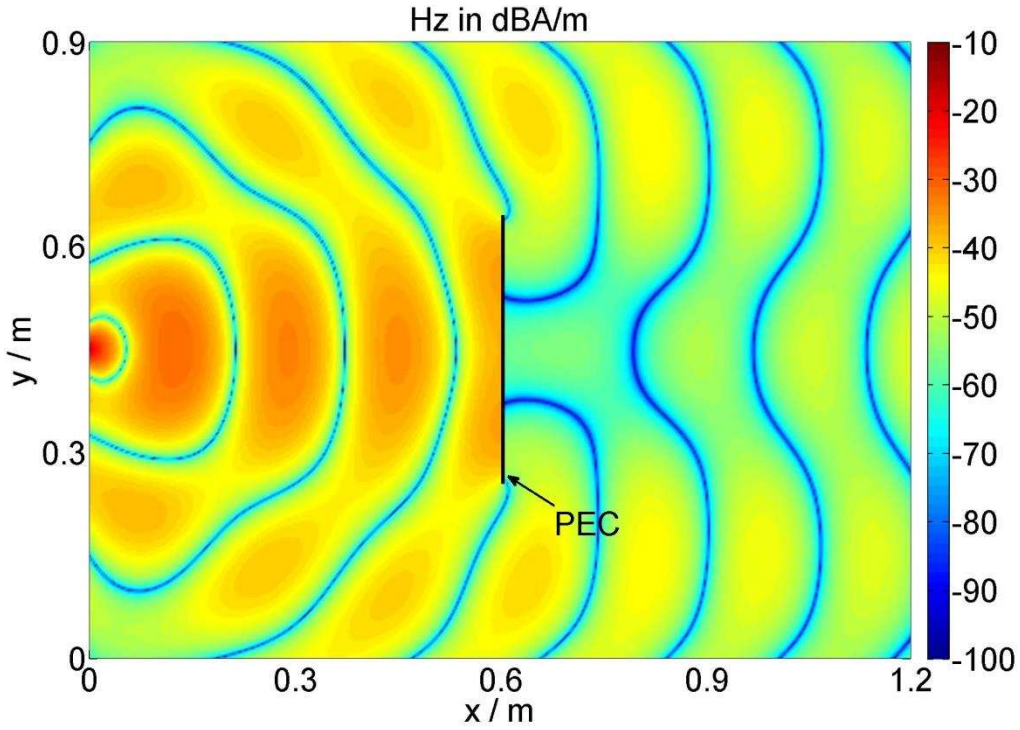
Hz in dBA/m
0.9
0.6
0.3
0
y / m
PEC
0
0.3
0.6
0.9
1.2
x / m
-10
-20
-30
-40
-50
-60
-70
-80
-90
-100

(a)

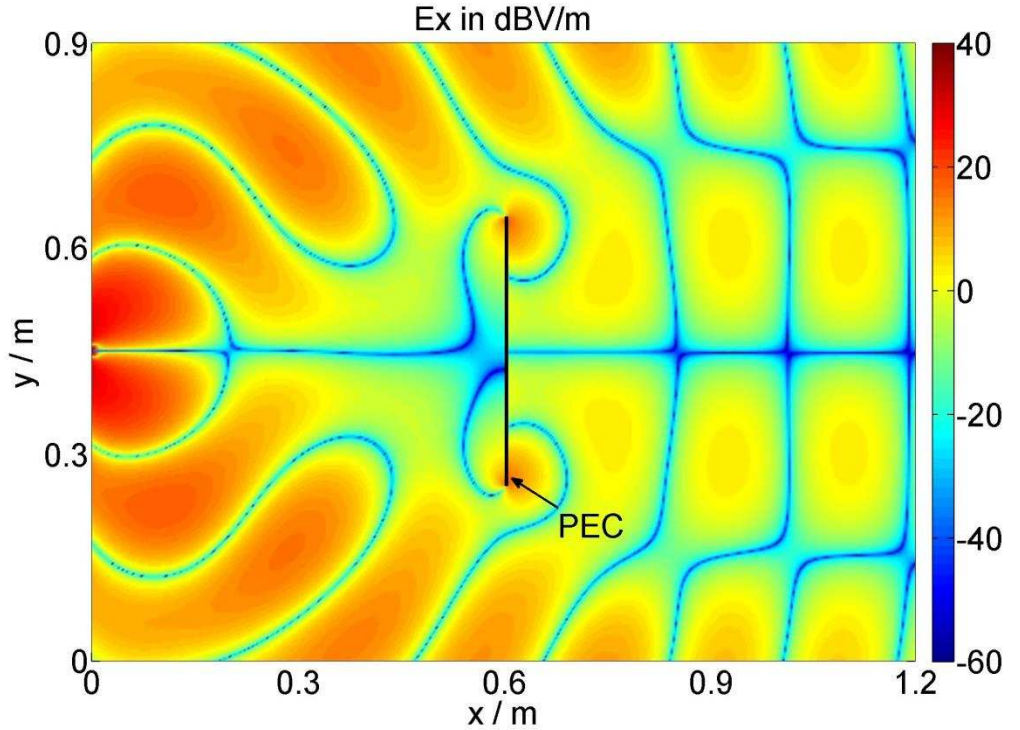
Ex in dBV/m
0.9
0.6
0.3
0
y / m
PEC
0
0.3
0.6
0.9
1.2
x / m
40
20
0
-20
-40
-60

(b)

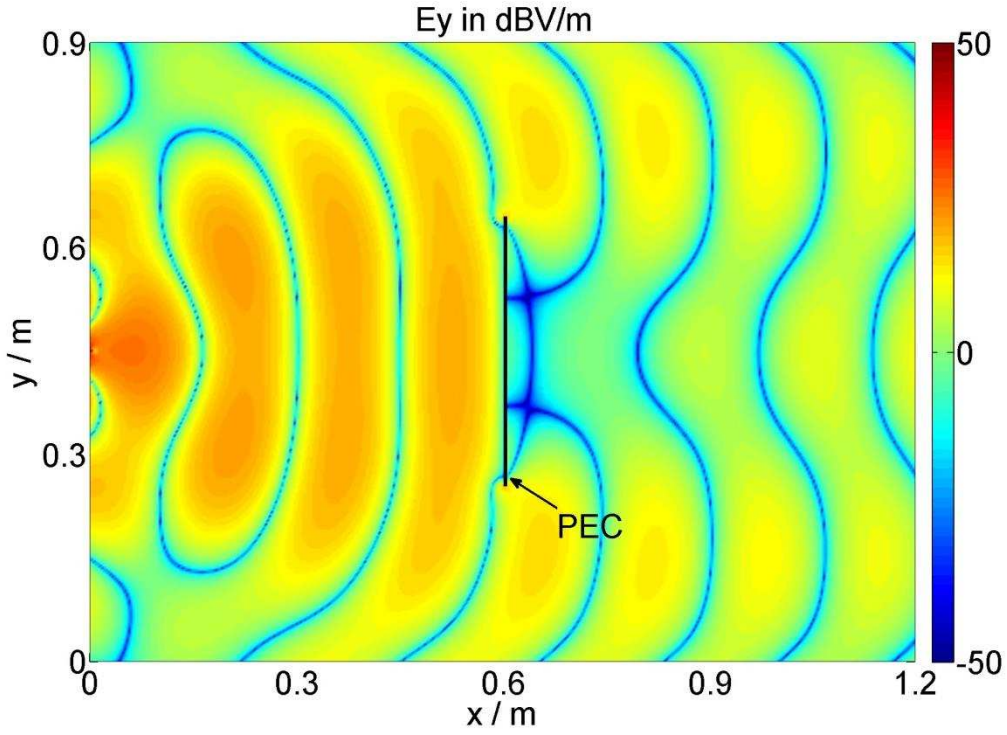

(c)

Fig.5-25 The field intensity distribution of (a) H_z, (b) E_x and (c) E_y components in the 2D space when the TM-polarised wave is incident onto the 0.384 m long zero thickness PEC.

Comparing Fig.5-22 and Fig.5-23 with Fig.5-24 and Fig.5-25, it can be seen that the filed intensity distributions in the presence of the finite length CFC panel are similar to those in the presence of the finite zero thickness PEC boundary. There is evidence of more penetration for the CFC panel with respect to the PEC boundary. The comparison validates the results shown in Fig.5-22 and Fig.5-23.

5.7. Conclusions

In this chapter, the thin film model developed in Chapter 3 has been embedded in the 2D TLM codes to account for arbitrary excitations. A simple case of a plane wave incident at a fixed angle was first presented and then the theory for arbitrary excitations was presented using the plane wave decomposition theory. Both TE and TM polarisations were considered.

The accuracy and convergence of the embedded model were verified using examples of plane waves obliquely incident onto infinitely long CFC panels at various fixed angles and over a wide frequency range. The embedded model was then applied to demonstrate the effects of the finite length of the CFC panel on the shielding performance for both polarisations.

The embedded model for arbitrary excitations was also proved to have the advantage of saving the computational overheads significantly, compared to the conventional TLM method.

In the next chapter, an embedded model for the curved thin film in the 2D TLM is presented. The model is used to analyse curved structures, such as circular and elliptical waveguides and an airfoil structure.

References

[5.1] S. Ramo, J. R. Whinnery, and T. Van Duzer, Fields and Waves in Communication Electronics, 3rd ed. John Wiley & Sons, Inc., 1997.

[5.2] S. J. Orfanidis, “Electromangetic Waves and Antennas,” [Online]. Available: http://www.ece.rutgers.edu/~orfanidi/ewa/, 1996

[5.3] J. W. Goodman, Introduction to Fourier Optics. Roberts and Company Publishers, 2005.

[5.4] H. Taub and D. L. Schilling, Principles of Communication Systems. McGraw-Hill Higher Education, 1986.

[5.5] C. Christopoulos, The Transmission-Line Modeling Method TLM. IEEE Press, 1995.

[5.6] D. M. Pozar, Microwave Engineering, 4th ed. John Wiley & Sons, Inc., 2011.

6.Embedded Curved Thin Film Model in the Two-Dimensional TLM Method

6.1. Overview

In previous chapters, the embedded models were used to model planar thin films. However, there are a number of instances where the thin films are curved, such as cylinder-shaped structures used in aircraft fuselages [6.1 ~ 6.2] and airfoil structures [6.3]. In this chapter, the embedded model developed in Chapter 3 is extended to model curved thin films. This is done by first linearising the curved thin films and then embedding the equivalent model between the adjacent two-dimensional (2D) TLM nodes allowing for arbitrary positioning between adjacent node centres. The accuracy and convergence of the embedded model are examined by comparing the resonant frequencies of the infinitely long, hollow, CFC circular and elliptical cylinders with those of the equivalent metal circular and elliptical cylinders. Furthermore, the embedded model is applied to analyse the shielding performance of a CFC airfoil with the profile of NACA2415. In addition, the impact of small gaps in the airfoil NACA2415 structure on its shielding performance is also presented.

6.2. Embedded Curved Thin Film Model

In this section, the approach for embedding a curved thin film within TLM is described.

Fig. 6-1 (a) shows the schematic of a curved thin film, represented by the solid curve (green), positioned within a coarse mesh of size dl, represented by dashed lines (black). The solid cross lines (red) represent the transmission link

lines along which the voltages travel, and the point of their intersection is defined as the TLM node centre.

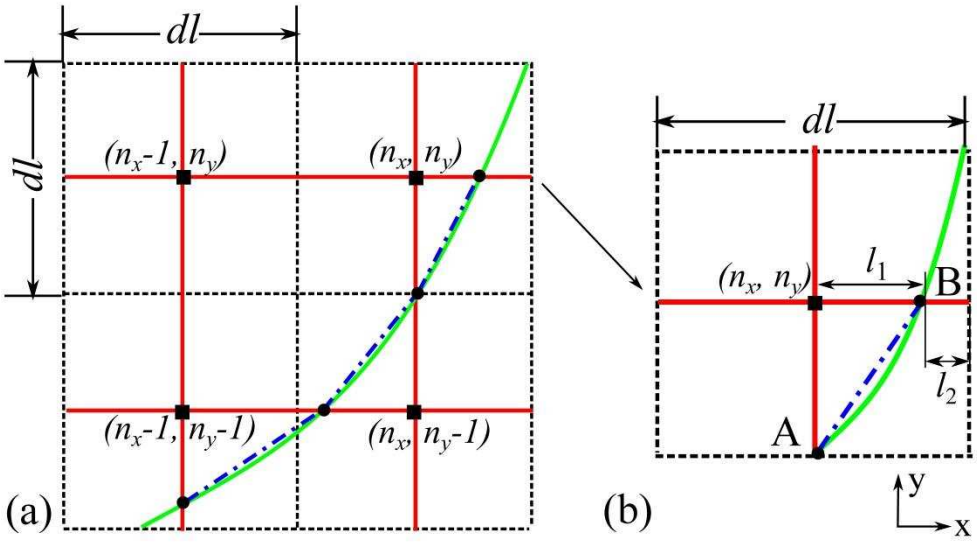

Fig. 6-1 (a) A curve thin film embedded between 2D TLM nodes (b) the enlarged TLM node $(n_x,\ n_y)$.

The curved thin film is firstly approximated by linear piece-wise segments, represented by dash-dot lines (blue), each of which can be viewed as a planar thin film. The linearisation is done by connecting the crossing points of the arc and the link lines of the nodes. The crossing point can be either exactly between two nodes as for point A on Fig. 6-1 (b) or can split the transmission line of a node at an arbitrary position as for point B in Fig. 6-1 (b). The curved panel thus needs to be embedded at each crossing point. If the arc is defined by a function $y = f(x)$, then the position of points A and B in an arbitrary node $(n_x,\ n_y)$ can be expressed as $(n_x \cdot dl,\ f(n_x \cdot dl))$ and $(f^{-1}(n_y \cdot dl),\ n_y \cdot dl)$, respectively.

At the crossing point A, the curved panel is modelled and embedded as a transmission line positioned centrally between the two adjacent nodes with coordinates $(n_x,\ n_y)$ and $(n_x,\ n_y - 1)$, which is done by modifying the TLM's connection process as discussed in section 3.2. However, at the crossing point B, the curved panel splits the transmission link line at the right side of the node $(n_x,\ n_y)$ into two segments of lengths l_1 and l_2. In this case,

the whole section of transmission line together with the section of the curved panel is modelled and embedded as a three-layer stack whereby the curved panel is sandwiched between two sections of transmission lines of lengths l_1 and l_2 as shown in Fig. 6-2.

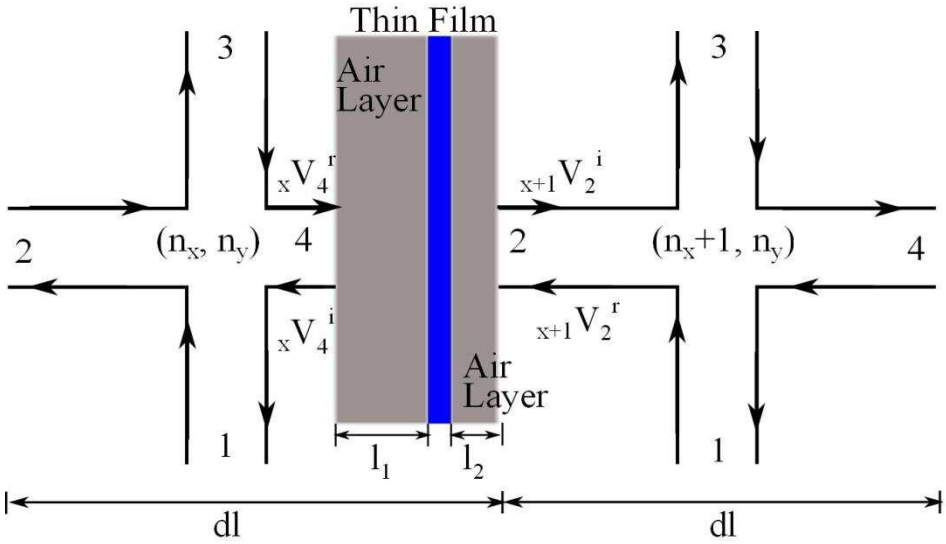

Fig. 6-2 Two layers of air together with the planar thin film are composed of a three-layer stack embedded between two adjacent 2D series nodes.

Fig. 6-2 shows the three-layer stack embedded between two 2D series nodes (n_x, n_y) and $(n_x + 1, n_y)$, where the two shaded layers represent the transmission lines of the node and the middle layer (blue) represents the curved panel. In the figure, $_xV_4^i$ and $_xV_4^r$ are the incident and reflected voltages at port 4 of the node (n_x, n_y), while $_{x+1}V_2^i$ and $_{x+1}V_2^r$ are the incident and reflected voltages at port 2 of the node $(n_x + 1, n_y)$.

The transmission line model of this three-layer stack embedded between two TLM nodes is shown in Fig. 6-3. Transmission lines of lengths l_1 and l_2 are, in this case, made of air but in general can represent any material parameters.

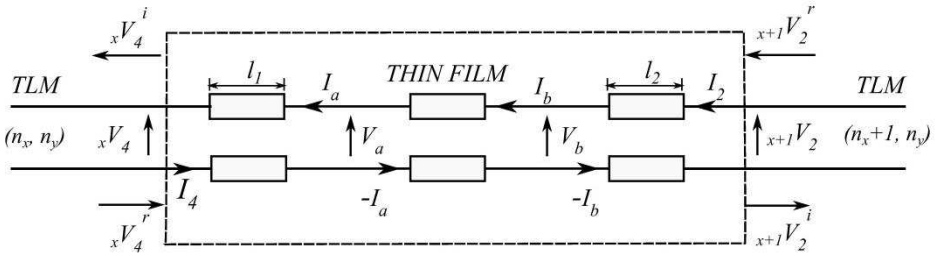

Fig. 6-3 Transmission line model of the three-layer stack embedded between two TLM nodes.

Since the transmission line model in Fig. 6-3 is similar to that depicted in Fig. 3-8 (b), the reflected voltages from the three-layer stack, i.e. ${}_{x+1}V_2^i$, ${}_xV_4^i$ as in Fig. 6-3, can be solved in terms of the incident voltages to the stack, i.e. ${}_{x+1}V_2^r$, ${}_xV_4^r$, using the three-layer thin film model described in section 3.3.2.

As discussed in section 3.3.2, the admittance matrix of each layer in the three-layer stack can be expressed as

$$\begin{pmatrix} I_4 \\ I_a \end{pmatrix} = \begin{pmatrix} y_{TL} - jY_0 cot\theta_1 & jY_0 csc\theta_1 \\ jY_0 csc\theta_1 & -jY_0 cot\theta_1 \end{pmatrix} \begin{pmatrix} {}_xV_4 \\ V_a \end{pmatrix}, \tag{6-1}$$

$$\begin{pmatrix} -I_a \\ I_b \end{pmatrix} = \begin{pmatrix} -jY_t cot\theta_t & jY_t csc\theta_t \\ jY_t csc\theta_t & -jY_t cot\theta_t \end{pmatrix} \begin{pmatrix} V_a \\ V_b \end{pmatrix}, \tag{6-2}$$

$$\begin{pmatrix} -I_b \\ I_2 \end{pmatrix} = \begin{pmatrix} -jY_0 cot\theta_2 & jY_0 csc\theta_2 \\ jY_0 csc\theta_2 & y_{TL} - jY_0 cot\theta_2 \end{pmatrix} \begin{pmatrix} V_b \\ {}_{(x+1)}V_2 \end{pmatrix}, \tag{6-3}$$

where Y_0 is the characteristic admittance of the air layer given by $Y_0 = \sqrt{\varepsilon_0/\mu_0}$, θ_1 and θ_2 are the electrical lengths of the layers with length l_1 and l_2 expressed as $\theta_1 = \omega l_1\sqrt{\mu_0\varepsilon_0}$ and $\theta_2 = \omega l_2\sqrt{\mu_0\varepsilon_0}$, respectively.

The electrical length of the thin film that represents the curved panel is $\theta_t = \omega d\sqrt{LC}$, where d is the thickness of the film and $Y_t = \sqrt{C/L}$ is the admittance of the thin film where L and C can be expressed as in [6.4]

$$L = \mu + \frac{\sigma_m}{j\omega}, C = \varepsilon + \frac{\sigma_e}{j\omega}. \tag{6-4}$$

Combining equations (6-1), (6-2) and (6-3), the linear matrix equations (6-5) can be obtained,

$$\begin{pmatrix} I_4 \\ 0 \\ 0 \\ I_2 \end{pmatrix} = \begin{pmatrix} y_{TL} - jY_0 cot\theta_1 & jY_0 csc\theta_1 & 0 & 0 \\ jY_0 csc\theta_1 & -jY_0 cot\theta_1 - jY_t cot\theta_t & jY_t csc\theta_t & 0 \\ 0 & jY_t csc\theta_t & -jY_t cot\theta_t - jY_0 cot\theta_2 & jY_0 csc\theta_2 \\ 0 & 0 & jY_0 csc\theta_2 & y_{TL} - jY_0 cot\theta_2 \end{pmatrix} \begin{pmatrix} {}_xV_4 \\ V_a \\ V_b \\ {}_{(x+1)}V_2 \end{pmatrix}. \tag{6-5}$$

The terms on the left hand side of equation (6-5) are known and are

$$I_4 = 2y_{TL} \cdot {}_xV_4^r, \qquad I_2 = 2y_{TL} \cdot {}_{(x+1)}V_2^r. \tag{6-6}$$

The unknown voltages on its right side, ${}_xV_4, V_a, V_b$ and ${}_{(x+1)}V_2$, can be solved using an iterative matrix solver based on the Gauss-Seidel method [6.5] as described in section 3.3.2. The solutions are given in the frequency domain and need to be transferred into the time domain to enable time-stepping of the TLM code. This is done by using an inverse Z-transform and digital filter theory.

In order to do that, the cotangent and cosecant functions in equation (6-5) are expanded as an infinite summation in the form of [6.6]

$$\begin{aligned} jYcot\theta &= j\sqrt{\frac{C}{L}}\left(\frac{1}{\theta} + 2\theta \sum_{k=1}^{N=\infty} \frac{1}{\theta^2 - k^2\pi^2}\right), \\ jYcsc\theta &= j\sqrt{\frac{C}{L}}\left(\frac{1}{\theta} + 2\theta \sum_{k=1}^{N=\infty} \frac{(-1)^k}{\theta^2 - k^2\pi^2}\right), \end{aligned} \tag{6-7}$$

where N denotes the number of terms in the expansion and determines the accuracy of the expansion.

With this expansion in place, the solutions of equation (6-5), i.e. ${}_xV_4, V_a, V_b$ and ${}_{(x+1)}V_2$ are first transferred to the s-domain using the transformation s=jω and then to the Z-domain using the transformation

$$s = \frac{2}{\Delta t} \cdot \frac{1 - z^{-1}}{1 + z^{-1}}. \tag{6-8}$$

The final solutions are expressed in the time domain using the inverse Z transform and general digital filter theory as in section 3.2.

The embedded curved thin film model can be simplified to simulate the curved perfect electric conductor (PEC) boundaries, for example, modelling a curved metal structure.

The same linearisation as in Fig. 6-1 is firstly used to model the curved PEC boundaries. As in Fig. 6-1 (b), the cross points may be exactly between two nodes as for point A in Fig. 6-1 (b) or split the transmission line of a node at an arbitrary position as for point B in Fig. 6-1 (b). At point A, the incident voltage to the transmission line equals the negative value of the reflected voltage from the transmission line due to the short circuit effects of the PEC boundaries. At point B, the three layer stack shown in Fig. 6-2 is reduced to only one layer transmission line since there is no transmission outside the PEC boundaries. Fig. 6-4 (a) shows the one layer model of the PEC boundaries when the point B is placed at distance l_1 away from the $(n_x,\ n_y)$ node. Fig. 6-4 (b) shows the equivalent transmission line model with the air layer represented by a transmission line of length l_1 and a metal layer represented by a short circuit (S/C) boundary.

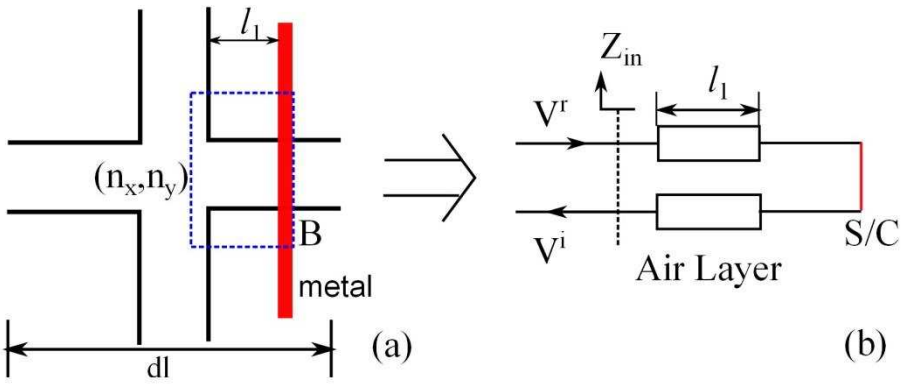

Fig. 6-4 (a) The one layer model of the PEC boundaries and (b) the equivalent transmission line model.

In Fig. 6-4 (b), V^i and V^r are the incident and reflected voltages along the right transmission line of a node (n_x, n_y), respectively. The relation between V^i and V^r can be expressed as,

$$V^i = R \cdot V^r, \tag{6-9}$$

where R is the reflection coefficient, given by [6.7]

$$R = \frac{Z_{in} - Z_{TL}}{Z_{in} + Z_{TL}} = \frac{jZ_0 tan\theta_{air} - Z_{TL}}{jZ_0 tan\theta_{air} + Z_{TL}} = \frac{Z_0 + Z_{TL} \cdot jcot\theta_{air}}{Z_0 - Z_{TL} \cdot jcot\theta_{air}}, \tag{6-10}$$

where Z_{in} is the input impedance and θ_{air} is the electrical length of the air layer.

Thus,

$$(Z_0 - Z_{TL} \cdot jcot\theta) \cdot V^i = (Z_0 + Z_{TL} \cdot jcot\theta) \cdot V^r. \tag{6-11}$$

The incident voltage V^i in equation (6-11) can be solved using the Z transform and digital filter technique as described in the section 3.2.

6.3. Validations

Since modelling curved thin films involves linearisation and embedding the structure into the TLM algorithm, the accuracy of the linearisation of the embedded curved thin film model is firstly tested by extracting the resonant frequencies of infinitely long, hollow, circular and elliptical PEC cylinders using the model for the curved PEC boundaries. Furthermore, the convergence and accuracy of the embedded curved thin film model are investigated by comparing the resonant frequencies of the infinitely long, hollow, circular and elliptical cylinders formed using CFC materials with those analytical values of the equivalent metal cylinders.

In the following examples, 2D series nodes and 2D shunts nodes, as discussed in Chapter 2, were used to model free space for TE and TM modes, respectively. A delta pulse was used as an excitation. Matched boundaries [6.4] were used to terminate the computational space.

6.3.1. Accuracy of Linearisation of Curved Structures

To verify the accuracy of the linearisation of the curved structures, the resonant frequencies of the infinitely long, hollow, circular and elliptical metal cylinder were calculated using the model for PEC boundaries. Results obtained are compared to those analytical values.

The resonant frequencies of a metal circular cylinder with a radius of r = 3 cm are calculated first. An input signal in the form of a delta pulse was launched from a point (3 cm, 3 cm). The TLM simulation was run for $2 \cdot 10^5$ time steps.

The analytical resonant frequencies of a metal cylinder for TE and TM modes, f_{mn}^{TE} and f_{mn}^{TM}, are calculated using the following equations from [6.8],

$$\begin{aligned} f_{mn}^{TE} &= \frac{\chi'_{mn}}{2\pi r\sqrt{\mu\varepsilon}}, \qquad m = 0,1,2,\ldots \quad n = 1,2,\ldots \\ f_{mn}^{TM} &= \frac{\chi_{mn}}{2\pi r\sqrt{\mu\varepsilon}}, \qquad m = 0,1,2,\ldots \quad n = 1,2,\ldots \end{aligned} \tag{6-12}$$

where χ'_{mn} are the zeroes of the derivative of the Bessel function $J_m(x)$, i.e. $J'_m(\chi'_{mn}) = 0$, χ_{mn} are the zeroes of the Bessel function $J_m(x)$, i.e. $J_m(\chi_{mn}) = 0$, and r is the radius of the circle.

Fig. 6-5 shows the percentage errors in resonant frequencies for the first six TE and TM modes calculated using the analytical method and the embedded TLM method for different discretisations, represented by the ratio r/dl, where the percentage errors are defined as

$$\text{Percentage Errors} = \frac{|f_{analytical} - f_{TLM}|}{f_{analytical}} \cdot 100\%, \tag{6-13}$$

where $f_{analytical}$ and f_{TLM} represent the resonant frequencies calculated using the analytical method and the embedded TLM method. Usually 2% error is deemed to be a very good accuracy [6.9] in numerical calculations.

Fig. 6-5 shows that as the mesh size decreases (the ratio r/dl increases), the percentage errors in the resonant frequencies for the first six TE and TM modes also decrease. When the mesh size is 0.3 mm, i.e. $\frac{r}{dl} = 100$, the errors

are very small, within 0.8%. It validates the accuracy and convergence of the linearisation of the curved thin film model.

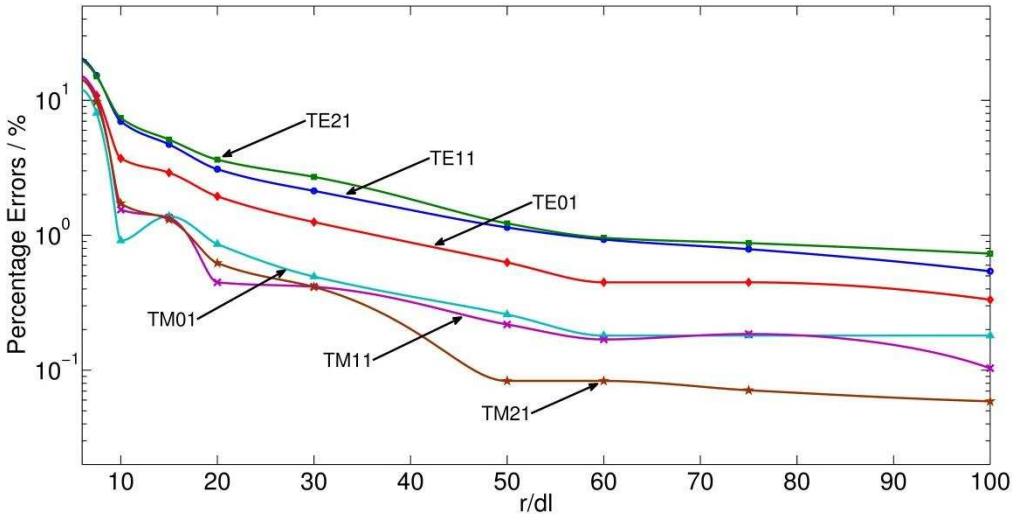

Fig. 6-5 The percentage errors in the resonant frequencies for TE and TM modes of metal circular cylinder.

To further validate the accuracy of the linearisation of the curved structures, the resonant frequencies of a metal elliptical cylinder with a major axis a = 10 cm and minor axis b = 6.614 cm [6.10] were calculated using the model for the PEC boundaries. An input signal in the form of a delta pulse was launched from a point located at the point (0.1 m, 0.06 m). The TLM simulation was run for $2 \cdot 10^5$ time steps.

Fig. 6-6 shows the percentage errors (defined in equation (6-13)) in resonant frequencies for the first six TE and TM modes calculated using the analytical method and the embedded TLM method for different discretisations, represented as the ratio $\frac{b}{dl}$. In the figure, e and o represent even and odd modes, respectively. The analytical values of the metal elliptical cylinder are taken from [6.10]. Fig. 6-6 shows that when the mesh size is 0.8 mm ($\frac{b}{dl} = 82.5$), the percentage errors in all resonant frequencies are very small, within 1.6%. The accuracy of the linearisation is further validated.

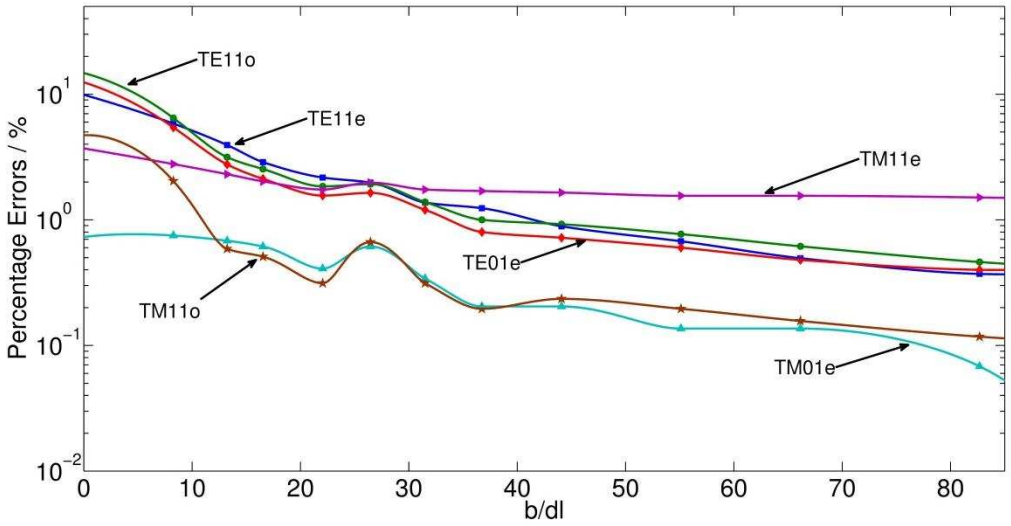

Fig. 6-6 The percentage errors in the resonant frequencies for TE and TM modes of metal elliptical cylinder.

6.3.2. CFC Circular Cylinder

In this section, the embedded curved thin film model is used to calculate the resonant frequencies of an infinitely long, hollow, circular CFC cylinder with the radius of r = 3 cm. Results obtained are compared against the analytical values for the equivalent metal circular cylinder.

The parameters of the CFC materials used in this section were chosen as in [6.11]: thickness $d = 1\,\mathrm{mm}$, effective permittivity $\varepsilon_r = 2$ and conductivity $\sigma_e = 10^4\,\mathrm{Sm}^{-1}$. The 2D computation window was chosen to be $18\,\mathrm{cm} \times 18\,\mathrm{cm}$ and terminated with matched boundaries. The number of time steps used in the calculation is $2 \cdot 10^5$.

Fig. 6-7 shows the relative differences in the resonant frequencies for the first six TE and TM modes of the CFC and metal circular cylinder for different mesh sizes represented by r/dl. The relative differences in the resonant frequencies are defined as

$$\text{Relative differences} = |f_{metal} - f_{CFC}|/f_{metal} \times 100\% \qquad (6\text{-}14)$$

where f_{metal} and f_{CFC} are the resonant frequencies of the metal and CFC cylinder, respectively.

Fig. 6-7 shows that the relative differences in the resonant frequencies of TE_{21} and TE_{11} mode converge to around 1% and the relative differences in the TE_{01} mode resonant frequencies converge to around 0.4%, as the mesh size decreases. The relative differences in the TM_{01}, TM_{11} and TM_{21} mode resonant frequencies converge to around 0.3%, 0.2% and 0.18%, respectively, as the mesh size decreases. Fig. 6-7 confirms the resonant frequencies of CFC cylinder are similar to those of the metal cylinder, confirming the metal-like properties of the CFC materials.

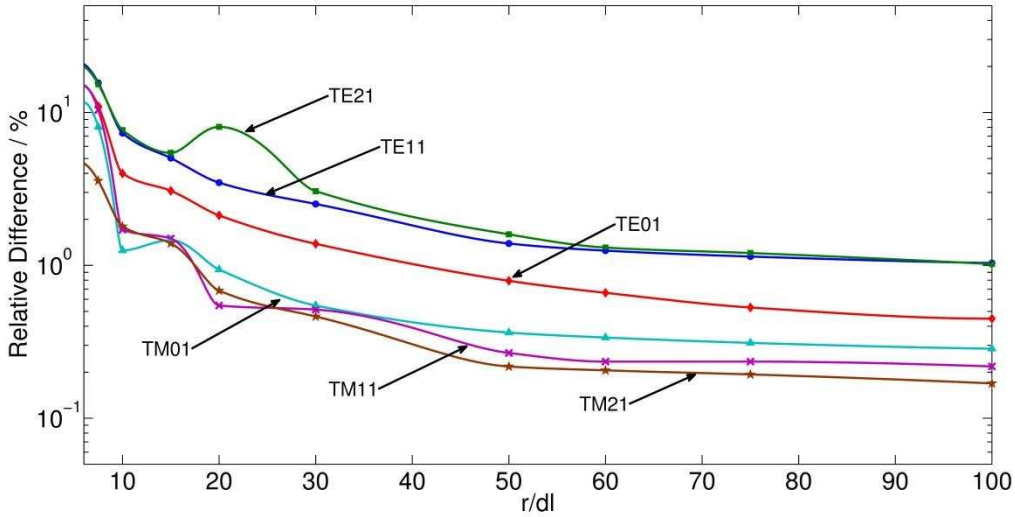

Fig. 6-7 The relative differences in the resonant frequencies for TE and TM modes of the CFC circular cylinder and the metal circular cylinder.

Table 6-1 further compares the resonant frequencies of the first six TE and TM modes of the CFC and metal circular cylinder when the mesh size $dl =$ 0.03 cm ($\frac{r}{dl} = 100$). It can be seen that the relative differences in the resonant frequencies of the CFC and metal cylinder are very small and within 1.02%.

Table 6-1 The resonant frequencies and relative percentage differences between the first three TE and TM modes of the CFC and metal circular cylinder.

Modes	Resonant Frequency (GHz)		Relative Differences (%)
	Metal Circular Cylinder	CFC Circular Cylinder	
TE_{11}	2.9283	2.899	1.00
TE_{21}	4.8575	4.808	1.02
TE_{01}	6.0943	6.067	0.45
TM_{01}	3.8249	3.814	0.28
TM_{11}	6.0943	6.081	0.22
TM_{21}	8.1668	8.153	0.17

6.3.3. CFC Elliptical Cylinder

In this section the embedded curved thin film model is used to extract the resonant frequencies of CFC elliptical cylinders. Results obtained are compared against the known analytical values for the equivalent metal elliptical cylinder.

The CFC elliptical cylinder has the same dimensions as that of the metal elliptical cylinder described in section 6.3.1. The parameters of the CFC materials used were chosen as in [6.11]: thickness $d = 1\,\text{mm}$, effective permittivity $\varepsilon_r = 2$ and conductivity $\sigma_e = 10^4\,\text{Sm}^{-1}$. The 2D computation window was set to $40\,\text{cm} \times 26\,\text{cm}$, and terminated with matched boundaries [6.4]. The number of time steps used in the calculation is $2 \cdot 10^5$.

Fig. 6-8 shows the relative differences (defined in equation (6-14)) in the resonant frequencies of the first six TE and TM modes of the CFC and metal elliptical cylinder for different mesh sizes represented by the $\frac{b}{dl}$ parameter. It can be seen that the relative differences in the even (e) and odd (o) TE_{11} mode resonant frequencies converge to around 0.7% and the relative differences in the even TE_{01} mode resonant frequencies converge to around 0.5% as the mesh size decreases. Fig. 6-8 also indicates that the relative differences in the even TM_{11} mode resonant frequencies converge to around 1.56% and the relative differences in the odd TM_{11} and even TM_{01} mode resonant frequencies

converge to around 0.2% as the mesh size decreases. Fig. 6-8 confirms that the resonant frequencies of the CFC resonator are close to those of the metal resonator, once more confirming the metal-like properties of the CFC material.

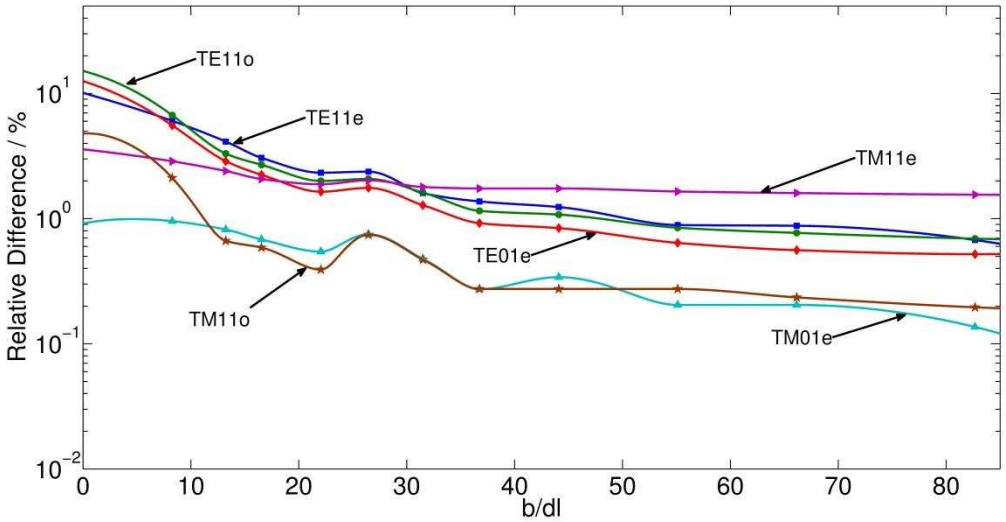

Fig. 6-8 The relative differences of the resonant frequencies for TE and TM modes in the CFC elliptical cylinder and metal elliptical cylinder.

Table 2 further compares the resonant frequencies of the metallic and CFC elliptical cylinder for the first six modes when the mesh size $dl = 0.8$ mm ($\frac{b}{dl} = 82.7$). It can be seen that the relative differences in the resonant frequencies of the CFC cylinder and metal cylinder are very small and within 1.56%.

Table 2 The resonant frequencies for the six lowest modes of an elliptical CFC cylinder compared to those of an elliptical metal cylinder

Modes	Resonant Frequency (GHz)		Relative Difference (%)
	Metal elliptical cylinder	CFC elliptical cylinder	
Even TE_{11}	0.889	0.883	0.67
Odd TE_{11}	1.30	1.291	0.69
Even TM_{01}	1.467	1.465	0.14
Even TM_{11}	2.124	2.091	1.56
Even TE_{01}	2.50	2.487	0.52
Odd TM_{11}	2.554	2.549	0.20

In summary, the convergence and accuracy of the embedded curved thin film model are verified by comparing the resonance frequencies of the circular and elliptical CFC cylinders with those analytical values of the equivalent circular and elliptical metal cylinders.

6.4. Applications

In this section, the embedded model for curved thin films is applied to analyse the shielding performance of a CFC airfoil with the profile NACA2415. Furthermore, the effect of small gaps in the airfoil structure on the shielding performance is also discussed.

In the following examples, 2D shunt nodes were used to model free space. The excitation was chosen to be in the form of a TE-polarised plane wave as described in section 5.4. The wave propagates from the bottom of the space to the top of the space. Matched boundaries [6.4] were set in the four boundaries to simulate the infinite space.

The parameters of the CFC materials used in this section were chosen as in [6.10]: thickness $d = 1\,\mathrm{mm}$, effective permittivity $\varepsilon_r = 2$ and conductivity $\sigma_e = 10^4\ \mathrm{Sm}^{-1}$.

6.4.1. Shielding Performance of a CFC Airfoil Structure

The profile of an airfoil structure is taken from the National Advisory Committee for Aeronautics (NACA) report [6.3]. An airfoil with the profile NACA2415 from the NACA four-digit series is taken as an example.

In the NACA four-digit series, the first digit specifies the maximum camber (m) in percentage of the chord (airfoil length ch); the second digit indicates the position of the maximum camber along the chord (p) in tenths of chord; the last two digits provide the maximum airfoil thickness (t) in percentage of chord. These terminologies in the airfoil are shown in Fig. 6-9.

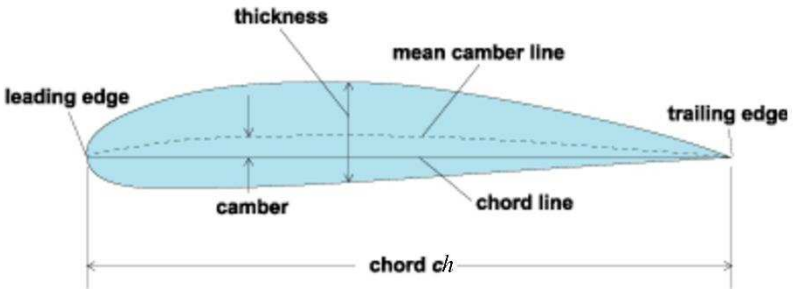

Fig. 6-9 Airfoil terminology

In the example of the airfoil NACA2415, the airfoil length ch was chosen as 1 m. It has a maximum thickness t = 0.15 m with a camber m = 0.02 m located 0.4 m back from the airfoil leading edge. Based on these values, the coordinates for the entire airfoil can be computed using the analytical equations reported in [6.3]. Fig. 6-10 shows the profile of the airfoil NACA2415 modelled using the TLM method, with a computational window size of 1.2 m $\times$ 0.3 m terminated with matched boundary conditions.

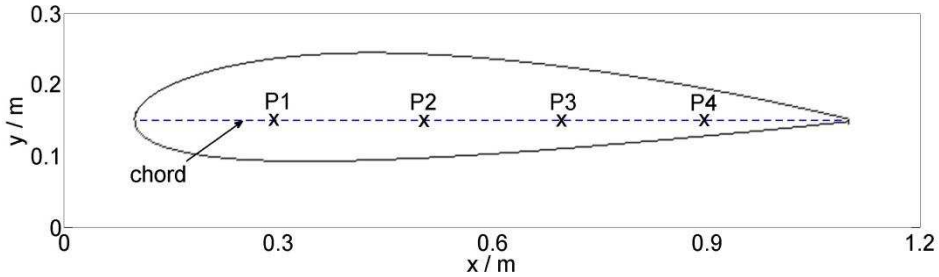

Fig. 6-10 The CFC airfoil NACA2415 modelled by TLM

The electric field shielding effectiveness SE_E in dB is defined as in [6.12],

$$SE_E = 20 \cdot \log_{10}(|E^{without}/E^{with}|) \tag{6-15}$$

where $E^{without}$ and E^{with} are the magnitudes of the electric field component at the same point without and with the shield.

The magnitude of the electric field component E_z is observed at four points along the chord, i.e. P1 (0.3 m, 0.15 m), P2 (0.5 m, 0.15 m), P3 (0.7 m, 0.15 m), and P4 (0.9 m, 0.15 m) as shown in Fig. 6-10, with and without the CFC airfoil. The electric shielding effectiveness (SE) is computed at these four specific points along the chord using equation (6-15).

Fig. 6-11 shows the electric field shielding effectiveness of the CFC airfoil NACA2415 at the points P1, P2, P3 and P4 in the frequency range from 1 GHz to 2 GHz. The TLM mesh size used was $dl = 2$ mm. It can be seen that the SE of the airfoil becomes much smaller at certain frequencies due to resonance effects [6.13]. Fig. 6-11 also indicates that the SE at the points P1 and P2 are similar in the frequency range from 1 GHz to 2 GHz, while the SE at the point P3 is higher than that at the points P1 and P2 at the frequencies below 1.2 GHz and the SE at the point P4 is much higher than that at the points P1 and P2 at the frequencies below 1.7 GHz. At higher frequencies, the SE is very similar for all the four points because the existence of the higher modes contributes to an even distribution of the electric field in the structure.

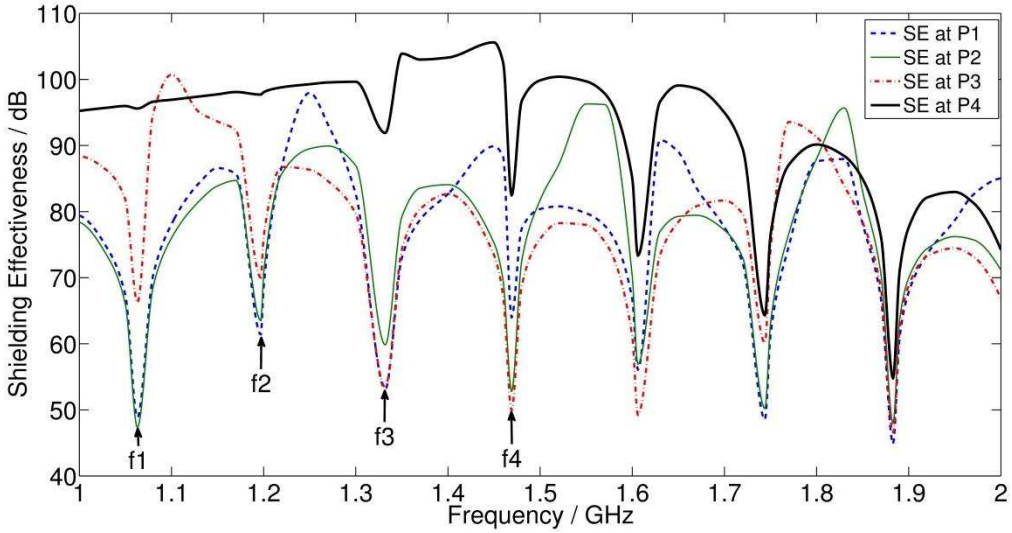

Fig. 6-11 The electric field shielding effectiveness of the CFC airfoil NACA2415.

To explain the lower SE at the points P1 and P2 at lower frequencies, compared to that at the points P3 and P4, the scattering of the CFC airfoil NACA2415 when illuminated by the TE wave at $f_1 = 1.063$ GHz is shown in Fig. 6-12. The electric field intensity in the 2D space at the $10^4 th$ time step is plotted in dB. As shown in the figure, due to the non-metallic properties of the CFC panel, the electric field penetrates the airfoil and excites the first resonant mode. The centre of the resonant mode is near the points P1 and P2, leading to the lower shielding effectiveness at these points at 1.063 GHz. The resonance

has little effect on the electric field at the point P4 so the SE at the point P4 is high.

It is emphasised that the field is shown on a logarithmic scale and that the intensity of the field inside the CFC airfoil is small compared to that of the excitation wave, as can be seen in Fig. 6-12.

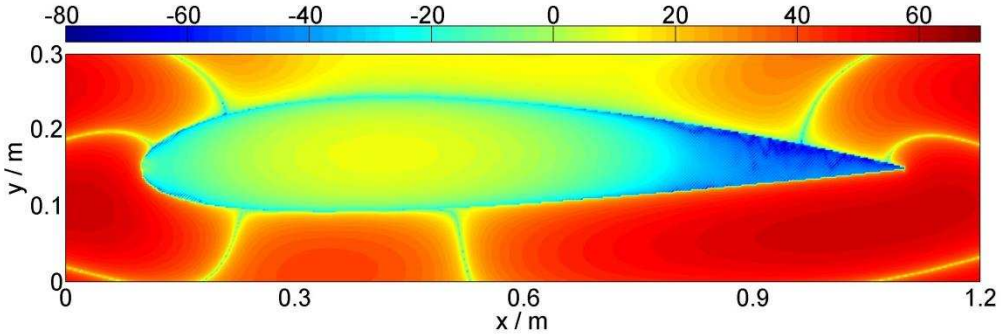

Fig. 6-12 The scattering of the CFC airfoil NACA2415 upon the 1.063 GHz TE wave illumination. The plot shows electric field intensity on a dB scale.

In order to show the convergence of the proposed model, the first four resonant frequencies of the CFC airfoil (labelled as f_1, f_2, f_3 and f_4 in Fig. 6-10) were calculated using different mesh sizes and are shown in Fig. 6-13 as a function of t/dl. The figure indicates that as the mesh size decreases, all four resonant frequencies converge.

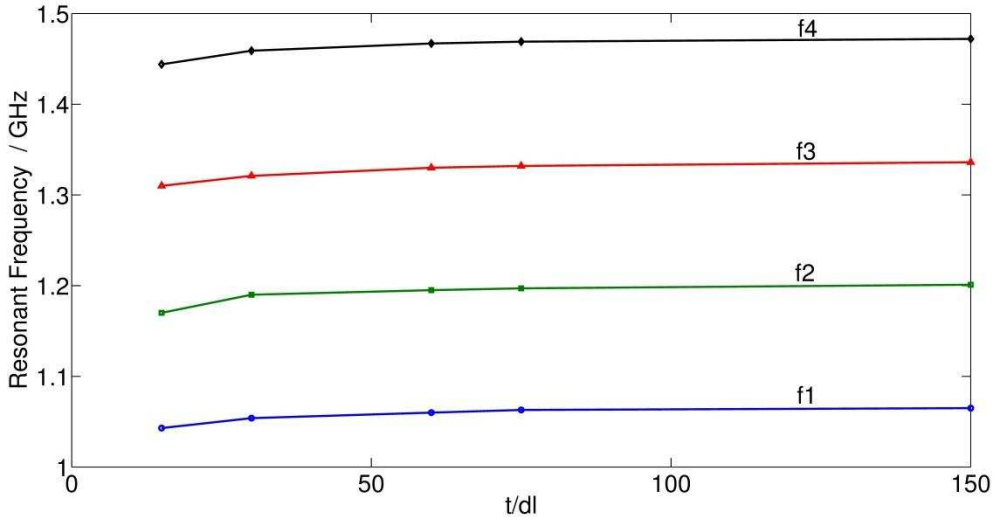

Fig. 6-13 The first four resonant frequencies of the CFC airfoil NACA2415 against t/dl.

If the conventional TLM method is used to model the CFC airfoil, the mesh size should be chosen as 0.025 mm as discussed in Chapter 4. Based on a mesh size of 0.025 mm, there would be $48{,}000 \times 12{,}000$ nodes only for the finite region of 1.2 m $\times$ 0.3 m, excluding the CFC panel. In addition, the number of time steps needed in the conventional TLM method is 80 times bigger than that needed in the embedded model in order to get the same frequency resolution. Therefore, the embedded model has the advantage of saving the computational costs significantly in terms of memory storage and the number of time steps, compared to the conventional TLM method.

6.4.2. Shielding Performance of CFC Airfoil Structure with Gaps

Imperfections on the airfoil, such as gaps, even if very small, can affect the SE of the structure [6.14]. This section investigates the impact of the gaps on the SE of the CFC airfoil.

The same CFC airfoil NACA2415 is used and the gap is positioned in the downside of the structure at $x = 0.9$ m. Two examples were chosen, one with a gap of 2 mm and the other with a gap of 6 mm. The excitation of the problem is the same as that for Fig. 6-11. The shielding effectiveness at the points P1 and P4 along the chord of the CFC airfoil is computed and shown in Fig. 6-14 (a) and (b), respectively, for two different size gaps in the airfoils and compared to the case of no gaps in the frequency range from 1 GHz to 2 GHz.

Fig. 6-14 (a) shows when the frequency is below 1.1 GHz, the gaps in the airfoil do not affect the SE at the point P1. However, as the frequency increases, the SE at the point P1 decreases rapidly for both airfoils with 2 mm and 6 mm gaps compared to the case of no gaps in the airfoil. For example, at the seventh resonant frequency (1.883 GHz), the shielding effectiveness of the airfoils with 2 mm and 6 mm gaps is around 25 dB and 14 dB, respectively, compared to 45 dB with the case of no gaps. This can be explained by the fact that at higher frequencies, the shorter wavelength of the signal results in an

increased penetration of fields through the gap, which change the field distribution in the airfoil.

Unlike the SE at the point P1, the SE at the point P4 is greatly influenced by the gaps in the airfoil as shown in Fig. 6-14 (b). The SE at the point P4 is drastically reduced in the frequency range from 1 GHz to 2 GHz, for both airfoils with 2 mm and 6 mm gaps compared to the case of no gaps in the airfoil. The reduction of the SE at the point P4 is more prominent at the lower frequency. For example, at 1.063 GHz, the SE at the point P4 of the airfoil with 2 mm and 6 mm gaps is reduced by around 40 dB and 50 dB, respectively, compared to that of the airfoil without gaps.

To explain the prominent reduction of the SE at the point P4 at lower frequencies, the scattering of the CFC airfoil NACA2415 with a 2 mm hole under illumination from a TE wave at $f_1 = 1.063$ GHz is shown in Fig. 6-15. The electric field intensity in the 2D space at the $10^4 th$ time step is plotted in dB. It can be seen that the small gap allows the incident field to more readily couple with the inside of the airfoil. Compared to Fig. 6-12, the field intensity is increased at the tail of the airfoil, resulting in reduced shielding performance of the airfoil at the point P4. Comparison of Fig. 6-12 and Fig. 6-15 indicates that the field penetrating through the gap does not greatly perturb the resonant field at point P1 at 1.063 GHz, so the SE at that point is not significantly affected by the gap, as seen in Fig. 6-14 (a).

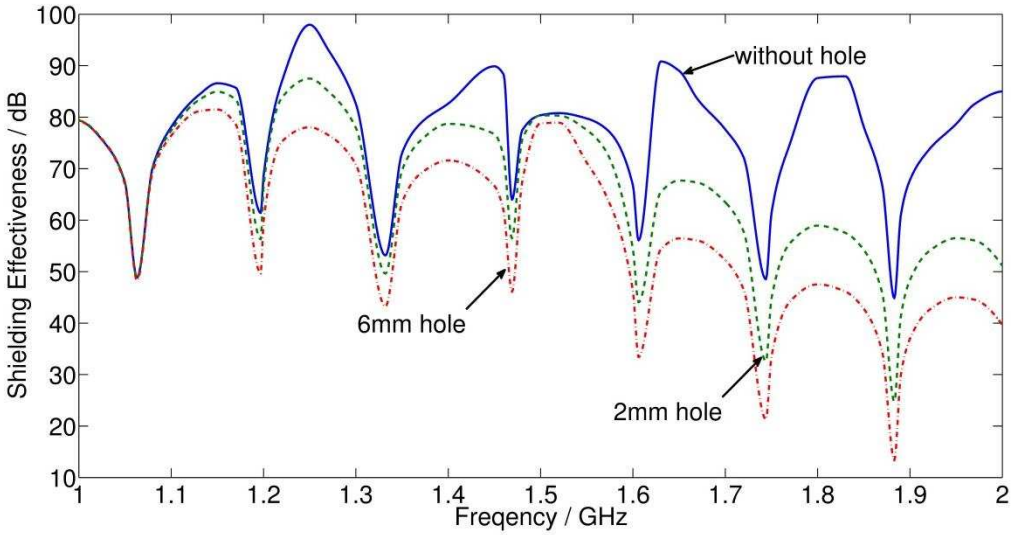

(a)

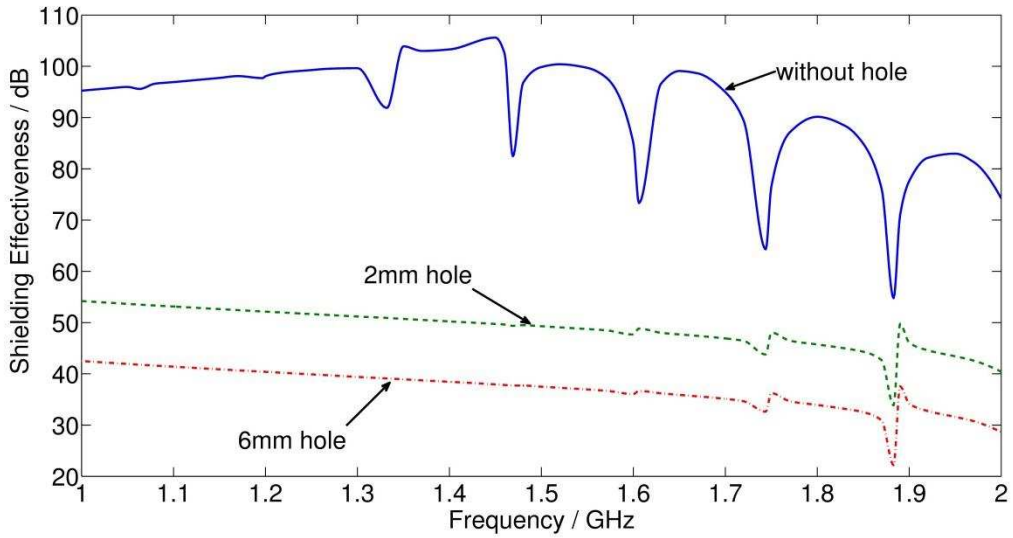

(b)

Fig. 6-14 The shielding effectiveness of the CFC airfoil NACA2415 with no gap, a 2 mm gap and 6 mm gap (a) at the point P1 and (b) at the point P4.

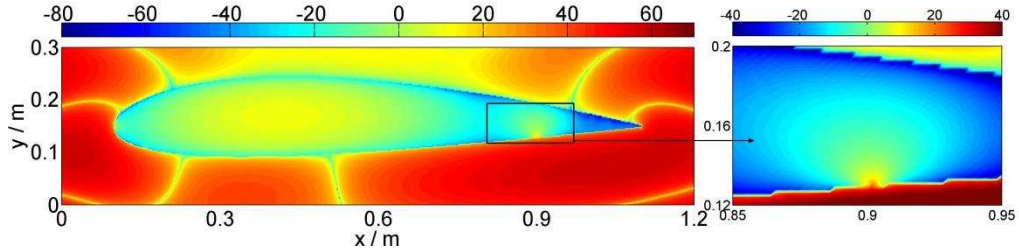

Fig. 6-15 The scattering of the CFC airfoil NACA2415 with 2 mm gap in the 1.063 GHz TE wave illumination. The plot shows electric field intensity on a dB scale.

6.5. Conclusions

In this chapter, an embedded TLM model for curved thin films is described. Its implementation in the 2D TLM algorithm is done by firstly, linearising the curvature of the panel and secondly, representing the panels as three-layer transmission lines to allow for arbitrary positioning of the panel within the mesh.

The embedded model is validated by firstly comparing the resonant frequencies of metallic 2D circular and elliptical resonators with analytical values to verify the accuracy of the linearisation. The differences between the CFC and metallic circular and elliptical resonators have also been obtained, confirming good metallic properties of the CFC material. Finally, the embedded model is applied to analyse the shielding performance of a CFC airfoil NACA2415 structure. The impact of small gaps in the CFC airfoil on the SE is also reported, showing considerable worsening in the SE performance.

The embedded model for curved structures was also proved to have the advantage of saving the computational overheads significantly since a relative large mesh size can be used, thus saving the memory storage and number of time steps.

References

[6.1] M. Apr, M. D. Amore, K. Gigliotti, M. S. Sarto, S. Member, and V. Volpi, “Lightning indirect effects certification of a transport aircraft by numerical simulation,” IEEE Transactions on Electromagnetic Compatibility, vol. 50, no. 3, pp. 513–523, 2008.

[6.2] B. D. Cordill, S. A. Seguin, and M. S. Ewing, “Shielding effectiveness of carbon–fiber composite aircraft using large cavity theory,” IEEE Transactions on Instrumentation and Measurement, vol. 62, no. 4, pp. 743–751, 2013.

[6.3] E. N. Jacobs, K. E. Ward, and R. M. Pinkerton, “The characteritics of 78 related airfoil sections from tests in the variable-density wind tunnel,” NACA report No.460, 1933.

[6.4] C. Christopoulos, The Transmission-Line Modeling Method TLM. IEEE Press, 1995.

[6.5] H. Press, A. Teukolsky, T. Vetterling, and P. Flannery, Numerical Recipes in C++. The Art of Computer Programming. Cambridge University Press, 2002.

[6.6] M. Abramowitz and I. A. Stegun, Handbook of Mathematical Functions with Formulas, Graphs, and Mathematical Tables. Washington, D.C.: Government printing office, 1972.

[6.7] S. Ramo, J. R. Whinnery, and T. Van Duzer, Fields and Waves in Communication Electronics, 3rd ed. John Wiley & Sons, Inc., 1997.

[6.8] C. A. Balanis, Advanced Engineering Electromagnetics. Wiley New York, 1989.

[6.9] G. D. Tsogkas, J. A. Roumeliotis, and S. P. Savaidis, “Cutoff wavelengths of elliptical metallic waveguides,” IEEE Trans. Microw. Theory Tech., vol. 57, no. 10, pp. 2406–2415, 2009.

[6.10] D. A. Goldberg, L. J. Laslett, and R. A. Rimmer, “Modes of elliptical waveguides: a correction,” IEEE Transactions on Microwave Theory and Techniques, vol. 38, no. 11, pp. 1603–1608, 1990.

[6.11] M. S. Sarto, “A new model for the FDTD analysis of the shielding performances of thin composite structures,” IEEE Transactions on Electromagnetic Compatibility, vol. 41, no. 4, pp. 298–306, 1999.

[6.12] C. R. Paul, Introduction to Electromagnetic Compatibility. Wiley New York, 1992.

[6.13] L. Klinkenbusch, “On the shielding effectiveness of enclosures,” IEEE Transactions on Electromagnetic Compatibility, vol. 47, no. 3, pp. 589–601, 2005.

[6.14] R. W. Scharstein, M. L. Waller, and T. H. Shumpert, “Near-Field and plane-wave electromagnetic coupling into a slotted circular cylinder : hard or TE polarization,” IEEE Transactions on Electromagnetic Compatibility, vol. 48, no. 4, pp. 714–724, 2006.

7. Conclusions

7.1. Overview of the Work Presented

Modern circuits and numerical problems are becoming increasingly multi-scale in their appearance in that they contain both large and small features. High operating frequencies in many applications mean that small features can no longer be ignored and need to be sampled with a suitable mesh size, which consequently requires large run time and memory storage. To solve such problems, an efficient and versatile approach for embedding small features in an otherwise coarse mesh has been presented in this thesis. The embedded model removes the need for discretisation within itself and allows for the relatively coarse mesh to be used, thus saving the computational overheads. The thesis focuses on thin film panels as small features although any small feature for which an analytical response is known can in practice be implemented. In this thesis the implementation of thin films in the one-dimensional (1D) and two-dimensional (2D) Transmission Line Modelling (TLM) methods has been presented. The accuracy, stability, convergence and efficiency have been verified using examples of lossy and lossless thin films, in particular, single and multiple CFC panels, AR coatings and Fibre Bragg gratings.

In Chapter 2, the Transmission Line Modelling (TLM) method was introduced. Based on the field-circuit equivalence, the procedures for modelling free space using the 1D, 2D and 3D TLM models were firstly presented. Furthermore, the stub techniques and the condensed nodes were briefly overviewed as methods of modelling material parameters different from free space. These models were used to model the background materials surrounding the thin films.

In Chapter 3, time domain embedded thin film models, including a single layer thin film model, a multi-layer thin film model and an anisotropic thin film model, were derived in the TLM method. The single layer thin film model was firstly introduced. In the model, the single layer thin film was seen as a section of transmission line, whose admittance matrix was used to describe the

frequency responses of the thin film. The admittance matrix was manipulated by expanding the constituent cotangent and cosecant functions using their analytical expansion equations, which were then transformed to the time domain from the frequency domain using the inverse Z transform and general digital filter theory. In this way, the frequency responses of the thin film were sucessfully embedded into the TLM algorithm by modifying its connection process. Based on the single layer thin film model, the multi-layer thin film model was derived by solving a linear matrix equation describing the scattering properties of the multi-layer thin film using a Gauss-Seidel method. In the end, an anisotropic thin film model was introduced by using two single layer thin film models.

In Chapter 4, the accuracy, stability, convergence and efficiency of the embedded thin film models were validated in the one-dimensional (1D) TLM method using examples of lossy, anisotropic and lossless thin films.

As examples of lossy thin films, the frequency responses of carbon fibre composite (CFC) panels and a titanium panel were investigated using the embedded thin film model. The reflection and transmission coefficients of both single (layer thickness of 1 mm) and multiple layer CFC panels (layer thickness of 1.8 mm) were calculated using the embedded thin film model with a mesh size of 10 mm. The accuracy was verified by comparing the numerical results with the analytical results. For a single layer CFC panel, the errors in the reflection coefficients are less than 0.0006% while the errors in the transmission coefficients are less than 0.8% in the frequency range from 0 to 1 GHz. For a multi-layer CFC panel, the errors in the reflection coefficients are less than 0.001% while the errors in the transmission coefficients are less than 1.5% in the frequency range from 0 to 1 GHz. The reflection and transmission coefficients of a titanium panel (thickness 1.2 mm) were also calculated using the embedded thin film model with a mesh size of 1000 mm. The errors in the reflection coefficients are less than 0.00003% while the errors in the transmission coefficients are less than 0.4% in the frequency range from 0 to 10 MHz. The high accuracy in the reflection coefficients is due to the requirement that the percentage errors in the transmission coefficients are less

than 2%. To examine the efficiency of the embedded thin film model, the conventional TLM method was also used to model the CFC panels and titanium panel. In order to achieve the same accuracy as that of the embedded thin film model, the mesh size of the conventional TLM method was chosen to be 0.025 mm ($1/40$ of the thickness of the single layer thin film or $1/72$ of the thickness of the multi-layer thin film or $1/48$ of the thickness of the titanium panel). Since the mesh size of the conventional TLM method is restrictive to the thickness of the thin film, while the mesh size of the embedded thin film model is determined by the smallest wavelength of interest, the mesh size used in the embedded thin film model is much larger than that in the conventional TLM method. Therefore, the embedded thin film model is proven to have the advantage of saving computational resources significantly, including the memory usage and run time.

As examples of lossless thin films, the frequency responses of an antireflection (AR) coating and a fibre Bragg grating (FBG) were investigated using the embedded thin film model. For a single layer AR coating in the visible frequency spectrum, the errors in the reflection coefficients compared to the analytical results are less than 2% when the number of expansion terms is very large, i.e. N = 400. It was shown that the embedded thin film model has slow convergence in the case of lossless thin films with large electrical length. To alleviate this, the cotangent and cosecant expansions used were manipulated so that they are centred at desired frequency at which they converge faster. By doing so, the number of terms needed to approximate the infinite expansions was reduced by 20 times at a desired frequency. However, the downside of this modified model is that it works well only for single layer films. The transmission coefficients of a FBG structure were also calculated using the embedded thin film model. The errors in the transmission coefficients are less than 0.2% in the desired wavelength range. The conventional TLM method was also used to model the AR coating and FBG structure in order to examine the efficiency of the embedded thin film model. In order to achieve the same accuracy as that in the embedded thin film model, the mesh size used in the conventional TLM method was chosen to be 0.2 nm for the AR coating (5 times smaller than that used in the embedded thin film model) and 1 nm for the

FBG structure (10 times smaller than that used in the embedded thin film model). Therefore, the efficiency of the embedded model is validated by using a larger mesh size compared to the conventional TLM method.

In Chapter 5, the thin film model developed in Chapter 3 was extended to the two-dimensional (2D) TLM method to account for arbitrary excitations. It was firstly used to model the infinitely long thin films at oblique incidence. Here thin films were viewed as a 1D model embedded into the TLM algorithm due to the introduction of a transverse impedance. The model was then extended to include thin films with finite length at arbitrary excitations by using the plane wave decomposition theory. It was the first time that the plane wave decomposition theory has been combined with the TLM method. In order to simulate a plane wave propagating in an infinite space at oblique incidence, plane wave excitation methods for both TE- and TM- polarised waves were presented.

After introducing the theory, the accuracy and convergence of the embedded thin film model for arbitrary excitations were verified by calculating the reflection and transmission coefficients of an infinitely long CFC panels with TE- and TM- polarised waves at different angles of incidence over a wide frequency range. In the end, the embedded thin film model for arbitrary excitations was applied to simulate a CFC panel with finite length with a point source excitation. The field propagation in the space with a CFC panel inside was shown at a certain time step for each field component. It was shown that the shielding performance of the CFC panel with finite length decreases rapidly as the distance from the panel increases because the finite length of the CFC panel allows the fields to propagate over the panel ends to the other side of the panel. In addition, the embedded model for arbitrary excitations was proved to have the advantage of saving the computational costs significantly, compared to the conventional TLM method.

In Chapter 6, the embedded thin film model developed in Chapter 3 was extended to model curved thin films in the 2D TLM method. Curved thin films were firstly linearised using piece-wise segments and then embedded into the TLM algorithm. The linear segment may split the link line of one TLM node

into two parts, so a three-layer stack was introduced to account for the arbitrary position of the linear segment within the TLM mesh.

The accuracy of the linearisation in the curved structure was firstly validated by comparing the resonant frequencies of 2D metallic circular and elliptical resonators calculated using the embedded thin film model and analytical method. The accuracy and convergence of the embedded thin film model was then verified by comparing the resonant frequencies of 2D CFC circular and elliptical resonators calculated using the embedded model with those of equivalent 2D metallic circular and elliptical resonators calculated using an analytical method. Furthermore, the embedded thin film model was applied to analyse the shielding performance of a CFC airfoil with the profile of NACA2415. It was shown that the shielding effectiveness inside the airfoil varies with the position of observation points. It was also noticed that the shielding performance of the airfoil become poor at certain frequencies because of the resonance effects. In addition, the worsening of the shielding effectiveness in the presence of small gaps in the airfoil was also reported. In addition, the embedded model for curved structures was proved to have the advantage of saving the computational costs significantly, compared to the conventional TLM method.

In conclusion, an embedded thin film model was developed in the Transmission Line Modelling method to solve a particular multi-scale problem, i.e. the presence of flat and curved thin film panels in a large space. In the presented model, thin films are not discretised so a relative large mesh size can be used in the simulation, thus saving the computational resources significantly. The accuracy, stability, convergence and efficiency have been validated in the one-dimensional TLM method using examples of lossy and lossless thin films. The embedded thin film model was also extended to two-dimensional TLM method to account for arbitrary excitations and curved thin film structures. The accuracy, efficiency and applicability of the embedded model in these two cases were validated using several examples.

It is noted that in the thesis, a significant reduction in the computational costs needed in the embedded model is based on the comparison with those needed

in the conventional TLM method. It is here emphasised graded and multi-grid techniques also reduce the computational costs; however, in these techniques, the problem that the time step is determined by the smallest of the mesh size still exists. In contrast to this, the embedded model developed in the thesis eliminates the need of discretising small features and thus keeps large mesh size and hence large number of time steps.

7.2. Future Work

Throughout the thesis, the embedded thin film model is discussed in the one-dimensional and two-dimensional Transmission Line Modelling (TLM) method. Whilst real three-dimensional (3D) problems can in some cases be approximated with equivalent 2D models, the full 3D model may be more useful in reality. The embedding of the thin film model in the 3D TLM method can be implemented by modifying its connection process as described in equations (2-36) – (2-47). The stability graph of the embedded model for all kinds of materials is another problem worth exploring.

To date small features such as thin panels and wires [7.1 ~ 7.2] have been embedded in the TLM method. However, this can be extended to include other electrically small objects such as bundles of wires, metal tracks on boards or small antennas.

Furthermore, recently a TLM algorithm based on unstructured TLM meshes [7.3 ~ 7.4] has been presented. An exciting area would be embedding the thin film model into the unstructured TLM method. The difficulty here is in dealing with the not-aligned position of the two node centres on both sides of the thin film that is imposed by the meshing algorithm.

In addition, another possible area of future work is the combination of the embedded model with a stochastic analysis. The uncertainty in the excitation or in material parameters caused by material in-homogeneities or fabrication and placement tolerance [7.5], makes the electromagnetic behaviour of the material difficult to predict. The perfect example is the placement of a bundle

of wires along the fuselage of an airplane for which it is necessary to include the stochastic analysis in the simulation [7.6]. Combining the stochastic analysis with an embedded model of the airframe may be another interesting subject of future work.

References

[7.1] X. Meng, P. Sewell, A. Vukovic, H. G. Dantanarayana, and T. M. Benson, "Efficient broadband simulations for thin optical structures," Optical and Quantum Electronics, vol. 45, no. 4, pp. 343–348, Oct. 2012.

[7.2] I. Scott, V. Kumar, C. Christopoulos, D. W. P. Thomas, S. Greedy, and P. Sewell, "Integration of behavioral models in the full-field TLM method," IEEE Transactions on Electromagnetic Compatibility, vol. 54, no. 2, pp. 359–366, Apr. 2012.

[7.3] P. Sewell, J. G. Wykes, T. M. Benson, C. Christopoulos, D. W. P. Thomas, and A. Vukovic, "Transmission-line modeling using unstructured triangular meshes," IEEE Transactions on Microwave Theory and Techniques, vol. 52, no. 5, pp. 1490–1497, 2004.

[7.4] P. Sewell, T. M. Benson, C. Christopoulos, D. W. P. Thomas, A. Vukovic, and J. G. Wykes, "Transmission-line modeling (TLM) based upon unstructured tetrahedral meshes," IEEE Transactions on Microwave Theory and Techniques, vol. 53, no. 6, pp. 1919–1928, 2005.

[7.5] A. Ajayi, S. Member, P. Ingrey, P. Sewell, S. Member, and C. Christopoulos, "Direct computation of statistical variations in electromagnetic problems," vol. 50, no. 2, pp. 325–332, 2008.

[7.6] L. R. A. X. de Menezes, A. Ajayi, C. Christopoulos, P. Sewell, and G. A. Borges, "Efficient computation of stochastic electromagnetic

problems using unscented transforms," IET Science, Measurement & Technology, vol. 2, no. 2, pp. 88–95, 2008.